



The ocean's global iron, phosphorus, and silicon cycles: inverse modelling and novel diagnostics

Author:

Pasquier, Benoit

Publication Date:

2017

DOI:

<https://doi.org/10.26190/unsworks/3239>

License:

<https://creativecommons.org/licenses/by-nc-nd/3.0/au/>

Link to license to see what you are allowed to do with this resource.

Downloaded from <http://hdl.handle.net/1959.4/58230> in <https://unsworks.unsw.edu.au> on 2024-07-30

The Ocean's Global Iron, Phosphorus, and Silicon Cycles: Inverse Modelling and Novel Diagnostics

Benoît Pasquier

A dissertation submitted in fulfilment
of the requirements for the degree of
Doctor of Philosophy



UNSW
AUSTRALIA

**The School of Mathematics and Statistics
The University of New South Wales**

19 June 2017 (document compilation)

THE UNIVERSITY OF NEW SOUTH WALES
Thesis/Dissertation Sheet

Surname or Family name: Pasquier

First name: Benoit

Other name/s: Jacques Charles

Abbreviation for degree as given in the University calendar: PhD

School: School of Mathematics and Statistics

Faculty: Faculty of Science

Title: The Ocean's Global Iron, Phosphorus, and Silicon Cycles:
Inverse Modelling and Novel Diagnostics

Abstract 350 words maximum: (PLEASE TYPE)

The ocean's biological pump is crucial for the carbon balance of the climate system, and the control of its three-dimensional "plumbing" on pump efficiency needed to be quantified. The nutrient cycles driving the biological pump are limited by dissolved iron (dFe). However, the iron cycle is poorly constrained, and the effects of iron source perturbations had never been quantified in a data-constrained model. In this thesis, we quantify the pathways and timescales of the biological pump, build an inverse model of the coupled phosphorus, silicon, and iron cycles, and explore the response of these cycles to changes in the aeolian iron supply.

We use Green-function methods to show that the Southern Ocean (SO) is where (62±2)% of regenerated phosphate (PO_4) reemerges after a mean sequestration time of 240±60yr. The pathways from productive regions to the SO contribute most to the biological pump, with a mean sequestration time of 130±70yr. Most PO_4 is carried by abyssal paths with transit times exceeding 700yr, while ~1/3 of the regenerated PO_4 from the equatorial Pacific that is destined for the SO is carried in Antarctic Intermediate Water.

We use the model of the coupled nutrient cycles in inverse mode to objectively determine biogeochemical parameters by minimizing the mismatch with observed nutrient and phytoplankton concentrations. We generate a family of estimates, all consistent with the observations, for a wide range of iron source strengths, themselves not constrainable by current observations. The carbon and opal exports are well constrained in magnitude and pattern. We quantify the systematics of the carbon and opal exports supported by aeolian, hydrothermal, and sedimentary dFe and find that aeolian dFe is the most efficient for supporting production.

The response to aeolian source perturbations is sensitive to the state of the iron cycle that is fitted to observations. A shutdown of the aeolian source does not completely untrap nutrients from the SO because sedimentary and hydrothermal dFe suffice to sustain production. A globally uniform 50-Gmol/yr aeolian iron addition fertilizes macronutrient-rich regions leading to increased deep regenerated and recycled dFe. This perturbation actually reduces iron fertilization supported by long-range transport because increased scavenging removes dFe before it can reach its destination. The response of the opal export is muted because the iron dependence of the Si:P uptake ratio counteracts fertilization.

Declaration relating to disposition of project thesis/dissertation

I hereby grant to the University of New South Wales or its agents the right to archive and to make available my thesis or dissertation in whole or in part in the University libraries in all forms of media, now or here after known, subject to the provisions of the Copyright Act 1968. I retain all property rights, such as patent rights. I also retain the right to use in future works (such as articles or books) all or part of this thesis or dissertation.

I also authorise University Microfilms to use the 350 word abstract of my thesis in Dissertation Abstracts International (this is applicable to doctoral theses only).

19 June 2017

.....
Signature

.....
Witness Signature

.....
Date

The University recognises that there may be exceptional circumstances requiring restrictions on copying or conditions on use. Requests for restriction for a period of up to 2 years must be made in writing. Requests for a longer period of restriction may be considered in exceptional circumstances and require the approval of the Dean of Graduate Research.

FOR OFFICE USE ONLY

Date of completion of requirements for Award:

Originality Statement

“I hereby declare that this submission is my own work and to the best of my knowledge it contains no materials previously published or written by another person, or substantial proportions of material which have been accepted for the award of any other degree or diploma at UNSW or any other educational institution, except where due acknowledgement is made in the thesis. Any contribution made to the research by others, with whom I have worked at UNSW or elsewhere, is explicitly acknowledged in the thesis. I also declare that the intellectual content of this thesis is the product of my own work, except to the extent that assistance from others in the project’s design and conception or in style, presentation and linguistic expression is acknowledged.”

Signed Benoît Pasquier
Date 19 June 2017 (document compilation)

Copyright Statement

“I hereby grant the University of New South Wales or its agents the right to archive and to make available my thesis or dissertation in whole or part in the University libraries in all forms of media, now or here after known, subject to the provisions of the Copyright Act 1968. I retain all proprietary rights, such as patent rights. I also retain the right to use in future works (such as articles or books) all or part of this thesis or dissertation. I also authorise University Microfilms to use the 350 word abstract of my thesis in Dissertation Abstract International (this is applicable to doctoral theses only). I have either used no substantial portions of copyright material in my thesis or I have obtained permission to use copyright material; where permission has not been granted I have applied/will apply for a partial restriction of the digital copy of my thesis or dissertation.”

Signed Benoît Pasquier
Date 19 June 2017 (document compilation)

Authenticity Statement

“I certify that the Library deposit digital copy is a direct equivalent of the final officially approved version of my thesis. No emendation of content has occurred and if there are any minor variations in formatting, they are the result of the conversion to digital format.”

Signed Benoît Pasquier
Date 19 June 2017 (document compilation)

Contents

Contents	ix
Acknowledgements	xiii
Abstract	xv
List of Figures	xvii
List of Tables	xix
Introduction	1
1 The Plumbing of the Global Biological Pump	11
1.1 Introduction	12
1.2 Model	13
1.2.1 Circulation	13
1.2.2 Phosphorus Cycle	14
1.3 Green-Function Diagnostics	15
1.4 Biological Pump Efficiency	16
1.5 Plumbing of the Biological Pump	18
1.5.1 Pumped and Leaked Phosphorus	18
1.5.2 $\Omega_i \rightarrow \Omega_f$ Phosphorus “Pipes”	21
1.5.3 Flow Rates of Bio Phosphorus	22
1.5.4 Timescales	27
1.5.5 Path Densities	28
1.6 Discussion and Conclusions	34
Appendices	38
1.A Origin/Destination and Transit-Time Partitioned Phosphorus . .	38
1.B Computational Methods	41
1.C Sensitivity of DOP and Phosphate Remineralization Rate . . .	43
1.D Basin Integrals of the Bio Phosphorus Path Density	46

1.E	Connection with Sequestration Efficiency Distribution	47
2	Inverse-Model estimates of the P, Si, and Fe cycles	49
2.1	Introduction	50
2.2	Biogeochemical Model	52
2.2.1	Circulation	53
2.2.2	Biogenic Transport	53
2.2.3	Uptake Rates	55
2.2.3.1	Nutrient Limitation	57
2.2.3.2	Light Limitation	57
2.2.3.3	Elemental Uptake Ratios	58
2.2.4	Iron Model	59
2.2.4.1	Iron Sources	59
2.2.4.2	Iron Sinks	60
2.3	Numerical Method, Parameter Optimization, and Family of Solutions	62
2.3.1	Steady-State Solution	62
2.3.2	Cost Function	63
2.3.3	Optimization Strategy	64
2.3.4	Family of Solutions	70
2.4	Fidelity to Observations	72
2.4.1	Nutrient Concentrations	72
2.4.2	dFe Profiles	74
2.4.3	Phytoplankton Distribution	75
2.5	Limiting Nutrients	77
2.6	Export Production	80
2.7	Iron Cycle	85
2.7.1	Iron Sources and Sinks	85
2.7.2	Dissolved Iron Concentration and Source Attribution	86
2.7.3	Iron-Type Attributed Export	88
2.7.3.1	Phosphorus Export	88
2.7.3.2	Opal Export	92
2.8	Discussion and Caveats	94
2.9	Summary and Conclusions	97
Appendices		101
2.A	Recycling Operators for Scavenged Iron	101
2.B	Biogenic Transport Operators with Subgrid Topography	102
2.C	Weights for Dissolved Iron Mismatch	103
2.D	Optimization Strategy Details	104
2.D.1	Prescribed Parameters	104

2.D.2	Choice of Initial Parameter Values	105
2.D.3	Sequential Optimization Steps	105
2.E	Iron Source and Sink Patterns	109
3	Iron control the phosphorus and silicon cycles	111
3.1	Introduction	112
3.2	Design of Iron Source Perturbations	114
3.2.1	Choice of Unperturbed States	114
3.2.2	Choice of Perturbations	115
3.3	Results	118
3.3.1	Response to Perturbations	118
3.3.1.1	Changes in Dissolved Iron	118
3.3.1.2	Changes in Euphotic Phosphate and Silicic Acid	122
3.3.1.3	Changes in the Export Production	128
3.3.1.4	Changes in the Biological Pump	136
3.3.2	Mechanisms of the Response	143
3.3.2.1	Southern Ocean Nutrient Trapping	143
3.3.2.2	Interior Distribution and Pathways of Dissolved Iron	148
3.4	Discussion	156
3.5	Conclusions	158
Appendices		162
3.A	Changes in Nutrient Limitation	162
3.B	Computations	165
3.B.1	Regenerated Nutrients	165
3.B.2	SO \rightarrow SO path densities for phosphate and silicic acid . .	165
3.B.3	Deposition-to-Uptake Path densities of Dissolved Iron .	166
Closing Remarks		167
Bibliography		171

Acknowledgments

First, I would like to thank my PhD supervisor Mark Holzer for the support he provided me during the past four years. My thesis could not have been completed without his extensive knowledge in mathematics, physics, computer science, and oceanography. Mark's motivation to teach me scientific writing has been invaluable. He devoted a lot of his time to instruct and shepherd me. My scientific wanderings have had similarities to a random walk without purpose at times, and he was always there to steer me back towards meaningful research. His continuous encouragements to help me push through conceptual and technical problems has proven priceless. He inspired me and taught me to become a scientist.

Pursuing my PhD was only possible thanks to the scholarships I received during the past four years. I am grateful to Monaco's Éducation Nationale de la Jeunesse et des Sports, the Scientific Centre of Monaco, the Frères Louis et Max Principale Foundation, the Cuomo Foundation, the UNSW Graduate Research School, and Mark for their financial support.

Looking back on the past four years, the University of New South Wales has been a wonderful place to work in and pursue my research. I thank the School of Mathematics and Statistics staff and students that I had the chance to work or collaborate with, who were always accessible, and from whom I have learned a lot. For my research, I heavily relied on the high-performance computational cluster, Katana, and I would like to thank the IT staff and Martin Thompson in particular for their technical support and their remarkable aptness to answer questions. I would also like to thank the Director of Postgraduate Studies, Pr. David Warton, for his unfaltering engagement and support.

I would like to thank my family and friends: My parents, Philippe and Brigitte, and my brother, Olivier, who have always supported me in my endeavour to study and work in academia. My friends, in Sydney and around the world, old and new, who were always present when needed, and encouraged me in my adventures.

Finally, I would like to thank Loren, for her unconditional love and support, and for the bliss she brings to my life.

Abstract

The ocean's biological pump is crucial for the carbon balance of the climate system, and the control of its three-dimensional "plumbing" on pump efficiency needed to be quantified. The nutrient cycles driving the biological pump are limited by dissolved iron (dFe). However, the iron cycle is poorly constrained, and the effects of iron source perturbations had never been quantified in a data-constrained model. In this thesis, we quantify the pathways and timescales of the biological pump, build an inverse model of the coupled phosphorus, silicon, and iron cycles, and explore the response of these cycles to changes in the aeolian iron supply.

We use Green-function methods to show that the Southern Ocean (SO) is where $(62 \pm 2)\%$ of regenerated phosphate (PO_4) reemerges after a mean sequestration time of 240 ± 60 yr. The pathways from productive regions to the SO contribute most to the biological pump, with a mean sequestration time of 130 ± 70 yr. Most PO_4 is carried by abyssal paths with transit times exceeding 700 yr, while $\sim 1/3$ of the regenerated PO_4 from the equatorial Pacific that is destined for the SO is carried in Antarctic Intermediate Water.

We use the model of the coupled nutrient cycles in inverse mode to objectively determine biogeochemical parameters by minimizing the mismatch with observed nutrient and phytoplankton concentrations. We generate a family of estimates, all consistent with the observations, for a wide range of iron source strengths, themselves not constrainable by current observations. The carbon and opal exports are well constrained in magnitude and pattern. We quantify the systematics of the carbon and opal exports supported by aeolian, hydrothermal, and sedimentary dFe and find that aeolian dFe is the most efficient for supporting production.

The response to aeolian source perturbations is sensitive to the state of the iron cycle that is fitted to observations. A shutdown of the aeolian source does not completely untrap nutrients from the SO because sedimentary and hydrothermal dFe suffice to sustain production. A globally uniform 50 Gmol yr^{-1} aeolian iron addition fertilizes macronutrient-rich regions leading to increased deep regenerated and recycled dFe. This perturbation actually reduces iron fertilization supported by long-range transport because increased scavenging removes dFe before it can reach its destination. The response of the opal export is muted because the iron dependence of the Si:P uptake ratio counteracts fertilization.

List of Figures

1.1	Schematic of the biological pump	17
1.2	Partition of the global euphotic zone into 14 regions	19
1.3	Fractions of the biological pumped and leaks	20
1.4	Percentage contributions to the biological pump efficiency	23
1.5	Percentage contributions to the biological pump leak	24
1.6	Normalized flow rates of bio pipes	26
1.7	Mean sequestration times	29
1.8	Residence-time distributions	31
1.9	Path densities of the bio pipes	33
1.10	Distribution of dissolved organic phosphorus	44
1.11	Basin-mean profiles of the model's phosphate remineralization rate	45
1.12	Volume integrals of the bio phosphorus path density	48
2.1	Schematic of the iron-cycle model	60
2.2	Total cost metric and RMS mismatch	71
2.3	Joint distribution of volume-weighted observed and modelled concentrations	73
2.4	Dissolved iron basin modeled and observed iron profiles	74
2.5	Modeled and observed phytoplankton	76
2.6	Nutrient limitation patterns	77
2.7	Local carbon, opal, and iron export production	81
2.8	Local carbon export production by phytoplankton class	84
2.9	Dissolved iron zonal averages and family of source-attributed profiles per basin	87
2.10	Geographical patterns of carbon export supported by each iron source	89
2.11	Fraction of carbon export supported by each iron source	90
2.12	Geographical patterns of opal export supported by each iron source	93
2.13	Fraction of opal export supported by each iron source	94
2.14	Geographical patterns of iron sources	107
2.15	Geographical patterns of iron sinks	108

3.1	Mean dissolved iron concentrations as a function of the perturbed aeolian iron source	119
3.2	Maps of unperturbed euphotic dFe and anomalies	121
3.3	Maps of unperturbed euphotic PO ₄ and anomalies	124
3.4	Maps of unperturbed euphotic Si(OH) ₄ and anomalies	126
3.5	Diatom phytoplankton class nutrient limitation patterns	127
3.6	Carbon and opal export production as a function of the perturbed aeolian iron source	129
3.7	Anomalies of the zonally integrated carbon and opal exports	131
3.8	Maps of local carbon and opal exports together with their anomalies	134
3.9	Global Biological pump efficiencies of phosphorus and silicon as a function of the perturbed aeolian iron source	137
3.10	Global zonal averages of regenerated and preformed PO ₄ together with their anomalies	139
3.11	Global zonal averages of regenerated and preformed Si(OH) ₄ together with their anomalies	141
3.12	Schematic of Southern Ocean nutrient trapping	143
3.13	Global zonal averages of the SO→SO uptake-to-uptake path densities of phosphate and silicic acid together with their anomalies . .	145
3.14	Trapping metric and trapping efficiency as a function of the perturbed aeolian iron source	149
3.15	Global zonal average of dFe together with anomalies	151
3.16	Global zonal average of long-range iron path-densities for the unperturbed and perturbed states	154
3.17	Large phytoplankton class nutrient limitation patterns	163
3.18	Small phytoplankton class nutrient limitation patterns	164

List of Tables

2.1	Prescribed paramaters	67
2.2	Optimized parameters	68
2.2	Optimized parameters (continued)	69
3.1	Iron source strengths of the typical, high-aeolian, and low-aeolian estimates	115

Introduction

The ocean's bottom is at least as important to us as the moon's behind.

Lill and Maxwell [1959], quoting a proverb of the American Miscellaneous Society.

The distributions of the chemicals necessary for life on earth are controlled by processes and pathways that transform and cycle these chemicals through the biosphere and through the physical components of the earth system. In the ocean, these biogeochemical cycles play a key role in sustaining the marine biosphere and in setting the energy and carbon balance of the climate system. A fascinating aspect of ocean biogeochemical cycles is that they are essentially a fluid phenomenon. Ocean biogeochemical cycles are embedded in the dynamically driven ocean circulation and shaped by the interaction of the biogenic particle transport with the physical advective-eddy-diffusive circulation. The global importance of ocean biogeochemical cycles is underlined by the fact that the marine biosphere accounts for about half the earth's net primary production [e.g., *Falkowski et al.*, 1998; *Field et al.*, 1998; *Alton and Bodin*, 2011].

More than eight decades ago, *Redfield* [1934] described the remarkable ubiquity and similarity of the elemental stoichiometric ratios in the deep ocean and within living organisms, and foresaw that the now famous Redfield ratios ($C:N:P = 106:16:1$) would "provide a valuable tool in the analysis of many oceanographic problems". More recently, it has been established that the Redfield ratios represent an average rather than being a fundamental feature of ocean biogeochemistry [e.g., *Arrigo*, 2005; *Loladze and Elser*, 2011]. The stoichiometric ratios with which elements are biologically utilized are known to vary with environmental conditions and among species [e.g., *Brzezinski*, 1985; *Sunda and Huntsman*, 1997; *Geider and Roche*, 2002; *Sterner et al.*, 2008; *Weber and Deutsch*, 2010]. A growing number of research projects are aimed at understanding the influence of deviations from the Redfield ratios on the biogeochemistry of the current, past, and future ocean [e.g., *Matsumoto et al.*, 2002; *Brzezinski et al.*, 2002; *Gilpin et al.*, 2004; *Beucher et al.*, 2007; *Garnier et al.*, 2010; *Deutsch and Weber*, 2012; *Teng et al.*, 2014; *Hutchins and Boyd*, 2016].

Models are essential for understanding how ocean biogeochemical cycles work and for predicting their response to changing conditions. To construct and validate such models, it is essential to have reliable observations of the relevant oceanographic variables. High quality climatologies of the macronutrients phosphate, nitrate, and silicic acid are available from global hydrographic surveys [e.g., WOCE, CLIVAR, GOSHIP — *Levitus*, 1983; *Levitus et al.*, 1993; *Ganachaud and Wunsch*, 2002], which have been objectively analyzed and gridded into the World Ocean Atlas, which is updated every four years [e.g., *Garcia et al.*, 2006, 2010, 2014]. However, trace elements such as dissolved iron (dFe) are difficult to measure because sampling is highly susceptible to contamination [e.g., *Measures et al.*, 2008]. Thus, very little data on marine dFe was available to researchers until recently [e.g., *Tagliabue et al.*, 2012]. The GEOTRACES project (www.geotrades.org) is an ongoing international research program aimed at systematically measuring trace metals and their isotopes along select hydro-

graphy lines in all ocean basins. While GEOTRACES is dramatically improving our knowledge of the distributions of trace metals in the ocean, sampling remains sparse in space and especially in time. The GEOTRACES data will not suffice to provide gridded climatologies and the modeling of trace-metal cycles will remain challenging.

Iron is intensively studied because of its well established role in limiting phytoplankton growth in High Nutrient Low Chlorophyll (HNLC) regions where a lack of the micronutrient prevents the complete utilization of the available macronutrients [e.g., *de Baar et al.*, 1995; *Lundry et al.*, 1997; *Martin and Fitzwater*, 1988; *de Baar et al.*, 2005; *Boyd et al.*, 2007]. Although there has been much progress in understanding the oceanic iron cycle in recent decades [e.g., the review by *Boyd and Ellwood*, 2010], much is still unknown. For example, there is no consensus on the strengths of the sources of iron to the ocean, which vary by up to 2 orders of magnitude in the literature [e.g., the iron model intercomparison by *Tagliabue et al.*, 2016]. This is due in part to the sparsity of available dFe observations, but more importantly due to the poor quantitative understanding of key components of the iron cycle such as iron scavenging by sinking particles, complexation with organic ligands, or aggregation and coagulation of colloidal iron.

This thesis focuses on the coupled global ocean phosphorus, silicon, and iron cycles. We key all biological production to phosphate utilization and ignore nitrate altogether to avoid the complications of denitrification and nitrogen fixation [e.g., *Najjar et al.*, 1992], and to limit the number of coupled tracers. The nutrient cycles start with utilization by phytoplankton in the euphotic layer to form organic matter via photosynthesis, releasing oxygen. This organic matter then sinks as particulate organic matter (POM) out of the euphotic zone and settles into the deep ocean as “marine snow”. The organic matter is eventually respired through bacterial action (consuming oxygen) to regenerate the nutrients and dissolved inorganic carbon (DIC). The advective-eddy-diffusive circulation eventually brings the regenerated nutrients and DIC back to the euphotic zone to be taken up again, completing the cycles [e.g., *Sarmiento and Gruber*, 2006].

The combination of uptake, POM sinking, and remineralization, which transports carbon from the surface to the deep ocean, is often referred to as the “soft-tissue pump” or “biological pump” [*Volk and Hoffert*, 1985]. The pump strips nutrients out of the euphotic zone and regenerates them at depth. Thus, nutrient concentrations are generally characterized by a nutricline with lower concentrations close to the surface [e.g., *Broecker et al.*, 1982]. The biological pump also regulates the air-sea exchange of CO₂ by stripping inorganic carbon out of the euphotic zone and setting the deep-ocean reservoir of respired carbon, which eventually upwells back to the surface. As a consequence, nu-

trient cycles played a crucial role in shaping paleoclimates [e.g., Broecker, 1982; Martin, 1990; Marinov *et al.*, 2008a,b; Sigman *et al.*, 2010]. The external sources of dFe to the ocean are known to have varied over the earth's history. Albani *et al.* [2016] estimated that dust deposition during the last glacial maximum (~24,500 years ago) was significantly larger than today, fertilizing more vigorous biological production which likely contributed to low atmospheric CO₂ concentrations and low temperatures. Because of the control of the biological pump on climate, researchers have considered geoengineering the iron cycle to mitigate climate change: Artificially adding iron to the ocean would fertilize biological production and draw down atmospheric CO₂ provided that the resulting organic matter stays sequestered in the deep ocean for a long time [e.g., Zeebe and Archer, 2005; Aumont and Bopp, 2006; Hauck *et al.*, 2016]. The interplay between changes in atmospheric CO₂ and the soft-tissue pump has broader implications for marine life. The additional influx of CO₂ contributes to ocean acidification which affects the ability of calcifying plankton (e.g., coccolithophores, foraminifera) to export carbon [e.g., Hofmann and Schellnhuber, 2009]. Because phytoplankton are *primary* producers at the bottom of the marine food chain, global changes in productivity have consequences for higher trophic levels of the marine ecosystem, and ultimately for fisheries.

A fascinating consequence of the fluid nature of ocean biogeochemical cycles is that perturbations of biological production in one part of the ocean can influence biological production on the other side of the world [e.g. Sarmiento *et al.*, 2004; Holzer and Primeau, 2013]. Quantifying the pathways and timescales of these teleconnections is essential for understanding the sensitivity of the global ocean ecosystem to perturbations of the current climate. The Southern Ocean (SO), which injects newly ventilated waters into the ocean interior via Subantarctic Mode Water (SAMW), Antarctic Intermediate Water (AAIW), and Antarctic Bottom Water (AABW), and where old waters from the interior upwell in Circumpolar Deep Water (CDW), plays a key role for these teleconnections. This is because the Southern Ocean circulation combines with biogenic particle transport to trap nutrients on a large scale, with important global consequences. Biological utilization strips nutrients out of the formation region of SAMW and AAIW, short-circuiting their preformed exit from the Southern Ocean and injecting regenerated nutrients into upwelling CDW that returns the nutrients to the Southern Ocean euphotic zone [e.g., Primeau *et al.*, 2013; Holzer *et al.*, 2014]. Because Si(OH)₄ is regenerated deep in the water column, silicon is strongly trapped in the Southern Ocean in the current climate [e.g., Holzer *et al.*, 2014]. The “silicic acid leakage hypothesis” posits that silicon could have been untrapped from the Southern Ocean during the last glacial maximum [Matsumoto *et al.*, 2002; Brzezinski *et al.*, 2002; Beucher *et al.*, 2007], because of evidence of decreased diatom silification with increases in available dFe [e.g.,

Takeda, 1998; Hutchins and Bruland, 1998; Franck *et al.*, 2000; Brzezinski *et al.*, 2003]. In this thesis we will explore the effects of iron dependent silicic-acid utilization on Southern Ocean silicon export and trapping.

Despite the vast taxonomic diversity of plankton, and despite the many complex biogeochemical processes that take place in the real ocean, our ability to fit global climatologies of phosphate (PO_4) and silicic acid (Si(OH)_4) very well using simple, single-nutrient models is remarkable [e.g. Primeau *et al.*, 2013; Holzer *et al.*, 2014]. This is because not all complexities exert significant influence on the large-scale solutions. Good models represent only the mechanisms relevant for setting the features of the solutions that illuminate the science questions of interest. While there is not yet a clear division between irrelevant and relevant variables in biogeochemistry as there is in the field of critical phenomena (statistical mechanics), it is clear that remarkably little detail is needed for capturing the large-scale distribution of the nutrients. For example, Najjar *et al.* [1992, 2007] modeled biological production by simply restoring surface nutrients to observations, and regenerating nutrients at depth with a globally uniform power law.

However useful for answering fundamental questions, simple models cannot answer questions relating to mechanisms that are not explicitly represented. For instance, nutrient-restoring models cannot represent the effects of nutrient colimitations. Designing or choosing a model of appropriate complexity to answer a specific scientific question is an arduous task, although one can hope that first order biogeochemical phenomena can be captured by models with only modest complexity [e.g., Galbraith *et al.*, 2015].

In this thesis, we ask the following main scientific questions:

1. How is the efficiency of the global biological pump set by the interplay of biogenic and physical transport, and what are the key teleconnections, pathways, and timescales that govern the biological pump?
2. Can we constrain the biogeochemical parameters of the coupled phosphorus, silicon, and iron cycles from currently available observational data?
3. How does iron supply control global biological productivity, and how do the biological pump and nutrient trapping in the Southern Ocean respond to changes in the aeolian iron supply?

A number of studies have used forward models to investigate how the circulation controls biological productivity by supplying nutrients to the euphotic zone [e.g., Pelegri and Csanady, 1991; Pelegri *et al.*, 1996; Sarmiento *et al.*, 2004; Marinov *et al.*, 2006; Williams *et al.*, 2006; Marinov *et al.*, 2008b; Palter

et al., 2010; *Williams et al.*, 2011]. However, the role of the combined biogenic and advective-eddy-diffusive transport in shaping the global nutrient cycles and their responses to perturbations remained underexplored excepting recent work employing highly efficient data-assimilated ocean and nutrient models [e.g. *DeVries et al.*, 2012; *Primeau et al.*, 2013; *Holzer and Primeau*, 2013]. In Chapter 1 we extend these studies to quantify the three-dimensional “plumbing” of the biological pump.

Many studies have investigated the role of the iron cycle in global biogeochemistry and its interaction with the macronutrient cycles [e.g., *Moore et al.*, 2001; *Aumont et al.*, 2003; *Moore et al.*, 2004; *Parekh et al.*, 2004; *Moore et al.*, 2004; *Parekh et al.*, 2005; *Dutkiewicz et al.*, 2005, 2006; *Vichi et al.*, 2007; *Matsumoto et al.*, 2008; *Galbraith et al.*, 2010; *Yool et al.*, 2011; *Dutkiewicz et al.*, 2012; *Yool et al.*, 2013; *Dutkiewicz et al.*, 2013; *Moore et al.*, 2013b; *Matsumoto et al.*, 2013; *Dunne et al.*, 2013; *Stock et al.*, 2014; *Dutkiewicz et al.*, 2014, 2015; *Aumont et al.*, 2015; *Völker and Tagliabue*, 2015]. Models that represent the iron cycle are typically prognostic forward models and range from simple coupling formulations with a few tracers [e.g., *Parekh et al.*, 2005] to complex ecosystem models with dozens of prognostic tracers [e.g., *Follows et al.*, 2007; *Dunne et al.*, 2013]. However, they tend not to fit the available dFe observations very well and different studies used widely different iron source strengths [e.g., *Tagliabue et al.*, 2016]. *Frants et al.* [2016] recently designed a simple inverse model carrying only a dFe tracer to show that a wide range of aeolian iron sources is consistent with currently available dFe observations because the compensating sinks are unconstrained and can be optimized to match the observed dFe concentrations. *Holzer et al.* [2016] used the efficient numerics of this model to partition the dFe concentration into its aeolian, sedimentary, and hydrothermal source contributions. *Holzer et al.* [2016] also computed the mean age of aeolian iron since deposition from the atmosphere, which showed that most of the dFe in the Southern Ocean is upwelled aeolian iron deposited several hundred years earlier. However, the model of *Frants et al.* [2016] cannot capture the feedback of changes in biological production on the iron cycle, a shortcoming we remedy with the model developed in Chapter 2.

In this thesis, we apply efficient numerical methods that allow us to use our model in inverse mode to constrain biogeochemical parameters through objective optimization. Optimizing biogeochemical parameters requires the steady-state tracer equations to be solved thousands of times, which can only be accomplished with a computationally efficient approach. Here, we use an implicit solver based on a multi-dimensional Newton Method [e.g., *Kelley*, 2003a,b], which typically converges to numerical accuracy in ~ 10 iterations. This has the considerable advantage of avoiding the large computational costs of spinning up the model to reach steady state, as is necessary for standard forward

models.

A major methodological theme of this thesis is the use of Green-function methods. To understand the inner workings of the nutrient cycles and the interaction between physical and biogenic transport, we label nutrients with labeling tracers (essentially “colouring” the nutrient), which allow us to follow nutrients from one place to another as they are transported and transformed. For example, we quantify the plumbing of the biological pump by following labeled phosphorus from its last biological utilization, through its biogenic particle transport and regeneration, to its next reemergence as phosphate in the euphotic zone. While the dynamics of the nutrient cycles are generally nonlinear in the nutrient concentrations (because of nonlinearities in uptake and/or scavenging, for example), the concentrations of the labels themselves obey linear tracer equations, which can therefore be subjected to the venerable machinery of Green functions [e.g., Morse *et al.*, 1953; Holzer and Hall, 2000]. Green function methods have previously been applied to oceanographic problems to track the surface-to-surface paths of water itself [e.g., Holzer and Primeau, 2008], and more recently also to nutrient cycles [e.g., DeVries *et al.*, 2012; Holzer and Primeau, 2013; Holzer *et al.*, 2014]. The Green function is fundamentally simply the response to an impulse in space and/or time from which all solutions for the same boundary conditions can be constructed by linear superposition. Here, we consider Green functions that propagate the concentrations of the labeling tracers. The linear equations for the concentrations of the labeling tracers can also be recast in adjoint form. The corresponding adjoint Green functions can be used to track nutrients backwards in time through the time-reversed adjoint flow [e.g., Holzer and Hall, 2000]. This affords not only conceptual insight, but can also afford enormous computational efficiencies. For example, calculating the distribution of nutrients in the ocean interior that are destined to reemerge in a given surface destination region using forward Green functions would require one to track a tracer from every interior grid cell, requiring the solution of as many tracer equations as there are grid cells¹. However, exactly the same information can be obtained by propagating only a single tracer that labels the nutrients at destination in the time-reversed flow. Moreover, we can rigorously define the density of nutrients that start in a given origin region that are destined for a given exit location by combining the forward and adjoint Green functions. This conditioned nutrient density is also the density of the corresponding transport paths, i.e., the corresponding path density. For the path density, Green functions label nutrient molecules that were injected in the ocean in one region and the adjoint Green function keeps track of where they will emerge (or be taken up) [e.g., Holzer and Primeau, 2006;

¹about 200 000 in our case.

Primeau and Holzer, 2006].

A matrix representation of the eddy-diffusive transport additionally affords us numerically efficient computations of time-independent quantities, as well as flexibility in using implicit or semi-implicit time-stepping. A matrix representation of the nutrient equations is achieved by discretizing the biogeochemical and transport equations and organizing fields into vectors, and any linear operators into matrices. The equations for the labeling tracers and Green functions then become simple linear matrix equations, that can be solved using highly efficient LU factorization [e.g., Press *et al.*, 1989].

The remainder of this thesis is organized into three Chapters. Chapter 1 is adapted from published work [*Pasquier and Holzer, 2016*] that was done as part of my thesis research. In Chapter 1, we systematically quantify the pathways and timescales that set the efficiency of the global biological pump by applying Green-function-based diagnostics to the data-assimilated phosphorus cycle of *Primeau et al.* [2013]. We consider phosphorus “bio pipes” that connect specified regions of last biological utilization with regions where regenerated phosphate first reemerges into the euphotic zone. The bio pipes that contribute most to the biological pump connect the HNLC regions to the Southern Ocean. For the largest bio pipes, $\sim 1/7$ of their phosphorus is carried by thermocline paths with transit times less than $\sim 300\text{--}400$ years, while $\sim 4/7$ of their phosphorus is carried by abyssal paths with transit times exceeding ~ 700 years. The path density reveals that AAIW carries about a third of the regenerated phosphate last utilized in the tropical HNLC regions that is destined for the Southern Ocean euphotic zone. The Southern Ocean, where most nutrients first reemerge from the aphotic zone, stands out as the nexus of biological teleconnections.

Chapter 2 develops a model of the coupled phosphorus, silicon, and iron cycles, which is embedded in the data-assimilated steady-state global ocean circulation of *Primeau et al.* [2013]. A version of this chapter has been submitted for publication. Our coupled nutrient model carries only three tracers whose three-dimensional steady-state distributions can be found efficiently using a Newton solver. The very efficient numerics allow us to use the model in inverse mode to objectively constrain many biogeochemical parameters by minimizing the mismatch between modelled and observed nutrient and phytoplankton distributions. We consider a family of possible solution corresponding to a range of external source strengths because source parameters themselves cannot objectively be determined due to local compensation with the scavenging sink. All members of our family match PO_4 and Si(OH)_4 observations similarly well with similar large-scale dFe distributions, although the relative contributions of aeolian, sedimentary, and hydrothermal iron differ depending on the sources. We diagnose the carbon and opal export supported by source-attributed dFe. Sedimentary dFe is a strong contributor in shelf and large-scale

upwelling regions, while hydrothermal dFe contributes to export mostly in the Southern Ocean. The globally integrated export supported by a given iron type varies systematically with the fractional contribution of its source to the total iron source. Aeolian iron is most efficient in supporting export in the sense that its fractional contribution to export exceeds its fractional contribution to the total source. For the same fractional contribution to the total source, hydrothermal iron is less efficient than sedimentary iron for supporting carbon export but about equally efficient for supporting opal export.

Chapter 3 uses the model developed in Chapter 2 to explore the response of the coupled nutrient cycles to perturbations in the aeolian iron supply. We perturb atmospheric iron deposition either in the global ocean, in the Southern Ocean, or in the tropics. We show that the response of the system is sensitive to the particular state of the iron cycle of the solution we chose from our family of estimates. We use a path-density diagnostic to quantify the response of Southern Ocean trapping. Contrary to the silicic-acid-leakage hypothesis, we find that silicon trapping increases with Southern Ocean fertilization. However, because changes in the iron-dependent diatom Si:P uptake ratio counteract changes in iron fertilization, the response of opal export is weaker than that of carbon. We find that for a complete aeolian source shutdown, macronutrients do not become completely untrapped from the Southern Ocean, where biological production is reduced but remains supported by sedimentary and hydrothermal dFe due to reduced scavenging. Reduced aeolian input leads to increased iron deficiency in productive regions, which allows more preformed macronutrients to be laterally transported into the oligotrophic subtropical gyres where production increases. Conversely, aeolian iron addition increases the biological pump efficiency by fertilizing HNLC regions at the expense of productivity in the subtropical gyres, which become even more PO₄-limited, consistent with the findings of Dutkiewicz *et al.* [2005]. Increased production and scavenging in HNLC regions inject additional regenerated and recycled dFe at depth. Surface dFe concentrations increase mostly within subtropical gyres where scavenging is low. To investigate the role of long-range transport in fertilizing regions remote from the aeolian iron source, we compute the path densities of dFe from deposition in a given source region to biological utilization in a specified destination region. Interestingly, globally uniform aeolian iron addition removes these long-range dFe paths because the increased scavenging takes out more dFe than the additional aeolian deposition adds.

Chapter 3 is followed by closing remarks.

Chapter 1

The Plumbing of the Global Biological Pump: Efficiency Control Through Leaks, Pathways, and Timescales

Perhaps the most impressive illustration of all is to suppose that you could label the molecules in a tumbler of water, threw it anywhere you please on the earth, and went away from the earth for a few million years while all the water on the earth, the oceans, rivers, lakes and clouds had had time to mix up perfectly. Now supposing that perfect mixing had taken place, you come back to earth and draw a similar tumbler of water from the nearest tap, how many of those marked molecules would you expect to find in it? Well, the answer is 2000. There are 2000 times more molecules in a tumbler of water than there are tumblers of water in the whole earth.

Francis William Aston, in Lecture (1936) [Needham and Pagel, 1938]

1.1 Introduction

The biological pump removes organic matter from the surface ocean and sequesters carbon at depth [e.g., *Raven and Falkowski*, 1999; *Archer et al.*, 2000] and therefore plays a crucial role in the atmosphere-ocean carbon balance, with implications for climate change and ocean acidification [e.g., *Broecker*, 1982; *Marinov et al.*, 2008a,b; *Sigman et al.*, 2010]. The efficiency of the biological pump is set by the interplay of the ocean's advective-diffusive circulation with the biological uptake of nutrients and subsequent biogenic particle transport and remineralization. This interplay between the physical and biogenic transport of nutrients shapes the global ocean ecosystem and establishes the global-scale teleconnections between nutrient utilization in one region and nutrient re-supply, and ultimately biological production, in another region. The paths and flow rates that mediate these teleconnections constitute the "plumbing" of the biological pump. Here, we systematically diagnose the nutrient pathways throughout the world oceans to quantify how this "plumbing" controls the global efficiency of the biological pump.

Because phosphate (PO_4) is necessary in the metabolism of all phytoplankton, it is common to approximate PO_4 as the limiting nutrient and key all biological production to the phosphorus cycle [e.g., *Smith*, 1984; *Howarth*, 1988], an approach we will follow here. Early studies quantified the efficiency of the biological pump in terms of the vertical gradients of dissolved organic carbon [e.g., *Volk and Hoffert*, 1985]. More recently, the biological pump efficiency has been defined in terms of regenerated phosphate by *Ito and Follows* [2005] to explore the sensitivity of the atmospheric CO_2 partial pressure to oceanic nutrient drawdown. Here we extend their study to analyze the circulation control on biological pump efficiency in detail. Over the last decade, a number of studies have addressed the high-latitude control on global nutrient cycles [e.g., *Sarmiento et al.*, 2004; *Marinov et al.*, 2006]. More recently, *Primeau et al.* [2013] used a simple data-assimilated phosphorus cycling model to investigate the response of the pump efficiency to altered nutrient utilization in the Southern Ocean. *Holzer and Primeau* [2013] investigated the pathways and timescales that connect utilization in the Southern Ocean with production in the subtropical and subpolar gyres of the North Atlantic, and how these change when Southern Ocean utilization is perturbed. A complementary study by *Palter et al.* [2010] used synthetic water-mass tracers within an ocean model to quantify the importance of various water masses, as well as the role of the overturning circulation in returning nutrients to the pycnocline. We extend and generalize these studies by systematically analyzing the global distribution of the pathways and timescales of the combined physical/biogenic nutrient transport in the current state of the ocean and how these control the global efficiency of

the biological pump. Our work is a natural extension and generalization of the study by *DeVries et al.* [2012] who related the distribution of times with which exported phosphate remains in the aphotic interior to the efficiency of the biological pump in terms of a geographically distributed sequestration efficiency.

Here we systematically analyze the ocean’s nutrient cycling to address the following key questions:

1. What is the geographic distribution of the biological pump and its leaks?
2. What are the dominant connections between nutrient uptake and nutrient re-supply across the world oceans?
3. What are the three-dimensional pathways, timescales, and flow rates that mediate these connections and how much do they contribute to the efficiency of the biological pump?

Our analysis quantifies the contributions of the global preformed and regenerated nutrient pathways to the biological pump efficiency. Pathways are quantified not only in terms of the geographic connections between nutrient suppliers and receptors, but also in terms of the three-dimensional, transit-time partitioned nutrient path density. The dominant contributors to the biological pump efficiency are paths from productive equatorial regions to the Southern Ocean (SO) as well as SO-to-SO “trapped” paths. The SO is thus not only the biological pump’s primary leak providing most of the world ocean’s preformed nutrients, but also the preferred destination of regenerated nutrients. A key pathway of regenerated nutrients to the SO is via recirculating Antarctic Intermediate Water (AAIW) accessed in tropical and subtropical regions through biogenic particle transport.

1.2 Model

1.2.1 Circulation

We use the data-assimilated, steady non-seasonal circulation of *Primeau et al.* [2013], which is similar to that of *DeVries and Primeau* [2011], except that the horizontal resolution has been increased to $2^\circ \times 2^\circ$, and CFC-11 and PO_4 have been incorporated as tracer constraints in addition to temperature, salinity, and radiocarbon. The circulation is constrained dynamically and the data assimilation used the wind-stress climatology of *Trenberth et al.* [1989] and specified horizontal and vertical viscosities of $5 \times 10^4 \text{ m}^2 \text{ s}^{-1}$ and $10^{-4} \text{ m}^2 \text{ s}^{-1}$, respectively. The circulation’s advective-diffusive transport operator has fixed horizontal and vertical eddy diffusivities of $10^3 \text{ m}^2 \text{ s}^{-1}$ and $10^{-5} \text{ m}^2 \text{ s}^{-1}$, respect-

ively. While the diffusivity tensor is not aligned with the isopycnals, the data assimilation adjusts the velocity field such that the overall advection-diffusion results in tracer fields and heat and fresh-water transports that have high fidelity to the observations [DeVries and Primeau, 2011]. Although it is possible that the velocity field has some unrealistic features to compensate for the non-rotated diffusivity, the integrated transport of tracers is well captured¹. This is underscored by the fact that if we repeat our calculations with the newer data-assimilated circulations of DeVries [2014] that all have a rotated diffusivity, we obtain virtually identical results, albeit with a slightly worse fit to the PO₄ field, which was not assimilated by DeVries [2014]. We emphasize that the circulation used effectively provides a ventilation-weighted transport because it has been optimized against PO₄ and the ventilation tracers CFC-11 and radiocarbon. The steady model circulation, which has no seasonal cycle, thus does not bias estimates of preformed nutrients as an annual-average circulation would.

1.2.2 Phosphorus Cycle

We base our diagnostics on a simple steady model of the phosphorus cycle that was jointly assimilated with the physical circulation by Primeau *et al.* [2013]. The optimized control variables of the phosphorus cycle are the phosphate uptake field, the Martin exponent of the organic particle flux profile (approximated as globally uniform), and the global phosphate inventory. The assimilation included a non-smoothness penalty for the uptake field. For details see the work of Primeau *et al.* [2013], where the model's export production, regenerated and preformed phosphate fields, and dissolved organic phosphorus (DOP) distributions are documented. The root-mean-square (RMS) volume-weighted mismatch between modelled and observed [PO₄] is a mere 4 % of the global mean with no systematic biases. Because the phosphorus cycle was jointly assimilated with the circulation, the steady ventilation-weighted circulation does not inappropriately bias the phosphorus cycle toward winter conditions. The model's global preformed PO₄ inventory is (61±4)%, which compares well with an independent estimate of 59 % based on apparent oxygen utilization [Primeau *et al.*, 2013].

The phosphorus cycle explicitly transports inorganic phosphate (PO₄) and dissolved organic phosphorus (DOP) and couples them via remineralization and biological utilization. Denoting the concentrations of PO₄ and DOP by P_I and

¹ Specifically, the sign of the vertical component of the optimized velocity can oscillate spatially on the grid scale, which may be one of the ways in which the assimilated velocity field is able to replicate the effects of a rotated diffusivity tensor.

P_O , respectively, we can write the phosphorus tracer equations as

$$\frac{\partial}{\partial t} \begin{bmatrix} P_I \\ P_O \end{bmatrix} + \begin{bmatrix} \mathcal{T} + \gamma & -\kappa \\ 0 & \mathcal{T} + \kappa \end{bmatrix} \begin{bmatrix} P_I \\ P_O \end{bmatrix} = \begin{bmatrix} -\gamma_g(P_I - \bar{P}_I) \\ \mathcal{S} \gamma P_I \end{bmatrix}, \quad (1.1)$$

where the operator \mathcal{T} is the advection-eddy-diffusion operator, $\gamma(\mathbf{r})$ is the PO_4 uptake rate constant at point \mathbf{r} , and κ is the globally uniform rate constant for remineralizing DOP. The uptake rate constants are diagnosed from the data-assimilated PO_4 uptake rate per unit volume, $J(\mathbf{r})$, as $\gamma(\mathbf{r}) = J(\mathbf{r})/P_I(\mathbf{r})$, which is nonzero only in the euphotic zone modelled as the upper 73.4 m of the water column (top 2 model layers). Note that Equation (1.1) has precisely the same solution as the data-assimilated phosphorus cycle, but is completely linear in the PO_4 and DOP concentrations, allowing us to use Green-function-based diagnostics to trace phosphorus through the ocean [Primeau *et al.*, 2013; Holzer and Primeau, 2013].

The source of DOP per unit volume is given by $\mathcal{S}J$, where the operator \mathcal{S} instantaneously reassigns the PO_4 uptake per unit volume, $\gamma(\mathbf{r})P_I(\mathbf{r})$, to a source of DOP throughout the water column: A fraction σ of the uptake is reassigned to a source of DOP in the euphotic zone, while the remaining fraction $(1 - \sigma)$ becomes a DOP source proportional to the divergence of a power-law particle-flux profile in the aphotic zone (Martin exponent b) – see the work of Kwon and Primeau [2006] and Primeau *et al.* [2013] for details. In (1.1), the weak relaxation to the observed global mean phosphate concentration \bar{P}_I , with a “geological” (subscript g) restoring timescale $\gamma_g^{-1} = 10^6$ yr, is introduced so that the total amount of phosphorus in the ocean is determined even for the steady-state equations (i.e., even without a specified initial phosphate field).

We use the parameter values $b = 0.70$, $\sigma = 1/3$, and $\kappa = (0.5 \text{ yr})^{-1}$ of the data-assimilated phosphorus cycle. Only b was optimized, σ and κ were specified. The relative sensitivity of the preformed and regenerated phosphate fields to variations in these parameters is documented in the work of Primeau *et al.* [2013]. (The maximum zonally averaged relative sensitivities $(\kappa/P_{\text{reg}})\partial P_{\text{reg}}/\partial \kappa$ and $(\kappa/P_{\text{pre}})\partial P_{\text{pre}}/\partial \kappa$ lie in the upper ocean and are $\sim 20\%$.) In the analyses below, the uncertainty δX in a quantity X was estimated from the linear sensitivities to b , σ , and κ as $\delta X = \sqrt{(\partial_b X \delta b)^2 + (\partial_\sigma X \delta \sigma)^2 + (\partial_\kappa X \delta \kappa)^2}$. We took $\delta b = 0.35$, $\delta \sigma = 0.15$, and $\delta \kappa = (0.25 \text{ yr})^{-1}$ as reasonable uncertainties in the parameters themselves.

1.3 Green-Function Diagnostics

The linearity of Equation (1.1) enables the use of Green functions to trace phosphorus through its biogenic and physical transport paths [e.g., Primeau *et al.*,

2013; Holzer and Primeau, 2013]. The fundamental Green function of the equation is obtained by replacing the source term on the right-hand-side of (1.1) with $\delta(\mathbf{r} - \mathbf{r}') \delta(t - t') \mathbf{I}$, where \mathbf{I} is the 2×2 identity matrix, and by replacing $[P_I, P_O]^\top$ with the corresponding response, that is, with the Green function

$$\mathbf{G} \equiv \begin{bmatrix} G_{II} & G_{IO} \\ G_{OI} & G_{OO} \end{bmatrix}, \quad (1.2)$$

which obeys the causality condition $\mathbf{G} = 0$ for $t < t'$. Matrix element $G_{II}(\mathbf{r}, t | \mathbf{r}', t')$ is the inorganic phosphate response at (\mathbf{r}, t) to an inorganic source at (\mathbf{r}', t') , G_{IO} is the inorganic remineralized phosphate response to a DOP source, G_{OO} is the DOP response to a DOP source, and $G_{OI} = 0$ because phosphate is not converted to DOP except through uptake, which we represented by a source in (1.1).

From \mathbf{G} , we calculate regenerated and preformed phosphate as well as DOP at point (\mathbf{r}, t) partitioned according to the time t_i and region Ω_i where the phosphorus was last in the euphotic zone (preformed PO_4 , denoted by P_{pre}) or last utilized (regenerated PO_4 and DOP). Regenerated phosphate, denoted by P_{reg} , is remineralized DOP that has not yet been in contact with the euphotic layer. Once P_{reg} reemerges in the euphotic layer, it is re-labeled as P_{pre} . The pathways and conversions between the phosphorus pools are illustrated schematically in Figure 1.1.

To partition phosphorus into P_{reg} and P_{pre} , and to compute the flux of first reemergence into the euphotic zone, we impose fast relaxation to zero in the euphotic zone with a timescale $\gamma_0^{-1} = 1 \text{ s}$. The fast relaxation effectively imposes the boundary condition of zero regenerated phosphate in the euphotic zone – see also Appendices 1.A and 1.B. From here on, we additionally impose this fast relaxation on G_{IO} and G_{II} so that the inorganic component of \mathbf{G} is the Green function for the regenerated phosphate system.

Using a suitable adjoint of (1.1), we also partition phosphorus according to the time t_f and regions Ω_f , where the phosphorus next emerges into the euphotic zone. From these partitioned quantities and their fluxes in and out of the euphotic zone, we can compute the mass, flow-rate, and path-density distributions of phosphorus in transit from euphotic region Ω_i to euphotic region Ω_f (subscript index notation i and f for “initial” and “final”) as detailed in Appendices 1.A and 1.B.

1.4 Biological Pump Efficiency

Following Ito and Follows [2005], we define the global efficiency of the biological pump in terms of the preformed phosphate inventory. Denoting the global

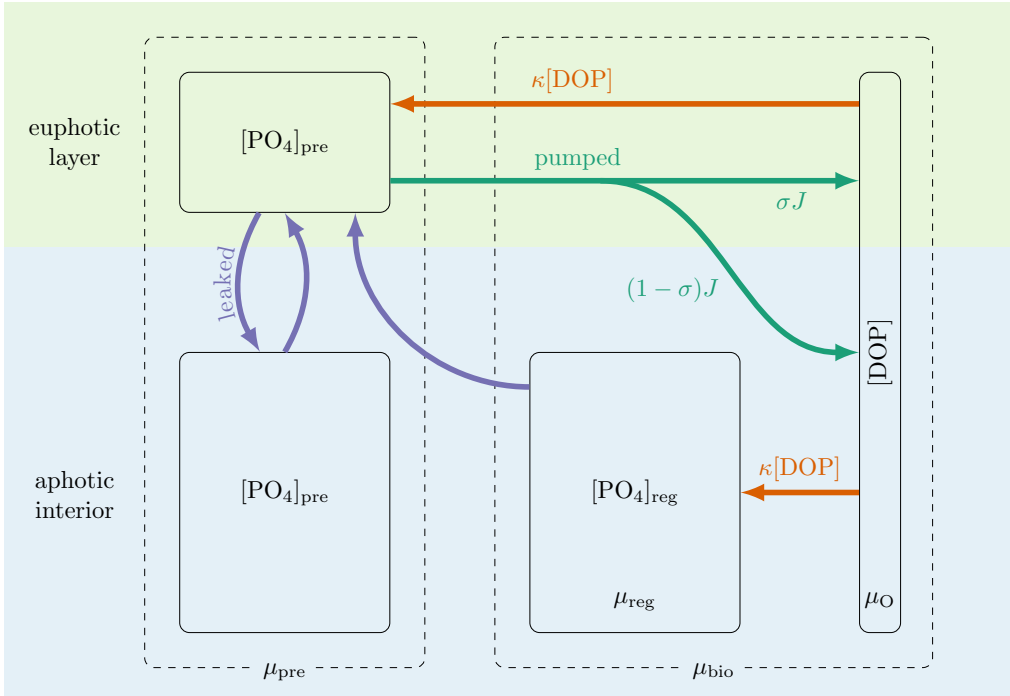


Figure 1.1: Schematic of the exchange between the phosphorus pools: Euphotic and aphotic preformed phosphate (global mass μ_{pre}), regenerated phosphate (global mass μ_{reg}), and dissolved organic phosphorus (DOP, global mass μ_O). Blue arrows represent physical transport by the circulation. Both phosphate and DOP are transported as tracers in our model. Green arrows represent the biogenic particle transport of organic phosphorus and its dissolution into the DOP pool, which is instantaneous in our model. The DOP production rate is σJ in the euphotic zone, and $(1 - \sigma)J$ in the aphotic zone, with PO_4 uptake rate J . Orange arrows represent the remineralization of DOP with rate constant κ . The total mass of bio phosphorus is denoted by $\mu_{\text{bio}} = \mu_{\text{reg}} + \mu_O$.

ocean inventory of phosphorus (in either mass units or moles) by μ_P and the inventory of phosphorus within preformed and regenerated phosphate by μ_{pre} and μ_{reg} , the global pump efficiency E_{bio} is defined by

$$E_{\text{bio}} \equiv \frac{\mu_P - \mu_{\text{pre}}}{\mu_P} = \frac{\mu_{\text{reg}} + \mu_O}{\mu_P} = \frac{\mu_{\text{bio}}}{\mu_P} . \quad (1.3)$$

In (1.3) we added the inventory of phosphorus in the form of DOP, μ_O , to account for all non-preformed, biologically utilized phosphorus, or “bio phosphorus” for short. The inventory of bio phosphorus is $\mu_{\text{bio}} = \mu_{\text{reg}} + \mu_O$. While adding μ_O to μ_{reg} is necessary to account rigorously for all bio phosphorous, we estimate μ_O to be a mere $(0.1 \pm 0.3)\%$ of μ_P in the current state of the ocean, and one could neglect μ_O and simply compute the efficiency as μ_{reg}/μ_P [e.g., Ito and

Follows, 2005; Primeau et al., 2013]. Here we keep μ_O for completeness and to demonstrate that one can easily track biologically utilized phosphorus through the DOP pool before it becomes regenerated phosphate. The global biological pump efficiency for our estimate of the phosphorus cycle is $E_{\text{bio}} = (39 \pm 4)\%$ [Primeau et al., 2013].

1.5 Plumbing of the Biological Pump

We now investigate how the efficiency of the biological pump is set by the combined physical and biogenic transport of phosphorus between different geographic regions of the euphotic zone. To keep the analysis manageable, we subdivide the global euphotic zone into the 14 regions Ω_i defined in Figure 1.2. We identify individual regions with abbreviations of their geographic description (e.g., SAAD for South of Antarctic Divergence, NAAD for North of Antarctic Divergence, EEqP for Eastern Equatorial Pacific), all of which are given in the caption of Figure 1.2. These regions have been defined so that their boundaries are either contours of constant production, constant latitude, or, for the partition between the SAAD and NAAD regions, the locus of maximum Ekman divergence in the Southern Ocean.

1.5.1 Pumped and Leaked Phosphorus

Each region Ω_i contributes to the global pump efficiency through the amount of phosphorus that it provides to the pump, $\mu_{\text{bio}}(\Omega_i)$, or equivalently through the amount that escapes or “leaks” from the pump, $\mu_{\text{pre}}(\Omega_i)$. We therefore define the fractional bio-pump contributions $\beta(\Omega_i)$ and the fractional leak contributions $\lambda(\Omega_i)$ as

$$\beta(\Omega_i) \equiv \frac{\mu_{\text{bio}}(\Omega_i)}{\mu_P} \quad \text{and} \quad \lambda(\Omega_i) \equiv \frac{\mu_{\text{pre}}(\Omega_i)}{\mu_P} , \quad (1.4)$$

so that the global pump efficiency is simply determined by the total fraction pumped, $\sum_i \beta(\Omega_i)$, or equivalently by the total fraction leaked, $\sum_i \lambda(\Omega_i)$:

$$E_{\text{bio}} = \sum_i \beta(\Omega_i) = 1 - \sum_i \lambda(\Omega_i) . \quad (1.5)$$

The inventories $\mu_{\text{bio}}(\Omega_i)$ and $\mu_{\text{pre}}(\Omega_i)$ from each region are computed as described in Appendices 1.A and 1.B.

Figure 1.3 shows the complementary views afforded by Equation (1.5) of how different regions contribute to the global pump efficiency. The pumped

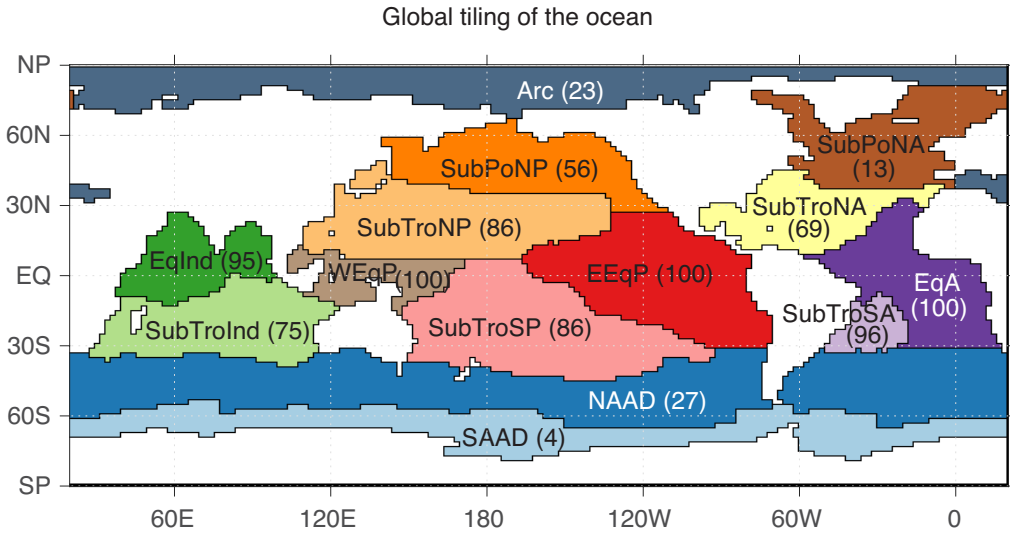


Figure 1.2: Partition of the global euphotic zone into 14 regions, denoted by Ω_i . The abbreviations that label the regions stand for: South of Antarctic Divide (SAAD), North of Antarctic Divide (NAAD), Subtropical South Atlantic (SubTroSA), Subtropical South Pacific (SubTroSP), Subtropical Indian Ocean (SubTroInd), Equatorial Atlantic (EqA), Eastern Equatorial Pacific (EEqP), Western Equatorial Pacific (WEqP), Equatorial Indian Ocean (EqInd), Subtropical North Atlantic (SubTroNA), Subtropical North Pacific (SubPoNP), Subpolar North Atlantic (SubPoNA), Subpolar North Pacific (SubPoNP), and Arctic (Arc). Non-Arctic regions plotted in saturated colors correspond to high-productivity regions (NAAD, EqInd, EEqP, SubPoNP, EqA, and SubPoNA). The numbers in parentheses are the local pump efficiencies of each region in percent, defined as $\mu_{\text{bio}}(\Omega_i \rightarrow \Omega) / \mu_{\text{P}}(\Omega_i \rightarrow \Omega)$, where Ω denotes the global euphotic zone.

fractions shown in the left slice of the pie partition the total pump efficiency of $(39 \pm 4)\%$. Highly productive regions contribute the most: the North of the Antarctic Divide (NAAD), Equatorial Indian Ocean (EqInd), Eastern Equatorial Pacific (EEqP), Subpolar North Pacific (SubPoNP), and Equatorial Atlantic (EqA) regions account for $(74 \pm 8)\%$ of E_{bio} , with the EEqP making the largest contribution of $(25 \pm 4)\%$.

The corresponding leaked fractions are shown in the right slice of the pie of Figure 1.3, which partitions the $(61 \pm 4)\%$ global fraction of preformed phosphate that escaped biological utilization. The euphotic zones of the high-latitude oceans are the largest leak: the Southern Ocean (SAAD and NAAD) and the subpolar North Pacific and Atlantic regions (SubPoNP and SubPoNA) account for $(96 \pm 1)\%$ of the global leak, with the SAAD and NAAD regions contributing $(43 \pm 4)\%$ and $(32 \pm 1)\%$, respectively. The incomplete utilization of the abundantly available macro nutrients in the Southern Ocean is due to a

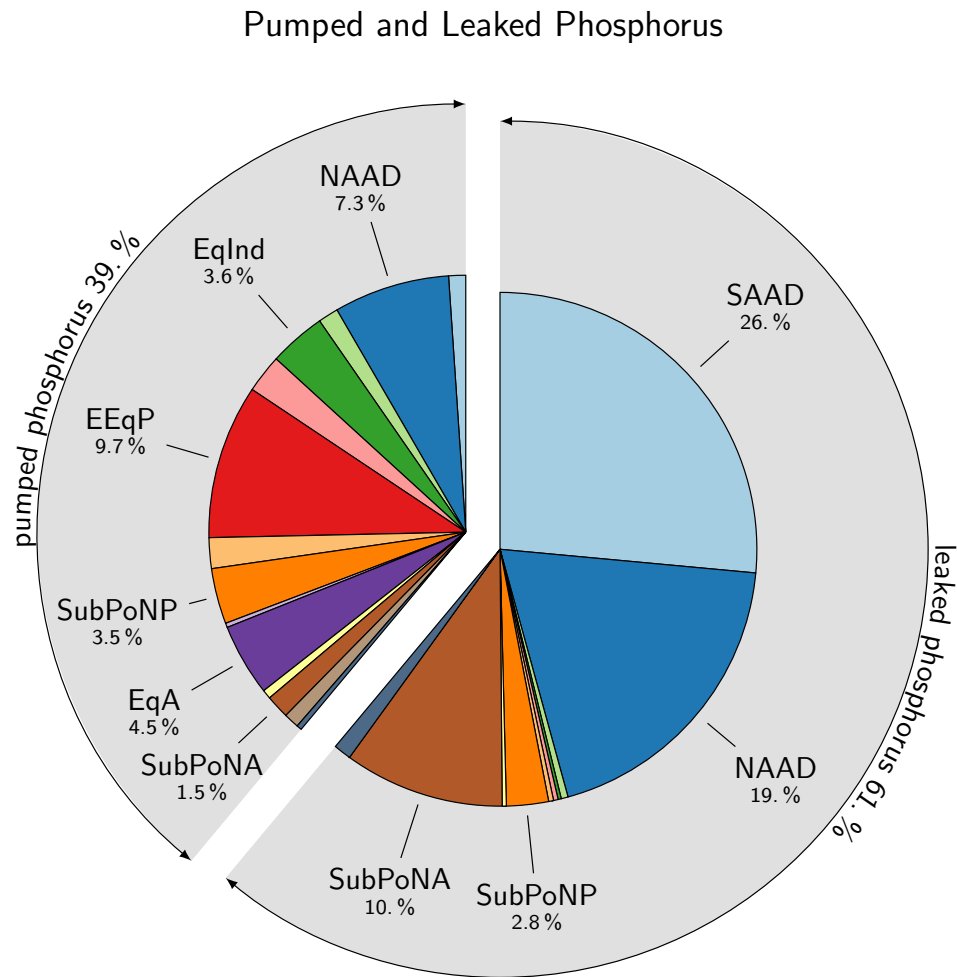


Figure 1.3: The biologically pumped and leaked fractions of phosphorus for each region Ω_i , color-coded as in Figure 1.2. On the left, the fractions $\beta(\Omega_i) \equiv \mu_{\text{bio}}(\Omega_i)/\mu_P$ represent the contribution of each patch to the global biological pump efficiency. On the right, the fractions $\lambda(\Omega_i) \equiv \mu_{\text{pre}}(\Omega_i)/\mu_P$ represent the contribution of each patch to the global pump leak (global preformed phosphate inventory).

number of limiting factors, including low micronutrients [e.g., Dutkiewicz *et al.*, 2006]. Equatorial regions have almost no leaks, with large-scale upwelling of nutrients being balanced by nearly complete nutrient utilization.

The relative size of the phosphorus amount pumped or leaked in a given region Ω_i can be summarized by defining a local biological pump efficiency for each Ω_i as the ratio of the bio phosphorus to the total phosphorus originating

from Ω_i . These local efficiencies are indicated in Figure 1.2 on the map defining the Ω_i patches. Equatorial patches, which provide near zero preformed phosphate because of the overall upwelling, stand out as being nearly 100 % efficient. By contrast, the Southern Ocean and subpolar North Atlantic are very inefficient because they are major leaks. Subtropical regions are sources of both preformed phosphate and bio phosphorus, and hence of intermediate efficiency. The subpolar North Pacific is a region of high production but includes regions of high phosphate so that, in spite of large-scale upwelling, enough preformed phosphate leaks out for a relatively low (60 ± 10)% local efficiency.

1.5.2 $\Omega_i \rightarrow \Omega_f$ Phosphorus “Pipes”

We now ask how much of the phosphate newly emerging into the euphotic zone of region Ω_f was last injected by the biological pump of region Ω_i and how much transited to Ω_f after leaking from the pump of Ω_i as preformed phosphate. Conceptually, we may consider the $\Omega_i \rightarrow \Omega_f$ transport as defining two $\Omega_i \rightarrow \Omega_f$ diffusive “pipes”: “preformed pipes” that transport preformed phosphate and “bio pipes” that transport bio phosphorus that either remineralizes en route to, or within, destination region Ω_f . We emphasize that “pipe” here is not meant to suggest bulk-advectional transport in any way and should not be confused with the purely advective nutrient streams considered by, e.g., Pelegri and Csanady [1991], Pelegri *et al.* [1996], and Williams *et al.* [2006, 2011]. Instead, we use the term as a convenient metaphor for organizing our discussion of the $\Omega_i \rightarrow \Omega_f$ flow of phosphorus. For each of the $14 \times 14 = 196$ $\Omega_i \rightarrow \Omega_f$ pipes, we now quantify the amount of phosphorus that is carried, the flow rate with which this phosphorus reemerges as phosphate in Ω_f , and the associated transport timescale of each pipe. These metrics quantify the global “plumbing” of the biological pump.

Figure 1.4 displays the fractions of the global phosphorus inventory, μ_P , in the $\Omega_i \rightarrow \Omega_f$ bio pipes, organized into a matrix so that rows correspond to origin (Ω_i) and columns correspond to destination (Ω_f). Summing these fractions over all possible $\Omega_i \rightarrow \Omega_f$ bio pipes yields the global biological pump efficiency, E_{bio} . Figure 1.4 thus quantifies both the mass within the $\Omega_i \rightarrow \Omega_f$ bio pipe and its contribution to E_{bio} . The 11 bio pipes carrying the largest phosphorus mass ((20 ± 4)% of μ_P) account for (52 ± 6)% of E_{bio} . The pattern of the $\Omega_i \rightarrow \Omega_f$ connections shows that highly productive equatorial regions, the NAAD region of the Southern Ocean, and the subpolar North Pacific supply regenerated phosphate to either themselves (the relatively large diagonal terms) or to regions of subpolar upwelling, especially the SAAD region of the Southern Ocean. The diagonal terms quantify physical nutrient trapping whereby organic phosphorus exported by biogenic particle transport is remineralized and returned to the eu-

photic zone through subsurface convergence and upwelling [e.g., Primeau *et al.*, 2013; Holzer *et al.*, 2014]. The subpolar regions are important conduits that connect to the interior nutrient pool through isopycnal transport along outcropping density surfaces and through convective vertical mixing: (62±2)% of the bio phosphorus inventory is destined for re-exposure in the Southern Ocean.

Figure 1.4 also shows the fractions of μ_P in the $\Omega_i \rightarrow \Omega$ and $\Omega \rightarrow \Omega_f$ bio pipes, where Ω denotes the global euphotic zone ($\Omega = \sum_k \Omega_k$). Each $\Omega_i \rightarrow \Omega$ fraction is represented as a horizontal bar on the left of the corresponding Ω_i row, and each $\Omega \rightarrow \Omega_f$ fraction is represented as a vertical bar on the top of the corresponding Ω_f column. The $\Omega_i \rightarrow \Omega$ fractions are by definition equal to the pumped fractions $\beta(\Omega_i)$ of Figure 1.3. The $\Omega \rightarrow \Omega_f$ fractions show that the SO is where (62±2)% of the global bio phosphorus inventory ((24±3)% of μ_P) first reemerges into the euphotic zone as remineralized PO_4 . Outside the SO, (13±1)% and (10±1)% of the global bio phosphorus inventory first reemerge as PO_4 in the SubPoNP and EEqP euphotic zones.

Figure 1.5 displays the fractions of the global phosphorus inventory, μ_P , in the preformed $\Omega_i \rightarrow \Omega_f$ pipes: These fractions quantify the size of the purely circulation-driven $\Omega_i \rightarrow \Omega_f$ preformed pipes and their contribution to the global pump leak. Southern Ocean trapped paths are the dominant contributors with (53±2)% of the global preformed PO_4 inventory ((32±1)% of μ_P) in $\text{SO} \rightarrow \text{SO}$ transit. The $\Omega_i \rightarrow \Omega$ fractions (left bar graph) are by definition equal to the leak contributions $\lambda(\Omega_i)$ of Figure 1.3. The $\Omega \rightarrow \Omega_f$ fractions (top bar graph) show that regardless of origin, (69±1)% of preformed phosphate ((42±2)% of μ_P) is in transit to the Southern Ocean euphotic zone. The Southern Ocean euphotic zone is thus not only the main leak of the biological pump, but also the primary recipient of preformed phosphate.

The patterns of $\mu_{\text{bio}}(\Omega \rightarrow \Omega_f)$ and $\mu_{\text{pre}}(\Omega \rightarrow \Omega_f)$ in Figures 1.4 and 1.5 are remarkably similar: Regenerated and preformed phosphate reemerge into the euphotic zone with a common geographic pattern. This is consistent with the fact that the bulk of preformed phosphate enters the ocean interior at deep-water formation sites and is hence primarily injected into deep waters, much like bio phosphorus that has access to deep waters through biogenic particle transport. Thus, preformed phosphate and bio phosphorus, while having different source distributions, reemerge with a similar pattern where deep waters upwell and/or are mixed back to the surface.

1.5.3 Flow Rates of Bio Phosphorus

The phosphorus masses in the bio pipes set the global efficiency of the biological pump, but by themselves they do not determine the $\Omega_i \rightarrow \Omega_f$ transport rates. We now examine the $\Omega_i \rightarrow \Omega_f$ flow rates and the corresponding mean

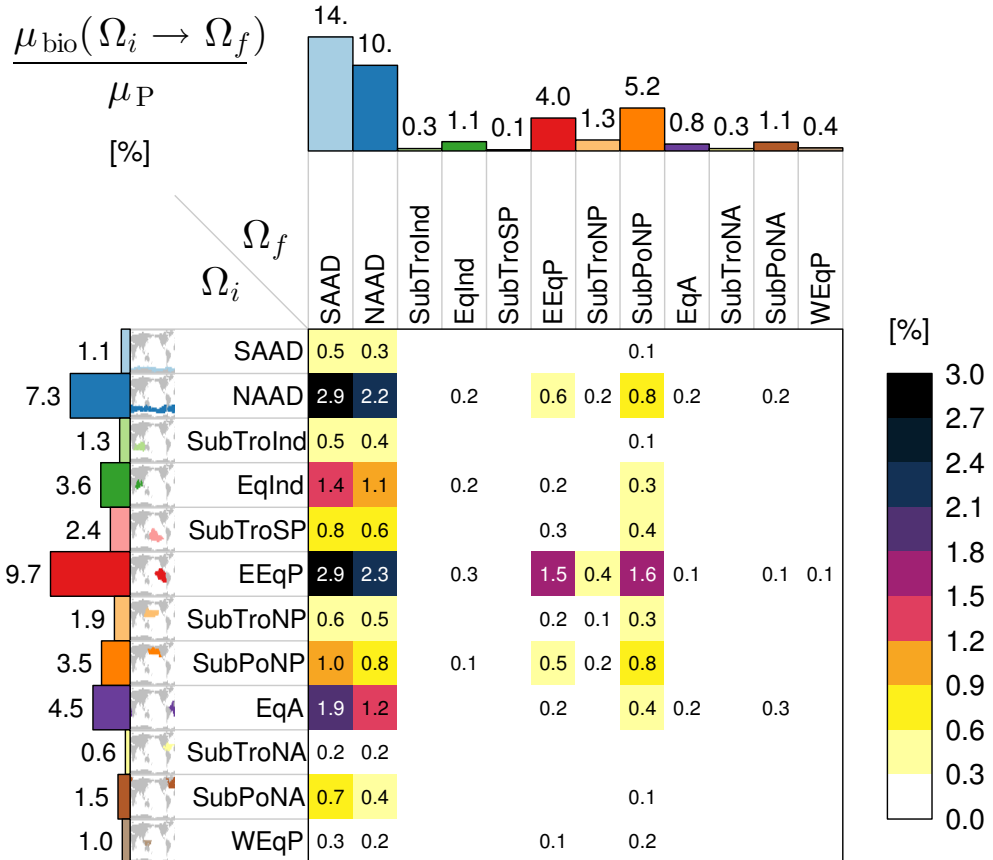


Figure 1.4: Percentage contributions to the biological pump efficiency E_{bio} by the $\Omega_i \rightarrow \Omega_f$ bio pipes that connect last phosphate uptake in Ω_i to first phosphate re-exposure in Ω_f , organized into matrix form. The left and top bar graphs are sums over Ω_f and Ω_i , respectively. The left bars thus represent the Ω_i -to-anywhere contributions to E_{bio} , and the top bars represent the anywhere-to- Ω_f contributions to E_{bio} . Summed over all matrix elements, these percentages sum to the $E_{\text{bio}} = (39 \pm 4)\%$ efficiency of the biological pump. The global inventory of bio phosphorus is $\mu_{\text{bio}}(\Omega \rightarrow \Omega) = 1.1 \text{ Pmol}$. For clarity, contributions less than 0.1 % have been omitted.

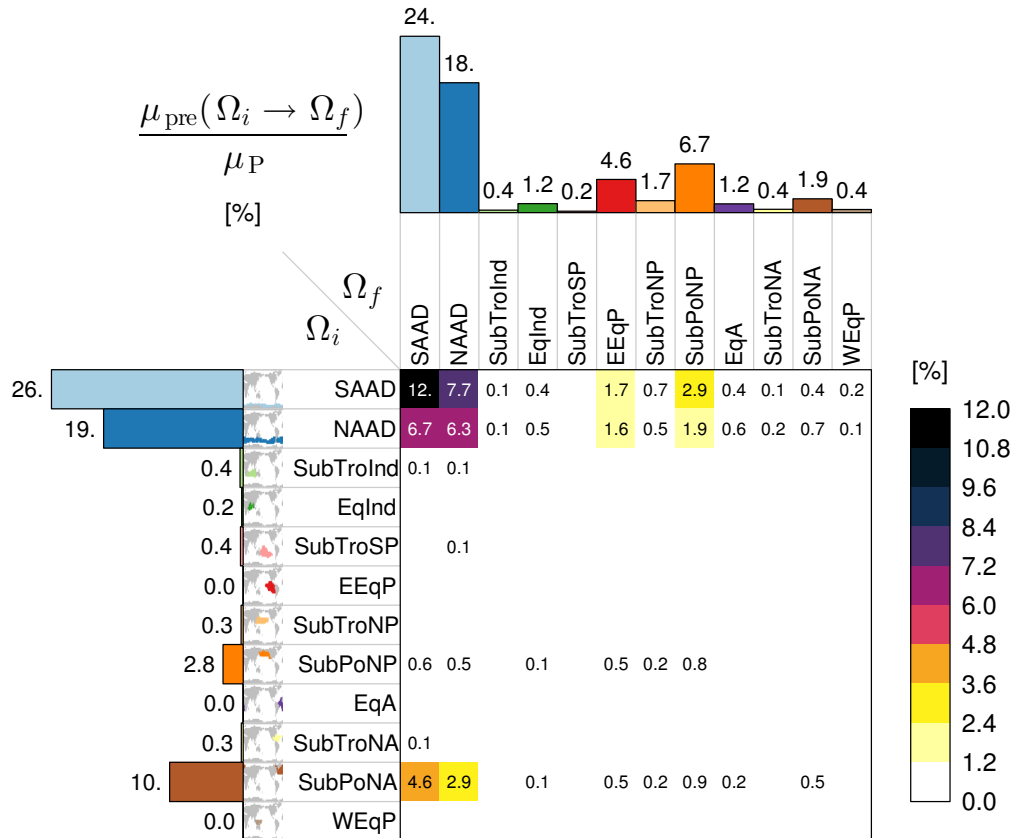


Figure 1.5: Percentage contributions to the biological pump leak by the $\Omega_i \rightarrow \Omega_f$ “preformed pipes” that connect last contact with the euphotic zone in Ω_i to first re-exposure in Ω_f , organized into matrix form. The left and top bar graphs are sums over Ω_f and Ω_i , respectively. The left bars thus represent the Ω_i -to-anywhere contributions to the pump leak, and the top bars represent the anywhere-to- Ω_f contributions to the pump leak. Summed over all matrix elements, these percentages sum to the $(61 \pm 4)\%$ leak of the biological pump. The global inventory of preformed phosphorus is $\mu_{\text{pre}}(\Omega \rightarrow \Omega) = 1.7 \text{ Pmol}$. For clarity, contributions less than 0.1 % have been omitted.

transport timescales. We only consider bio pipes here because the flow rates of preformed phosphate are completely dominated by short paths connecting Ω_i to itself or an abutting region. The dominance of these short paths is due to an underlying diffusive singularity that has been documented in a number of contexts [e.g., Hall and Holzer, 2003; Primeau and Holzer, 2006]. For a finite numerical resolution, this singularity is not realized, resulting in merely large but not infinite self-connections. For the bio pipes, however, these diffusive singularities would not even manifest in the continuum limit because the flow rates are limited by (i) finite uptake in Ω_i (finite pumping) and by (ii) the finite remineralization rate as all phosphorus in the bio pipes first passes through the DOP pool. The $\Omega_i \rightarrow \Omega_i$ self connections are still expected to have the largest flow rates because eddy diffusion provides the fastest route back to Ω_i .

Figure 1.6 displays the flow rates $\Phi_{\text{bio}}(\Omega_i \rightarrow \Omega_f)$ of the bio pipes, normalized by the corresponding global flow rate, $\Phi_{\text{bio}}(\Omega \rightarrow \Omega)$, where Ω again denotes the global euphotic zone. The expected dominance of the eddy-diffusive transport for self connections can be seen in the diagonal elements $\Omega_i = \Omega_f$, which are finite but at least an order of magnitude larger than all other terms. Because the flow rate in the $\Omega_i \rightarrow \Omega_f$ bio pipe is set by the uptake rate in Ω_i , the largest flow rates connect highly productive regions to themselves: NAAD (16 ± 3)%, EEQP (16 ± 4)%, EqA (7 ± 2)%, SubPoNP (6 ± 1)% and EqInd (5 ± 1)%, which together account for (49 ± 8)% of the total flow rate in all the bio pipes. A change in κ^{-1} by ± 0.25 yr results in less than 10% changes in the self-teleconnection flow rates. (See Appendix 1.C for details on the sensitivity of DOP and the remineralization rate κP_O to changes in κ .)

Figure 1.6 also shows the $\Omega_i \rightarrow \Omega$ (left bar graphs) and $\Omega \rightarrow \Omega_f$ (top bar graphs) flow rates. The pattern of the $\Omega_i \rightarrow \Omega$ flow rates is very similar to the pattern of the amount of bio phosphorus in the corresponding $\Omega_i \rightarrow \Omega$ pipes (Figure 1.4), suggesting that $\Phi_{\text{bio}}(\Omega_i \rightarrow \Omega)$ and $\mu_{\text{bio}}(\Omega_i \rightarrow \Omega)$ are approximately proportional at least for these large regions. The flow rates regardless of origin ($\Omega \rightarrow \Omega_f$) are largest for the SO and EEQP receptors, both of which are characterized by strong nutrient trapping (self-connections) that is the dominant contribution to their $\Omega \rightarrow \Omega_f$ flow rates.

The bio pipes that make the largest contributions to E_{bio} are those that carry the largest bio phosphorus mass, which does not necessarily correspond to the strongest flow rate. For example, NAAD \rightarrow SAAD and EEQP \rightarrow SAAD bio pipes together account for (15 ± 2)% of the total mass of bio phosphorus, μ_{bio} , but only (5 ± 3)% of the total flow rate. Conversely, the NAAD \rightarrow NAAD and EEQP \rightarrow EEQP bio pipes together only account for (10 ± 1)% of the total μ_{bio} , but (32 ± 5)% of the flow rate. The natural link between the mass and flow rate of the bio pipes is a measure of the mean time within the pipe, which we examine next.

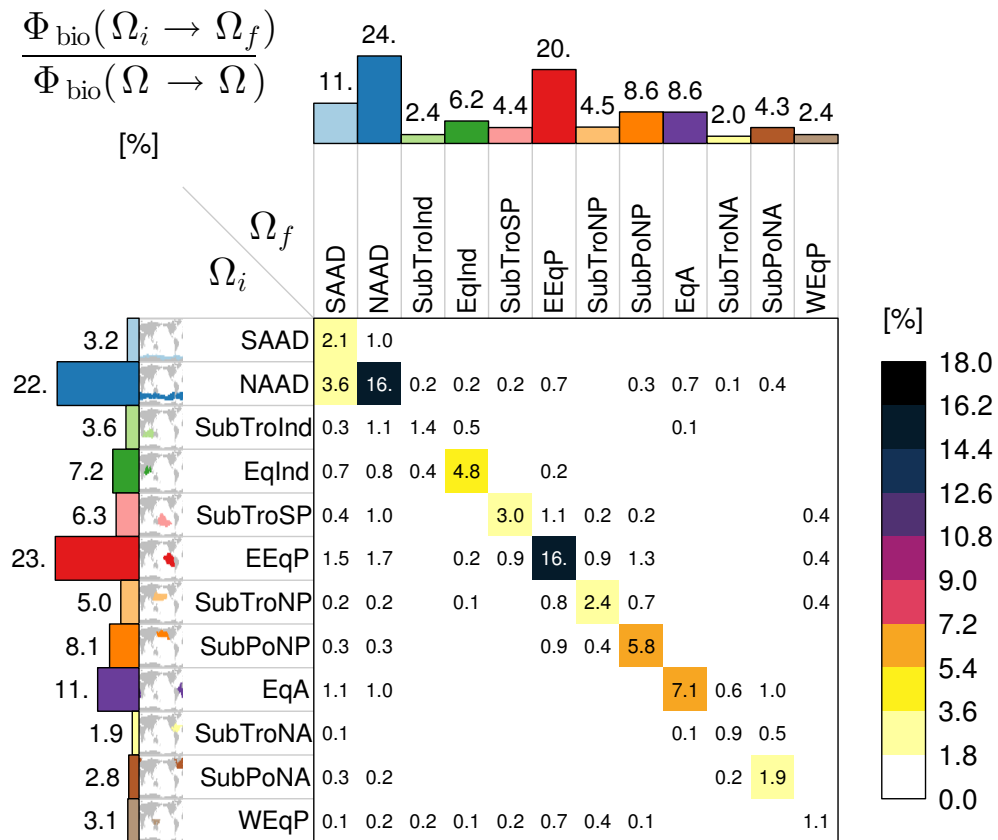


Figure 1.6: The normalized flow rates, Φ_{bio} , of the $\Omega_i \rightarrow \Omega_f$ bio pipes organized as in Figure 1.4. The flow rates have been normalized by the anywhere-to-anywhere ($\Omega \rightarrow \Omega$) flowrate of bio phosphorus and are expressed as a percentage. The left and top bar graphs are sums over Ω_f and Ω_i , representing the $\Omega_i \rightarrow \Omega$ and $\Omega \rightarrow \Omega_f$ flow rates, respectively. The global anywhere-to-anywhere flow rate of bio phosphorus is $\Phi_{\text{bio}}(\Omega \rightarrow \Omega) = 8.4 \text{ Tmol yr}^{-1}$. Flow rates less than 0.1 % of $\Phi_{\text{bio}}(\Omega \rightarrow \Omega)$ have been omitted for clarity.

1.5.4 Timescales

The timescale Γ_{bio} defined for the $\Omega_i \rightarrow \Omega_f$ pipe by the ratio

$$\Gamma_{\text{bio}}(\Omega_i \rightarrow \Omega_f) \equiv \frac{\mu_{\text{bio}}(\Omega_i \rightarrow \Omega_f)}{\Phi_{\text{bio}}(\Omega_i \rightarrow \Omega_f)} , \quad (1.6)$$

is the mean age on exit for phosphorus analogous to the mean age on exit of fluid defined by *Holzer et al.* [2012]. Γ_{bio} is the mean transit time from Ω_i to Ω_f averaged over the population of bio phosphorus molecules last utilized in Ω_i that reemerge into the euphotic zone of Ω_f either as regenerated PO₄, or as DOP that remineralizes there. Equivalently, because we are in steady state, Γ_{bio} is also the mean $\Omega_i \rightarrow \Omega_f$ transit time averaged over the population of phosphorus molecules utilized in Ω_i that are destined for reemergence in Ω_f as regenerated PO₄ or as DOP that remineralizes in Ω_f . (Γ_{bio} is also the first temporal moment of the transit-time partitioned flow-rate distribution \mathcal{J}_{bio} – see Appendix 1.A.) The phosphorus mean age on exit should not be confused with the mean transit time of phosphorus averaged over the population in transit in the ocean interior, which is typically much longer [*Holzer et al.*, 2012; *Holzer and Primeau*, 2013]. The timescale Γ_{bio} is also naturally interpreted as a mean sequestration time because, in steady state, it is the mean time that the population of bio phosphorus molecules entering the interior at Ω_i spends in the interior before reemerging into the euphotic zone at Ω_f .

Figure 1.7 shows the mean sequestration times Γ_{bio} for all $\Omega_i \rightarrow \Omega_f$, $\Omega_i \rightarrow \Omega$, and $\Omega \rightarrow \Omega_f$ bio pipes, as well as for the global $\Omega \rightarrow \Omega$ bio pipe. The longest mean sequestration times of 13 to 16 centuries are associated with phosphorus paths beginning in the North and tropical Atlantic and ending in the euphotic zone of the Indian and Pacific Oceans. The biogenic particle transport accesses North Atlantic Deep Water which then carries the phosphorus to these destinations in the deep branch of the diffusive conveyor [*Holzer and Primeau*, 2006, 2008]. However, these paths make only minor contributions to the biological pump efficiency because the corresponding flow rates are small and translate to small masses of bio phosphorus. The bio pipes exiting in the Southern Ocean, all of which make significant contributions to E_{bio} , are characterized by mean ages on exit that range from ~ 50 years (for NAAD → NAAD) to ~ 980 years (for SubPoNP → SAAD). The shortest mean sequestration times for exit in the Southern Ocean are associated with nutrient trapping, while the longest mean sequestration times are for paths from the North Pacific, where the biogenic particle transport injects phosphorus into very old waters. The mean sequestration time of bio phosphorus that first reemerges (as regenerated PO₄ or remineralizing DOP) in the Southern Ocean (SAAD and NAAD) euphotic zone, regardless of the location of last utilization, is 240 ± 60 years. Bio pipes from the

Southern Ocean are associated with relatively long timescales if they start in the SAAD region associated with southward transport and Antarctic Bottom Water (AABW) formation, and with relatively short timescales if they start in the NAAD region associated with northward Ekman transport and mode and intermediate waters. The exception are the NAAD-to-North Pacific pipes, which have roughly 1200-year mean sequestration times because of the very weak upwelling in the North Pacific. Short return timescales of decades or less characterize all diagonal elements of Figure 1.7 because of the very high flow rates associated with eddy-diffusive return flow.

The global $\Omega \rightarrow \Omega$ sequestration timescale is 130 ± 70 years, set by global biological production and the inventory of bio phosphorus (equivalently the pump efficiency). The longest mean phosphorus ages on exit regardless of where entry occurred ($\Omega \rightarrow \Omega_f$) are 430 ± 30 years for exit in SAAD, 210 ± 80 years for exit in the subpolar North Pacific, and 150 ± 50 years for exit in NAAD. All other regions have anywhere-to- Ω_f mean sequestration times that are significantly shorter (10–100 years). This pattern arises because the Southern Ocean and subpolar North Pacific re-expose both very old waters and nutrients, while the EEqP upwells old waters but also a significant proportion of relatively recently exported nutrients, leading to relatively long sequestration times for the subpolar regions and relatively short sequestration times for equatorial upwelling regions. Remarkably, the phosphorus mean age on exit anywhere (i.e., $\Omega_i \rightarrow \Omega$) is in the 100–180 years range and insensitive to where entry occurred. This restates the fact that the $\Omega_i \rightarrow \Omega$ flow rates and bio phosphorus masses are approximately proportional, as noted above. A similar feature was also evident in the study by *DeVries et al.* [2012], where a map of grid box $\rightarrow \Omega$ sequestration times shows little variation across the globe around a value of roughly 150 years except at the localized deep-water formation regions in the North Atlantic and Weddell Sea, where the sequestration time is much longer (exceeding 400 years in the study of *DeVries et al.* [2012]). These localized effects are averaged out for our flow rates that are calculated for the large regions of Figure 1.2.

Although the $\Omega_i \rightarrow \Omega_f$ masses, flow rates, and mean sequestration times give an indication of the nature of the nutrient paths taken by the bio phosphorus, the detailed spatial pathways through the ocean interior, determined by both biogenic and physical transport, are not obvious a priori. We therefore quantify the three-dimensional, transit-time partitioned paths of the bio pipes by computing their path density.

1.5.5 Path Densities

The path density $\eta_{\text{bio}}(\mathbf{r}|\tau : \Omega_i \rightarrow \Omega_f)$ is simply the concentration of bio phosphorus molecules at point \mathbf{r} that are in transit from last utilization in Ω_i to first

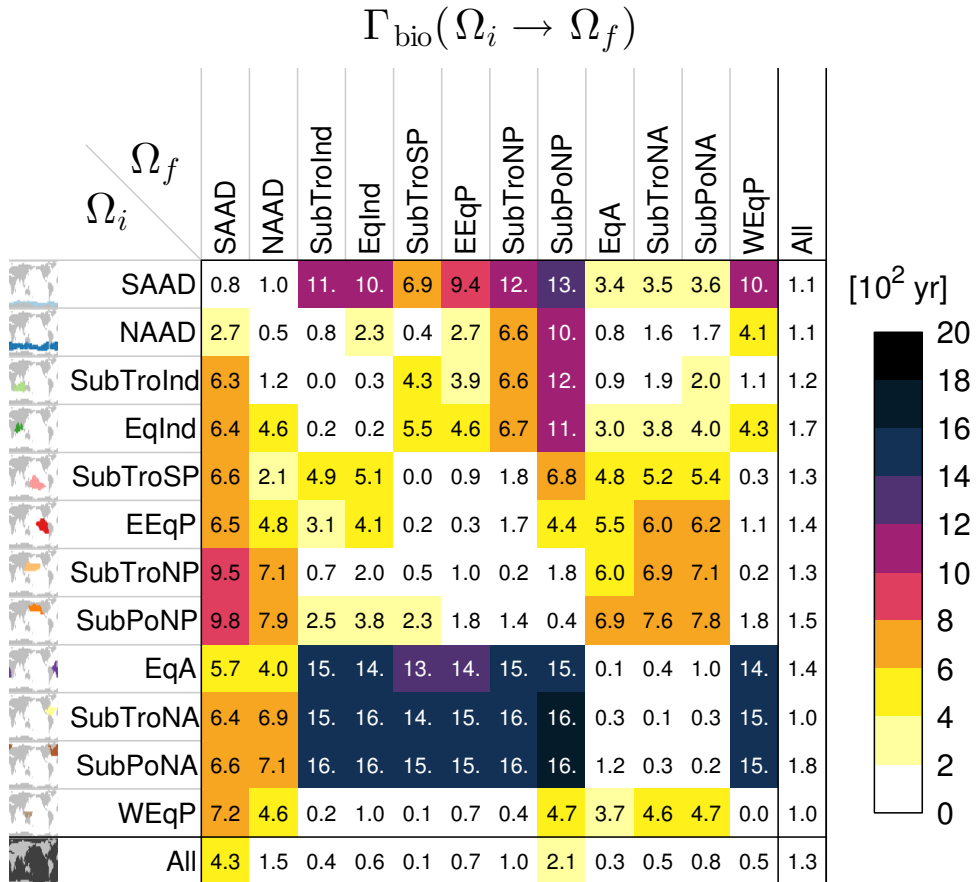


Figure 1.7: The mean sequestration times, Γ_{bio} , of the $\Omega_i \rightarrow \Omega_f$ bio pipes organized as in Figure 1.4. The mean sequestration times of the $\Omega \rightarrow \Omega_f$, and $\Omega_i \rightarrow \Omega$ bio pipes have been included as a separate row and column, respectively.

reemergence into Ω_f (as regenerated PO₄ or remineralizing DOP) in transit-time interval $(\tau, \tau + d\tau)$. Because each bio phosphorus molecule also traces out a path from Ω_i to Ω_f , this concentration is also the density of these paths [Holzer and Primeau, 2006, 2008, 2013]. In steady state, this path density is efficiently computed using forward and adjoint Green functions of the phosphorus tracer equations as detailed in Appendices 1.A and 1.B.

Because the path density is very information rich, we focus on the six most massive $\Omega_i \rightarrow \Omega_f$ bio pipes (i.e., on those with the largest $\mu_{\text{bio}}(\Omega_i \rightarrow \Omega_f)$). To summarize the transit-time dependence of the path density, we first analyze the transit-time partitioned mass of bio phosphorus in the pipes, which is given by $\mathcal{R}_{\text{bio}}(t : \Omega_i \rightarrow \Omega_f) = \int d^3r \eta_{\text{bio}}(\mathbf{r}|t : \Omega_i \rightarrow \Omega_f)$, so that $\mu_{\text{bio}}(\Omega_i \rightarrow \Omega_f) = \int_0^\infty dt \mathcal{R}_{\text{bio}}(t : \Omega_i \rightarrow \Omega_f)$ (see Appendix 1.A).

Figure 1.8 shows the transit-time partitioned mass \mathcal{R}_{bio} plotted with a logarithmic time axis to show the full distribution. The mode of these distributions, except for the self-connected NAAD → NAAD case, lies roughly between 200 and 400 years. For the NAAD → SAAD, NAAD → NAAD, and EqA → SAAD cases, a secondary mode can be seen around residence times between 1000 and 2000 years. Basin integrals of the path density (see Appendix 1.D) reveal that this secondary mode is due to deep bimodal Pacific paths: A century timescale mode is associated with the deep overturning cell [Lumpkin and Speer, 2007], while a millennial mode is presumably associated with advective-diffusive paths that stagnate in the old waters of the deep North Pacific [Holzer and Primeau, 2006, 2008]. Interestingly, basin integrals also show that the mass of bio phosphorus in transit from the Equatorial Atlantic to SAAD has greater contributions from paths in the Pacific and Indian Oceans than from paths in the Atlantic. Bio phosphorus on its way to Antarctica gets swept by the Antarctic Circumpolar Current into the Indian and Pacific Oceans, where some of it can recirculate for several centuries before reemerging in the SAAD euphotic zone. The distribution \mathcal{R}_{bio} for the NAAD → NAAD case exhibits a very fast mode of ~ 2 decades and a very long broad tail. The fast mode is due to nutrient trapping and recirculation in mode and intermediate waters. The long tail has contributions from paths in all basins, with a bimodal contribution from the Pacific (century and millennial modes as discussed above).

To summarize the spatial pattern of the path density, we distinguish fast, medium, and slow transit times by the 1/7 and 3/7 quantiles (first and third septiles) of \mathcal{R}_{bio} . By definition, fast paths thus carry 1/7 of the bio phosphorus mass, medium paths carry 2/7 of the mass, and slow paths carry 4/7 of the mass in the $\Omega_i \rightarrow \Omega_f$ bio pipe, with proportional contributions to E_{bio} . While this definition of fast, medium, and slow transit-time bands is somewhat arbitrary, experimentation with different time bands showed that the first and third septiles are well positioned to separate out different flow regimes as quantified

$$\mathcal{R}_{\text{bio}}(t) = t \mathcal{J}_{\text{reg}}(t)$$

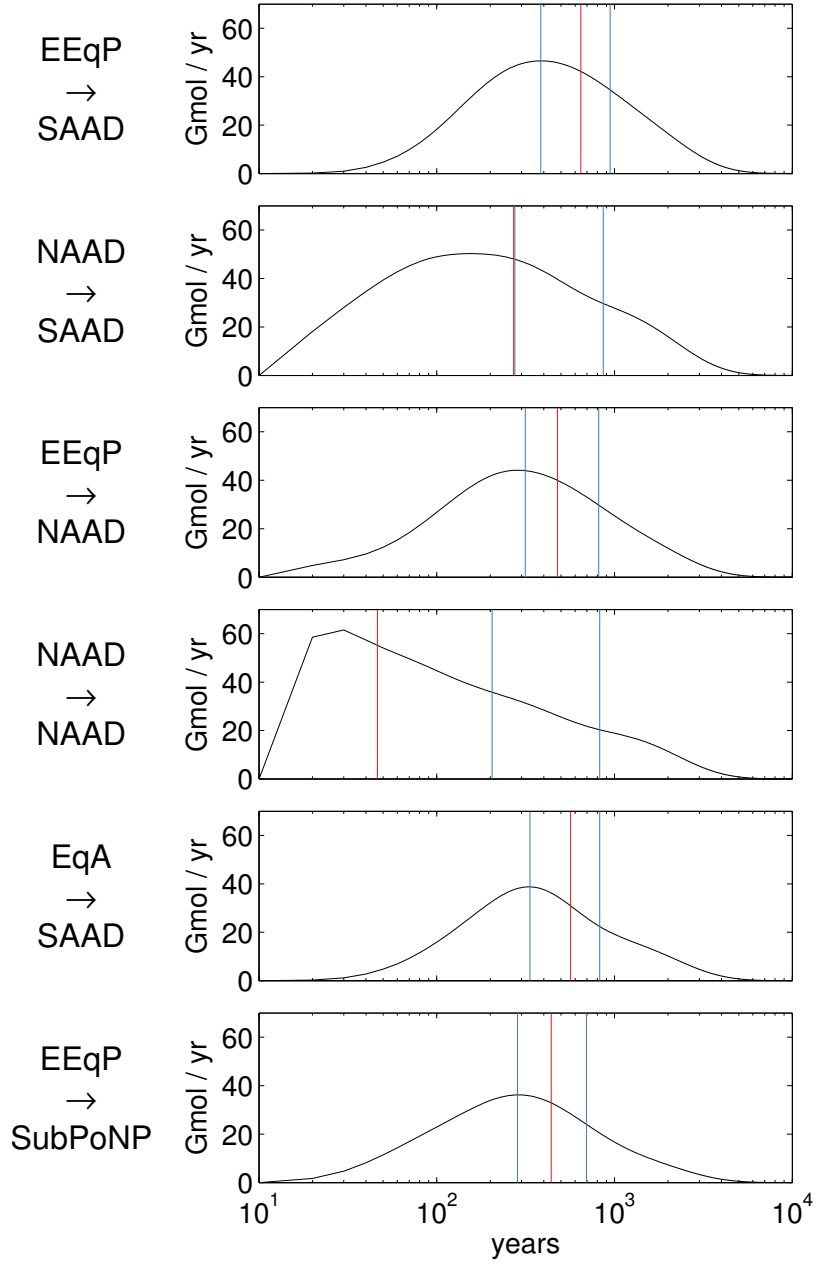


Figure 1.8: The residence-time distributions $\mathcal{R}_{\text{bio}}(t) = t \mathcal{J}_{\text{reg}}(t)$ for the bio pipes with the 6 dominant masses $\mu_{\text{bio}}(\Omega_i \rightarrow \Omega_f)$. The mean sequestration time (phosphorus mean age on exit), Γ_{bio} , is indicated as a red line and the first and third septiles of \mathcal{R}_{bio} are indicated as vertical blue lines.

below. The first and third septiles are indicated on Figure 1.8. Except for the self-connected NAAD→NAAD case, the first septile roughly tracks the mode of \mathcal{R}_{bio} , while the third septile lies between 700 and 1000 years. The mean sequestration time, Γ_{bio} , falls between the first and third septiles, except for the overlapping NAAD→NAAD and abutting NAAD→SAAD cases. For the NAAD→NAAD case, Γ_{bio} is much shorter than the first septile and close to the decadal mode.

Figure 1.9 displays the global zonal averages of the path density η_{bio} integrated over the fast, medium, and slow transit-time bands, respectively. Note that the local magnitude of the time-integrated path density is directly proportional to its contribution to the biological pump efficiency. Because of their order 1000-year timescale, the slow paths tend to lie in the abyssal ocean, are highly eddy-diffusive, and disperse the bio phosphorus they carry throughout the world oceans. The fast paths tend to be concentrated in the directly wind-driven thermocline. The EqA→SAAD paths are the exception with fast paths that are more diffusive and access upwelling Circumpolar Deep Water (CDW). Because of the eddy-diffusive component of the transport, a general feature of the $\Omega_i \rightarrow \Omega_f$ path density for non-overlapping origin and receptor regions is that it goes to zero close to both Ω_i and Ω_f . This is because phosphorus molecules close to Ω_i tend to trace out $\Omega_i \rightarrow \Omega_i$ paths, and those close to Ω_f tend to trace out $\Omega_f \rightarrow \Omega_f$ paths [Holzer, 2009; Holzer and Primeau, 2006, 2008, 2013].

Figure 1.9 shows that the density class ($27.0 < \sigma_0 < 27.6$) kg m⁻³, broadly associated with AAIW [Talley, 1996], carries a significant fraction of the bio phosphorus exported from the Eastern Equatorial Pacific (EEqP) that is destined for the Southern Ocean, with a similar pattern for destinations SAAD and NAAD. Volume integrating η_{bio} , we find that the AAIW density class carries ~50 % of the fast and medium EEqP→SO paths. Regardless of transit time, the AAIW density class carries ~35 % of all EEqP→SO bio phosphorus, with the remaining ~65 % being carried by denser water, including CDW that upwells in the Southern Ocean. AAIW is commonly associated with the export of pre-formed nutrients out of the Southern Ocean [e.g., Sarmiento *et al.*, 2004; Palter *et al.*, 2010; Holzer *et al.*, 2014]. However, the bio phosphorus path density reveals that eddy diffusion and recirculation in these water masses additionally allows nutrients last exported into the deeper waters of the EEqP to return to the Southern Ocean euphotic zone. The path density furthermore shows that the long timescale EEqP→SO pathways explore the entire world ocean, but are concentrated at mid depths in the North Pacific, which holds the ocean's oldest waters.

The paths connecting the Southern Ocean to itself that contribute most to E_{bio} (NAAD→SAAD and NAAD→NAAD) are confined to the Southern Ocean for the fast paths, with the NAAD→SAAD paths extending deeper, presumably

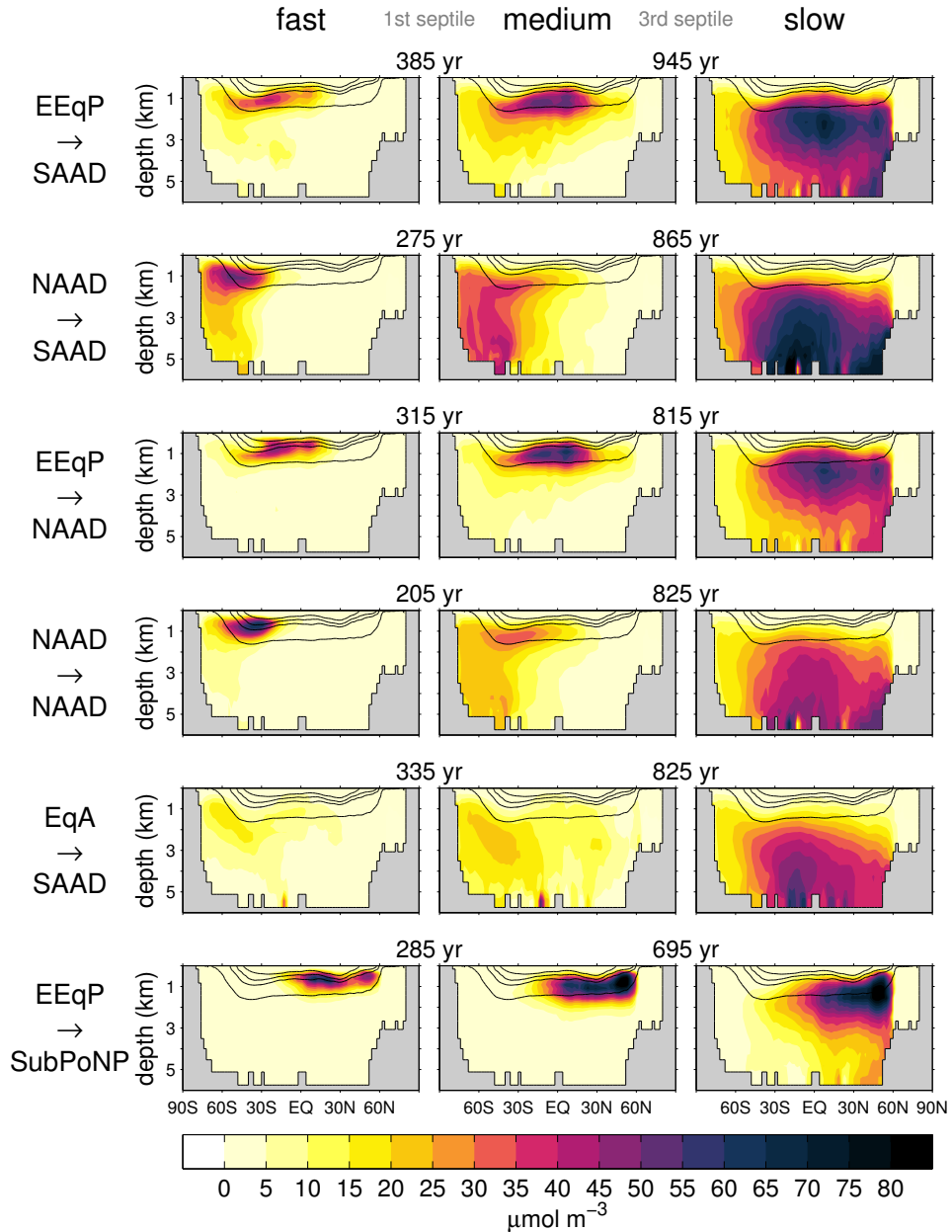


Figure 1.9: The path densities of the bio pipes with the 6 dominant masses $\mu_{\text{bio}}(\Omega_i \rightarrow \Omega_f)$, zonally averaged over the entire world ocean. These are the spatial patterns associated with the distributions of Figure 1.8. The path densities have been integrated over the fast, medium, and slow transit-time bands bounded by the first and third septiles of \mathcal{R}_{bio} indicated between the three panels of each $\Omega_i \rightarrow \Omega_f$ pathway. The black contours indicate the σ_0 isopycnals at 26.6, 27.0, 27.2, and 27.6 kg m^{-3} , with AAIW typically considered to lie between 27.0 and 27.6 kg m^{-3} .

because return to the SAAD surface occurs through deep vertical mixing. At intermediate timescales, the NAAD→SAAD paths access the deep SO and Antarctic Bottom Water with greater density than the NAAD→NAAD paths, which are mostly concentrated in intermediate and mode waters. At long timescales, both the NAAD→SAAD and NAAD→NAAD paths explore the abyssal ocean, with greater density for the NAAD→SAAD paths as return to SAAD dictates access to the deep cell of the global overturning circulation.

Fast and medium timescale paths from the Equatorial Atlantic to the SAAD region of the Southern Ocean (EqA→SAAD) are dominated by upwelling CDW, while for long timescales these paths lie in the abyssal ocean. Finally, the paths from the Eastern Equatorial Pacific to the subpolar North Pacific (EEqP→SubPoNP) are dominated by thermocline waters. For the EEqP→SubPoNP paths relatively little of the abyssal ocean is explored even for the slow transit-time band because most of the deep paths do not connect efficiently to the North Pacific surface [e.g., Schmitz, 1995; Toggweiler and Samuels, 1993; Sun and Bleck, 2001; Ganachaud and Wunsch, 2000].

1.6 Discussion and Conclusions

We have systematically analyzed the combined biogenic and physical transport of nutrients in the global ocean and how this transport determines the global efficiency of the biological pump, defined by the size of the global non-preformed phosphorus pool. Non-preformed phosphorus, which we have dubbed bio phosphorus, is comprised of regenerated phosphate and DOP. Unlike previous approaches that assess the importance of a particular region by perturbing its nutrient uptake (for example by forcing complete utilization in the Southern Ocean) [e.g., Sarmiento *et al.*, 2004; Primeau *et al.*, 2013], and computing the resulting anomaly from the unperturbed base state, we have used synthetic Green-function tracers to assess the transport from and to specified regions within an unperturbed, data-assimilated estimate of the global phosphorus cycle. This has the advantage of diagnosing the nutrient cycle as it operates within the current climate, rather than diagnosing the response to altering the nutrient cycle, a response that is highly nonlinear in the perturbed biogeochemical parameters.

This work is closely related to that of DeVries *et al.* [2012] on sequestration efficiency. For the case where the destination region is not specified, and in the limit of instant remineralization (no DOP pool), Γ_{bio} is equal to the mean sequestration time introduced by DeVries *et al.* [2012]. In that case and limit, the flow rate Φ_{bio} reduces to the export production of Ω_i , and the transit-time partitioned flow rate \mathcal{J}_{bio} in the $\Omega_i \rightarrow \Omega$ bio pipe is proportional to the “sequestration efficiency” of DeVries *et al.* [2012]. Our approach here generalizes the results of

DeVries et al. [2012] to the case of nonzero remineralization timescale (nonzero DOP pool), and to re-exposure destinations Ω_f that are specified subregions of the global euphotic zone. The corresponding generalized sequestration efficiency of a given region is the cumulative form of the flow-rate distribution \mathcal{J}_{bio} developed here (see Appendix 1.E where the precise connections are developed). Another key distinction with the work of *DeVries et al.* [2012] is that we diagnose the nutrient transport in terms of the interior “plumbing” of the biological pump, rather than solely in terms of the geographic surface distribution of the sequestration efficiency.

Our analysis provides a new view of the inner workings of the global biological pump that quantifies the importance of different geographic regions for pumping or leaking phosphorus, as well as the timescales and pathways interconnecting these regions. Our key findings are as follows:

- While biological productivity alone is insufficient to guarantee high pump efficiency without correspondingly long sequestration times, the equatorial and subpolar regions of high productivity are nevertheless the largest contributors to the biological pump: the Eastern Equatorial Pacific (EEqP), North of the Antarctic Divergence (NAAD), Equatorial Atlantic (EqA), Subpolar North Pacific (SubPoNP), Subpolar North Atlantic (SubPoNA), and Equatorial Indian (EqInd) regions together account for $(77 \pm 7)\%$ of the pump efficiency.
- Consistent with previous studies [*DeVries et al.*, 2012; *Primeau et al.*, 2013], the high-latitude regions are the largest leaks of the biological pump: the Southern Ocean (SAAD and NAAD), subpolar North Atlantic, and subpolar North Pacific, account for $(96 \pm 1)\%$ of the global pump leak. The SAAD and NAAD regions of the Southern Ocean make comparable contributions to the leak of $(43 \pm 4)\%$ and $(32 \pm 1)\%$, respectively.
- Of the $14 \times 14 = 196$ possible $\Omega_i \rightarrow \Omega_f$ pathways of bio phosphorus (“bio pipes”) considered, a mere 11 carry $(52 \pm 6)\%$ of the biological pump efficiency (i.e., $(20 \pm 4)\%$ of the global bio phosphorus inventory). The bio pipes contributing most to E_{bio} connect the Eastern Equatorial Pacific and Equatorial Atlantic oceans to the Southern Ocean $(21 \pm 3)\%$, the Southern Ocean to itself $(15 \pm 3)\%$, the Eastern Equatorial Pacific to the subpolar North Pacific $(4 \pm 1)\%$, and the Eastern Equatorial Pacific to itself $(4 \pm 1)\%$. By contrast, more than half $(53 \pm 2)\%$ of the preformed inventory is carried by just the four preformed pipes that connect the Southern Ocean to itself.
- The patterns with which remineralized bio phosphorus and preformed phosphate first reemerge into the euphotic zone are qualitatively similar. For both bio phosphorus and preformed phosphate the dominant receptors are the

SAAD and NAAD regions of the Southern Ocean, with significant secondary receptors in the equatorial and subpolar Pacific. $(69 \pm 1)\%$ of the global preformed phosphate inventory and $(61 \pm 2)\%$ of the global bio phosphorus inventory first reemerge as phosphate into the Southern Ocean euphotic zone. The similarity between bio and preformed reexposure patterns is likely due to the fact that particle transport injects bio phosphorus into the same deep waters that carry the bulk of preformed phosphate. Thus, preformed and bio phosphorus, while having different source distributions, reemerge with a similar geographic pattern.

- The $\Omega_i \rightarrow \Omega_f$ flow rates of bio phosphorus are dominated by the $\Omega_i = \Omega_f$ “self-connections”. This is a consequence of the top-loaded power-law distribution of DOP production and the eddy-diffusive nature of the physical circulation, which returns fluid elements to the surface after a short residence time in the interior [Primeau and Holzer, 2006; Hall *et al.*, 2007]. The largest flow rates are associated with the NAAD \rightarrow NAAD and EEQp \rightarrow EEQp bio pipes, which contribute $(16 \pm 3)\%$ and $(16 \pm 4)\%$, respectively, to the global anywhere-to-anywhere flow of bio phosphorus, but only $(5 \pm 1)\%$ and $(4 \pm 1)\%$, respectively, to the efficiency of the biological pump.
- The mean sequestration time (phosphorus mean age on exit) for the global anywhere-to-anywhere bio pipe is 130 ± 70 years, set by the global export production and the efficiency of the biological pump. Bio pipes connecting the North and Equatorial Atlantic to the Indian and Pacific Oceans follow the deep diffusive conveyor circulation [Holzer and Primeau, 2006, 2008] and have a mean sequestration time of ~ 1300 – 1600 years. Including all possible export regions (i.e., anywhere-to- Ω_f bio pipes), the Southern Ocean and the subpolar North Pacific have the longest mean ages on exit (~ 150 – 430 years). All other regions have anywhere-to- Ω_f mean ages on exit that are significantly shorter (~ 10 – 100 years). The phosphorus mean age on exit anywhere (i.e., Ω_i -to-anywhere) is relatively insensitive to where entry occurred at values ranging 100 – 180 years, reflecting an approximate proportionality between the $\Omega_i \rightarrow \Omega$ flow rates and bio phosphorus masses. Perturbations in biological productivity are thus expected to affect the nutrient supply across the globe on a timescale of about a century.
- The path density of bio phosphorus allowed us to quantify the three-dimensional structure of the bio pipes. Distinct patterns were identified for the fast, intermediate, and slow paths, defined so that they carry $1/7$, $2/7$, and $4/7$ of the bio phosphorus masses in the pipes. For the most massive, non-self-connected bio pipes, the fast paths have transit times less than ~ 300 – 400 years, while the slow paths have transit times longer than ~ 700 – 900 years. The fast

paths are generally concentrated in the thermocline, medium paths additionally access upwelling CDW, while the slow paths tend to explore most of the deep ocean. Southern Ocean self-connected slow paths and slow paths to the SAAD region of the Southern Ocean tend to be concentrated in the abyssal ocean, while other major slow paths tend to be concentrated in the very old waters of the mid-depth North Pacific.

- The path density revealed that the dominant bio pipes from the Eastern Equatorial Pacific to the Southern Ocean (SAAD and NAAD) carry about a third of their bio phosphorus mass in the density class associated with AAIW, while the rest is carried by denser waters, including CDW. Particle export of bio phosphorus in the equatorial Pacific accesses these water masses in which the phosphorus can return to the Southern Ocean via eddy diffusion and gyre recirculation. Thus, the Southern Ocean not only supplies tropical and Northern Hemisphere waters with preformed nutrients via mode and intermediate waters, but the Southern Ocean also receives a significant amount of regenerated nutrients via AAIW.

Our study has a number of limitations that should be kept in mind. Chief among these is that our circulation is steady. While the circulation represents a ventilation-weighted time average whose transport was optimized to reproduce annual-mean tracer observations, our analysis cannot capture covariances between seasonal biological productivity and seasonal physical flow. Our model also has coarse resolution and production in shallow shelf areas (less deep than the euphotic zone) has not been captured [Primeau *et al.*, 2013]. The phosphorus cycle itself makes approximations such as a globally uniform Martin exponent and a single remineralization timescale [Kwon and Primeau, 2006; Primeau *et al.*, 2013]. In a future study we plan to relax some of these approximations and to explore how the plumbing of the biological pump responds to perturbations in the micronutrient supply by dynamically coupling the phosphorus and iron cycles.

Appendices

1.A Origin/Destination and Transit-Time Partitioned Phosphorus

Following *Holzer and Primeau* [2013], the contribution to P_{reg} from production in region Ω_i a time t ago during time interval dt , denoted as $dt g_{\text{reg}}(\mathbf{r}, t | \Omega_i)$ so g_{reg} is a distribution with respect to t , is given by

$$g_{\text{reg}}(\mathbf{r}, t | \Omega_i) = \int d^3\mathbf{r}' G_{\text{IO}}(\mathbf{r}, t | \mathbf{r}', 0) \mathcal{S}J(\mathbf{r}') \Omega_i(\mathbf{r}') , \quad (1.7)$$

where $d^3\mathbf{r}'$ is the volume element with respect to \mathbf{r}' and the integral is over the entire ocean. The mask Ω_i is unity everywhere beneath surface patch Ω_i . Similarly, the contribution to P_{O} from production in Ω_i a time t ago during dt , denoted as $dt g_{\text{O}}(\mathbf{r}, t | \Omega_i)$, is given by

$$g_{\text{O}}(\mathbf{r}, t | \Omega_i) = \int d^3\mathbf{r}' G_{\text{OO}}(\mathbf{r}, t | \mathbf{r}', 0) \mathcal{S}J(\mathbf{r}') \Omega_i(\mathbf{r}') . \quad (1.8)$$

The contribution to the bio phosphorus field is thus given by $g_{\text{bio}} \equiv g_{\text{reg}} + g_{\text{O}}$.

The preformed phosphate last in contact with the euphotic zone in Ω_i during dt a time t ago is given by $dt g_{\text{pre}}(\mathbf{r}, t | \Omega_i)$, where g_{pre} satisfies [*Holzer et al.*, 2012]

$$(\partial_t + \mathcal{T}) g_{\text{pre}}(\mathbf{r}, t | \Omega_i) = -\gamma_0(\mathbf{r}) [g_{\text{pre}}(\mathbf{r}, t | \Omega_i) - \delta(t) P_{\text{I}}(\mathbf{r}) \Omega_i(\mathbf{r})] , \quad (1.9)$$

where $\gamma_0(\mathbf{r})$ is only nonzero for points \mathbf{r} in the euphotic zone, where $\gamma_0^{-1} = 1 \text{ s}$, ensuring fast relaxation to the boundary conditions. The Dirac delta function acts as a source of preformed PO_4 , and for $t > 0$, the fast relaxation ensures that all preformed PO_4 reemerging into the euphotic zone is quickly set to zero. We thus obtain

$$g_{\text{pre}}(\mathbf{r}, t | \Omega_i) = \int d^3\mathbf{r}' G_{\text{II}}(\mathbf{r}, t | \mathbf{r}', 0) \gamma_0(\mathbf{r}') P_{\text{I}}(\mathbf{r}') \Omega_i(\mathbf{r}') . \quad (1.10)$$

Note that here γ_0 controls both the source and sink for G_{II} .

The inventories μ_X (total mass or moles of phosphorus) for $X = \text{pre}, \text{reg}$, or O are given by

$$\mu_X(\Omega_i) = \int_0^\infty dt \int d^3\mathbf{r} g_X(\mathbf{r}, t | \Omega_i) . \quad (1.11)$$

The total mass of bio phosphorus last taken up on Ω_i is $\mu_{\text{bio}}(\Omega_i) = \mu_{\text{reg}}(\Omega_i) + \mu_O(\Omega_i)$. The total phosphorus inventory is given by $\mu_P = \sum_i [\mu_{\text{bio}}(\Omega_i) + \mu_{\text{pre}}(\Omega_i)]$.

Phosphorus Flow Rates and Timescales

The flow rate of regenerated or preformed phosphate newly emerging into the euphotic zone of Ω_f , partitioned according to transit time and origin Ω_i follows from (1.7) and (1.10) as

$$dt \mathcal{J}_X(t : \Omega_i \rightarrow \Omega_f) \equiv dt \int d^3\mathbf{r} \Omega_f(\mathbf{r}) \gamma_0(\mathbf{r}) g_X(\mathbf{r}, t | \Omega_i) , \quad (1.12)$$

where $X = \text{pre}$ or reg . We note that all DOP remineralizing en route to, or within Ω_f , is accounted for by g_{reg} and hence by \mathcal{J}_{reg} .

The total mass of bio and preformed phosphorus transiting from $\Omega_i \rightarrow \Omega_f$ with a transit time in the interval $(t, t + dt)$ are thus given by

$$dt \mathcal{R}_{\text{bio}} = t dt \mathcal{J}_{\text{reg}} \quad \text{and} \quad dt \mathcal{R}_{\text{pre}} = t dt \mathcal{J}_{\text{pre}} . \quad (1.13)$$

The total $\Omega_i \rightarrow \Omega_f$ mass and flow rate of bio phosphorus regardless of transit time are obtained as

$$\mu_{\text{bio}}(\Omega_i \rightarrow \Omega_f) = \int dt \mathcal{R}_{\text{bio}}(t : \Omega_i \rightarrow \Omega_f) , \quad (1.14)$$

$$\Phi_{\text{bio}}(\Omega_i \rightarrow \Omega_f) = \int dt \mathcal{J}_{\text{bio}}(t : \Omega_i \rightarrow \Omega_f) . \quad (1.15)$$

The mean age on exit of bio phosphorus, equal to the mean sequestration time in steady state, is given by

$$\Gamma_{\text{bio}} = \frac{\langle t \mathcal{J}_{\text{bio}}(t) \rangle}{\langle \mathcal{J}_{\text{bio}}(t) \rangle} = \frac{\mu_{\text{bio}}}{\Phi_{\text{bio}}} , \quad (1.16)$$

where $\langle x(t) \rangle \equiv \int_0^\infty x(t) dt$.

Phosphorus Path Density

The fraction of PO_4 at (\mathbf{r}, t) that will reemerge as phosphate in Ω_f after a transit time in the interval $(\tau, \tau + dt\tau)$ is denoted by $d\tau \tilde{\mathcal{G}}_I(\mathbf{r}, \tau - t|\Omega_f)$. The corresponding fraction of DOP is denoted by $d\tau \tilde{\mathcal{G}}_O(\mathbf{r}, \tau - t|\Omega_f)$. These quantities are given by

$$\tilde{\mathcal{G}}_I(\mathbf{r}, \tau - t|\Omega_f) = \int d^3\mathbf{r}' \Omega_f(\mathbf{r}') \gamma_0(\mathbf{r}') G_{II}(\mathbf{r}', \tau - t|\mathbf{r}, 0) , \quad (1.17)$$

and

$$\tilde{\mathcal{G}}_O(\mathbf{r}, \tau - t|\Omega_f) = \int d^3\mathbf{r}' \Omega_f(\mathbf{r}') \gamma_0(\mathbf{r}') G_{IO}(\mathbf{r}', \tau - t|\mathbf{r}, 0) , \quad (1.18)$$

where the fast relaxation with rate constant γ_0 captures PO_4 first reemerging in the euphotic zone of Ω_f .

The $\Omega_i \rightarrow \Omega_f$ path density is now simply given by the $\Omega_i \rightarrow \mathbf{r}$ phosphorus contributions g multiplied by the $\mathbf{r} \rightarrow \Omega_f$ arrival fractions $\tilde{\mathcal{G}}$ integrated over all possible intermediate times as \mathbf{r} [Holzer and Primeau, 2006, 2013]:

$$\eta_{\text{reg}}(\mathbf{r}|\tau : \Omega_i \rightarrow \Omega_f) = \int_0^\tau dt \tilde{\mathcal{G}}_I(\mathbf{r}, \tau - t|\Omega_f) g_{\text{reg}}(\mathbf{r}, t|\Omega_i) , \quad (1.19)$$

and

$$\eta_O(\mathbf{r}|\tau : \Omega_i \rightarrow \Omega_f) = \int_0^\tau dt \tilde{\mathcal{G}}_O(\mathbf{r}, \tau - t|\Omega_f) g_O(\mathbf{r}, t|\Omega_i) , \quad (1.20)$$

where τ is the $\Omega_i \rightarrow \Omega_f$ transit, and hence residence, time. The path density of bio phosphorus is given by $\eta_{\text{bio}} = \eta_{\text{reg}} + \eta_O$.

We also note that $\int d^3\mathbf{r} \eta_{\text{bio}}(\mathbf{r}|t : \Omega_i \rightarrow \Omega_f) = \mathcal{R}_{\text{bio}}(t : \Omega_i \rightarrow \Omega_f)$, where the spatial integral is over the entire ocean domain. This follows from the definition of the path density in terms of the Green functions of the forward and time-reversed adjoint phosphate cycles, and the Chapman-Kolmogorov identity for these Green functions [e.g., Holzer and Primeau, 2008, 2013].

1.B Computational Methods

We apply the framework of *Holzer and Primeau* [2013] (see their appendix B). The spatially discretized fields are organized into column vectors whose rows map to grid locations \mathbf{r} . The fields g_{pre} , g_{reg} , and g_O therefore become N -element column vectors (denoted in bold) so that we can write

$$\mathbf{A} = \begin{bmatrix} \mathbf{T} + \mathbf{L}_0 & -\kappa \mathbf{I} \\ 0 & \mathbf{T} + \kappa \mathbf{I} \end{bmatrix}, \quad \text{and} \quad \mathbf{g} = \begin{bmatrix} \mathbf{g}_{\text{pre}} & \mathbf{g}_{\text{reg}} \\ 0 & g_O \end{bmatrix}, \quad (1.21)$$

where \mathbf{T} is the $N \times N$ discrete version of \mathcal{T} , $\mathbf{L}_0 \equiv \text{diag}(\gamma_0)$, and \mathbf{I} is the $N \times N$ identity matrix. The matrix of distributions \mathbf{g} satisfies the initial value problem:

$$(\partial_t + \mathbf{A})\mathbf{g}(t) = 0 \quad \text{with} \quad \mathbf{g}(0) = \begin{bmatrix} \mathbf{L}_0 \mathbf{P}_I \boldsymbol{\Omega}_i & 0 \\ 0 & \mathbf{S} \mathbf{L} \mathbf{P}_I \boldsymbol{\Omega}_i \end{bmatrix}, \quad (1.22)$$

where $\boldsymbol{\Omega}_i$ is an N -element column vector for the mask $\Omega_i(\mathbf{r})$, $\mathbf{P}_I \equiv \text{diag}(\mathbf{P}_I)$, \mathbf{S} is the discretized matrix version of the operator \mathcal{S} , and $\mathbf{L} \equiv \text{diag}(\boldsymbol{\gamma})$. To compute the fields $g_X(t)$, we time-step (1.22) from the initial condition using a Crank-Nicholson scheme. Multiplying on the left by $\boldsymbol{\Omega}_f^\top \mathbf{V}$, where \mathbf{V} is the diagonal matrix of volume elements $d^3 \mathbf{r}$, corresponds to the volume integral on the mask $\Omega_f(\mathbf{r})$, therefore the field $\mathcal{J}_X(t)$ can be directly computed from $\mathbf{g}(t)$ by multiplying its components on the left by $\boldsymbol{\Omega}_f^\top \mathbf{V} \mathbf{L}_0$ for the inorganic part. $\mathcal{R}_{\text{bio}}(t)$ follows from (1.13). Integrating (1.22) over all times yields

$$\mathbf{A} \langle \mathbf{g}(t) \rangle = \mathbf{g}(0), \quad (1.23)$$

which can be solved for $\langle \mathbf{g}(t) \rangle$ by direct matrix inversions of the two columns of $\mathbf{g}(0)$. Similarly as for $\mathcal{J}(t)$, The flow rates Φ_X are computed directly by multiplication on the left of (1.23) by $\boldsymbol{\Omega}_f^\top \mathbf{V} \mathbf{L}_0$. Finally, computing μ_X requires the moment $\langle t \mathbf{g}(t) \rangle$, which is the solution to

$$\mathbf{A} \langle t \mathbf{g}(t) \rangle = \langle \mathbf{g}(t) \rangle, \quad (1.24)$$

obtained by time integrating (1.22) after multiplying by t which can be solved for $\langle t \mathbf{g}(t) \rangle$ by direct inversion of the columns of $\langle \mathbf{g}(t) \rangle$.

We calculate the distributions $\tilde{\mathcal{G}}_I$ and $\tilde{\mathcal{G}}_O$ similarly, but we use an adjoint approach for computational efficiency so that we need only one tracer per patch Ω_f rather than one tracer per interior point \mathbf{r} . Organizing the spatial field $\tilde{\mathcal{G}}_X$ into column vector $\tilde{\mathcal{G}}_X$, we define

$$\tilde{\mathcal{G}} = \begin{bmatrix} \tilde{\mathcal{G}}_I \\ \tilde{\mathcal{G}}_O \end{bmatrix} \quad \text{and} \quad \tilde{\mathbf{A}} = \begin{bmatrix} \tilde{\mathbf{T}} + \mathbf{L}_0 & 0 \\ -\kappa \mathbf{I} & \tilde{\mathbf{T}} + \kappa \mathbf{I} \end{bmatrix}, \quad (1.25)$$

where $\tilde{\mathbf{T}} \equiv \mathbf{V}^{-1}\mathbf{T}^\top\mathbf{V}$ is the adjoint of \mathbf{T} with respect to the volume-weighted inner product and \mathbf{V} is the diagonal matrix of grid volumes $d^3\mathbf{r}$). $\tilde{\mathbf{G}}$ satisfies the adjoint final value problem:

$$(-\partial_t + \tilde{\mathbf{A}})\tilde{\mathbf{G}}(t) = 0 \quad \text{with} \quad \tilde{\mathbf{G}}(0) = \begin{bmatrix} \mathbf{L}_0 \boldsymbol{\Omega}_f \\ 0 \end{bmatrix} , \quad (1.26)$$

which we time step backward from the final value $\tilde{\mathbf{G}}(0)$. Note that this evolves $\tilde{\mathbf{G}}(t)$ in the time-reversed adjoint flow from the final value. Without this adjoint technique, one would need to go through the expensive computation of the full $2N \times 2N$ matrix of $\mathbf{G}(\mathbf{r}, t | \mathbf{r}', 0)$ to obtain to $\tilde{\mathbf{G}}(t)$. Integrating (1.26) in time, we get

$$\tilde{\mathbf{A}}\langle\tilde{\mathbf{G}}(t)\rangle = \tilde{\mathbf{G}}(0) , \quad (1.27)$$

which we solve for $\langle\tilde{\mathbf{G}}(t)\rangle$ by direct inversion.

The discrete versions of the path densities $\eta_X(t)$ are computed by the convolution of the element-wise product of the time-stepped $\mathbf{g}(t)$ and $\tilde{\mathbf{G}}(\tau - t)$. The time-integrated path densities $\langle\eta_X(t)\rangle$ are computed as the element-wise product of $\langle\mathbf{g}(t)\rangle$ and $\langle\tilde{\mathbf{G}}(t)\rangle$ using a change in the order of integration.

1.C Sensitivity of DOP and Phosphate Remineralization Rate

Here we quantify the sensitivity of the DOP concentration and of the phosphate remineralization field to the poorly known rate constant κ (inverse remineralization timescale). Figure 1.10 shows the DOP concentration zonally averaged over each basin for the base state with $\kappa^{-1} = 0.5 \text{ yr}$. The pattern of DOP is identical to that of oxygen utilization rate (OUR) plotted by *Primeau et al.* [2013] for the same model, using a constant stoichiometry of $R_{\text{O}_2:\text{P}} = 170$. The DOP concentration falls off rapidly with depth in accord with the divergence of the Martin particle-flux profile defining the operator \mathcal{S} in Equation (1.1). To quantify the sensitivity of DOP to the value of κ , Figure 1.10 also shows basin-mean profiles of DOP for $\kappa^{-1} = 0.25 \text{ yr}$ and 0.75 yr (i.e., $\kappa = 4.0 \text{ yr}^{-1}$ and 1.3 yr^{-1}). These perturbed DOP profiles are to a good approximation given by $\pm 50\%$ of the base-state profile throughout the water column, which shows that the DOP concentration is approximately proportional to κ^{-1} .

While DOP itself is sensitive to κ , the steady-state phosphate distribution only depends on the phosphate remineralization rate per unit volume, κP_{O} . Figure 1.11 plots κP_{O} expressed as OUR using $[\text{OUR}] = R_{\text{O}_2:\text{P}} \kappa P_{\text{O}}$, with $R_{\text{O}_2:\text{P}} = 170$, for the base state and for the two perturbed cases with $\kappa = 4.0 \text{ yr}^{-1}$ and 1.3 yr^{-1} . The OUR in Figure 1.11 can be compared with the observational estimates of OUR by *Sonnerup et al.* [2013, 2015] for the Pacific. These observations show magnitudes of $\sim 10 \pm 5 \mu\text{mol kg}^{-1} \text{ yr}^{-1}$ around 100–200 m depth and a rapid decay to near zero by 800 m depth, consistent with our modeled OUR. Figure 1.11 also shows that the sensitivity of κP_{O} is roughly $\pm 5\%$ near the surface, consistent with the $\sim 10\%$ sensitivity of the self-connected flow rates to the same changes in κ .

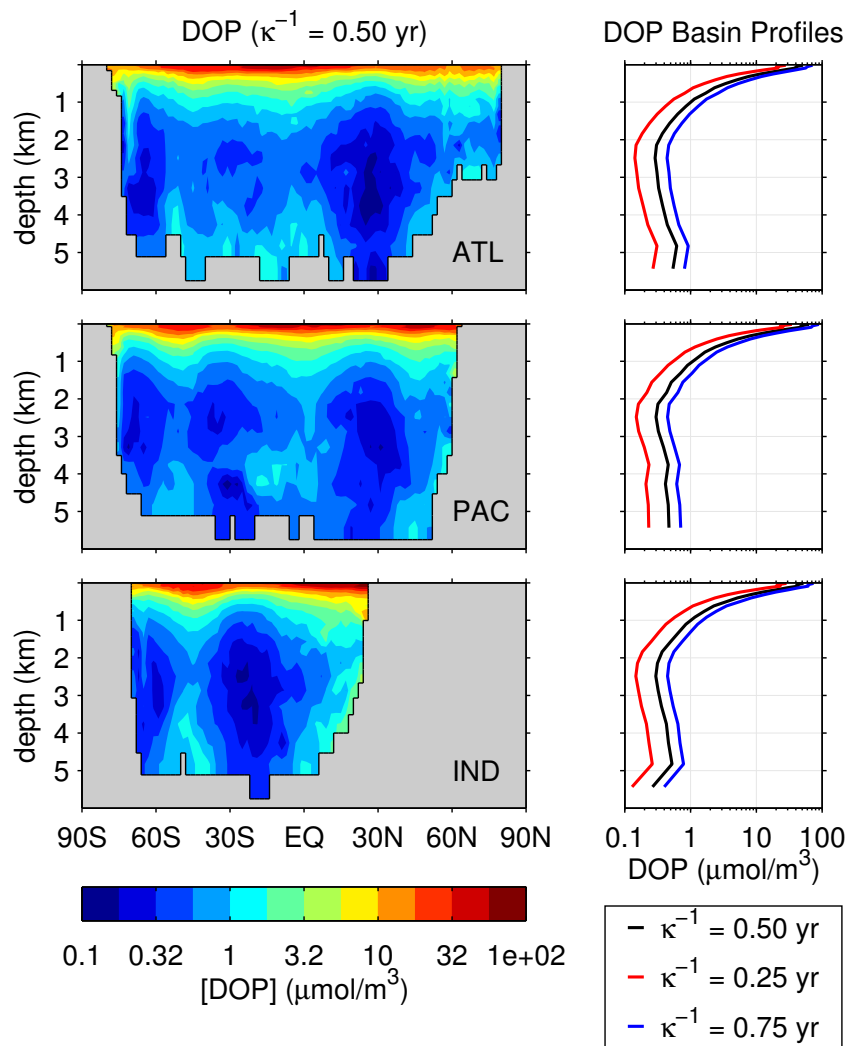


Figure 1.10: Left: Zonally averaged DOP concentrations for each ocean basin (ATL, PAC, IND). Note the logarithmic color scale. Right: Corresponding basin-mean DOP profiles for the base state with $\kappa^{-1} = 0.5 \text{ yr}$, and for $\kappa^{-1} = 0.25 \text{ yr}$ and 0.75 yr .

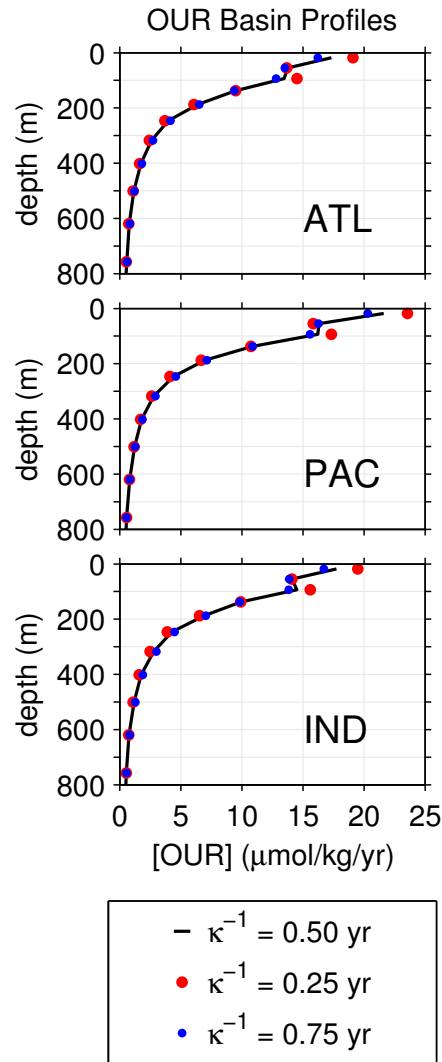


Figure 1.11: Basin-mean profiles of the model's phosphate remineralization rate per unit volume, $\kappa[\text{DOP}]$, expressed as oxygen utilization rate $[\text{OUR}] = R_{\text{O}_2:\text{P}} \kappa[\text{DOP}]$, with $R_{\text{O}_2:\text{P}} = 170$. Shown is the base state for $\kappa^{-1} = 0.5 \text{ yr}$, together with solutions for $\kappa^{-1} = 0.25 \text{ yr}$ and 0.75 yr .

1.D Basin Integrals of the Bio Phosphorus Path Density

Figure 1.12 shows the path densities $\eta_{\text{bio}}(\mathbf{r}|t : \Omega_i \rightarrow \Omega_f)$ volume integrated over each ocean basin above and below 1000 m depth. For a given origin Ω_i and destination Ω_f , summing these integrals over all basins and over the upper and lower components gives the corresponding residence-time distribution $\mathcal{R}_{\text{bio}}(t : \Omega_i \rightarrow \Omega_f)$ shown in Figure 1.8. Further integrating the curves of Figure 1.12 over transit time quantifies the mass of bio phosphorus in $\Omega_i \rightarrow \Omega_f$ transit that resides in the upper or lower basin. (Note that Figure 1.12 has a logarithmic time axis so that the transit-time integral is not simply the area under the curve on the plot.)

Figure 1.12 shows that the phosphorus in the $\Omega_i \rightarrow \Omega_f$ bio pipes considered resides mostly below 1000 m depth, with residence times of several centuries. As discussed in Section 1.5.5, the deep Pacific distributions (dashed blue lines) of the NAAD → SAAD, NAAD → NAAD, and EqA → SAAD bio pipes are bimodal, with a distinct millennial mode. The deep, slow bio-phosphorus paths are particularly important for E_{bio} because they carry a large portion of the global regenerated phosphate inventory. For the NAAD → NAAD bio pipe, the partition between upper and lower paths confirms that the early decadal peak of its \mathcal{R}_{bio} distribution is due to nutrient trapping and recirculation in the upper Southern Ocean.

1.E Connection with Sequestration Efficiency Distribution

The sequestration efficiency $\mathcal{E}(t|\Omega_i, t_i)$ of surface region Ω_i at time t_i defined by DeVries *et al.* [2012] is the fraction of the phosphate exported in Ω_i (generalized to bio phosphorus here) that has remained sequestered in the aphotic interior for a time t or longer, regardless of where it next reemerges into the euphotic zone. Note that Ω_i can be shrunk to a single grid box or taken to the continuum limit when sums over patches become surface integrals. Here, we develop the relation between $\mathcal{E}(t|\Omega_i, t_i)$ and our partitioned flow rates.

The bio phosphorus mass that was injected in Ω_i during time interval $(t_i, t_i + dt_i)$, and that remains in the ocean without emerging as phosphate into the euphotic zone for a time t or longer, can be obtained as the $\Omega_i \rightarrow \Omega$ flow rate \mathcal{J}_{bio} accumulated from time $t_i + t$ onward. Denoting this mass by $\phi_{\text{bio}} dt_i$ so that ϕ_{bio} has units of moles per unit injection time, we thus have

$$dt_i \phi_{\text{bio}}(t_i + t|\Omega_i, t_i) = dt_i \int_t^\infty dt' \mathcal{J}_{\text{bio}}(t_i + t'|\Omega_i \rightarrow \Omega, t_i) . \quad (1.28)$$

The total bio phosphorus (regardless of sequestration time) exported at Ω_i during $(t_i, t_i + dt_i)$ is given by $\Phi_{\text{bio}}(\Omega_i \rightarrow \Omega, t_i) dt_i$. Thus, by definition, and after cancelling the dt_i , we have

$$\mathcal{E}(t|\Omega_i, t_i) = \frac{\phi_{\text{bio}}(t_i + t|\Omega_i, t_i)}{\Phi_{\text{bio}}(\Omega_i \rightarrow \Omega, t_i)} . \quad (1.29)$$

Using the relation (1.28) between ϕ_{bio} and \mathcal{J}_{bio} , plus the fact that $\Phi_{\text{bio}}(\Omega_i \rightarrow \Omega, t_i) = \int_0^\infty dt' \mathcal{J}_{\text{bio}}(t_i + t'|\Omega_i \rightarrow \Omega, t_i)$, it is apparent that \mathcal{E} is the (complementary) cumulative distribution of the normalized transit-time partitioned flow rate \mathcal{J}_{bio} . It follows that $\Gamma_{\text{bio}}(\Omega_i \rightarrow \Omega, t_i) = \int_0^\infty \mathcal{E}(t|\Omega_i, t_i) dt$ and

$$\frac{\mathcal{J}_{\text{bio}}(t_i + t|\Omega_i \rightarrow \Omega, t_i)}{\Phi(\Omega_i \rightarrow \Omega, t_i)} = -\frac{\partial}{\partial t} \mathcal{E}(t|\Omega_i, t_i) , \quad (1.30)$$

as can be verified analytically by explicit calculation.

In the model of DeVries *et al.* [2012], which carries no DOP and has a single grid layer euphotic zone (or represents the euphotic layer as a 2d surface in the continuum limit), the sequestration efficiency becomes independent of phosphate uptake and hence export production. This is because (i) without DOP, ϕ_{bio} becomes export production, and (ii) because with a single grid layer euphotic zone (or 2d euphotic surface), ϕ_{bio} becomes simply proportional to Φ_{bio} , which cancels in (1.29).

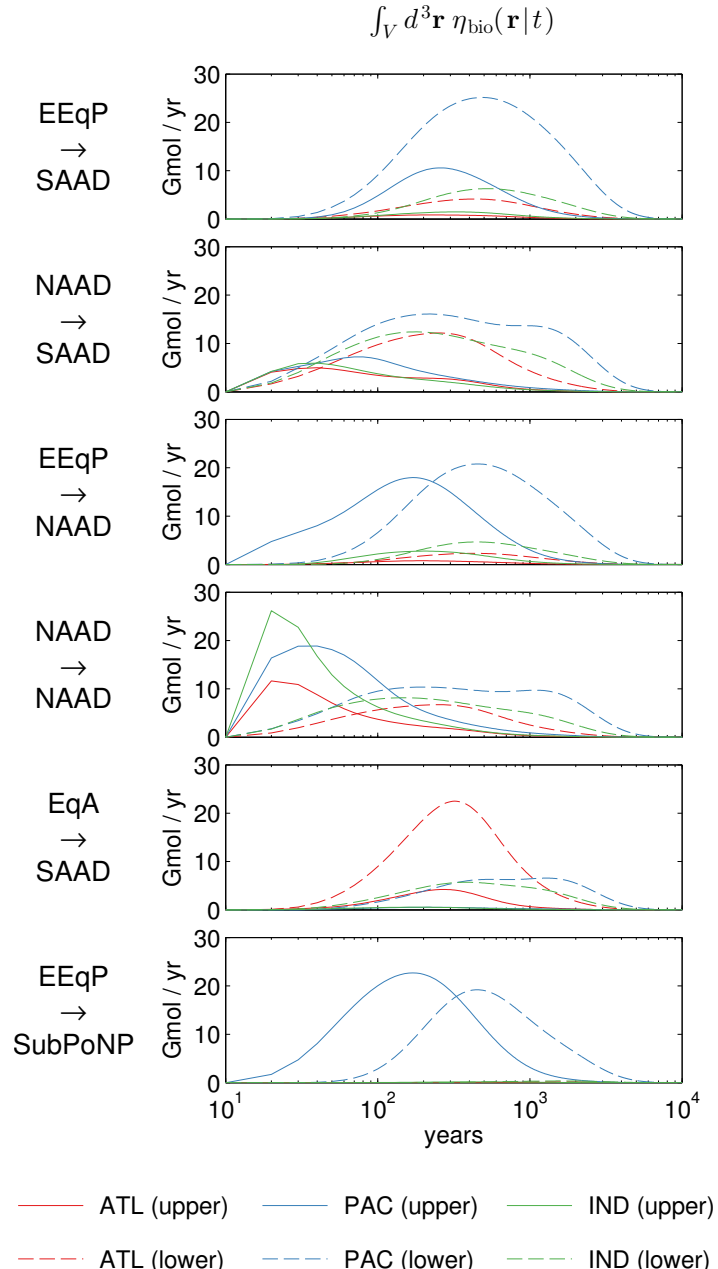


Figure 1.12: Volume integrals $\int_V d^3\mathbf{r} \eta_{\text{bio}}(\mathbf{r}|t)$ of the bio phosphorus path density over the upper and deep Atlantic (red), Pacific (blue), and Indian Ocean (green). The solid lines indicate the integrals over the upper 1000 m of the basin, while the dashed lines indicate the integral over the basin below 1000 m depth.

Chapter 2

Inverse-model estimates of the ocean's coupled phosphorus, silicon, and iron cycles

Essentially, all models are wrong, but some are useful.

Box and Draper [1986]

2.1 Introduction

The ocean's nutrient cycles control the primary productivity of the global marine ecosystem and the ocean's biological carbon pump, which are crucial components of the global carbon cycle that regulate atmospheric CO₂ concentrations. The nutrient cycling of the ocean is governed by the interplay of the ocean's advective-diffusive circulation, biological utilization, biogenic particle transport, and the external sources and sinks of nutrients. The cycles of macro and micronutrients are coupled through colimitation on biological uptake, and through the scavenging of micronutrients such as iron by sinking organic matter.

We focus on dissolved iron (dFe) as a key micronutrient because of its well-documented fundamental role in primary production [e.g., *Boyd and Ellwood*, 2010]. Indeed, dFe was suggested to limit oceanic phytoplankton growth as early as the 1930's [e.g., *Gran et al.*, 1931; *Hart*, 1934]. Since then, numerous studies have reported that iron deficiency limits productivity over vast regions of the ocean, particularly high-nutrient low-chlorophyll (HNLC) regions like the Southern Ocean [e.g., *de Baar et al.*, 1995; *Lundry et al.*, 1997; *Martin and Fitzwater*, 1988; *Boyd et al.*, 2007; *Boyd and Ellwood*, 2010]. *Martin* [1990] went as far as to suggest that perturbations in the iron cycle played a crucial role in past climate fluctuations. More recently, iron-enrichment field experiments [e.g., *Boyd et al.*, 2007] and model simulations [e.g., *Nickelsen and Oschlies*, 2015] have demonstrated the importance of iron for the global biological pump.

With a changing climate, we expect not only changes in ocean circulation, but also changes in the aeolian iron supply in response to changes in the winds, hydrological cycle, and land use. To understand how such changes impact the global ocean nutrient cycles it is necessary to model the coupling between the nutrients mechanistically. While global biogeochemistry models have been extensively used for this purpose [e.g., *Tagliabue et al.*, 2014; *Nickelsen and Oschlies*, 2015], here it is our goal to constrain a model of the coupled nutrient cycles by optimizing the biogeochemical parameters against available observations. To that end, we build a model of intermediate complexity that focuses on the ocean's phosphorus, silicon, and iron cycles.

We model phosphate (PO₄) because it is essential to the metabolism of all living organisms [e.g., *Smith*, 1984; *Howarth*, 1988], which allows all biological production to be keyed to phosphate utilization [e.g., *Kwon and Primeau*, 2008; *Primeau et al.*, 2013; *Holzer and Primeau*, 2013]. Silicic acid (Si(OH)₄) was considered because of the importance of diatoms in marine ecosystems, particularly in the Southern Ocean [e.g., *Nelson et al.*, 1995; *Buesseler*, 1998; *Moore et al.*, 2004; *Brzezinski et al.*, 2011a], and because the pronounced silicon trapping of the Southern Ocean [e.g., *Holzer et al.*, 2014] might be sensitive to iron

availability.

The intercomparison of iron models by *Tagliabue et al.* [2016] showed that current models of the iron cycle contain significant uncertainties. Despite the fact that the models have iron source strengths that range over nearly two orders of magnitude, all models can be tuned to roughly the same mean dFe concentration with an inter-model variance of only 27 %. This is due to essentially unconstrained scavenging rates so that models are free to employ different scavenging strengths to balance the sources at roughly comparable dFe concentrations. All models of the intercomparison are three-dimensional prognostic forward models that are computationally too costly to explore the biogeochemical parameter space systematically, or to compute the sensitivity with respect to multiple parameters [*Kwon and Primeau*, 2006].

Recently, *Frants et al.* [2016] designed a simple inverse model of the global iron cycle embedded in the steady data-assimilated circulation of *Primeau et al.* [2013]. A matrix representation of the associated transport operator and biogeochemical processes afforded numerically highly efficient solutions. This made it possible not only for biogeochemical parameters to be systematically optimized, but also for novel diagnostics to be computed such as a mean iron age and rigorous source attribution of dFe [*Holzer et al.*, 2016]. Consistent with the findings of the iron-model intercomparison, *Frants et al.* [2016] showed that current dFe observations cannot constrain the iron sources because of local compensation between sources and sinks. *Frants et al.* [2016] therefore explored a family of solutions corresponding to a range of aeolian source strengths, all of which are consistent with the currently available dFe observations.

Here, we build on the iron model of *Frants et al.* [2016], but we do not prescribe the phosphate cycle and instead explicitly couple the iron, phosphorus, and silicon cycles through their mutual colimitations so that the macro nutrients can respond to changes in dFe. We furthermore refine the modelling of the sedimentary iron source, the representation of iron scavenging that now includes explicit representation of re-dissolution, and we model three functional phytoplankton classes, whose concentrations are derived from a steady-state logistic equation [*Dunne et al.*, 2005].

The model's biogeochemical parameters are optimized by minimizing the quadratic mismatch of the nutrient and phytoplankton concentrations with the available observations. Following *Frants et al.* [2016], we consider a family of dFe solutions corresponding to a range of sources, expanded here to a greater range of sediment and hydrothermal sources. The spread in key metrics (e.g., the global carbon export) across our family of solutions is used as a measure of the metric's uncertainty.

We use the model to establish the geographic patterns of nutrient limitation and co-limitation, and to quantify the export of each nutrient by each functional

phytoplankton class. By partitioning dFe into contributions from the aeolian, sedimentary, and hydrothermal sources, we quantify the role and efficiency of each dFe type in supporting carbon and opal export.

2.2 Biogeochemical Model

We distinguish three phytoplankton functional groups: non-diatom small and large phytoplankton as well as diatoms, with a nominal separation between small and large at a cell diameter of 2 µm. We denote the molar PO₄ uptake rate per unit volume of each class by U_c , where the subscript $c \in \{\text{lr}, \text{sml}, \text{dia}\}$ identifies functional class. The uptake rates U_c are only non-zero in the model's upper 73.4 m (2 layers), the model's euphotic zone.

We consider the three nutrients PO₄, Si(OH)₄, and dFe and denote their concentrations by χ^i , with $i \in \{\text{P}, \text{Si}, \text{Fe}\}$. We write the steady-state tracer equations for these concentrations by keying all biological production to the uptake U_c of phosphate as follows:

$$\mathcal{T}\chi_{\text{P}} = \sum_c (\mathcal{S}_c^{\text{P}} - 1)U_c - \gamma_g(\chi_{\text{P}} - \bar{\chi}_{\text{P}}^{\text{obs}}), \quad (2.1)$$

$$\mathcal{T}\chi_{\text{Si}} = (\mathcal{S}^{\text{Si}} - 1)R^{\text{Si:P}}U_{\text{dia}} - \gamma_g(\chi_{\text{Si}} - \bar{\chi}_{\text{Si}}^{\text{obs}}), \quad (2.2)$$

$$\begin{aligned} \mathcal{T}\chi_{\text{Fe}} = & \sum_c (\mathcal{S}_c^{\text{Fe}} - 1)R_c^{\text{Fe:P}}U_c \\ & + (\mathcal{S}^{s,\text{POP}} - 1)J_{\text{POP}} + (\mathcal{S}^{s,\text{bSi}} - 1)J_{\text{bSi}} - J_{\text{dst}} \\ & + s_{\text{A}} + s_{\text{S}} + s_{\text{H}} . \end{aligned} \quad (2.3)$$

In Equations (2.1)–(2.3), \mathcal{T} is the advection-eddy-diffusion operator, the operators \mathcal{S}_c^i model the biogenic transport and remineralization of nutrient i taken up by functional class c , and the operators $\mathcal{S}^{s,\text{POP}}$ and $\mathcal{S}^{s,\text{bSi}}$ model the particle transport of scavenged iron and its partial re-dissolution at depth as the scavenging particles remineralize or dissolve (details in section 2.2.2). Note that we carry a single tracer for iron: Equation (2.3) explicitly transports total dFe only. The concentrations of chelated (or ligand-bound) and free iron are determined locally by the chemical equilibrium between iron and ligands (details in section 2.2.4.2). The iron scavenging rates per unit volume are J_{POP} for scavenging by particular organic phosphorus (POP), J_{bSi} for scavenging by opal particles, and J_{dst} for scavenging by mineral dust (details in section 2.2.4.2). The terms s_{A} , s_{S} , and s_{H} are the aeolian, sediment, and hydrothermal iron sources (details in section 2.2.4.1). The factors $R^{\text{Si:P}}$ and $R_c^{\text{Fe:P}}$ are the stoichiometric uptake ratios that allow us to key all production to phosphorus. These ratios are functions of the nutrient concentrations as described in section 2.2.3.3.

The terms proportional to γ_g in (2.1) and (2.2) fix the global mean phosphate and silicic acid concentrations through weak relaxation to their observed global means $\bar{\chi}_P^{\text{obs}}$ and $\bar{\chi}_{\text{Si}}^{\text{obs}}$. This is necessary because the phosphorus and silicon cycles have no external sources and sinks to set the global mean in steady state. (For phosphate and silicic acid, external sources, e.g., riverine input and loss to sediment burial, are neglected.) We choose the restoring timescale $\gamma_g^{-1} = 10^6$ years (“geological” restoring); there is no sensitivity to the precise value of γ_g .

Equations (2.1)–(2.3) are coupled via the uptake of PO_4 , which depends on the concentrations of all three nutrients, via the iron scavenging that depends on the export fluxes of organic matter and opal, and via the sedimentary release of dFe, which is keyed to the flux of organic matter onto the sediments [Elrod *et al.*, 2004], as discussed in detail below.

2.2.1 Circulation

We use the data-assimilated, steady (non-seasonal) circulation of Primeau *et al.* [2013] which has a horizontal resolution of $2^\circ \times 2^\circ$ and 24 vertical levels whose thickness increases with depth. Temperature, salinity, and radiocarbon, CFC-11, and PO_4 have been used as constraints in the data assimilation. The circulation is constrained dynamically and the data assimilation used the wind-stress climatology of Trenberth *et al.* [1989] and specified horizontal and vertical viscosities of $5 \times 10^4 \text{ m}^2 \text{ s}^{-1}$ and $10^{-4} \text{ m}^2 \text{ s}^{-1}$, respectively. The circulation’s advective-diffusive transport operator has fixed horizontal and vertical eddy diffusivities of $10^3 \text{ m}^2 \text{ s}^{-1}$ and $10^{-5} \text{ m}^2 \text{ s}^{-1}$, respectively. We emphasize that the circulation effectively provides a ventilation-weighted transport because it has been optimized against PO_4 and the ventilation tracers CFC-11 and radiocarbon. The steady model circulation, which has no seasonal cycle, thus does not bias estimates of preformed nutrients in the way an annual-average circulation would.

2.2.2 Biogenic Transport

Organic matter sinks as POP, dissolves, and remineralizes at depth. Inverse models of the phosphorus cycle [Primeau *et al.*, 2013; Holzer and Primeau, 2013; Pasquier and Holzer, 2016] suggest that dissolved organic phosphorus (DOP) represents a relatively small fraction of the total dissolved phosphorus that we neglect here for simplicity and numerical efficiency (no DOP tracer). Because the particle transport is much faster than the fluid transport across a grid box, we approximate particle transport and remineralization, which acts as an interior source of nutrients, as instantaneous. We model this process for each phytoplankton functional group by the “source” operator, S_c^P , which reassigns

a “detrital” fraction f_c of the uptake rate to a remineralization rate throughout the water column, while a fraction $1 - f_c$ remineralizes in situ where the uptake occurred. We therefore express \mathcal{S}_c^P in terms of a biogenic redistribution operator \mathcal{B}^P as

$$\mathcal{S}_c^P = 1 - f_c + \mathcal{B}^P f_c . \quad (2.4)$$

(The operator \mathcal{B}^P does not have a functional subscript c because it redistributes a unit uptake with the same profile regardless of functional class.) Following *Dunne et al.* [2005], we model the detrital fraction as decreasing with temperature T so that $f_c = f_c^0 e^{-k_\sigma T}$, with $k_\sigma = 0.032\text{ }(\text{°C})^{-1}$ independent of class, $f_{\text{sml}}^0 = 0.14$, $f_{\text{lrg}}^0 = 0.74$, and we assign $f_{\text{dia}} = f_{\text{lrg}}$. We assume that the remineralization of organic matter releases dFe and phosphate in the same ratio with which they were taken up. Therefore, $\mathcal{S}_c^{\text{Fe}} = \mathcal{S}_c^P$.

Following *Najjar et al.* [1992], we assume that the detrital production rate is fluxed as POP through the base of the euphotic zone at $z_e = 73.4\text{ m}$ with $\phi^{\text{POP}}(z_e) = \int_{z_e}^0 f_c U_c dz$, and that the POP flux attenuates with depth according to the Martin power law $\phi^{\text{POP}}(z) = \phi^{\text{POP}}(z_e)(z/z_e)^{-b}$ due to remineralization in the aphotic zone. The operator \mathcal{B}^P therefore injects PO_4 with the divergence of ϕ^{POP} into the aphotic water column. The flux into the ocean bottom is remineralized in the lowest grid box as in the work of *Primeau et al.* [e.g., 2013]. The exponent b was determined to be $b = 0.82$ using a restoring-type phosphate-only model. (Most parameters were optimized for the full coupled model – for details of our optimization strategy see section 2.3.3.)

The redistribution operator \mathcal{B}^{Si} similarly injects silicic acid into the aphotic water column with the divergence of the opal flux, ϕ^{bSi} , which attenuates because of temperature dependent opal dissolution following *Gnanadesikan* [1999] and *Holzer et al.* [2014]. For each latitude and longitude, ϕ^{bSi} is computed as the solution to $\partial_z \phi^{\text{bSi}}(z) = -(\kappa_{\text{Si}}^{\text{max}}/w_{\text{Si}}) \exp(-T_E/T(z)) \phi^{\text{bSi}}(z)$, with the boundary condition $\phi^{\text{bSi}}(z_e) = \int_{z_e}^0 R^{\text{Si:P}} f_{\text{dia}} U_{\text{dia}} dz$. We use $T_E = 11,481\text{ K}$ as *Gnanadesikan* [1999] and the same detrital fraction f_{dia} for the opal export and diatom POP export. The parameter combination $\kappa_{\text{Si}}^{\text{max}}/w_{\text{Si}}$ has nearly the same value as determined by *Holzer et al.* [2014], but was re-optimized here for a simple restoring-type model that takes subgrid topography into account (see below).

The scavenging operators $\mathcal{S}^{s,\text{POP}}$ and $\mathcal{S}^{s,\text{bSi}}$ act on J_{POP} and J_{bSi} to redistribute a fraction of the iron scavenged at every layer throughout the water column below the layer. In terms of the corresponding redistribution operators, we write

$$\mathcal{S}^{s,\text{POP}} = f^{\text{POP}} \mathcal{B}^{s,\text{POP}} \quad \text{and} \quad \mathcal{S}^{s,\text{bSi}} = f^{\text{bSi}} \mathcal{B}^{s,\text{bSi}} , \quad (2.5)$$

where the fractions f^{POP} and f^{bSi} are optimizable parameters. The operators $\mathcal{B}^{s,\text{POP}}$ and $\mathcal{B}^{s,\text{bSi}}$ in effect “recycle” scavenged iron. They are very similar to \mathcal{B}^P and \mathcal{B}^{Si} but in addition to distributing scavenged iron from the euphotic zone to the aphotic zone, they also redistribute the scavenging rates of every aphotic layer to a source of redissolving iron with the divergence of the scavenging particle fluxes. The flux of scavenged iron into the bottom is assumed to be lost forever so that there would be iron loss even for 100 % efficient recycling of scavenged iron. (For details see Appendices 2.A and 2.B.)

To compute accurate particle fluxes for constructing all \mathcal{S} operators, we take sub-grid topography into account [as done by *Moore and Braucher*, 2008], using the high-resolution ETOPO2V2c data set [*National Geophysical Data Center*, 2006]. This is done by calculating for each grid box the fractional area occupied by the sub-grid topography, which is also the fraction of the particle flux that is intersected by the sub-grid topography. For each grid box, the fraction of the flux intersected is instantly remineralized or dissolved (details in Appendix 2.B).

2.2.3 Uptake Rates

The PO_4 uptake rate at a point is a function of the local temperature T , irradiance I , and nutrient concentrations. The uptake rate for functional class c is calculated as the product of its phytoplankton concentration, p_c , and its specific growth rate, μ_c , as

$$U_c = \mu_c p_c = \frac{p_c^{\max}}{\tau_c} e^{\kappa T} (F_{I,c} F_{N,c})^2 , \quad (2.6)$$

where τ_c is the timescale for growth, p_c^{\max} is the phytoplankton concentration under ideal conditions, and $F_{I,c}$ and $F_{N,c}$ are dimensionless factors in the interval $[0, 1]$ that represent light and nutrient limitation, respectively, as defined below. We derive equation (2.6) similarly to *Dunne et al.* [2005] and *Galbraith et al.* [2010] as follows.

First, p_c is calculated diagnostically by assuming steady state between growth and mortality, which avoids the need to carry explicit plankton concentration tracers. This is justified by the coarse resolution of our model, which implies transport timescales across a grid box much larger than the typical timescales for phytoplankton growth. Based on *Dunne et al.* [2005]’s mortality formulation, p_c can be modelled by a logistic equation

$$\partial_t p_c = \mu_c p_c - \lambda \left(\frac{p_c}{p_c^*} \right) p_c , \quad (2.7)$$

where p_c/p_c^* scales the specific mortality rate λ , and p_c^* has also been referred to as the “pivotal” population density [e.g., *Dunne et al.*, 2005; *Galbraith et al.*, 2010]. Equation (2.7) has a nontrivial steady state, given by

$$p_c = \left(\frac{\mu_c}{\lambda} \right) p_c^* . \quad (2.8)$$

We assume that all phytoplankton classes share the same specific mortality rate λ , which depends only on temperature. For simplicity, following *Galbraith et al.* [2010], we approximate the T dependence of the mortality rate to be identical to that of the growth rate. We adopt the T dependence of the growth rate that was determined by *Eppley* [1972] to have the exponential form $e^{\kappa T}$. Thus, the mortality rate is given by $\lambda = \lambda_0 e^{\kappa T}$, where λ_0 is a constant and T is in $^{\circ}\text{C}$.

Our formulation differs from that of *Dunne et al.* [2005] and *Galbraith et al.* [2010], who raise the ratio p_c/p_c^* to a power α_c with $\alpha_{\text{sml}} = 1$ and $\alpha_{\text{lrg}} = 1/3$ to differentiate between phytoplankton classes. Here, we chose $\alpha_c = 1$ for all classes and instead differentiate between classes by assigning them different half-saturation rates and maximum uptake rate constants similarly to the work of *Matsumoto et al.* [2008] (details in sections 2.2.3.1 and 2.2.3.3).

We model the specific growth rate μ_c as multiplicatively colimited [*Saito et al.*, 2008] by temperature, light, and nutrients:

$$\mu_c = \frac{1}{\tau_c} e^{\kappa T} F_{I,c} F_{N,c}, \quad (2.9)$$

where τ_c is the growth timescale at 0°C under ideal conditions and the temperature dependence $e^{\kappa T}$ [*Eppley*, 1972] is identical to what we use in the mortality rate [e.g., *Galbraith et al.*, 2010]¹. To group parameters for more efficient optimization, we define $p_c^{\max} = p_c^*/(\lambda_0 \tau_c)$, so that diagnostic equation (2.8) for the phytoplankton concentration becomes

$$p_c = F_{I,c} F_{N,c} p_c^{\max} . \quad (2.10)$$

Substituting (2.9) and (2.10) into $U_c^P = \mu_c p_c$ gives (2.6), which is similar to the uptake formulation of *Doney et al.* [2006] and *Matsumoto et al.* [2008].

We note that in the Sea of Japan the model’s circulation produces unrealistic nutrient trapping, likely due to under resolved currents. For this reason we set the specific growth rate in the Sea of Japan to zero, effectively removing it from the computational domain of the biogeochemical model.

¹ If we used a different temperature dependence parameter, κ_m , for mortality, then κ in equation (2.6) would be replaced by $\kappa^* = 2\kappa - \kappa_m$. We acknowledge that treating κ^* as an optimizable parameter could potentially affect our results, but would likely lead to some additional compensations with the other optimized uptake parameters. Therefore, we simply approximate $\kappa_m = \kappa$ as in the work of *Dunne et al.* [2005] and *Galbraith et al.* [2010].

2.2.3.1 Nutrient Limitation

We model the limitation of functional class c by nutrient i by a Monod function [Monod, 1942] of the concentration, $\chi_i / (\chi_i + k_c^i)$, where k_c^i is the half-saturation constant that determines the scale on which the concentration influences uptake. (Because only diatoms take up silicon $k_{\text{lr}}^{\text{Si}} = 0$ and $k_{\text{sml}}^{\text{Si}} = 0$.) For the colimitation of all three nutrients, we use the type-I multiplicative form [Saito *et al.*, 2008]

$$F_{N,c} = \prod_i \frac{\chi_i}{\chi_i + k_c^i}. \quad (2.11)$$

We chose the Monod model over the arguably more realistic quota model [e.g., Flynn, 2003] for simplicity. Moreover, the shortcomings of the Monod formulation likely only come into play for rapidly evolving transient blooms, which our steady-state formulation does not attempt to capture.

Using a minimum over nutrient type i [Liebig's rule, e.g., de Baar, 1994], rather than the product (2.11) is thought to fit the observational data slightly better [e.g., Droop, 2009; Rhee, 1978]. However, here we prefer the smoothness of the multiplicative formulation because differentiability is a theoretical requirement for Newton's method to converge [e.g., Kelley, 2003a]. A product of PO₄, dFe, and irradiance Monod terms was also used by Parekh *et al.* [2005] and Dutkiewicz *et al.* [2006] in the uptake formulation of their coupled phosphorus-iron model.

2.2.3.2 Light Limitation

We prescribe irradiance I and model light limitation with a simple Monod factor

$$F_{I,c} = \frac{I}{I + k_{I,c}}, \quad (2.12)$$

with half-saturation constant $k_{I,c}$ for class c [e.g., Doney *et al.*, 2006]. We use an annual mean I derived from photosynthetically active radiation (PAR) measured over the period 2002–2015 by the Modis Aqua satellite [NASA Goddard Space Flight Center, 2014]. The surface PAR at location (x, y) , denoted by $I_0(x, y)$, was converted to W m⁻² using 2.77×10^{18} quanta s⁻¹ W⁻¹ [Morel and Smith, 1974]. Irradiance is modelled as exponentially attenuated with depth z so that

$$I(x, y, z) = I_0(x, y) e^{-k_w z}, \quad (2.13)$$

with $k_w^{-1} = 25$ m.

2.2.3.3 Elemental Uptake Ratios

Because we key all biological production to PO₄ utilization, we must specify the Fe:P and Si:P elemental uptake ratios for the iron and silicon cycles. The Fe:P uptake ratio, $R_c^{\text{Fe:P}}$, is known to increase and saturate with increasing dFe concentration [e.g., *Sunda and Huntsman*, 1997]. We follow *Galbraith et al.* [2010] and model the dFe dependence as a simple Monod term

$$R_c^{\text{Fe:P}} = R_0^{\text{Fe:P}} \frac{\chi_{\text{Fe}}}{\chi_{\text{Fe}} + k_{\text{Fe:P}}} , \quad (2.14)$$

where $R_0^{\text{Fe:P}}$ is the maximal Fe:P uptake ratio. In principle, $R_0^{\text{Fe:P}}$ and $k_{\text{Fe:P}}$ could be different for different functional classes. However, we find that when optimized they tend to be nearly equal for different classes, so that we chose for simplicity to use the same values of $R_0^{\text{Fe:P}}$ and $k_{\text{Fe:P}}$ for all classes. As noted by *Galbraith et al.* [2010], this formulation ignores the effects of light limitation suggested by several studies [e.g., *Sunda and Huntsman*, 1997; *Strzepek et al.*, 2012]. Equation (2.14) also does not encode a minimum iron requirement. When we introduced such a minimum it tended to be optimized to zero and we therefore ignore it for simplicity. The Monod formulation (2.14) does capture luxury iron uptake [e.g., *Marchetti et al.*, 2009a] when the half-saturation constant of (2.14) exceeds the half-saturation constant of the iron limitation in (2.11), as made explicit by *Galbraith et al.* [2010]. This is the case for our optimized value of $k_{\text{Fe:P}}$ so that phytoplankton has the luxury to increase its iron uptake with increasing dFe concentration even when iron is not limiting.

Our representation of the $R^{\text{Si:P}}$ uptake ratio takes into consideration field studies and iron enrichment experiments, which have indicated that in HNLC regions and upwelling regions iron limitation leads to increased diatom silicification, i.e., increased cellular Si:N and Si:P ratios [e.g., *Takeda*, 1998; *Hutchins and Bruland*, 1998; *Franck et al.*, 2000; *Brzezinski et al.*, 2003]². However, there is no literature consensus on a mechanistic formulation of the iron dependence of silicic-acid uptake. For example, *Matsumoto et al.* [2013] assume a Si:N uptake ratio inversely proportional to the dFe concentration (capped at a minimum), while *Jin et al.* [2006] assume the Si:N ratio to depend only on the Si(OH)₄ concentration. Others suggest that the dFe concentration only impacts the diatom growth rate and not the cellular Si:C ratio, while the Si(OH)₄ concentration impacts the cellular Si:C ratio and not growth rate [e.g., *Marchetti et al.*, 2009b; *Brzezinski et al.*, 2011b]. Here, we chose to retain the effects of increased silicification due to iron limitation and the impact of high Si(OH)₄ concentration

² Plots of the experimental data that show increased silicification under conditions of low dFe can be seen in Figure 6 in the work of *Franck et al.* [2000] and in Figure 7 in the work of *Brzezinski et al.* [2003]

on silicification (Brzezinski 2016, personal communication). We model these effects with the formulation

$$R^{\text{Si:P}} = R_0^{\text{Si}} + (R_m^{\text{Si}} - R_0^{\text{Si}}) \frac{k_{\text{Si:P}}^{\text{Fe}}}{\chi_{\text{Fe}} + k_{\text{Si:P}}^{\text{Fe}}} \frac{\chi_{\text{Si}}}{\chi_{\text{Si}} + k_{\text{Si:P}}^{\text{Si}}} . \quad (2.15)$$

The ratio involving the χ_{Fe} produces increased silicification when iron is deficient, while the Monod term for χ_{Si} produces increased silicification in silicon-replete environments: If $\chi_{\text{Fe}} \rightarrow 0$ and $\chi_{\text{Si}} \gg k_{\text{Si:P}}^{\text{Si}}$, then $R^{\text{Si:P}} \rightarrow R_m^{\text{Si}}$, while if $\chi_{\text{Fe}} \gg k_{\text{Si:P}}^{\text{Fe}}$ or $\chi_{\text{Si}} \rightarrow 0$, then $R^{\text{Si:P}} \rightarrow R_0^{\text{Si}}$. The minimum and maximum Si:P ratios R_0^{Si} and R_m^{Si} , as well as the constants $k_{\text{Si:P}}^{\text{Fe}}$ and $k_{\text{Si:P}}^{\text{Si}}$ were tuned rather than fully optimized to achieve the observation-based fractional uptake of each functional class (see section 2.3.3 on optimization for details).

2.2.4 Iron Model

2.2.4.1 Iron Sources

The aeolian source, s_A , is based on the spatial pattern of the surface flux of atmospheric soluble iron of *Luo et al.* [2008], obtained from an atmospheric model for current climate conditions that includes size-partitioned mineral dust, biomass burning, and industrial emissions. Because the global strength σ_A of the aeolian source is highly uncertain [e.g., *Tagliabue et al.*, 2016], we scale the global amplitude of this pattern to an initial guess of the global source strength that is then refined in our final optimization step (see sections 2.3.3 and 2.3.4 below). We note that the model of *Luo et al.* [2008] estimate a soluble aeolian iron flux into the ocean of $\sigma_A \sim 6 \text{ Gmol yr}^{-1}$.

The sedimentary source, s_S , has the pattern of the POP flux reaching the sediments [*Elrod et al.*, 2004; *Frants et al.*, 2016] and accounts for both resolved and subgrid topography. The amplitude of this pattern is the global sediment iron source strength σ_S , which is an optimized parameter. The dependence of the sediment redox reaction on dissolved oxygen [e.g., *Galbraith et al.*, 2010] is ignored here for simplicity and to avoid carrying another tracer equation. Unlike in the model of *Frants et al.* [2016], the phosphorus cycle and POP flux are not prescribed but coupled to the iron and silicon cycles as described above.

To model the hydrothermal source, s_H , we use the ${}^3\text{He}$ source pattern of the OCMIP protocol [*Dutay et al.*, 2004], and jointly optimize the hydrothermal iron source strengths $\sigma_{H,\text{ATL}}$, $\sigma_{H,\text{PAC}}$, $\sigma_{H,\text{IND}}$, and $\sigma_{H,\text{SO}}$ of the Atlantic, Pacific, Indian, and Southern Ocean ridge systems, as in the work of *Frants et al.* [2016]. (The iron sources are schematically represented in Figure 2.1.)

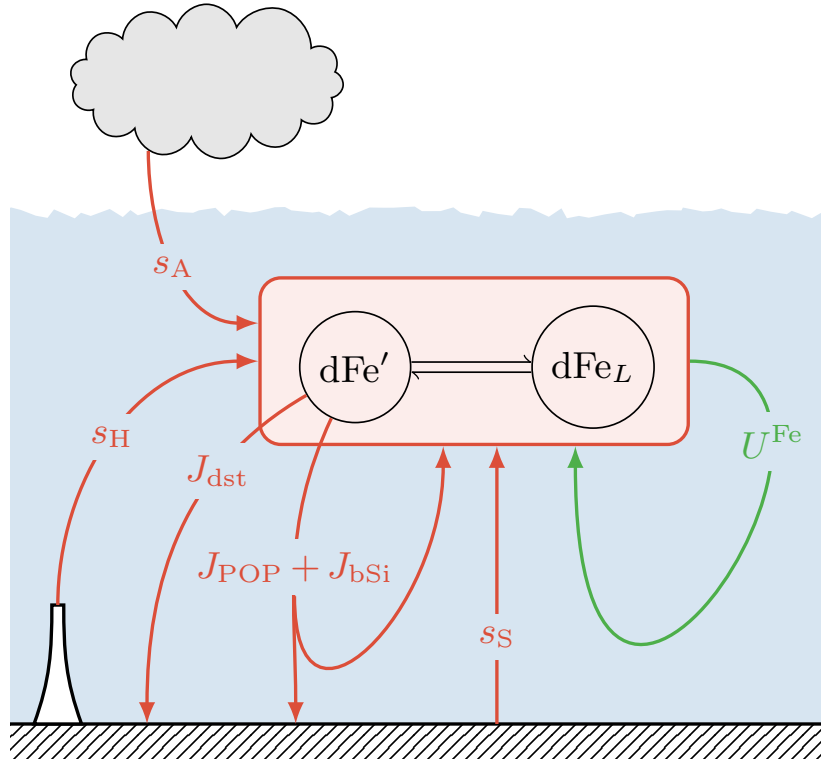


Figure 2.1: Schematic of the iron-cycle model. The aeolian, sedimentary, and hydrothermal iron sources (red arrows labeled s_A , s_S , and s_H , respectively) supply dFe to the ocean, while scavenging by sinking dust particles (red arrow labeled J_{dst}) and scavenging by POP and opal (red arrows labeled J_{POP} and J_{bSi} , respectively) remove dFe from the system. A fraction of the dFe scavenged by POP and opal is recycled when the scavenging particles remineralize or redissolve. Biological uptake, export, and regeneration of dFe is represented by the green arrow labeled U^{Fe} . The total dFe concentration is comprised of free iron (dFe') and ligand-bound iron (dFe_L), which are in chemical equilibrium.

2.2.4.2 Iron Sinks

Dissolved iron can be chelated by ligands or “free”. We assume that the scavenging acts only on the concentration $\chi_{Fe'}$ of free iron so that chelation by ligands protects dFe from being scavenged. Scavenging is modelled as a first order process [e.g., Aumont *et al.*, 2015] so that the scavenging rate is proportional to the product of $\chi_{Fe'}$ and the concentration of the scavenging particles χ^j , for $j \in \{POP, bSi, dst\}$, the three types of particles considered. (The scavenging sinks are schematically represented in Figure 2.1.) For each particle type, the

scavenging rate per unit volume is thus modelled as

$$J_j = \kappa_{\text{scv}}^j \chi^j \chi_{\text{Fe}'} , \quad (2.16)$$

where the scavenging rate constants $\kappa_{\text{scv}}^{\text{POP}}$, $\kappa_{\text{scv}}^{\text{bSi}}$, or $\kappa_{\text{scv}}^{\text{dst}}$ are optimizable parameters.

To compute the concentration of the scavenging particles, we use the fact that the flux divergences generated by the biogenic transport operators must be balanced by local remineralization or dissolution rates, that is,

$$\mathcal{B}^{\text{P}} \sum_c f_c U_c = \kappa_{\text{P}} \chi^{\text{POP}} \quad (2.17)$$

and

$$\mathcal{B}^{\text{Si}} f_{\text{dia}} U_{\text{dia}} = \kappa_{\text{Si}} \chi^{\text{bSi}} . \quad (2.18)$$

Although we use the nominal values of κ_{P} and κ_{Si} listed in Table 2.1, note that these constants only enter the scavenging rates (2.16) through the combinations $\kappa_{\text{scv}}^{\text{POP}} / \kappa_{\text{P}}$ and $\kappa_{\text{scv}}^{\text{bSi}} / \kappa_{\text{Si}}$, where $\kappa_{\text{scv}}^{\text{POP}}$ and $\kappa_{\text{scv}}^{\text{bSi}}$ are optimized. The concentration of dust particles is modelled as vertically uniform due to sinking dust particles that do not dissolve or re-suspend from sediments [e.g., *Moore and Braucher*, 2008]. We use the geographic pattern of the dust mass flux into the ocean provided by *Luo et al.* [2008], which we convert to a particle concentration using a nominal sinking speed of $w_{\text{dst}} = 50 \text{ m day}^{-1}$. The exact value of w_{dst} does not matter because the dust scavenging rate depends only on $\kappa_{\text{scv}}^{\text{dst}} / w_{\text{dst}}$ and $\kappa_{\text{scv}}^{\text{dst}}$ is optimized.

The key control on shaping the free iron concentration, and hence the scavenging, is the ligand concentration L . Chemical equilibrium between ligands, total dFe, and free iron determines $\chi_{\text{Fe}'}$ as a quadratic function of the (total) dFe concentration [see, e.g., *Frants et al.*, 2016]:

$$\chi_{\text{Fe}'}^2 + (L - \chi_{\text{Fe}} + K_L^{-1}) \chi_{\text{Fe}'} - K_L \chi_{\text{Fe}} = 0 . \quad (2.19)$$

For the ligand stability constant we adopted the value $K_L = 8 \times 10^{10} \text{ kg (mol Lig)}^{-1}$ from the work of *Frants et al.* [2016], which corresponds to the low-irradiance value used by *Galbraith et al.* [2010]. This value of K_L falls within the range of $10^{10}\text{--}10^{13} \text{ kg (mol Lig)}^{-1}$ that can be found in the literature [e.g., *Parekh et al.*, 2004, and references therein]. However, it is important to keep in mind that the precise value of K_L is not crucial here because of compensation with other parameters that are optimized (see Appendix 2.D for details).

Ligand concentrations have been observed to be elevated in old waters [*Misumi et al.*, 2013] and within hydrothermal plumes [e.g., *Bennett et al.*, 2008;

Hawkes et al., 2013]. Our ligand formulation therefore follows *Frants et al.* [2016] and increases L in older waters and in hydrothermal plumes: We assume that there is a minimum background concentration, L_b , and write

$$L = \max(L_H + L_{sw}, L_b) , \quad (2.20)$$

where L_H and L_{sw} are the elevated hydrothermal and aged “sea water” ligand concentrations, which we model as follows. The hydrothermal ligand plumes are computed from the source-sink balance

$$\mathcal{T} L_H = -\frac{1}{\tau_b} L_H - \frac{\Delta_v}{\tau_v} (L_H - L_v) , \quad (2.21)$$

where Δ_v is a mask that is unity for grid boxes containing vent sites (taken from the OCMIP ^3He source [*Dutay et al.*, 2004]) and zero elsewhere. The timescale $\tau_v = 1$ s clamps the ligand concentration to L_v at the vents, and the timescale τ_b controls the plume spread by setting the rate with which L_H decays away from the vents. The ligand concentration L_{sw} is enhanced in old waters according to

$$L_{sw}(\mathbf{r}) = \frac{\Gamma(\mathbf{r})}{\Gamma_{\max}} L_{\max} , \quad (2.22)$$

where $\Gamma(\mathbf{r})$ is the ideal mean water age (easily computed for our model), we choose $\Gamma_{\max} = 1600$ yr following *Frants et al.* [2016], and L_{\max} together with τ_b , L_v , and L_b are optimizable parameters.

As is the case for most iron models, there is no need to explicitly represent the chemical precipitation of dFe. This is because in most formulations the scavenging rates increase rapidly when dFe exceeds a certain threshold. For our model this threshold is set by the ligand concentration L , with $\chi_{\text{Fe}'}$, and hence the scavenging rate, rising rapidly in chemical equilibrium when dFe concentrations exceed L .

2.3 Numerical Method, Parameter Optimization, and Family of Solutions

2.3.1 Steady-State Solution

All three-dimensional fields (e.g., the concentrations χ_i) are discretized on our model grid and organized into column vectors (length $n = 191\,169$ at our resolution). Linear operators such as \mathcal{T} , \mathcal{S}_c^i , and $\mathcal{S}^{s,j}$ are correspondingly organized into $n \times n$ sparse matrices. The steady-state tracer equations (2.1)–(2.3) then

become a system of $3n \times 3n$ equations that are nonlinear because of the iron scavenging and the colimitation of the PO_4 uptake.

The $3n \times 3n$ system is solved efficiently using Newton's method [e.g., *Kelley*, 2003a,b]. Convergence of the Newton method depends on the initial guess for the solution and is not guaranteed. For the initial guess of χ_{P} and χ_{Si} we use the annual mean fields of the World Ocean Atlas [*Garcia et al.*, 2014] interpolated to our grid, and for the initial guess of χ_{Fe} we use the dFe fields estimated by *Frants et al.* [2016]. The Newton solver typically converges to numerical precision in ~ 10 iterations.

2.3.2 Cost Function

We optimize the model parameters by systematically minimizing a quadratic cost function of the mismatch between modelled and observed fields. For PO_4 and $\text{Si}(\text{OH})_4$, for which gridded climatologies are available, we define the weights based on the grid-box volumes, organized into vector \mathbf{v} , as

$$\mathbf{w}_{\text{P}} = \frac{\mathbf{v}}{(\bar{\chi}_{\text{P}}^{\text{obs}})^2 V} , \quad \text{and} \quad \mathbf{w}_{\text{Si}} = \frac{\mathbf{v}}{(\bar{\chi}_{\text{Si}}^{\text{obs}})^2 V} , \quad (2.23)$$

where we have normalized the weights by the total ocean volume V and the squared global mean observed concentrations. This non-dimensionalizes the quadratic cost terms and scales them to the same order of magnitude. For dFe, for which only sparse observations are available, we also define weights \mathbf{w}_{Fe} based on grid box volumes, but observations that are part of a vertical profile receive additional weight as detailed in Appendix 2.C.

With diagonal weight matrix $\mathbf{W}_i = \text{diag}(\mathbf{w}_i)$ for the i^{th} nutrient, its cost for the mismatch with observations is then given by

$$E_i = \delta \boldsymbol{\chi}_i^T \mathbf{W}_i \delta \boldsymbol{\chi}_i , \quad (2.24)$$

where $\delta \boldsymbol{\chi}_i \equiv \boldsymbol{\chi}_i - \boldsymbol{\chi}_i^{\text{obs}}$. For $\chi_{\text{P}}^{\text{obs}}$ and $\chi_{\text{Si}}^{\text{obs}}$ we use the annual mean phosphate and silicic-acid fields of the World Ocean Atlas [*Garcia et al.*, 2014]. For $\chi_{\text{Fe}}^{\text{obs}}$, we used the GEOTRACES intermediate data product [*Mawji et al.*, 2015] and the data set compiled by *Tagliabue et al.* [2012].

The cost terms for the nutrient mismatch do not provide a strong constraint on the relative sizes of the phytoplankton class because the nutrients are determined by their combined export. We therefore include additional terms in our cost function that constrain the phytoplankton concentrations p_c to the recent satellite derived estimates of *Kostadinov et al.* [2009]. These estimates provide phytoplankton concentrations for picophytoplankton ($0.5\text{--}2\text{ }\mu\text{m}$ in diameter), nanophytoplankton ($2\text{--}20\text{ }\mu\text{m}$), and microphytoplankton ($20\text{--}50\text{ }\mu\text{m}$),

which we identify with our small, large, and diatom functional groups. We use the entire mission composite data set as the satellite climatology [Kostadinov *et al.*, 2016].

Because of the large dynamic range of the phytoplankton concentrations, we consider mismatches in the log of the concentrations, that is, $\delta\pi_c \equiv \log[(p_c + \epsilon_c)/p_0] - \log[(p_c^{\text{obs}} + \epsilon_c)/p_0]$, where $\epsilon_c = \overline{p_c^{\text{obs}}}$ is introduced to limit the logarithm where the phytoplankton concentration falls to zero. For each class, we construct normalized weight vectors

$$\mathbf{w}_c = \frac{\mathbf{v}}{[\log(\overline{p_c^{\text{obs}}}/p_0)]^2 V_{\text{eup}}} , \quad (2.25)$$

where V_{eup} is the global euphotic volume, and $p_0 = 1 \text{ mg C m}^{-3}$ non-dimensionalizes the argument of the logarithm.

Organizing mismatches and weights into vectors and diagonal matrices, we calculate the cost for the phytoplankton concentration mismatch as

$$E_{\text{plk}} = \sum_c \delta\boldsymbol{\pi}_c^T \mathbf{W}_c \delta\boldsymbol{\pi}_c , \quad (2.26)$$

and combine the costs for the nutrient and plankton mismatches into the total cost

$$E_{\text{tot}} = \omega_P E_P + \omega_{\text{Si}} E_{\text{Si}} + \omega_{\text{Fe}} E_{\text{Fe}} + \omega_{\text{plk}} E_{\text{plk}} , \quad (2.27)$$

which we minimize to constrain our model parameters by the available observations. In (2.27) the ω weights were chosen such that the four cost terms contribute roughly equally to the total cost for a typical member of our family of solutions. This was achieved with $(\omega_P, \omega_{\text{Si}}, \omega_{\text{Fe}}, \omega_{\text{plk}}) = (1, 0.47, 0.044, 0.30)$, the smaller weight for dFe reflecting its larger root-mean-square (RMS) mismatch and hence much larger cost E_{Fe} .

2.3.3 Optimization Strategy

Our model has ~ 50 biogeochemical parameters that can in principle be determined through objective optimization given appropriate observational data. However, even with perfect data, some parameters can compensate for others (e.g., two parameters appearing as a ratio) so that not all parameters are independent. Other parameters cannot be optimized because the mismatch with available nutrient and phytoplankton data is not sensitive to their value. In practice, it therefore is not possible to optimize all parameters, and care is needed to optimize only those parameters that independently shape the nutrient and phytoplankton concentrations.

The parameters associated with the remineralization of phosphate and dissolution of opal are well constrained by the high-quality climatologies of PO_4 and Si(OH)_4 . However, the iron cycle is relatively poorly constrained because the dFe data is much more sparse in both time and space, and estimates of the iron sources range over two orders of magnitude [e.g., Tagliabue *et al.*, 2016]. Moreover, the ligand field that determines the scavengable free iron is highly uncertain. Given these challenges, the recent inverse model of the iron cycle by Frants *et al.* [2016] considered a family of solutions for a range of external source strengths, an approach we will follow here for our coupled model.

Another key consideration is computational cost. Even with the numerically efficient Newton Solver, optimization typically requires hundreds of solutions of equations (2.1)–(2.3) per optimized parameter. We therefore optimized no more than ~ 13 parameters at a time. We acknowledge that the minimum attained by sequentially optimizing groups of independent parameters is generally different than jointly optimizing all independent parameters, but computational and practical considerations demanded a sequential approach. We justify this *a posteriori* by the fact that we are able to achieve fits to the observed nutrient fields that compare well to other recent nutrient models in the sense of similar RMS mismatches [e.g., Primeau *et al.*, 2013; Holzer *et al.*, 2014; Frants *et al.*, 2016]. Given these considerations, we adopted the following strategy:

- (i) Parameters that are measurable and considered well-known, as well as parameters that are unconstrainable by our cost function or whose value is not critical because they are strongly compensated by other parameters, were assigned values from the literature as collected in Table 2.1. The considerations that entered our choice of prescribed parameters are detailed in Appendix 2.D.
- (ii) The parameters that set the phosphate remineralization and opal dissolution profiles were optimized by minimizing the mismatch with PO_4 and Si(OH)_4 concentration data from the WOA13 [Garcia *et al.*, 2014] using separate single-nutrient models. For the Si cycle, we used the model of Holzer *et al.* [2014] and verified that the opal sinking speed parameter w_{Si} was not affected by the inclusion of sub-grid topography (Appendix 2.B). For the P cycle, we used a similar conditional restoring model without POP, but with subgrid topography, and optimized the Martin exponent b . The resulting values of w_{Si} and b (Table 2.1) were held fixed for all optimizations of the coupled nutrient cycling model.
- (iii) The remaining parameters were optimized using our coupled model. We first assign initial values for all these parameters and then sequentially update these initial values by optimizing subsets of parameters as detailed in Appendix 2.D. Both initial and final optimized parameter values are collected in Table 2.2.

(For the parameters of the iron cycle, Table 2.2 gives the values of our typical solution and the range across a family of solutions, different members of which have different external iron sources.)

Table 2.1: Parameters that were prescribed from the literature, or that were separately optimized in a submodel.

Parameter	Description	Value	Unit	Source
κ	Growth and mortality temperature coefficient	0.063	$(^{\circ}\text{C})^{-1}$	Eppley [1972]
k_w	Irradiance attenuation coefficient	0.040	m^{-1}	Dutkiewicz <i>et al.</i> [2005]
K_L	Ligand stability constant	8×10^{10}	$\text{kg} (\text{mol Lig})^{-1}$	Galbraith <i>et al.</i> [2010]
Γ_{\max}	Age coefficient for ligand parameterization	1600.	yr	Frants <i>et al.</i> [2016]
f^{POP}	Recyclable fraction of POP-scavenged dFe	0.90	–	Moore and Braucher [2008]
f^{bSi}	Recyclable fraction of opal-scavenged dFe	0.90	–	Moore and Braucher [2008]
f_{dia}^0	Diatom class detrital fraction at 0°C	0.74	–	Dunne <i>et al.</i> [2005]
f_{lrg}^0	Large class detrital fraction at 0°C	0.74	–	Dunne <i>et al.</i> [2005]
f_{sml}^0	Small class detrital fraction at 0°C	0.14	–	Dunne <i>et al.</i> [2005]
$\kappa_{\text{Si}}^{\max}$	Opal dissolution rate coefficient	13×10^{15}	d^{-1}	Gnanadesikan [1999]
T_E	Temperature scale for opal dissolution	11481.	K	Gnanadesikan [1999]
$k_{\text{dia}}^{\text{Si}}$	Diatom class Si(OH)_4 half-saturation constant	1.0	mmol Si m^{-3}	Matsumoto <i>et al.</i> [2013]
w_{Si}	Opal sinking speed	40.	m d^{-1}	Submodel optimization
b	POP flux Martin exponent	0.82	–	Submodel optimization

Table 2.2: Optimized parameters and range across family of solutions.

Parameter	Description	Initial Value	Optimized Value	Range	Unit
$k_{I,\text{dia}}$	Diatom class irradiance half-saturation rate	20.	8.1	–	W m^{-2}
$k_{I,\text{lrq}}$	Large class irradiance half-saturation rate	20.	9.0	–	W m^{-2}
$k_{I,\text{sml}}$	Small class irradiance half-saturation rate	20.	8.8	–	W m^{-2}
R_m^{Si}	Diatom maximum Si:P	160.	220.	–	$\text{mol Si} (\text{mol P})^{-1}$
R_0^{Si}	Diatom minimum Si:P	8.0	13.	–	$\text{mol Si} (\text{mol P})^{-1}$
$k_{\text{Si:P}}^{\text{Si}}$	Silicon half-saturation constant in Si:P	30.	4.0	–	mmol Si m^{-3}
$k_{\text{Si:P}}^{\text{Fe}}$	Iron hyperbolic constant in Si:P	1.0	0.077	–	nM Fe
$k_{\text{Fe:P}}$	Iron half-saturation constant in Fe:P	0.74	0.74	–	nM Fe
$k_{\text{dia}}^{\text{P}}$	Diatom class PO ₄ half-saturation constant	0.39	0.72	–	mmol P m^{-3}
$k_{\text{lrq}}^{\text{P}}$	Large class PO ₄ half-saturation constant	0.39	0.72	–	mmol P m^{-3}
$k_{\text{sml}}^{\text{P}}$	Small class PO ₄ half-saturation constant	0.030	0.13	–	mmol P m^{-3}
$k_{\text{dia}}^{\text{Fe}}$	Diatom class dFe half-saturation constant	0.10	0.30	–	nM Fe
$k_{\text{lrq}}^{\text{Fe}}$	Large class dFe half-saturation constant	0.10	0.29	–	nM Fe
$k_{\text{sml}}^{\text{Fe}}$	Small class dFe half-saturation constant	0.010	0.11	–	nM Fe
p_{dia}^{\max}	Diatom class maximum concentration	23.	42.	–	mg C m^{-3}
p_{lrq}^{\max}	Large class maximum concentration	23.	61.	–	mg C m^{-3}
p_{sml}^{\max}	Small class maximum concentration	23.	21.	–	mg C m^{-3}
τ_{dia}	Maximal Diatom growth timescale	6.0	0.65	–	d
τ_{lrq}	Maximal Large growth timescale	6.0	1.5	–	d
τ_{sml}	Maximal Small growth timescale	6.0	7.4	–	d

Table 2.2: Optimized parameters and range across family of solutions (continued).

Parameter	Description	Initial Value	Optimized Value	Range	Unit
$R_0^{\text{Fe:P}}$	Maximum Fe:P uptake ratio	5.0	2.0	0.00047–3.0	$\text{mmol Fe} (\text{mol P})^{-1}$
$\kappa_{\text{scv}}^{\text{POP}}$	POP scavenging rate constant	0.13	1.0	0.015–7.9	$(\text{mmol POP m}^{-3})^{-1} \text{d}^{-1}$
$\kappa_{\text{scv}}^{\text{bSi}}$	Opal scavenging rate constant	3.1	1.3	0.85–13.	$(\text{mol bSi m}^{-3})^{-1} \text{d}^{-1}$
$\kappa_{\text{scv}}^{\text{dst}}$	Dust scavenging rate constant	10000.	9.4	8.5–10.	$(\text{g dust m}^{-3})^{-1} \text{d}^{-1}$
L_b	Background ligand concentration	1.0	0.51	0.40–0.72	nM Lig
L_v	Maximal hydrothermal vent ligand concentration	3.0	1.2	0.68–1.4	nM Lig
τ_b	Hydrothermal vent plume restoring timescale	10.	5.7	3.0–7.5	yr
L_{\max}	Maximal age-enhanced ligand conc.	2.3	0.97	0.82–1.3	nM Lig
σ_A	Aeolian source strength	1.9	5.3	0.63–22.	Gmol Fe yr^{-1}
σ_S	Sedimentary source strength	4.2	1.7	0.11–22.	Gmol Fe yr^{-1}
$\sigma_{H,\text{ATL}}$	Hydrothermal source strength, Atlantic	0.098	0.19	0.00013–0.50	Gmol Fe yr^{-1}
$\sigma_{H,\text{PAC}}$	Hydrothermal source strength, Pacific	0.21	0.42	0.035–2.9	Gmol Fe yr^{-1}
$\sigma_{H,\text{IND}}$	Hydrothermal source strength, Indian Ocean	0.066	0.13	0.011–0.81	Gmol Fe yr^{-1}
$\sigma_{H,\text{SO}}$	Hydrothermal source strength, Southern Ocean	0.066	0.13	0.011–1.2	Gmol Fe yr^{-1}

2.3.4 Family of Solutions

Figure 2.2 shows the quality of the fit to nutrient and phytoplankton data for all our optimized solutions, which span a wide range of source strengths. For ease of presentation, solutions are divided at $\sigma_H = 1 \text{ Gmol yr}^{-1}$ into low and high hydrothermal cases, with σ_H spanning a range from 0.073 to 11 Gmol yr^{-1} . For high σ_H , we focused on correspondingly higher aeolian and sedimentary source regimes. Source-parameter space was not explored uniformly because (i) the final step of our optimization adjusted our initial choice of sources, and because (ii) some source choices produced spurious numerical difficulties for the Newton solver.

All solutions fit the macronutrient fields about equally well, but the overall quality of fit as quantified by the square root of the quadratic mismatch (“total cost”, top panels of Figure 2.2) gets systematically worse with increasing aeolian source strength, σ_A , especially for high hydrothermal sources. This worsening fit for high σ_A is reflected in the mismatch of all three nutrients. We define our family of solutions as the set of solutions whose total cost remains within $\sim 5\%$ of the smallest misfit (total cost less than 15.4), which essentially eliminates solutions with $\sigma_A \gtrsim 22 \text{ Gmol yr}^{-1}$ and $\sigma_H \gtrsim 5 \text{ Gmol yr}^{-1}$ (black crosses in Figure 2.2). (If we include the “crossed-out” solutions for plots of subsequent sections that show scatter across the family of solutions, the visual impact is virtually imperceptible.) While it is clear from Figure 2.2 that high- σ_A solutions are less likely, we hasten to add that the cost threshold for inclusion in the family is arbitrary as we do not have a formal error covariance to convert the cost into a likelihood.

In terms of total cost, there is little sensitivity to the strength of the sedimentary source – scavenging can be optimized for a sedimentary source ranging over 2 orders of magnitude for an overall similar quality of fit. For low σ_H , there are small opposing RMS mismatches for PO₄ and dFe, with a slightly better PO₄ fit for higher sedimentary source and a slightly better dFe fit for lower sedimentary source, although the variation in the mismatch is less than 1% of the global mean concentrations.

While the mismatch for dFe is substantial at $\sim 45\%$ of the global mean dFe concentration, the smallest dFe mismatch occurs when all three sources are low. The dFe mismatch rapidly increases with σ_A , consistent with the findings of the much simpler model of *Frants et al.* [2016]. The overall cost and the mismatch for each nutrient are insensitive to the strength of the hydrothermal source.

While Figure 2.2 shows some variations with the source strengths in the overall quality of the fit, it is clear that the iron sources and scavenging sinks are poorly constrained by the available nutrient and phytoplankton observa-

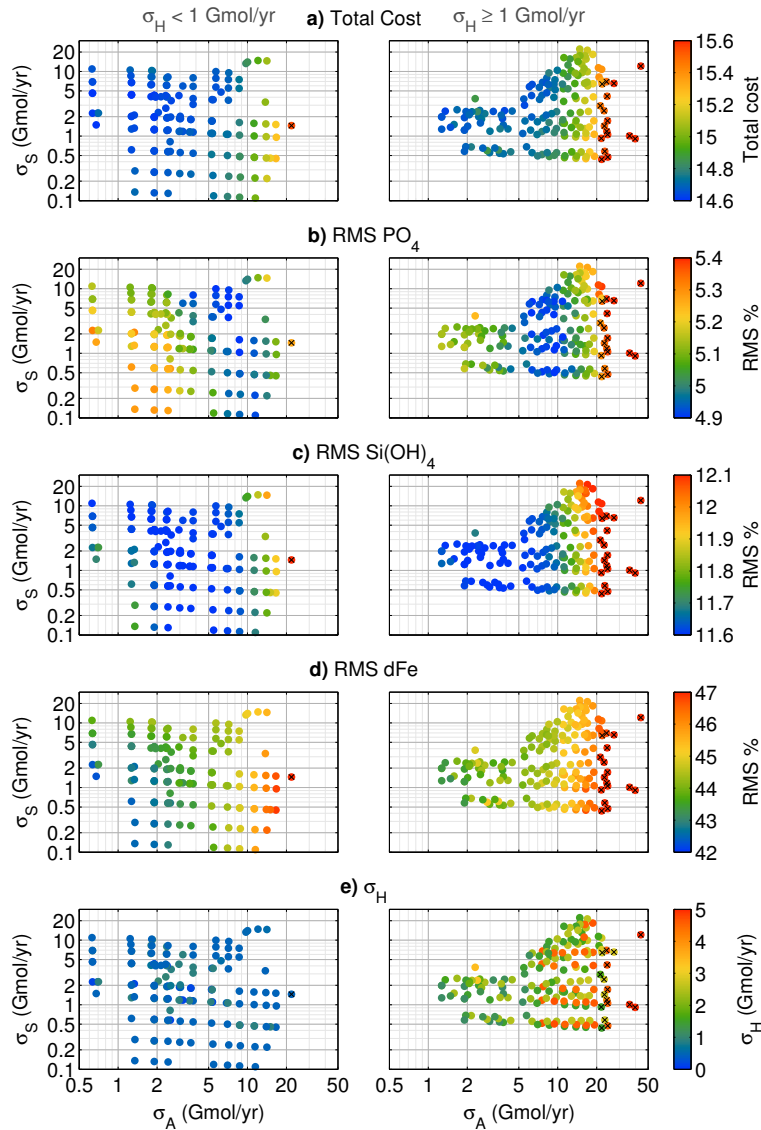


Figure 2.2: Total cost metric and RMS mismatch of the nutrient concentrations as a function of the aeolian, hydrothermal, and sedimentary iron source strengths ($\sigma_A, \sigma_S, \sigma_H$) plotted for all our optimized solutions. Solutions whose total cost exceed 15.4 are indicated by black crosses and were excluded from our family of solutions. Plots on the left show solutions for which $\sigma_H < 1 \text{ Gmol yr}^{-1}$, while for plots on the right $\sigma_H \geq 1 \text{ Gmol yr}^{-1}$. (a) Square root of the total cost expressed as a nominal percentage representative of the mean RMS mismatch of the nutrient and phytoplankton concentrations. (b) RMS mismatch of the PO_4 concentration as a percentage of the global mean PO_4 concentration. (c) As (b) for Si(OH)_4 . (d) As (b) for dFe. (e) The value of the hydrothermal source σ_H for each family member.

tional data. Given the uncertainties in the sources and the small cost differential between family members, it is not appropriate to single out the solution with the numerically lowest cost as the most realistic solution. We therefore use the entire family of solutions below to assess the robustness of our results in terms of the spread across the family, and to elucidate the systematic variations of the carbon and opal exports with the fractional size of each iron source type (aeolian, sedimentary, hydrothermal).

As a typical representative of our family of solutions, for which we plot patterns and typical results below, we selected the state for $(\sigma_A, \sigma_S, \sigma_H) = (5.3, 1.7, 0.9)$ Gmol yr⁻¹. This state is typical in that it lies at the mode of the distribution of overall RMS misfit values and, for most quantities, tends to lie in the middle of the range across the family.

We emphasize that the variations across the family of solutions explored here are variations of the *fully optimized* biogeochemical states. These variations cannot be used to infer the system's response to dFe perturbations for which the other biogeochemical parameters would not change. Such perturbations, which are of great interest in themselves, are examined in Chapter 3.

2.4 Fidelity to Observations

We now examine in more detail how well our solutions match the observations against which they were optimized. Where there is little variation across the family, we focus on our typical solution. For iron-related quantities that have by construction significant spread across the family, we will focus on the systematic variations of the optimized states with the dFe sources.

2.4.1 Nutrient Concentrations

The nutrient concentrations are well constrained for all members of our family of solutions. We quantify the overall fit of the modelled nutrient concentrations in terms of the joint probability density function (pdf) of the modelled and observed concentrations. This joint pdf may be thought of as the binned scatter plot of the modelled versus observed values for all grid boxes. The binning for a given nutrient was weighted by the corresponding weights of the associated mismatch cost. These joint pdfs are shown in Figure 2.3 for all three nutrients for our typical solution. Both the PO₄ and Si(OH)₄ pdfs fall close to the 1:1 line, showing high fidelity to observations. For PO₄ the cost-weighted RMS error is 5.0 % of its global mean of 2.17 μM. In comparison, Primeau *et al.* [2013] achieved an RMS mismatch of 3 % by jointly optimizing the uptake rate of each grid grid box with the circulation. Silicic acid has a slightly larger RMS

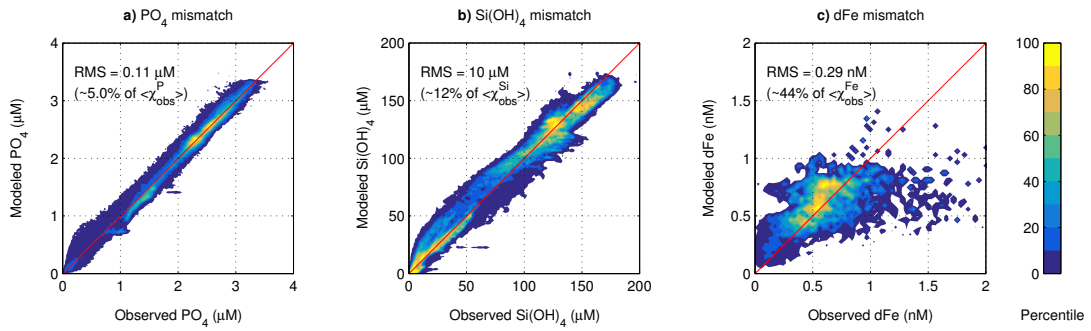


Figure 2.3: Joint distribution of the volume-weighted observed and modelled concentrations of PO₄ (a), Si(OH)₄ (b), and dFe (c). The percentiles of the cumulative distribution are defined such that $x\%$ of the distribution lies outside the x -percentile contour. Large percentiles thus correspond to high densities. For PO₄ and Si(OH)₄, the observations were interpolated to our model grid from the World Ocean Atlas [Garcia *et al.*, 2014]. The dFe observations were interpolated to our model grid from the data compilation of Tagliabue *et al.* [2012] and the GEOTRACES data [Mawji *et al.*, 2015].

mismatch of 12. % relative to its 89.1 μM global mean. This is similar to the 13 % RMS error reported by Holzer *et al.* [2014], who used the same circulation but a much simpler model of the silicon cycle.

The global mean dFe concentration is well constrained within the narrow range of 0.56 – 0.68 nM across the family of solutions. For iron, the joint probability is by necessity computed using only those grid boxes that contain dFe observations. The scatter from the 1:1 line is much larger than for the macronutrients with a substantial RMS mismatch of 0.29 nM, or 44 % of the mean. This mismatch is comparable to that of other models [e.g., Tagliabue *et al.*, 2016]. Compared to the simpler model of Frants *et al.* [2016], the joint pdf shows that our dFe field has a wider, more realistic dynamic range. We note that while Frants *et al.* [2016] report an RMS mismatch of only 0.19 nM, they also employed different weights for the model-observation mismatch. If we re-compute the RMS mismatch of the optimized dFe field of Frants *et al.* [2016] using the weights of this work, we also obtain a 0.29 nM mismatch.

The relatively large mismatch for dFe not only quantifies model deficiencies, but to a large degree also reflects the fact that we are comparing snapshot observations against a steady-state climatological model. The dFe observations have difficult-to-quantify temporal and spatial sampling biases, and dFe being a trace element, it is sensitive to episodic events in the aeolian source [e.g., Croot *et al.*, 2004], and possibly to internal episodic events such as submarine volcanism [e.g. Massoth *et al.*, 1995].

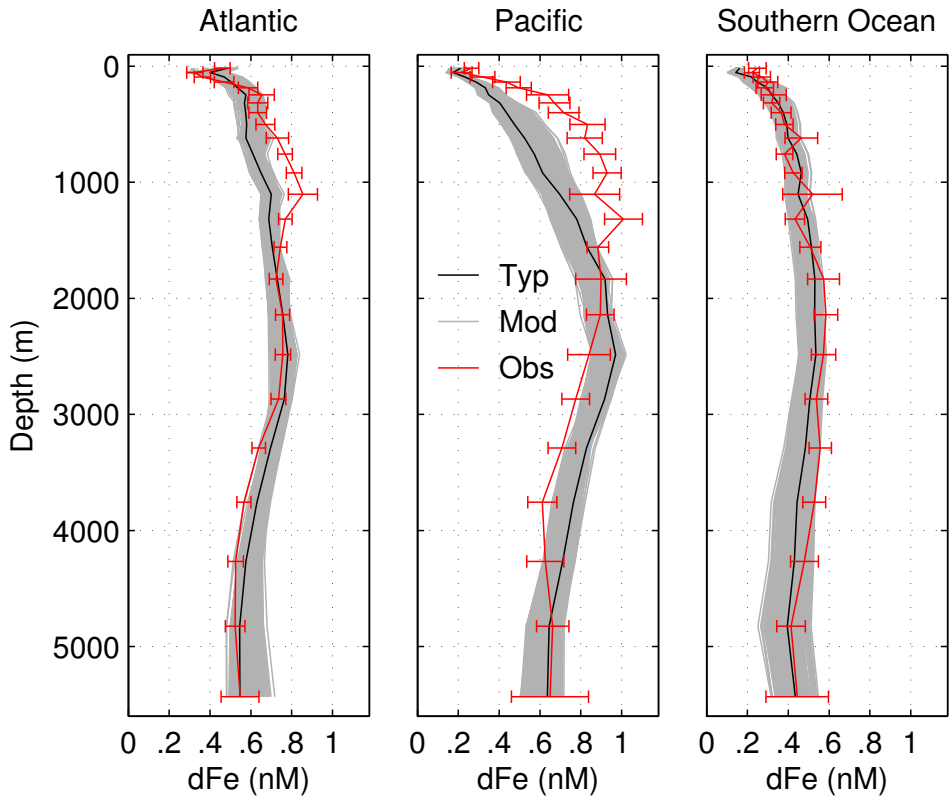


Figure 2.4: Basin-wide, cost-weighted average profiles of the (red) observed and (grey) modelled dFe concentrations for the Atlantic and Pacific oceans (both north of 40°S), and the Southern Ocean (south of 40°S). The profiles of our typical solution are highlighted in black. The error bars represent the combined standard error associated with the spatial standard deviation from the basin-mean profile and the observational standard deviation for each grid box. These were added in weighted quadrature using the weights for dFe mismatch from our cost function.

2.4.2 dFe Profiles

To quantify the spatial structure of the dFe mismatch, we examine vertical profiles for each basin. For both model and observations, we only use the grid boxes that contain observations and average horizontally over the basins using the E_{Fe} cost weights. The resulting profiles are shown in Figure 2.4. The family of model profiles generally overlaps with the observational uncertainties. The estimates are particularly close to the observations near the surface. In the abyssal oceans, the spread in the family of profiles is larger. The spread across the family is in part a reflection of the weights in our cost function. Most dFe

observations are available in the upper ocean, implying a small variance of the mean concentration and hence large weights, while deep observations tend to be sparser with smaller weights (for details on the weights see Appendix 2.C).

Figure 2.4 also shows systematic biases in the inferred dFe concentrations. Biases are particularly strong in the Pacific where the observations tend to be underpredicted by as much as ~ 0.3 nM above ~ 1500 m and overpredicted by ~ 0.2 nM below ~ 2000 m depth. The typical estimated Pacific profile is too linear in the upper 1500 m, with vertical gradients that are too weak above ~ 300 m and too strong below ~ 1000 m. In the Atlantic, a smaller low bias of ~ 0.15 nM can be seen between ~ 500 and ~ 1300 m depth.

These biases could be due to deficiencies in our model such as, for example, oversimplified ligand parameterization, but one must also keep in mind that there are hard-to-quantify biases in the observations. The observations are too sparse to form a reliable climatology, and it is remarkable that we can fit the available observations as well as we do. The larger biases in the Pacific could well be due to the absence of Pacific transects in the GEOTRACES Intermediate Data Product 2014, which means that mismatches in the Pacific incur a relatively smaller penalty in our cost function.

2.4.3 Phytoplankton Distribution

Figure 2.5 shows a model–observation comparison of the phytoplankton concentration (plotted in C units using a constant Redfield ratio of C:P = 106). Although the distinction between our phytoplankton classes is functional and not determined by size, we compare our Small, Large, and Diatom concentrations with the picophytoplankton ($0.5\text{--}2\ \mu\text{m}$), nanophytoplankton ($2\text{--}20\ \mu\text{m}$), and microphytoplankton ($20\text{--}50\ \mu\text{m}$) of the satellite-based estimates of Kostadinov *et al.* [2016], consistent with the construction of our E_{plk} cost function. We note that although the observation-based phytoplankton concentrations of Kostadinov *et al.* [2016] are used to constrain the model parameters in the optimization, there is no a priori guarantee that the model will produce a good fit to these phytoplankton concentrations. This is in part because the mismatch of each functional class accounts for only $\sim 10\%$ of the total cost. (Recall that the purpose of including E_{plk} in the total cost is to apply separate constraints on the concentrations of each phytoplankton functional class.)

The inverse-model estimates capture the broad global patterns of the phytoplankton concentrations reasonably well, although some biases are also evident. The observation-based Diatom and Large concentration has a minimum at $\sim 60^\circ\text{S}$, a feature our estimates do not capture. This may be related to seasonality issues, which our approach cannot capture. Our estimates for the Large and Small concentrations have higher concentrations in the subtropical gyres and

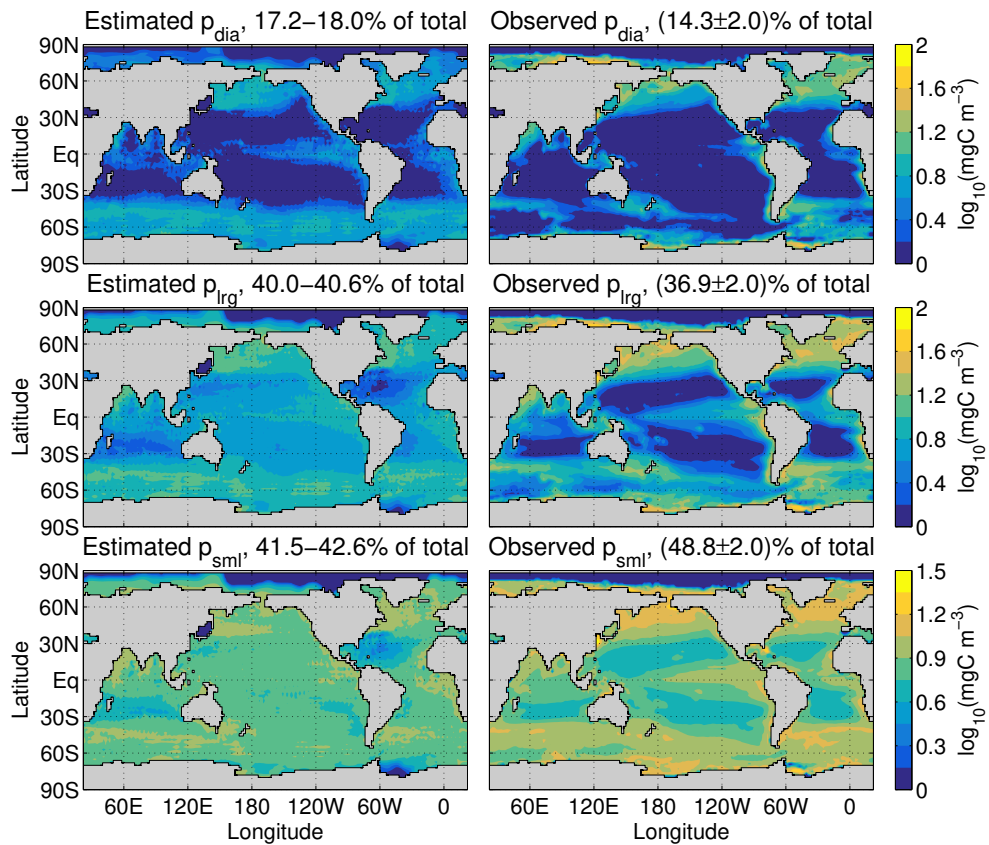


Figure 2.5: Comparison of model estimates (left) and satellite-based observational estimates from Kostadinov *et al.* [2016] (right) of phytoplankton concentrations averaged vertically over the model euphotic zone. The Diatom concentration is shown in the top row, the Large phytoplankton concentration in the middle row, and the Small phytoplankton concentration in the bottom row. Note the logarithmic colour scales with separate ranges for each functional class.

weaker meridional gradients with lower high-latitude and tropical concentrations than observed. These discrepancies may again be related to the absence of seasonality. Another factor is that the phytoplankton mismatch carries less penalty in our cost than the combined misfit terms of the three nutrient fields.

The global mean phytoplankton concentration of each functional class was remarkably stable across all members of our family of solutions with ranges of $\bar{p}_{\text{sml}} = (2.63 - 2.87) \text{ mg C m}^{-3}$, $\bar{p}_{\text{lrg}} = (6.16 - 6.53) \text{ mg C m}^{-3}$, and $\bar{p}_{\text{dia}} = (2.63 - 2.87) \text{ mg C m}^{-3}$. This indicates that the satellite data provides a good constraint on the global-scale ecosystem composition.

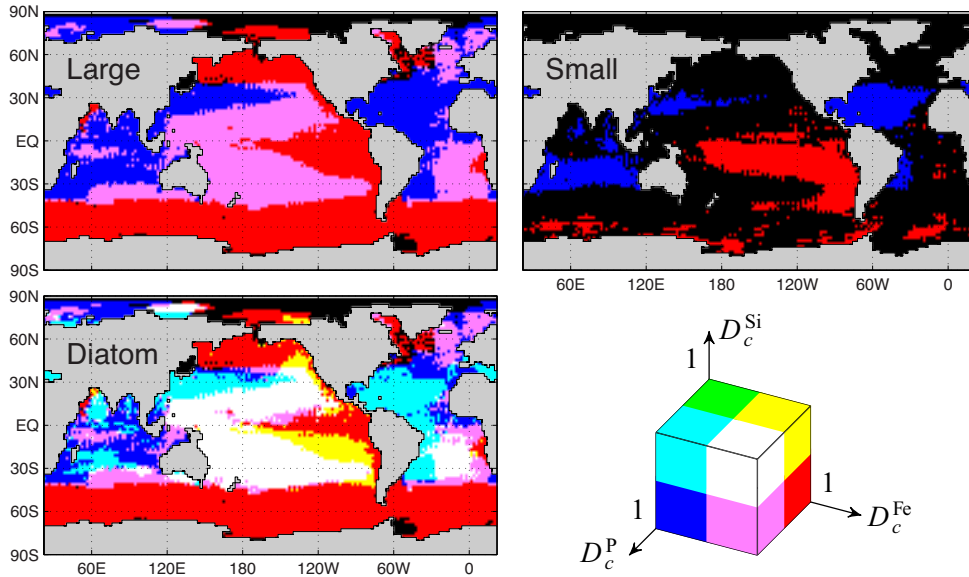


Figure 2.6: The patterns of limiting nutrients for each phytoplankton functional class. The colour cube at the bottom right shows the eight possible limitation regimes of our inverse model: Red corresponds to dFe limitation, blue to P limitation, and green to Si limitation. Cyan, yellow, and magenta correspond to colimitations of P and Si, dFe and Si, and P and dFe, respectively. White corresponds to colimitation of all three nutrients while black indicates no limitation. (See text for the definitions of the deficiencies D_c^P , D_c^{Si} , and D_c^{Fe} of the cube axes.)

2.5 Limiting Nutrients

For a given phytoplankton functional group, different nutrients are known to limit biological production in different parts of the ocean [e.g., Moore *et al.*, 2001]. These geographic limitation patterns are a fundamental fingerprint of upper-ocean ecosystem dynamics. Knowledge of the limitation patterns is important for understanding how the global nutrient cycles operate in the current climate and for assessing possible future changes of the global ocean ecosystem.

Limiting nutrients can be determined observationally [e.g., Moore *et al.*, 2013a], and from biogeochemical models [e.g., Moore *et al.*, 2004]. Here, we estimate the limitation patterns from our optimized inverse-model solutions. In our model, the biological uptake of each functional class (2.6) is limited through $F_{N,c}$, the product defined in (2.11) of three Monod terms, one for each nutrient. We define the deficiency D_c^i of functional class c in nutrient i as the complement of the corresponding Monod factor, i.e., as $D_c^i \equiv 1 - \frac{\chi_i}{\chi_i + k_c^i}$. We deem nutrient i to be “limiting” class c if $D_c^i > 0.5$ or, equivalently, if $\chi_i < k_c^i$, i.e., if

the nutrient concentration falls below its half-saturation value for uptake.

To display the pattern of the nutrient limitations, we could use the fact that we have three nutrients to define an RGB color as $(D_c^P, D_c^{Si}, D_c^{Fe})$. However, because the resulting colors vary continuously, it is hard to quantify the resulting patterns. We therefore define the limiting RGB color as $(L_c^P, L_c^{Si}, L_c^{Fe})$, where $L_c^i = 1$ if $D_c^i > 0.5$ and $L_c^i = 0$ otherwise. This partitions the RGB color cube into 8 possible colors that define and identify the 8 nutrient limitation regimes shown in Figure 2.6. Specifically, black $(0, 0, 0)$ results from all nutrients being available in sufficient quantities so that none are deemed limiting, white $(1, 1, 1)$ if all three nutrients are limiting, red $(1, 0, 0)$ if only dFe is limiting, green $(0, 1, 0)$ if only $Si(OH)_4$ is limiting, and blue $(0, 0, 1)$ if only PO_4 is limiting. The remaining three possibilities correspond to 2 nutrients being colimiting: magenta $(1, 0, 1)$ if dFe and PO_4 are colimiting, cyan $(1, 1, 0)$ if PO_4 and $Si(OH)_4$ are colimiting, and yellow $(0, 1, 1)$ if $Si(OH)_4$ and dFe are colimiting. Only a few grid boxes in the Arctic are solely limited by silicic acid (green).

Figure 2.6 shows the limitation patterns of all three phytoplankton classes. The Large and Diatom classes have similar patterns of iron limitation in the Southern Ocean, eastern tropical Pacific, and North Pacific. For both classes, the Indian Ocean and northern North Atlantic are largely PO_4 limited. The subtropical gyres of the Indian Ocean and North Atlantic are PO_4 limited for the Large class, and PO_4 - $Si(OH)_4$ colimited for Diatoms. The differences between the Large and Diatom classes come from the $Si(OH)_4$ dependency of diatoms. Because the Large group requires zero silicic acid, its limitation map show no areas where all three nutrients are limiting (white). The subtropical gyres of the Pacific and South Atlantic are dFe and PO_4 colimited for the Large class, while for diatoms the centre of these gyres are limited in all three nutrients. For diatoms, the eastern margins of the Pacific subtropical gyres show Si-Fe colimitation (yellow). The completely nutrient replete regions of the Arctic and Weddell Sea reflect the low biological utilization there driven in our model by light limitation through the prescribed PAR irradiance field.

The small phytoplankton class shows a much simpler limitation pattern. Limitation occurs primarily in the subtropical oceans with small patches of iron limitation also in the Southern Ocean and tropical Pacific. Iron limitation dominates the subtropical South Pacific, while PO_4 limitation occurs primarily in the subtropical gyres of the south Indian Ocean and North Atlantic. The rest of the ocean is largely nutrient replete for the Small functional class.

The broad features of the limitation pattern of Figure 2.6 are robust across all members of our family of solutions, with areas of each type of limitation generally varying by $\pm 5\%$ or less across the family of solutions.

The general features seen in Figure 2.6 broadly agree with the observational

data (in situ and bottle nutrient addition experiments) reported by *Moore et al.* [2013a]. Like our estimates, the observations show Fe limitation in the Southern Ocean, subpolar North Pacific, and eastern tropical Pacific. The observations also indicate Fe limitation in the North Atlantic, which for our solutions is also present in small patches in the western subpolar North Atlantic and becomes slightly more pronounced for the family members with higher total iron source. *Moore et al.* [2013a] report Si limitation in the Pacific sector of the Southern Ocean at its northern boundary, where the silicic acid concentration sharply decreases. This is consistent with our yellow region of joint Si and Fe limitation along the eastern edge of the Pacific subtropical gyres. Consistent with our estimates, the observations reported by *Moore et al.* [2013a] show secondary PO₄ limitation in the North Atlantic subtropical gyre and in the equatorial Atlantic, where the primary limitation is nitrogen (N) limitation.

Because we do not include the N-cycle in our model, we cannot make any statements about N limitation. However, NO₃:PO₄ ratios of the pelagic ocean are observed to be strikingly constant [Redfield, 1934]. *Tyrrell* [1999] suggested that this is a consequence of N₂ fixation, which increases when NO₃ concentrations are low and decreases otherwise, thereby regulating NO₃ concentrations (a process *Tyrrell* dubbed the “nitrostat”). It is therefore possible that regions identified in our model as P-limited are also N-limited. However, this does not mean that P-limitation equates to N-limitation, given that deviations from the N:P Redfield ratio have been reported [e.g., *Tyrrell and Law*, 1997]. *Weber and Deutsch* [2014] attribute these deviations to the geographic distribution of N₂ fixers and denitrifiers, which play an important role in shaping global production patterns. The fact that there are local sources and sinks of nitrate that have no equivalence in the phosphate cycle underscores that N and P limitations are not necessarily interchangeable.

Our limitation patterns can also be compared to those calculated for summer conditions in the BEC model of *Moore et al.* [2004]. However, it must be kept in mind that (i) the BEC model has a different circulation and a different representation of the ocean’s biogeochemical cycles (e.g., explicitly representing the nitrogen cycle and diazotrophs) and that (ii) *Moore et al.* [2004] define limitation in terms of the minimum Monod factor, while we use a threshold of 1/2 for the Monod factors and jointly consider three Monod terms to define the type of limitation. For diatoms, the Fe limitation pattern reported by *Moore et al.* [2004] is similar to ours including bands of Si limitation surrounding the tongue of Fe limitation in the tropical eastern Pacific. For non-diatom phytoplankton, there are also broad similarities, such as iron limitation in the eastern tropical Pacific, subpolar North Pacific, and Southern Ocean. In the BEC model, most of the Atlantic is phosphate or nitrate limited. While we do not model nitrate, nitrate limitation in our estimates would be reflected as phosphate limitation, and

our limitation patterns show most of the Atlantic deficient in phosphate. The BEC model's Small phytoplankton class shows nitrogen limitation surrounding the tropical tongue of iron limitation in the Pacific, while with our definitions there is very little PO₄ limitation in the Pacific for the Small class, which is iron limited or nutrient replete in most of the Pacific. Finally, we note that the annual-mean nature of our estimates is another possible reason for differences.

2.6 Export Production

A key metric of the nutrient cycles is their export production, which determines the strength of the biological pump (see, e.g., Chapter 1). Export production is not directly available from satellite measurements, but observationally constrained estimates are easily calculated from our inverse model. The phosphorus export flux, Φ^P , is simply the flux of organic phosphorus into the aphotic zone that is remineralized there, which we compute using the operators \mathcal{S}_c^P (sinking and remineralization) as

$$\Phi^P = \sum_{c=1}^3 \int_a dz \mathcal{S}_c^P U_c . \quad (2.28)$$

For plotting, we convert Φ^P to a carbon export flux using a constant C:P ratio of 106:1. We similarly calculate the opal export as

$$\Phi^{Si} = \int_a dz \mathcal{S}_{dia}^P R_{dia}^{Si:P} U_{dia} , \quad (2.29)$$

and the iron export associated with the remineralization of organic matter as

$$\Phi^{Fe} = \sum_{c=1}^3 \int_a dz \mathcal{S}_c^P R_c^{Fe:P} U_c , \quad (2.30)$$

where the vertical integrals are over the model aphotic zone (bottom to 73.4 m depth).

Figure 2.7a shows a map of the carbon export flux, together with its zonal integral for each member of our family of solutions. The spatial pattern shows some differences with the estimate of *Primeau et al.* [2013] (blue curve in Figure 2.7a). Our estimate of the carbon export has 1.5–2 times larger tropical and high latitude peaks, but is closer to the satellite-derived estimates of *Dunne et al.* [2007]. Our estimate also has sharper meridional gradients, which is arguably more realistic considering the sharp gradients in satellite-derived estimates of production [e.g., *Frants et al.*, 2016]. Our globally integrated carbon export

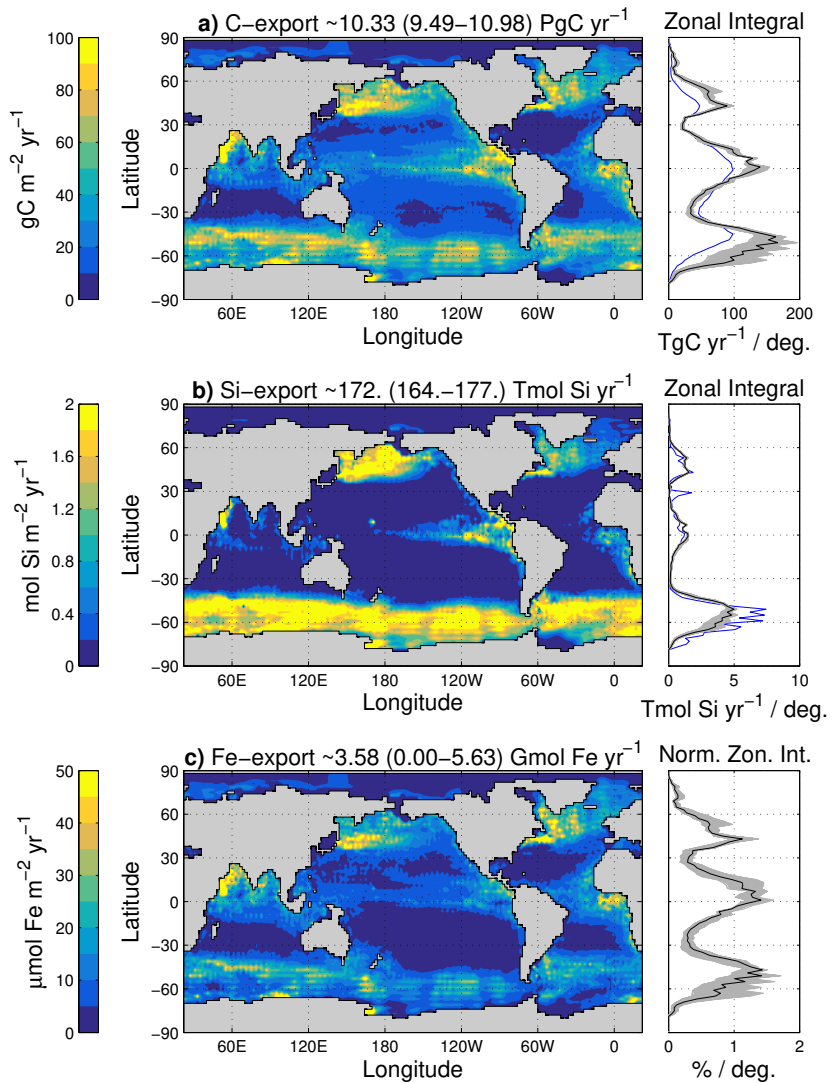


Figure 2.7: Local export production for each nutrient (maps on the left) and its zonal integral (curves on the right). Maps are shown for our typical solution, while we plot the zonal integral of each family member (scaled for dFe) in grey and the typical solution in black. (a) Phosphorus export, expressed in carbon units using C : P = 106 : 1. The blue zonal integral is the export production estimate of [Primeau et al., 2013]. (b) Opal export, where the blue zonal integral is the estimate of [Holzer et al., 2014]. (c) Iron export, with its zonal integrals scaled by the mean Fe:P ratio.

of $9.49\text{--}11.0 \text{ Pg C yr}^{-1}$ is also larger than the $\sim 7.5\pm 2.5 \text{ Pg C yr}^{-1}$ estimate of Primeau *et al.* [2013].

The differences with the estimate of Primeau *et al.* [2013] are likely due to very different uptake parameterizations: Primeau *et al.* [2013] consider the phosphorus cycle in isolation and optimize a single spatially varying uptake timescale for each grid box, while we explicitly represent three phytoplankton functional classes with different, optimized globally uniform uptake timescales, τ_c . We note that if we use the same growth timescale for each phytoplankton class, our model’s C-export remains close to that of Primeau *et al.* [2013].

Our estimates of the C-export production compare well with the satellite-based estimates of $9.7\text{--}12 \text{ Pg C yr}^{-1}$ by Gnanadesikan *et al.* [2004]. Our estimates also lie within the wide range of $9\text{--}28 \text{ Pg C yr}^{-1}$ of the Ocean-Carbon Cycle Model Intercomparison Project 2 [OCMIP-2, Najjar *et al.*, 2007], and compare well the OCMIP-2 mean particle export of $13\pm 3 \text{ Pg C yr}^{-1}$. (Because our model does not carry DOP, its particulate carbon export is given by its total carbon export.)

Figure 2.7b shows a map of the opal export, together with its zonal integral. As expected, opal export is most pronounced at high latitudes, particularly in the Southern Ocean. In spite of our relatively complex formulation of silicic acid utilization in terms of colimitations, the spatial pattern of the opal export and its global total of $164\text{--}177 \text{ Tmol Si yr}^{-1}$ compare well with the estimates by Holzer *et al.* [2014] ($171\pm 31 \text{ Tmol Si yr}^{-1}$). Other estimates of the global opal export range from 69 to $185 \text{ Tmol Si yr}^{-1}$ [e.g., Moore *et al.*, 2004; Sarmiento *et al.*, 2007; Heinze *et al.*, 2003].

There is very little spread in the carbon and opal export production across our family of solutions as can be seen by the tightly clustered zonal integrals plotted in grey in Figures 2.7a,b. This shows that the carbon and opal exports are well constrained despite the wide range of iron inputs. Note, however, that export productions are sensitive to the parameters that set the biological uptake rate, which were optimized before generating the family of optimal solutions with different iron sources.

Figure 2.7c shows a map of the iron export associated with organic matter, but not including the iron export carried by scavenging particles. The phosphorus and iron exports have broadly similar patterns, with differences that reflect variations in the local Fe:P uptake ratio. In the iron deficient Southern Ocean, the Fe:P ratio is smaller than its global mean, which results in Southern Ocean iron export that is less efficient than that of phosphorus (for iron, the peak Southern Ocean export relative to the tropical peak is lower than for phosphorus). As expected from the widely varying iron source strengths across our family of solutions, the globally integrated iron export covers a wide range

of 9.6×10^{-4} – 5.6 Gmol Fe yr $^{-1}$ ³. However, the geographic pattern of the iron export is robust across the family: The zonally integrated iron exports normalized by their global integrals collapse onto a well-defined cluster of curves. The spread in the thus normalized iron export is similar to the spread in the (unnormalized) carbon export, but slightly larger due to variations in the Fe:P ratio.

All export fields of Figure 2.7 show near-zero export in the Weddell Sea, in contrast to what restoring-type models tend to show. For example, the opal export estimated by Holzer *et al.* [2014] has a local maximum in the Weddell Sea. The Weddell Sea minimum here is due to near-zero satellite measurements of photosynthetically active radiation in this region. This may well be an artifact of the satellite data, for which the irradiance in the Weddell Sea varies substantially depending on which years are averaged.

Figure 2.8 shows the carbon export partitioned according to each functional class. The bulk of the carbon export is accomplished by the Large and Diatom phytoplankton classes (~53 and 41 %, respectively), while the remainder (~6 %) is exported by the Small class. In the tropics, the Large class dominates the C-export, while in the high latitudes, and particularly in the Southern Ocean, the Diatom class dominates. This partition between the three phytoplankton classes is the result of the adjustments of the class-specific growth timescales, τ_c , and of the parameters of the Si:P ratio to bring the fractional uptake by each class into alignment with the satellite-based estimates of Uitz *et al.* [2010]. For our typical solution, these uptake fractions are 38 %, 42 %, and 30 % for the Diatom, Large, and Small classes, respectively. This compares to 32 %, 44 %, and 24 % for micro-, nano-, and picophytoplankton, respectively, in the satellite-based estimates. (We find that if we use only a single optimized timescale for all three classes, the Small phytoplankton class completely dominates the phosphorus export, underlining the need for class-specific growth timescales.)

Export by the Diatom class has the sharpest meridional gradients. This is due to the diatoms' larger half-saturation rates, larger maximum phytoplankton concentrations, and their Si-limitation. Conversely, the carbon export by the Small class has the least spatial variation. This is consistent with satellite estimates of plankton concentration that show the least spatial variability for

³ This range reflects the variation of the optimized values of $R_0^{\text{Fe:P}}$ (see Table 2.2). Very low values of $R_0^{\text{Fe:P}}$ correspond to very high sources via the following mechanism: High iron sources are balanced by high scavenging through large optimized values of the scavenging rate constant. Because a large fraction of the scavenged iron redissolves at depth, high scavenging provides a large transport of iron to depth. To match the observed interior dFe concentrations, there must therefore be a correspondingly smaller iron export (due to remineralization) forcing the value of $R_0^{\text{Fe:P}}$ to be small.

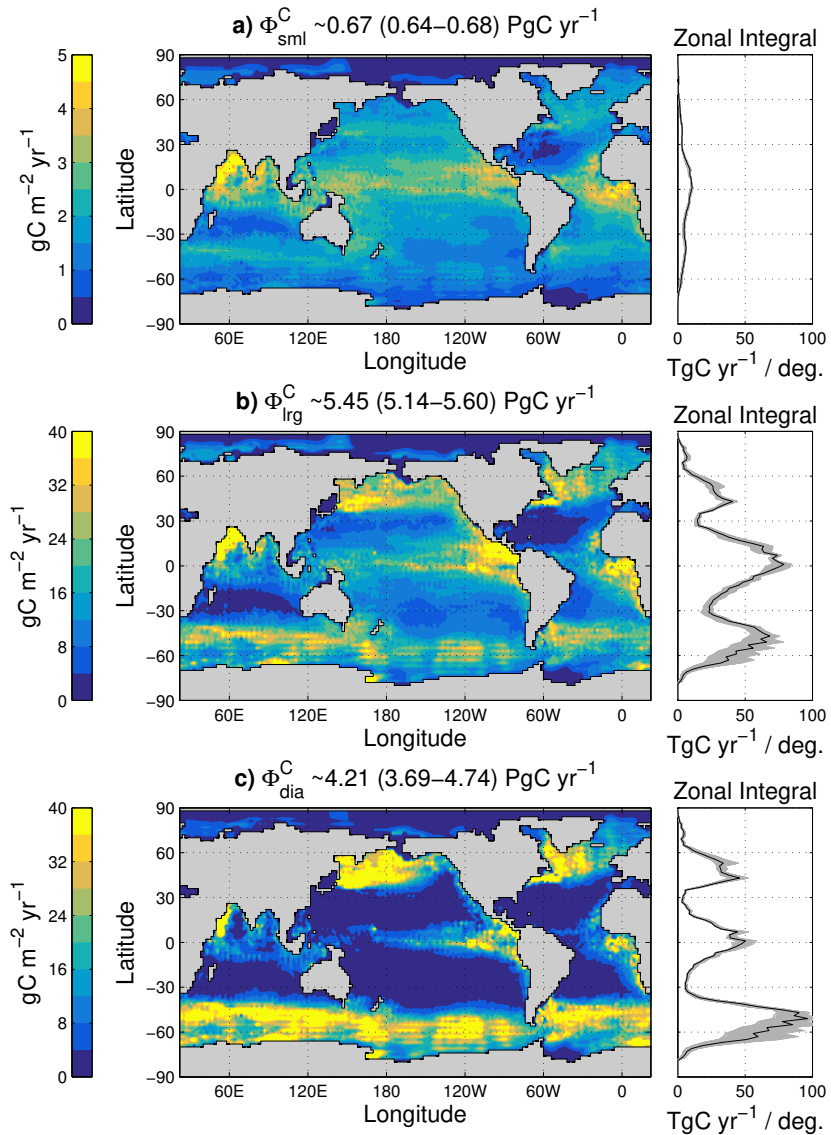


Figure 2.8: Local export production (maps on left) and its zonal integral (curves on the right) expressed in carbon units (using C : P = 106 : 1). Maps are shown for our typical solution, while we plot the zonal integral of each family member in grey and the typical solution in black. The export productions are plotted for each phytoplankton functional class: Small (top plots, a), Large (middle plots, b), and Diatom (bottom plots, c). Note the different colour scale for the Small class.

pico-phytoplankton [Kostadinov *et al.*, 2016]: Ubiquitous small phytoplankton are better adapted to nutrient-limited conditions, but do not benefit from nutrient abundance as much as larger phytoplankton.

2.7 Iron Cycle

Here we document some of the key features of the iron cycle as constrained by our inverse model. Certain features such as the dFe concentration field are robustly constrained by the observations regardless of iron source strengths, while other features such as, e.g., the relative importance of hydrothermal iron, vary systematically with the source strengths.

2.7.1 Iron Sources and Sinks

The pattern of the aeolian source is identical for all family members because we only vary its global source strength, σ_A . The sediment source is keyed to export production, which is well constrained across the family of solutions. Therefore, the sedimentary iron source patterns are very similar across all solutions, with only the global strength σ_S of the pattern varying among solutions. The initial hydrothermal pattern is set by the OCMIP ^3He source [Dutay *et al.*, 2004], but for total hydrothermal sources larger than $\sim 0.5 \text{ Gmol yr}^{-1}$, the optimized contributions from each basin changed substantially. Across our family of solutions the mean and standard deviations of the percentage contributions from each basin to the total hydrothermal source are $(15 \pm 9)\%$ for the Atlantic, $(52 \pm 6)\%$ for the Pacific, $(16 \pm 2)\%$ for the Indian Ocean, and $(17 \pm 3)\%$ for the Southern Ocean (south of 40°S). For reference, the vertically integrated iron sources of our typical solution are plotted in Appendix 2.E.

Because of the small variations in the source patterns, the vertically integrated total sinks of dFe, $\int dz(1 - \mathcal{S}_s^P)J_{\text{POP}}$, $\int dz(1 - \mathcal{S}_s^{\text{Si}})J_{\text{bSi}}$, and $\int dz J_{\text{dst}}$, have patterns that also vary little across the family of solutions (see Appendix 2.E for plots of the vertically integrated sinks of our typical solution). Note that these sinks balance the total source exactly because we are in steady state. The dominant iron sink is due to scavenging by organic particles (POP). The sink due to scavenging by biogenic silicon accounts for roughly half of the total sink. The patterns of POP and opal scavenging are determined by the phosphorus and opal exports and by the concentration of free iron. Consequently, the organic scavenging sink is strongest in the tropics, and the opal scavenging sink is strongest in the Southern Ocean. The sink due to mineral dust scavenging reflects the pattern of the aeolian dust input modulated by the free iron concentration. However, for our family of solutions, the sink due to dust scav-

enging is essentially negligible, being about 3 orders of magnitude smaller than the POP and opal scavenging.

2.7.2 Dissolved Iron Concentration and Source Attribution

Figure 2.9 shows our typical solution’s zonally averaged dFe concentration for each basin and for the global ocean. For each zonal average, we also show the corresponding profile of horizontally averaged dFe for each member of our family of solutions. The profiles are tightly clustered showing that the large-scale features of the dFe field are well constrained despite the large variations of the iron sources. The inverse model fits the observed dFe field for widely different sources by adjusting the corresponding scavenging. While these adjustments keep the total dFe field close to the observations, the relative contributions from the aeolian, sediment, and hydrothermal sources are unconstrained and can vary widely.

We calculate dFe concentrations due to each source following *Holzer et al.* [2016] by replacing the dFe concentration tracer equation (2.3) by an equivalent linear diagnostic system that has the same solution. This linear system, corresponding to a given solution of the full nonlinear system, is obtained by replacing the iron uptake and scavenging by linear operators. Specifically, the dFe uptake $R^{\text{Fe:P}} U_c$ is replaced with $L_{U,c} \chi_{\text{Fe}}$ and the scavenging rate J_j with $L_{J,j} \chi_{\text{Fe}}$, where the linear operators, organized into matrix form, are simply specified from the uptake and scavenging rates of the nonlinear solution as $\mathbf{L}_{U,c} = \text{diag}(R^{\text{Fe:P}} U_c / \chi_{\text{Fe}})$ and $\mathbf{L}_{J,j} \chi_{\text{Fe}} \equiv \text{diag}(J_j / \chi_{\text{Fe}})$. The dFe concentration χ_{Fe}^k due to source s_k (with $k \in \{\text{A}, \text{S}, \text{H}\}$) is then computed by replacing the total source in the linear equivalent system by the source s_k of the component of interest and computing the corresponding concentration.

Figure 2.9 also shows the profiles of the individual source components of dFe, colour coded according to the fractional strength of the aeolian source. In contrast to the profiles of the total dFe, these individual source components vary widely across the family of solutions, but in such a way that the total concentration $\chi_{\text{Fe}} = \chi_{\text{Fe}}^{\text{A}} + \chi_{\text{Fe}}^{\text{S}} + \chi_{\text{Fe}}^{\text{H}}$ is tightly constrained. For example, for low aeolian sources (yellow profiles in Figure 2.9), the concentration of aeolian iron $\chi_{\text{Fe}}^{\text{A}}$ is relatively low, but largely compensated by a relatively larger sediment contribution $\chi_{\text{Fe}}^{\text{S}}$. The concentrations of hydrothermal iron vary less systematically with the aeolian source, but all family members have very similarly shaped hydrothermal dFe profiles. However, the amplitudes of the hydrothermal dFe profiles can be seen to vary by roughly a factor of 2 across the majority of solutions, effectively fine tuning the total dFe concentration to be

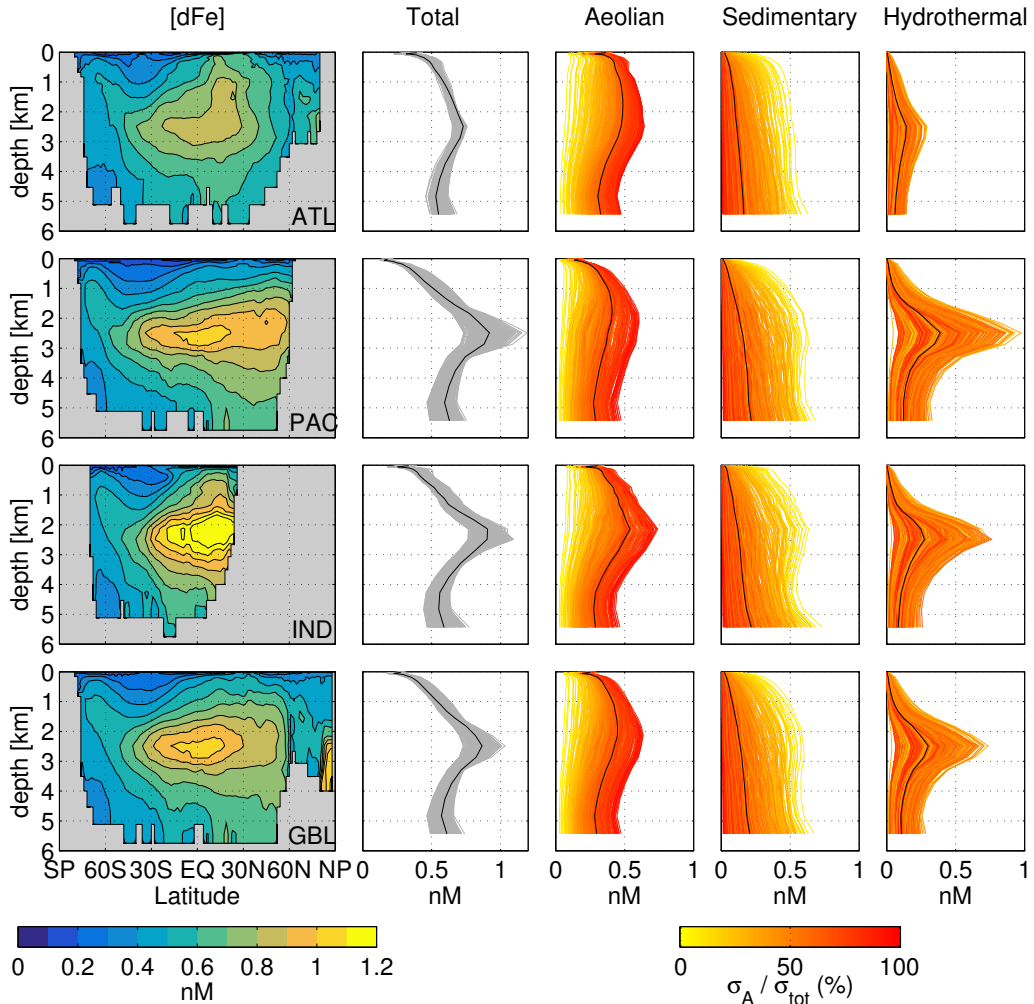


Figure 2.9: Estimates of the dFe concentration in each basin (ATL, PAC, IND) and globally (GBL). The zonal averages in depth-latitude space on the left show the total dFe field of our typical solution. The corresponding horizontally averaged profiles of total dFe are shown in grey for each family member and in black for the typical solution. The three columns of plots on the right show the source-partitioned dFe profiles, i.e., the profiles of the aeolian, sedimentary, and hydrothermal component of dFe for each family member. The individual source-partitioned profiles are colour coded according to the percent contribution of the aeolian iron source to the total iron source, with our typical solution in black.

as close to the observations as possible.

2.7.3 Iron-Type Attributed Export

2.7.3.1 Phosphorus Export

We quantify the contribution of each iron type to the export production as follows. In our formulation, non-zero dFe is necessary for non-zero phosphate uptake U_c . The uptake $U_c(\mathbf{r})$ inferred at point \mathbf{r} is supported by the dFe concentration at \mathbf{r} , which is a mixture of aeolian, sedimentary, and hydrothermal dFe. Thus, the uptake supported by dFe type k is given by $(\chi_{\text{Fe}}^k(\mathbf{r})/\chi_{\text{Fe}}(\mathbf{r})) U_c(\mathbf{r})$, that is, the local uptake supported by dFe of type k must be in proportion to the concentration fraction $\chi_{\text{Fe}}^k/\chi_{\text{Fe}}$ (note that $\sum_k \chi_{\text{Fe}}^k/\chi_{\text{Fe}} = 1$). For a given non-linear solution, the export phosphorus production supported by dFe of type k , denoted by ϕ_k^P is therefore calculated by replacing the uptake U_c in (2.28) with $(\chi_{\text{Fe}}^k/\chi_{\text{Fe}}) U_c(\mathbf{r})$.

While the total export production is well constrained regardless of the chosen iron source strengths, the production supported by a given dFe type varies substantially with the magnitude of the corresponding source. (Summing over the three dFe types yields the well-constrained total.) However, regardless of the source amplitudes, the patterns of the export supported by each dFe type is similar across the entire family of solutions.

Figure 2.10 shows $\widehat{\Phi}_k^P \equiv \Phi_k^P / \langle \Phi_k^P \rangle$, which is the export flux supported by dFe type k normalized by the global mean export $\langle \Phi_k^P \rangle$. The $\widehat{\Phi}_k^P$ patterns are plotted for our typical solution, together with zonal averages of $\widehat{\Phi}_k^P$ for all family members. The patterns can be seen to differ little among family members. Even the pattern of the export supported by hydrothermal dFe, which varies most across the family, has the broadly similar features of peak export in the Southern Ocean, with a secondary peaks in the tropics and in the Northern Hemisphere subpolar oceans, for all family members.

Figure 2.10a show that aeolian iron supports export primarily in the tropics and in the subpolar oceans. The tropics receive direct input of fresh aeolian iron, while the subpolar oceans receive upwelling regenerated iron [Holzer *et al.*, 2016]. The aeolian-dFe-supported export pattern is very similar to the pattern of the total export flux shown in Figure 2.7a (note that here we plot zonal averages, while Figure 2.7 shows zonal integrals). For sedimentary dFe to support export it must be transported from the ocean bottom into the euphotic zone. Consequently, the pattern of the export supported by sedimentary dFe (Fig. 2.10b) is dominated by regions of upwelling in the tropical and subpolar oceans and by regions of shallow depth (both resolved and subgrid) where there is high organic matter flux, such as the seas around Indonesia. The me-

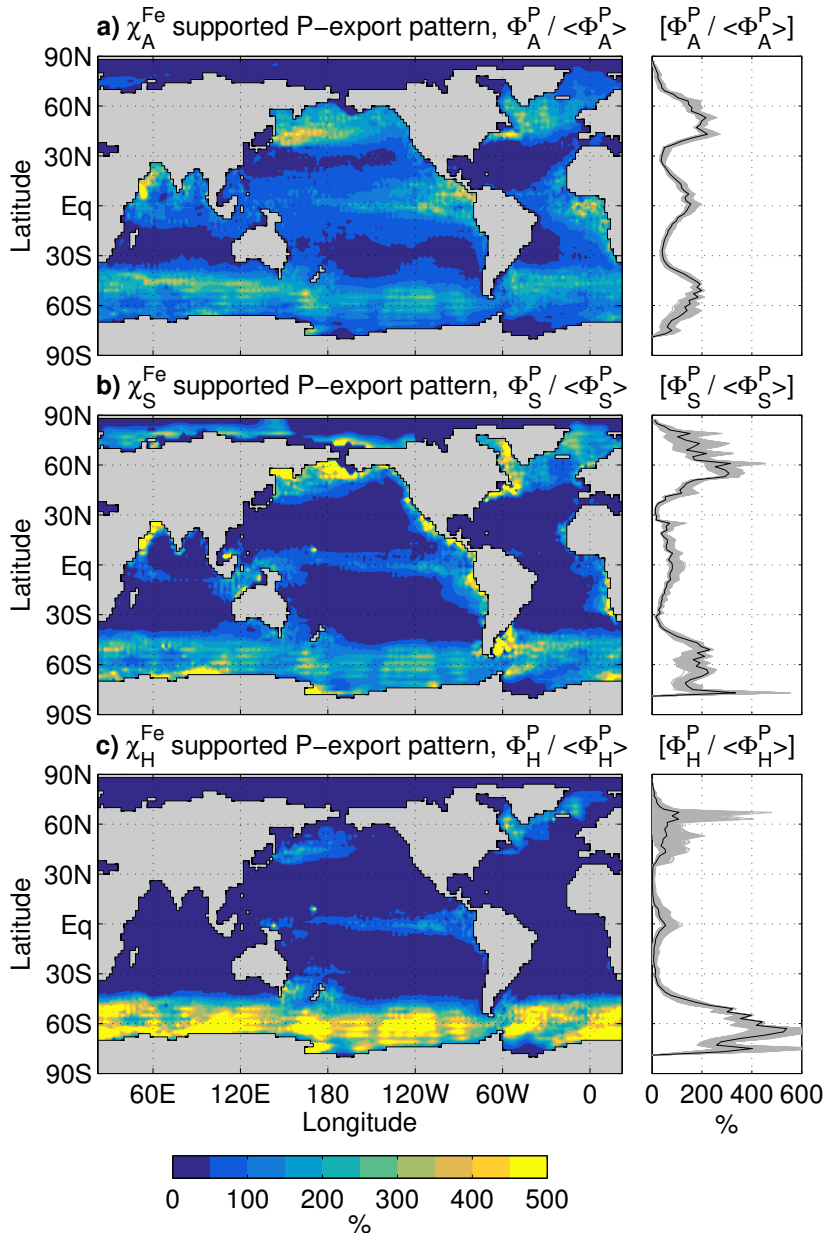


Figure 2.10: Phosphorus export supported by each dFe type [aeolian (a), sedimentary (b), hydrothermal (c)] normalized by its global mean. The maps show our typical solution, while zonal averages of the normalized phosphorus export are shown for each family member in grey, with the typical solution in black.

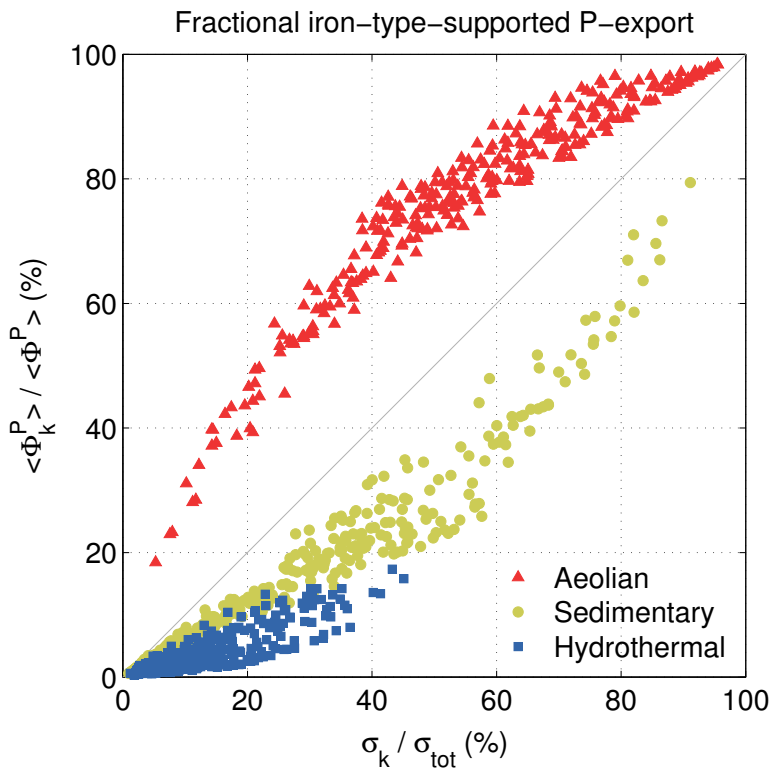


Figure 2.11: Percent global phosphorus export (equivalently carbon export) supported by each iron type (aeolian, sedimentary, hydrothermal) versus the corresponding fractional source of that iron type.

ridional gradients of the sedimentary-dFe-supported export are much sharper than for the aeolian-dFe-supported export, presumably because of the lack of large-scale direct surface input for sedimentary dFe. The pattern of export supported by hydrothermal dFe (Fig. 2.10c) is dominated by the Southern Ocean, where most of the density classes into which hydrothermal fluid is injected outcrop. The secondary regions hydrothermal-dFe-supported export are associated with upwelling in the tropics and in the subpolar oceans of the Northern Hemisphere.

Underscoring the similar source distribution of hydrothermal dFe and mantle ${}^3\text{He}$, the pattern of hydrothermal-dFe-supported export production is similar to the pattern with which mantle ${}^3\text{He}$ outgases to the atmosphere [e.g., Holzer *et al.*, 2017]. We do not expect an exact correspondence in the patterns because hydrothermal dFe is subject to scavenging losses, while ${}^3\text{He}$ is not, and our ratio of hydrothermal dFe source to mantle ${}^3\text{He}$ source is different for

different basins. (The ranges of the ratio of the optimized hydrothermal iron source to the mantle ${}^3\text{He}$ source across the family of inverse-model estimates were $(0.0 - 3.3)$, $(0.097 - 8.2)$, $(0.20 - 15.)$, and $(0.025 - 2.8)$ in units of $(\text{Mmol Fe yr}^{-1}) (\text{mol } {}^3\text{He yr}^{-1})^{-1}$, for the Atlantic, Pacific, Indian, and Southern Ocean basins, respectively.)

While the total phosphorus export is well constrained and varies little across our family of solutions, the magnitude of the dFe-type-supported export production varies systematically with the relative source strength of each iron type. To quantify these systematic variations, Figure 2.11 plots the fraction $\langle \Phi_k^P \rangle / \langle \Phi^P \rangle$ of the globally averaged iron-type- k -supported export to the total global export as a function of the corresponding fractional global iron source strengths $\sigma_k / \sigma_{\text{tot}}$, where $\sigma_{\text{tot}} \equiv \sum_k \sigma_k$. Note that if a given source strength σ_k constitutes 100 % of the total, then it must support 100 % of the export and that if $\sigma_k = 0$ then it supports 0 % of the export.

Figure 2.11 shows a number of interesting systematic features of our family of solutions. First, the aeolian dFe supports $\sim 20 - 100$ % of the global export, with the low end of the range corresponding to an aeolian source of only ~ 5 % of the total source (we did not explore lower fractional aeolian sources). Sedimentary iron supports $\sim 0 - 80$ % of the global export, with the high end of the range corresponding to a sediment source as high as ~ 90 % of the total source. Hydrothermal iron supports the least export ranging from $\sim 0 - 18$ % for fractional hydrothermal sources as large as ~ 45 % of the total source.

A key point of Figure 2.11 is that aeolian iron may be considered to be the most important type of iron for supporting export production: For a given fraction of the total source, the fraction of export supported by aeolian iron is larger (i.e., the aeolian points all lie above the 1:1 line). For the fractional aeolian sources between ~ 20 and ~ 50 %, the corresponding export fraction is as much as ~ 30 % greater than the fractional source. As the fractional aeolian source approaches 100 % from below or 0 % from above, it comes close to supporting an equal fraction of the export because the relation between fractional production and fractional source must pass through the points $(0\%, 0\%)$ and $(100\%, 100\%)$. The ability of aeolian iron to make disproportionately large contributions to supporting phosphate and carbon export is presumably due to fresh aeolian iron being directly injected into the euphotic zone. This view is supported by the fact that if we compute the fractional export only for the Southern Ocean, where the aeolian source is small and most aeolian iron is supplied as upwelled regenerated iron [Holzer *et al.*, 2016], the deviation of the fractional aeolian-iron-supported export from the 1:1 line is roughly halved.

Sedimentary and hydrothermal dFe make fractional contributions to the export that are less than their fractional sources (the sedimentary and hydrothermal points lie below the 1:1 line by as much as ~ 20 %). Over the range

of the fractional hydrothermal source, the hydrothermal-dFe-supported export fraction is roughly two thirds the corresponding sedimentary-dFe-supported export fraction. The lower efficiency of hydrothermal iron presumably reflects the fact that most large sedimentary sources are relatively shallow and can thus supply iron more readily to the euphotic zone compared to the deep hydrothermal sources. This is consistent with the fact that hydrothermal and sedimentary iron have roughly equal efficiency for the fractional exports computed for the Southern Ocean only (not shown).

2.7.3.2 Opal Export

The opal export supported by each dFe type can be calculated analogously, and the corresponding geographic patterns are shown in Figure 2.12. Similar to the total opal export (Figure 2.7b), the patterns of the opal export supported by each iron type emphasize regions with high diatom concentrations, namely the Southern Ocean and subpolar North Pacific and North Atlantic where there is also upwelling and/or vertical mixing. Aeolian-dFe-supported opal export (Fig. 2.12a) is large in the Southern Ocean, but most pronounced in the subpolar North Pacific, where both diatom production is significant and aeolian input is high downwind from Asia's deserts. While tropical opal export is of secondary importance, the tropics are most pronounced for aeolian-supported export, again because of the direct source there. The pattern of sedimentary-dFe-supported opal export (Fig. 2.12b) is broadly similar to that for aeolian dFe, but weaker in the tropics. The pattern of hydrothermal-dFe-supported opal export (Fig. 2.12c) is dominated by the Southern Ocean, where diatom production is high and where most hydrothermal iron upwells. The patterns of dFe-type-supported opal export have tightly clustered zonal means with a similar spread across the family as for the phosphorus export.

The amplitude of the opal-export patterns varies systematically with the iron source strength as summarized in Figure 2.13, which shows the fractional dFe-type-supported opal export as a function of the corresponding fractional dFe source. While aeolian dFe is still the most efficient iron type for supporting opal export, aeolian dFe is less efficient for opal export than for phosphorus export (the aeolian points fall closer to the 1:1 line by ~10 % fractional export). For a given fractional aeolian source strength between 20 % and 60 %, the supported fractional opal export is typically ~20 % larger, though there is significant scatter. Conversely, sedimentary iron is slightly more efficient in supporting opal export than in supporting phosphorus export, and hydrothermal dFe is only slightly less efficient than sedimentary dFe.

The lower per-source efficiency of aeolian iron for supporting opal export is consistent with the fact that opal export occurs primarily in the Southern

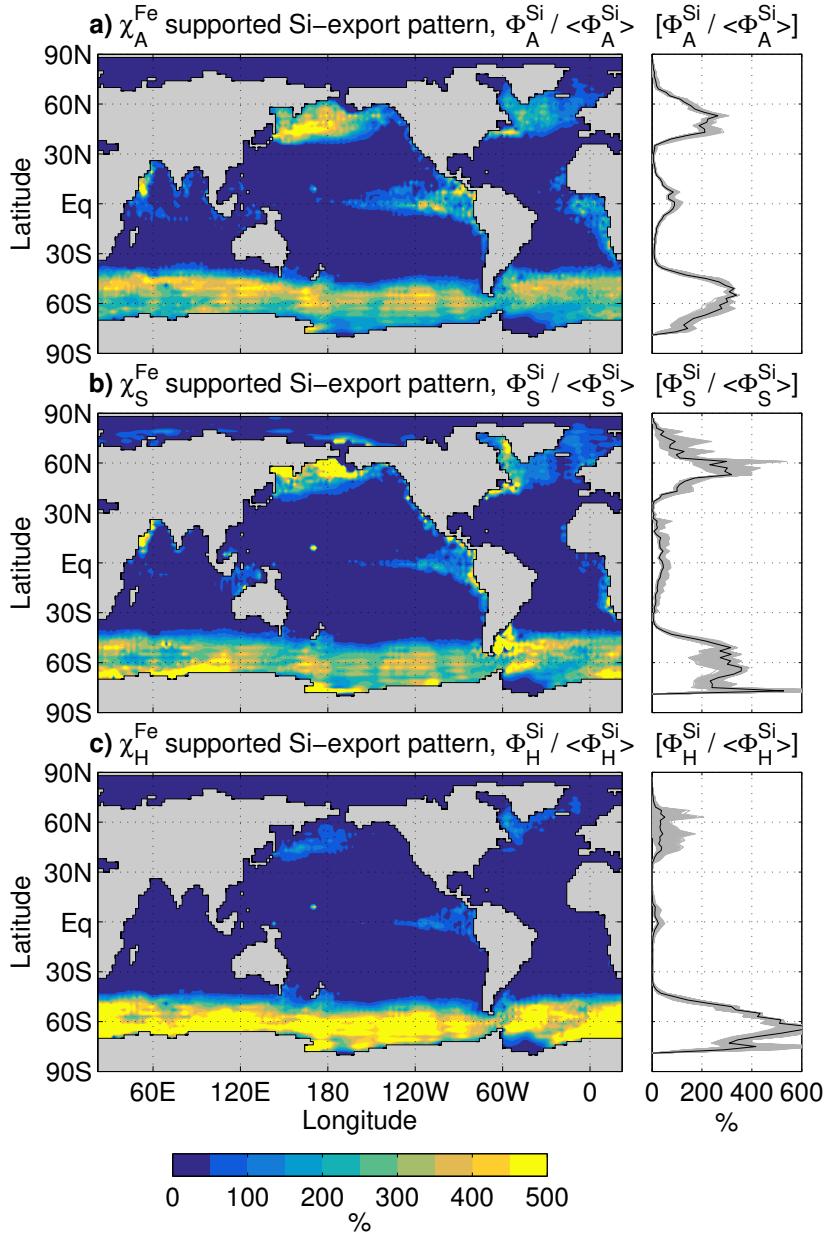


Figure 2.12: Opal export supported by each dFe type [aeolian (a), sedimentary (b), hydrothermal (c)] normalized by its global mean. The map is for our typical solution, while zonal averages of the normalized opal export are shown for each family member in grey, with the typical solution in black.

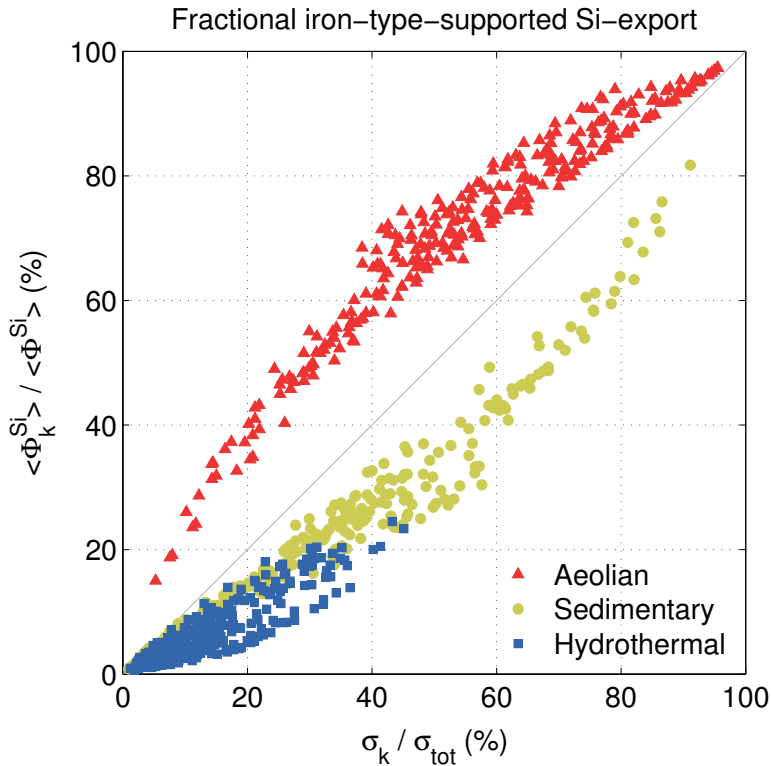


Figure 2.13: Percent global opal export supported by each iron type (aeolian, sedimentary, hydrothermal) versus the corresponding fractional source of that iron type.

Ocean, where direct aeolian input is small. Similarly, the greater per-source efficiency of sedimentary and hydrothermal iron is consistent with the bulk of the opal export occurring in the upwelling regions of the Southern Ocean where access to deep iron sources is greatest. This is supported by the fact that a plot of the fractional *phosphorus* export of the Southern Ocean only (not shown) versus the fractional iron sources is nearly identical to the plot of fractional *global* opal export of Figure 2.13.

2.8 Discussion and Caveats

Our approach has a number of limitations that must be kept in mind. Most importantly, inverse-model estimates are only as good as the data used to constrain them. The dFe observations are too sparse in space and time to construct a gridded annual mean climatology like those available for PO₄ and Si(OH)₄. We averaged the available dFe data to minimize observational biases, but in

many places observations are only available for one time of year and the observations likely contain seasonal biases. Other biases are likely introduced when dFe measurements are aliased by episodic source events such mineral dust downwind from the major deserts [e.g., *Croot et al.*, 2004; *Johnson et al.*, 2010]. In the near future, GEOTRACES will release an expanded data product that will include Pacific transects that were not available for the intermediate data product used here. The additional dFe observations will help constrain the hydrothermal sources, particularly the strength of the Pacific source relative to that of the other basins.

Important non-nutrient observational fields for our inverse model are the satellite measured photosynthetically active radiation (PAR) and ocean-color derived estimates of the size-partitioned phytoplankton concentrations. Small-scale features of the PAR field, e.g., in the Weddell Sea where ice and cloud cover play a role, are uncertain with the PAR for different time averages showing different features. The satellite-based estimates of phytoplankton concentrations also carry unquantified uncertainties due to a number of assumptions [*Kostadinov et al.*, 2016]. In our inverse model, these estimates provide crucial constraints on how carbon export is partitioned among the different functional classes. The unquantified uncertainties warrant re-evaluation as independent satellite-derived estimates become available in the future.

Most biogeochemical parameters are determined through objective optimization against available observations, but the construction of the cost function, and the choice of which parameters are optimized and which are prescribed, necessarily involves subjective choices. For example, choosing a different set of weights ($\omega_P, \omega_{Fe}, \omega_{Si}, \omega_{plk}$) to combine the four terms of the cost function would result in different optimal parameters. Similarly, assigning greater weight to dFe data measured as part of a vertical profile introduces another arbitrary weight. As for any nonlinear least-squares problem, it is also important to recognize that any minimum of the cost function found numerically is not guaranteed to be the global minimum and it is always possible that a better fit exists for a different set of parameters. Conversely, depending on the choice of initial state, the optimizer may find a local minimum that has grossly unrealistic features and must be rejected.

We addressed the uncertainty in our estimates that results from the nearly unconstrained strengths of the external iron sources. The uncertainty in key metrics (e.g., global carbon export) was quantified in terms of their spread across our family of solutions and in terms of systematic variations with the iron source strengths. While our efficient numerics allow us to easily determine the linear sensitivities of any metric with respect to all parameters (from which one can also estimate uncertainty), we did not do so here because the spread in the metric across the family is more relevant. Given the large set

of parameters x_j and several interesting metrics M_i , a detailed investigation of all the sensitivities $\partial M_i / \partial x_j$ evaluated at the optimal states is beyond the scope of this study. In principle, one can also estimate the uncertainty of the optimal parameters themselves using a Bayesian framework [e.g., Teng *et al.*, 2014]. However, this requires the construction of suitable covariances and is also beyond the scope of this study.

A key limitation of our approach is that seasonality is ignored and we use a steady circulation. This circulation is constructed so that its transport reproduces the annual-mean observed temperature, salinity, CFC, radiocarbon, and PO₄ fields with minimal error. The circulation is hence not a simple average, but an effective ventilation-weighted mean. However, we acknowledge that effects due to the seasonal covariance of biological production and circulation cannot be captured.

Our models of the nutrient cycles make a number of simplifying assumptions. We ignore external inputs of silicic acid, and consistent with our steady-state assumption we therefore also neglect permanent burial of opal in sediments. While this approximation has been shown to have negligible impact on particle fluxes [Sarmiento *et al.*, 2007], we acknowledge that our estimates will miss features such as, e.g., silicic-acid plumes due crustal fluid venting [Johnson *et al.*, 2006]. The uncertainty of the silicon cycle that is most difficult to quantify stems from our simple parameterization of opal dissolution, which does not account for partial frustule protection by decaying organic covering or the effect of digestion by zooplankton. Another key uncertainty lies in our model of the Si:P uptake ratio and its dependence on dFe. While our empirical formulation captures known dependencies qualitatively, a first-principles derivation based on cell biology is currently lacking. These remarks apply equally to the Fe:P uptake ratio.

Although our model of the iron cycle includes an explicit representation of the re-dissolution of scavenged iron, effects of subgrid topography, and dynamic coupling to the phosphorus and silicon cycles, and is thus much more complex and mechanistic than the iron model of Frants *et al.* [2016], it was still necessary to make a number of simplifying assumptions. Specifically, we do not model ligands dynamically, ignore colloidal iron [e.g., Fitzsimmons and Boyle, 2014], and do not represent some iron sources that may be locally important such as input from icebergs [Klunder *et al.*, 2011, 2014]. We also assume that PO₄ and dFe are remineralized with the same Martin curve and in the same ratio in which they were utilized. The recent work by Twining *et al.* [2014] suggests that sinking diatoms release phosphorus higher in the water column than iron, but we do not have sufficient information to model these effects. Given the large uncertainties in the external iron sources, the neglected details are likely of second order for estimating the large-scale dFe concentration.

Other uncertainties concern the phosphorus cycle itself, to which the uptake of the other elements is keyed. While our phosphate estimates have the smallest misfit with observations, our model of the phosphorus cycle makes several simplifying assumptions. The Martin exponent is assumed to be globally uniform although in reality it almost certainly varies spatially [Weber *et al.*, 2016], potentially leading to underestimated gradients in our model. To avoid carrying an additional tracer, we approximated DOP to have zero lifetime. In reality, DOP has a wide range of lifetimes, which for semi-labile DOP is typically assumed to be a fraction of a year [e.g., Primeau *et al.*, 2013]. However, the neglect of DOP is unlikely to seriously affect our estimates: By using a Martin exponent optimized for a restoring model without DOP, we were able to match PO_4 closely to the observations.

We emphasize that the carbon export reported here was merely a unit conversion of our estimates of phosphorus export. No effort was made to compute a more realistic carbon export such as could be achieved with an explicit representation of the carbon cycle (which would require additional tracers and was numerically too expensive) and the C:P export ratio was treated as globally uniform. While a globally uniform export ratio is acceptable for a unit conversion, the true C:P export ratio is now known to vary spatially [Teng *et al.*, 2014].

2.9 Summary and Conclusions

We have formulated a steady-state model of the coupled phosphorus, silicon, and iron cycles that is embedded in a steady data-assimilated global circulation. The model is of intermediate complexity and couples the nutrient cycles through co-limitations on biological uptake and through the scavenging of iron by organic particles. The concentrations of the small, large, and diatom phytoplankton functional classes is calculated diagnostically and not explicitly represented by a tracer variable. We explicitly represent iron scavenging by organic, opal, and mineral dust particles, and the redissolution of organically scavenged iron. Subgrid topography is parameterized for the sedimentary iron sources and intercepts all vertical fluxes. The relative simplicity of the biogeochemical model and the matrix formulation of the steady-state advective-diffusive transport afford highly efficient numerics. Steady-state solutions are readily found using a Newton solver, which permits the model to be used in inverse mode to constrain many of the biogeochemical parameters through objective optimization. The optimization minimizes the mismatch with observed nutrient concentrations and with satellite-derived estimates of phytoplankton concentrations.

Our optimized estimates of the macronutrient concentration fields closely match the observational climatology with volume-weighted RMS errors of 5 % for phosphate and 12 % for silicic acid relative to the global mean concentrations. The modelled dFe concentration has a larger cost-weighted RMS mismatch of $\sim 44\%$ of the global mean dFe concentration. However, the cost-weighted basin-averaged vertical dFe profiles for the Atlantic and Southern Ocean generally lie within the observational uncertainties. The Pacific dFe profiles show systematic biases, in part because the Pacific basin contains relatively few dFe observations in the currently available data sets. The estimated phytoplankton concentrations have generally weaker meridional gradients than observed possibly because of our use of a globally uniform Martin exponent. However, the fraction of the global plankton biomass represented by each functional class lies within at most $\sim 6\%$ of the fraction in the corresponding size class as estimated by *Kostadinov et al.* [2009] from ocean colour observations.

Given that even the order of magnitude of the iron sources is uncertain, we generated a family of solutions for a wide range of source strengths. Because our inverse-model estimates compensate for different source strengths by adjusting the scavenging parameters, each family member fits the available observations with roughly the same fidelity. This means that the available observed dFe and phytoplankton concentrations by themselves are insufficient to constrain the sources. This conclusion can also be gleaned from the model intercomparison of *Tagliabue et al.* [2016] and was reached using an inverse model by *Frants et al.* [2016], who also considered a family of solutions. However, while *Frants et al.* [2016] varied primarily the aeolian source, our family of solutions explores a range of sedimentary and hydrothermal source strengths in addition to a wide range of aeolian source strengths.

We partitioned the dFe concentration field into its aeolian, sedimentary, and hydrothermal components without perturbing the system using the approach of *Holzer et al.* [2016]. We find that the individual source components vary widely depending on the source strengths, but that the total dFe concentration, given by the sum of the source components, is well constrained. Variations in the aeolian component are compensated primarily by sedimentary dFe.

Nutrient limitation patterns were defined by jointly considering if the PO_4 , Si(OH)_4 , and dFe concentrations fell below their half-saturation values for uptake. Iron limitation was thus deemed to occur where only dFe fell below its half-saturation value, phosphate–iron co-limitation where both PO_4 and dFe fell below their half-saturation values, and so on. The resulting limitation patterns are robust across our family of solutions and broadly consistent with direct observations [*Moore et al.*, 2013a] and with alternately defined limitation patterns in the BEC model [*Moore et al.*, 2004]. The Large and Diatom func-

tional classes show iron limitation in the Southern Ocean, eastern tropical Pacific and subpolar North Pacific, with $\text{PO}_4\text{-dFe}$ (for diatoms $\text{PO}_4\text{-Si(OH)}_4\text{-dFe}$) co-limitations in the Pacific and South Atlantic subtropical gyres. The Indian Ocean, tropical Atlantic, and North Atlantic are largely iron replete (i.e., not limited in the sense defined) with PO_4 limitation (or $\text{PO}_4\text{-Si(OH)}_4$ co-limitation for diatoms).

The export productions of phosphorus and opal are well constrained across our family of solutions, both in terms of pattern and magnitude. Because of our representation of three functional classes with distinct, optimized uptake time scales, our carbon export of $9.5\text{--}11.$ Pg C yr $^{-1}$ is $\sim 30\text{--}45\%$ larger than that estimated by *Primeau et al.* [2013] and closer in spatial pattern to the empirical satellite-based estimates of *Dunne et al.* [2007]. The range of our opal export of $164\text{--}177$ Tmol Si yr $^{-1}$ overlaps with the estimate of *Holzer et al.* [2014], who used a simple restoring-type model of the silicon cycle (uncoupled to other nutrients).

We estimate that the fractions of carbon exported by the Small, Large, and Diatom functional classes are about $(6.4\pm 0.3)\%$, $(52\pm 2)\%$, and $(41\pm 3)\%$, respectively. These fractions were not well constrained by the nutrient and phytoplankton concentration data and required joint tuning of the parameters of the Si:P uptake ratio and of the uptake time scales so that the fractional uptake by each class approximately matched the satellite-based estimates of *Uitz et al.* [2010].

We examined the role of the iron cycle in shaping the carbon and opal export productions. We find that each source type of iron (aeolian, sedimentary, hydrothermal) supports phosphorus and opal export with a distinct geographic pattern that is robust across the family of solutions. The export pattern supported by a given iron type reflects the nature of its source. Sedimentary- and hydrothermal-dFe-supported carbon export is dominantly shaped by the large-scale patterns of upwelling that brings these iron types to the surface. Aeolian-dFe-supported export is shaped by both the pattern of direct aeolian input and by large-scale upwelling, which brings regenerated aeolian iron, as well as re-dissolved scavenged aeolian iron, back into the euphotic zone. For opal export, the signature of each iron type is qualitatively similar, but compared to carbon export, the opal export patterns tend to be weaker in the tropics and stronger at high latitudes, especially in the Southern Ocean where diatom concentrations and silicon trapping are strongest.

The amplitude of the export pattern supported by a given iron type varies systematically with the fractional global source of that iron type. These variations summarize and quantify the efficiency of each source for supporting export. Aeolian iron is most efficient in the sense that the percentage of the export it supports exceeds the percentage of the aeolian source by as much

as $\sim 30\%$ for carbon export and $\sim 20\%$ for opal export. Globally, sedimentary and hydrothermal iron are inefficient, supporting a fraction of export that is smaller than their fractional sources. For carbon export, hydrothermal iron is least efficient supporting about 1/3 less fractional export than sedimentary iron. When the effect of direct aeolian deposition is minimized by calculating the exports for the Southern Ocean only, the efficiency of a given iron type is similar regardless of whether carbon or opal export is considered. This reflects the similar oceanic transport paths of all iron types into the Southern Ocean euphotic zone, where the bulk of aeolian iron is supplied in regenerated form through upwelling.

Our optimized model is ideally suited to investigate the response of the global ocean ecosystem to a variety of perturbations. We will report on the model's response to perturbations in the iron supply in the next chapter, and detail more comprehensively the detailed workings of the iron cycle in a future publication.

Appendices

2.A Recycling Operators for Scavenged Iron

The recycling operator for POP-scavenged iron, $\mathcal{B}_s^{\text{POP}}$, comprises two parts: For dFe scavenged in the euphotic layer, i.e., above z_e , $\mathcal{B}_s^{\text{POP}}$ acts identically to \mathcal{B}^P . For dFe scavenged below z_e , we solve the flux equation of scavenged iron for continuous z . We assume that iron scavenged by POP below the mixed layer continuously sinks and can be recycled in the same grid cell in which it was scavenged. (We assume that the mixed layer coincides with the euphotic zone.) As shown by *Kriest and Oschlies* [2008], the Martin curve can be simply modeled with a sinking speed linearly increasing with depth, an approach we follow here. The equation for the flux or iron, $\phi_{\text{Fe}}^{\text{POP}}$, that was scavenged by POP below the mixed layer is thus

$$\frac{\partial \phi_{\text{Fe}}^{\text{POP}}}{\partial z} + \frac{b}{z} \phi_{\text{Fe}}^{\text{POP}} = -f^{\text{POP}} J_{\text{POP}} , \quad (2.31)$$

where b is the Martin exponent of the POP flux, and with the condition that $\phi_{\text{Fe}}^{\text{POP}} = 0$ for $z > z_e$ because here we only consider dFe scavenged below z_e . The solution is given by

$$\phi_{\text{Fe}}^{\text{POP}}(z) = - \int_z^{z_e} \left(\frac{z}{z'} \right)^{-b} f^{\text{POP}} J_{\text{POP}}(z') dz' . \quad (2.32)$$

And the rate per unit volume at which POP-scavenged dFe is recycled is thus given by

$$\mathcal{B}_s^{\text{POP}} f^{\text{POP}} J_{\text{POP}} = \mathcal{B}^P f^{\text{POP}} J_{\text{POP}} + \frac{b}{z} \phi_{\text{Fe}}^{\text{POP}} , \quad (2.33)$$

where the first term is for iron that was scavenged in the euphotic zone, and the second term for iron that was scavenged in the interior.

Similarly, the recycling operator for opal-scavenged iron, $\mathcal{B}_s^{\text{bSi}}$, has a euphotic part identical to \mathcal{B}^{Si} , and an aphotic interior part. In the interior, we solve the continuous equation for the flux of iron, $\phi_{\text{Fe}}^{\text{bSi}}$, that was scavenged by

opal below the mixed layer. The flux obeys

$$\frac{\partial \phi_{\text{Fe}}^{\text{bSi}}}{\partial z} + \frac{\kappa_{\text{Si}}^{\max}}{w_{\text{Si}}} e^{-T_E/T(z)} \phi_{\text{Fe}}^{\text{bSi}} = -f^{\text{bSi}} J_{\text{bSi}} , \quad (2.34)$$

with the condition that $\phi_{\text{Fe}}^{\text{bSi}} = 0$ for $z > z_e$. The solution is of the form

$$\phi_{\text{Fe}}^{\text{bSi}}(z) = - \int_z^{z_e} Q(z, z') f^{\text{bSi}} J_{\text{bSi}}(z') dz' , \quad (2.35)$$

so that the flux of opal-scavenged iron at z integrates all the scavenging of dFe by opal that occurs above z (and below z_e) and that is not recycled before reaching z . This is accomplished by $Q(z, z')$, given by

$$Q(z, z') = \exp \left(- \int_z^{z'} \frac{\kappa_{\text{Si}}^{\max}}{w_{\text{Si}}} e^{-T_E/T(z'')} dz'' \right) , \quad (2.36)$$

which removes all the recycling that occurs between the current depth z and the depth of scavenging z' . The rate per unit volume at which opal-scavenged dFe is recycled is thus given by

$$\mathcal{B}_s^{\text{bSi}} f^{\text{bSi}} J_{\text{bSi}} = \mathcal{B}^P f^{\text{bSi}} J_{\text{bSi}} + \frac{\kappa_{\text{Si}}^{\max}}{w_{\text{Si}}} e^{-T_E/T(z)} \phi_{\text{Fe}}^{\text{bSi}} , \quad (2.37)$$

where the first term is for iron that was scavenged in the euphotic zone, and the second term for iron that was scavenged in the aphotic interior.

2.B Biogenic Transport Operators with Subgrid Topography

We follow *Moore and Braucher* [2008] to include the effects of the more realistic, high-resolution topographic data from the *National Geophysical Data Center* [2006]. The subgrid topography parameterization must be reflected in the redistribution operators. Here we explain how this is done, based on the biogenic redistribution operators \mathcal{B}^P and \mathcal{B}^{Si} , which link biological production in the euphotic zone to the remineralization or redissolution in the aphotic zone. The operators \mathcal{B}^P and \mathcal{B}^{Si} are related to the divergence of the aphotic particle fluxes through [*Primeau et al.*, 2013; *Holzer et al.*, 2014] :

$$\mathcal{B}^P f_c U_c = \frac{\partial}{\partial z} [\Theta(z - z_b) \phi_{\text{POP}}(z)] , \quad (2.38)$$

and

$$\mathcal{B}^{\text{Si}} f_{\text{dia}} U_{\text{dia}} = \frac{\partial}{\partial z} [\Theta(z - z_b) \phi_{\text{bSi}}(z)] , \quad (2.39)$$

where z_e and z_b are the height coordinates at the base of the euphotic zone, and at the ocean bottom, respectively. The Heaviside function, $\Theta(z - z_b)$, ensures that the fraction of POP that reaches z_b is redissolved and remineralized there.

The subgrid topography parameterization is implemented by applying equations (2.38)–(2.39) to the high-resolution topography. In practice, for each model grid cell, we calculate the fraction of the flux that should remineralize where it hits the topography. Note, to ensure that \mathcal{B}^P and \mathcal{B}^{Si} are conservative, special care is required where subgrid topography is present within euphotic grid cells. In this case, a corresponding fraction of sinking particles must remineralize in that cell. We similarly implemented the same subgrid topography parameterization to the scavenging redistribution operators, \mathcal{B}_s^{POP} and \mathcal{B}_s^{bSi} .

2.C Weights for Dissolved Iron Mismatch

We use the dFe observations of both the global data set compiled by *Tagliabue et al.* [2012] (TFE) and the GEOTRACES Intermediate Data Product v3 [*Mawji et al.*, 2015]. We combine both data sets and remove dFe observations above 2.71 nM which probably correspond to transient states with short timescales that cannot be captured by our steady state model. In order to compensate the fact that most dFe observations are close to the surface, we give more weight to observations that are part of a “profile”. (A dFe observation is deemed to belong to a “profile” if there are 10 or more observations at the same latitude and longitude, and if one of those was recorded deeper than 2000 m.) Because the dFe observations do not sample the seasonal cycle uniformly, we adopt an approach similar to *Frants et al.* [2016] to reduce potential sampling bias when we interpolate the data to our model grid: If multiple dFe observations lie in the same grid cell, we first take the seasonal averages, which we then averaged again to estimate the annual mean.

As in equations (2.23) for PO_4 and $Si(OH)_4$, we use volume weights to evaluate the dFe concentration mismatch with observations. However, because not all model grid cells contain dFe observations, we define a dFe-specific vector of grid-box volumes, \mathbf{v}_{Fe}^{all} , which has nonzero elements only for grid boxes that contain at least one dFe observation. We also define a dFe “profile-specific” vector, \mathbf{v}_{Fe}^{pro} , which is nonzero only for grid boxes that contain “profile” observations. The corresponding weights are defined by

$$\mathbf{w}_{Fe}^{all} = \frac{\mathbf{v}_{Fe}^{all}}{(\bar{\chi}_{Fe}^{obs})^2 V_{Fe}^{all}} \quad \text{and} \quad \mathbf{w}_{Fe}^{pro} = \frac{\mathbf{v}_{Fe}^{pro}}{(\bar{\chi}_{Fe}^{obs})^2 V_{Fe}^{pro}} , \quad (2.40)$$

where $V_{\text{Fe}}^{\text{all}}$ is the total volume of grid cells which contain a dFe observation, and $V_{\text{Fe}}^{\text{pro}}$ the total volume of grid cells containing “profile” observations. We define the total dFe weight vector, \mathbf{w}_{Fe} , for the mismatch with observations in equation (2.24), by

$$\mathbf{w}_{\text{Fe}} = \frac{1}{5}\mathbf{w}_{\text{Fe}}^{\text{all}} + \frac{4}{5}\mathbf{w}_{\text{Fe}}^{\text{pro}} , \quad (2.41)$$

where we give extra weight to the “profile” observations. The 1:4 ratio was manually adjusted until “profile” observations were deemed to have sufficiently strong influence on the solutions. We also tried different approaches to weight the model-observation dFe mismatch, including the use of inverse variances [Frants *et al.*, 2016], but we found no significant difference in our results.

2.D Optimization Strategy Details

2.D.1 Prescribed Parameters

The following considerations determined which parameters were not optimized and how their values were chosen. The ligand stability constant K_L , which sets the fraction of free iron, was fixed at the value used by Frants *et al.* [2016], which is the low-irradiance value in the work of Galbraith *et al.* [2010]. The precise value chosen for K_L is not important here because K_L compensates directly with the optimized parameters associated with ligands and scavenging as also noted by Frants *et al.* [2016]. The recyclable fractions of POP and opal scavenging, f^{POP} and f^{bSi} , compensate with the maximum Fe:P uptake ratio, $R_0^{\text{Fe:P}}$, and thus were prescribed at 90 % [Moore and Braucher, 2008]. (This compensation results from the biological iron pump having almost the same effect as the combination of scavenging and recycling iron.) Similarly, the detrital fractions, f_c^0 , which set the particle export ratio, are directly compensated by all the other parameters in the uptake formulation. We therefore followed Dunne *et al.* [2005] and assigned their “small” detrital fraction to f_{sml}^0 and their “large” detrital fraction to both f_{lrg}^0 and f_{dia}^0 . When trying to optimize the silicon half-saturation rate $k_{\text{dia}}^{\text{Si}}$, starting from a value of 1 mmol m⁻³ [e.g., Matsumoto *et al.*, 2013], we found that the optimal value always remained within a few percent of this initial value. This is in part due to the fact that in regions of high diatom concentration the Monod term for silicic acid is near saturation so that there is little sensitivity to the precise value of $k_{\text{dia}}^{\text{Si}}$. Moreover, there appears to be consistency across the literature that $k_{\text{dia}}^{\text{Si}} = 1 \text{ mmol m}^{-3}$. We therefore simply fixed $k_{\text{dia}}^{\text{Si}}$ at this value for numerical efficiency.

2.D.2 Choice of Initial Parameter Values

We first chose an initial set of values for the remaining parameters as collected in Table 2.2. The parameters of the iron cycle were taken from of the typical solution of *Frants et al.* [2016] except for the half-saturation constant of the Fe:P ratio, which was taken from the work of *Galbraith et al.* [2010], and the scavenging-rate parameters. The initial parameters for POP and opal scavenging, $\kappa_{\text{scv}}^{\text{POP}}$ and $\kappa_{\text{scv}}^{\text{BSI}}$, were determined so that the globally integrated scavenging of each process was initially $\sim 5 \text{ Gmol Fe yr}^{-1}$ (the typical total source/sink strength reported by *Frants et al.* [2016]). The initial value of the dust scavenging rate parameter, $\kappa_{\text{dst}}^{\text{POP}}$, was chosen so that the sink due to dust scavenging was $\sim 10\%$ of the total sink of the initial state.

The initial irradiance half-saturation constants were taken from the work of *Doney et al.* [2006]. The initial uptake half-saturation constants k_c^i were taken from the work of *Matsumoto et al.* [2013]. The uptake time scales τ_c were set to an initial value of 6 days and optimized subject to the constraint $\tau_{\text{sml}} \geq \tau_{\text{lrg}} \geq \tau_{\text{dia}}$. The initial values of the maximum phytoplankton concentrations were calculated as $p_c^{\max} = p^*/(\lambda_0 \tau_c)$ using $p^* = 0.018 \text{ mmol P m}^{-3}$ [*Galbraith et al.*, 2010] and $\lambda_0^{-1} = 5.26 \text{ d}$ [*Dunne et al.*, 2005].

The initial values of the parameters of the Si:P ratio were set so that $k_{\text{Si:P}}^{\text{Fe}}$ and $k_{\text{Si:P}}^{\text{Si}}$ where on the order of typical dFe and Si(OH)₄ concentrations, while R_0^{Si} and R_m^{Si} were based on corresponding Si:N uptake ratios found in the literature and converted using N:P = 16:1. Thus, in terms of Si:N units, R_0^{Si} was chosen to be on the order of the minimum Si:N uptake ratio used by *Matsumoto et al.* [2013] and R_m^{Si} was chosen to be on the order of the maximum Si:N uptake ratio reported by *Franck et al.* [2000] and *Brzezinski et al.* [2002].

2.D.3 Sequential Optimization Steps

- (a) We first optimized the hydrothermal iron source parameters $\sigma_{\text{H,ATL}}$, $\sigma_{\text{H,PAC}}$, $\sigma_{\text{H,IND}}$, and $\sigma_{\text{H,SO}}$ forcing $\sigma_{\text{H,IND}} = \sigma_{\text{H,SO}}$. Although we adjusted the overall source strength of the hydrothermal iron source when generating our family of iron cycling estimates, we did not re-optimize the relative strength of the 4 basin amplitudes until the final step of our strategy.
- (b) We jointly optimize the three irradiance half-saturations k_c^I and then keep these fixed because of potential compensation with the half-saturation constants k_c^i .
- (c) We jointly optimized the half-saturations k_c^i of the nutrient-limitation Monod terms.

(d) We were not able to optimize the Si:P uptake ratio parameters, because they are not well constrained due to compensation with the parameters that set the uptake by diatoms. We therefore separately tuned the parameters R_m^{Si} , R_0^{Si} , $k_{\text{Si:P}}^{\text{Si}}$, and $k_{\text{Si:P}}^{\text{Fe}}$ together with the three growth time scales τ_c to match the fractions of total uptake by each phytoplankton class as estimated by *Uitz et al.* [2010].

(e) Because of compensation with the maximum Fe:P uptake ratio, the associated half-saturation rate, $k_{\text{Fe:P}}$, was optimized on its own.

(f) We then jointly re-optimized the 13 parameters k_c^{P} , k_c^{Fe} , $k_{\text{dia}}^{\text{Si}}$, p_c^{\max} , and τ_c .

(g) Only the parameters of the iron cycle remain to be optimized. Because of a significant degree of in situ compensation between effective iron sources and sinks, source and sink parameters cannot be optimized jointly [*Frants et al.*, 2016]. To generate our family of estimates, we therefore first assigned the aeolian, sedimentary, and hydrothermal source-strength parameters (keeping the same ratio of basin hydrothermal source strengths to global hydrothermal source strength), and held these fixed while jointly optimizing the parameters determining the iron scavenging, namely $R_0^{\text{Fe:P}}$, $\kappa_{\text{scv}}^{\text{POP}}$, $\kappa_{\text{scv}}^{\text{bSi}}$, $\kappa_{\text{scv}}^{\text{dst}}$, L_v , L_{\max} , L_b , and τ_b .

(h) As a final step, we jointly optimized all source-strength parameters σ_A , σ_S , $\sigma_{H,\text{ATL}}$, $\sigma_{H,\text{PAC}}$, $\sigma_{H,\text{IND}}$, and $\sigma_{H,\text{SO}}$ primarily to give the hydrothermal source pattern (relative strength in each basin) a chance to adjust from its initial state. We find that if the total hydrothermal source strength, σ_H , is below 1 Gmol yr^{-1} , the final optimization step hardly changes σ_H , while larger hydrothermal source strengths tend to be reduced by up to $\sim 0.5 \text{ Gmol yr}^{-1}$.

If $\sigma_H < 0.5 \text{ Gmol yr}^{-1}$, the fractional hydrothermal source strength of each basin tends to remain unchanged during this last step, while if $\sigma_H \geq 0.5 \text{ Gmol yr}^{-1}$, the fractional hydrothermal sources for the Pacific and Southern Ocean tend to increase by order 10 %, the fractional Indian Ocean source tends to decrease order 5 %, and the Atlantic source is typically reduced by order 10 % and for some solutions to near zero. The aeolian iron source strength, σ_A , tends to be reduced by $\sim 10 \%$, while the sedimentary iron source strength, σ_S , stays within 10 % of its previous value for most family members but can more than double for cases with high hydrothermal and aeolian sources.

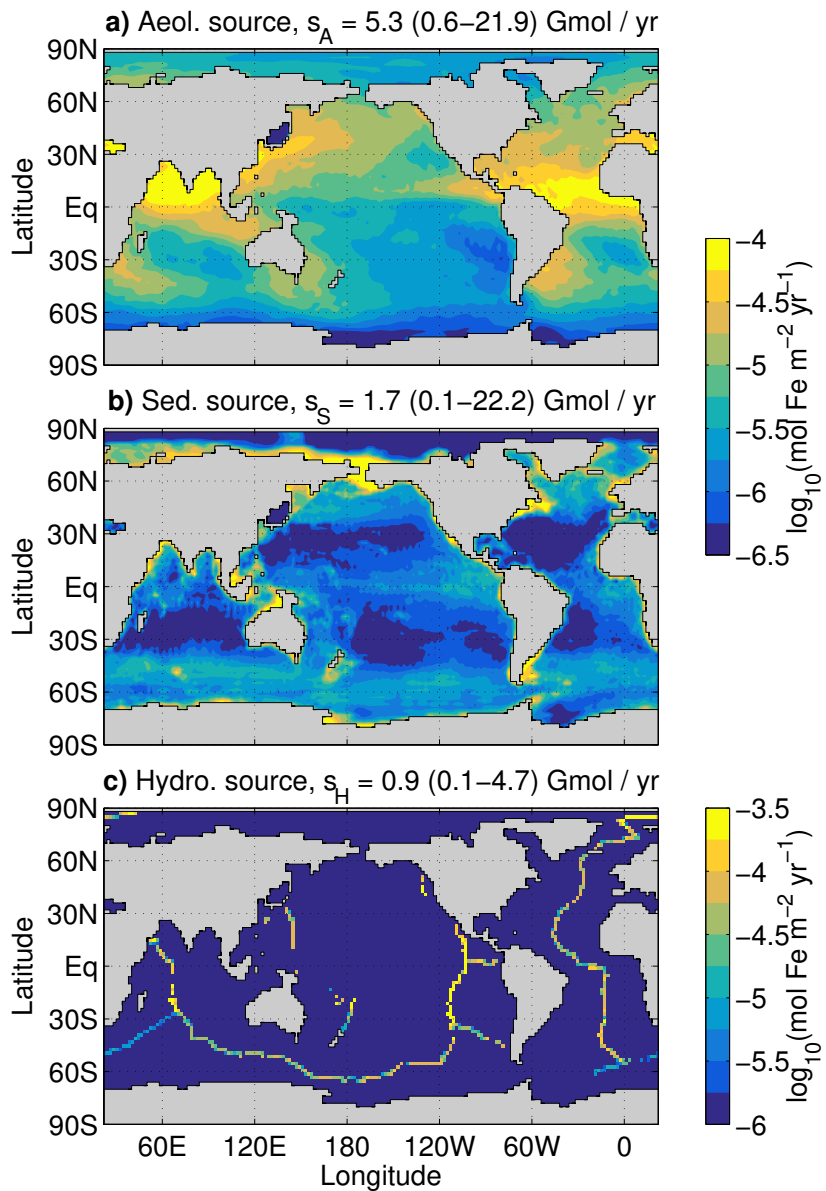


Figure 2.14: Vertically integrated sources of aeolian dFe (top, a), sedimentary dFe (middle, b), and hydrothermal dFe (bottom, c) for our typical solution. Note the logarithmic colour scales.

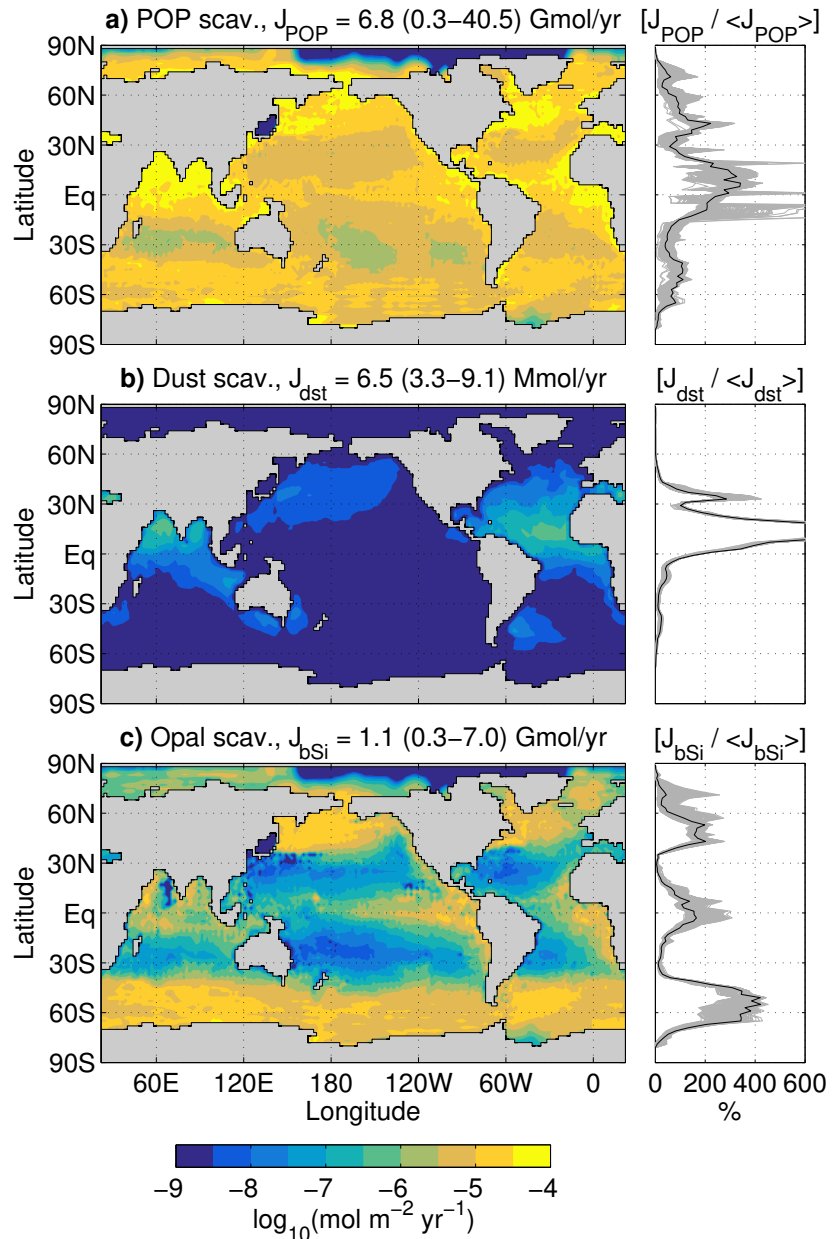


Figure 2.15: Maps of the vertically integrated iron sinks of our typical solution due to (a) POP, (b) mineral dust, and (c) sinking opal particles. Plotted to the right are the zonal averages of the vertically integrated sinks normalized by their global mean, with each family member in grey and our typical solution in black.

2.E Iron Source and Sink Patterns

Figure 2.14 shows the vertically integrated sources of dFe with a logarithmic colour scale. The aeolian soluble iron deposition pattern is identical to that of the study of *Luo et al.* [2008], albeit limited to the oceans. The tropical Atlantic close to the Sahara, the Arabian Sea, and the Bay of Bengal are the regions largest aeolian iron deposition. The hydrothermal iron sources follow the mid-ocean ridges with the pattern of the OCMIP protocol, but independently scaled for the Atlantic, Pacific, Indian, and Southern Ocean basins. Sedimentary iron is more intense where export production is large and in areas where oceans are shallower, because in both cases, a large flux of organic matter (or POP in our model) reaches the sediment. The sub-grid topography plays a significant role in the pattern of sedimentary iron, in particular for coastal regions and large underwater plateaus, e.g., near the Kerguelen islands or the Falkland islands. Because of unrealistic circulation features in the Sea of Japan, we zero all sources there consistent with our zeroing out production in the Sea of Japan.

Figure 2.15 shows the vertically integrated sinks that balance the sources of Figure 2.14. The scavenging due to sinking mineral dust particles is about 3 orders of magnitude smaller than the sink due to organic and opal particle scavenging and could be neglected without changing our estimates appreciably. Although the pattern of the scavenging sinks has significant local variations among the members of our family of solutions, the zonally averaged pattern (vertically integrated sink normalized by its global mean) is broadly similar across the family.

Chapter 3

Iron control on the global ocean phosphorus and silicon cycles: data-constrained estimates

Give me a half tanker of iron, and I will give you an ice age.

John Martin, in Lecture (1988) [Weier, 2001]

3.1 Introduction

Because dissolved iron (dFe) is a key limiting micronutrient [e.g., *Gran et al.*, 1931; *Hart*, 1934; *Martin and Fitzwater*, 1988; *de Baar et al.*, 1995; *Lundry et al.*, 1997], changes in the external source of iron to the ocean have the potential to change the global nutrient cycles and the efficiency of the biological carbon and silicon pumps. This has been recognized by a number of investigators [e.g., *Martin*, 1990; *Boyd et al.*, 2007; *Boyd and Ellwood*, 2010]. Several considered artificially increasing the ocean's iron supply as a geoengineering effort to mitigate climate change [e.g., *Zeebe and Archer*, 2005; *Aumont and Bopp*, 2006; *Hauck et al.*, 2016], while others were motivated by trying to understand changes in the ocean's biogeochemical cycles in response to large changes in atmospheric dust loading since the last glacial maximum [e.g., *Dutkiewicz et al.*, 2005; *Nickelsen and Oschlies*, 2015].

In a suite of global idealized aeolian iron input perturbation experiments, *Dutkiewicz et al.* [2005] found that a stronger aeolian input increased biological productivity of high-nutrient low-chlorophyll (HNLC) regions while decreasing productivity in the subtropical gyres. *Dutkiewicz et al.* [2005] suggested that increased particle export into upwelling waters, that bring remineralized nutrients back to the surface, trap nutrients. This in turn reduces their lateral transport into oligotrophic regions where production drops as a result.

Aumont and Bopp [2006] ran a set of global iron source perturbations by forcing the mixed layer dFe concentrations to 2 nM (about 10 times larger than the mean surface concentration) for 100 years. This increased production in HNLC regions “at the expense of increasing the severity and the spatial extent of the oligotrophic regions”, similar to the findings of *Dutkiewicz et al.* [2005]. We note that their experimental design to simulate iron enrichment used an annual dFe input of $\sim 100 \text{ Gmol yr}^{-1}$, that is, ~ 20 times the amount of iron that is supplied to the ocean by dust deposition in the current climate according to *Luo et al.* [2008]. *Aumont and Bopp* [2006] concluded that silicic-acid limitation should be taken into account for its role in HNLC regions, and that fertilizing the ocean outside the Southern Ocean was largely inefficient.

Hauck et al. [2016] ran similar fertilization experiments (a 10- to 100-year perturbation) by injecting olivine, $(\text{Mg}, \text{Fe})_2\text{SiO}_4$, which provides dFe but also Si(OH)_4 and alkalinity. They found that the response saturates when the iron input reaches $\sim 50 \text{ Gmol yr}^{-1}$. *Zeebe and Archer* [2005] calculated that an additional $\sim 25\text{--}250 \text{ Gmol yr}^{-1}$ of dFe is required to significantly increase carbon export and draw down $p\text{CO}_2$, and concluded that iron geoengineering efforts to fertilize HNLC regions are not feasible technologically.

Martin [1990] suggested that perturbations in the iron cycle played a crucial role in past climate fluctuations. *Albani et al.* [2016] estimated the soluble iron

input to the oceans since the Last Glacial Maximum (LGM) by reconstructing the global dust cycle in paleoclimates and using different approximations for atmospheric dust processing and sensitivity to aerosol abundance. They found that the LGM aeolian source fell in the $\sim 3.6\text{--}14.9 \text{ Gmol yr}^{-1}$ range, while the preindustrial aeolian source lies within $\sim 1.5\text{--}7.1 \text{ Gmol yr}^{-1}$.

Here we use the data-constrained inverse model of Chapter 2 to investigate the effect of aeolian iron perturbations on the global phosphorus and silicon cycles. Our study is guided by the following questions about the response to aeolian iron source perturbations:

1. How do the export productions of carbon and opal change and what are the underlying mechanisms?
2. How do the distributions and inventories of preformed and regenerated macronutrients change and what are the consequences for the biological carbon and silicon pump efficiencies?
3. What role does Southern Ocean nutrient trapping play?
4. What are the iron pathways that mediate the teleconnections identified in the response to regional aeolian source perturbations?

These questions follow studies that explored and quantified in detail the biological pump efficiency, its pathways and timescales, using the same circulation: The fraction of the regenerated nutrient inventory, is a natural metric to explore the efficiency of the biological pump [e.g., *Ito and Follows*, 2005]. *Primeau et al.* [2013] used a simple phosphorus cycle model to quantify the response of the biological pump efficiency to changes in nutrient utilization in the Southern Ocean. *Holzer and Primeau* [2013] used the same model to quantify the pathways and timescales that connect Southern Ocean biological production to subtropical and North Atlantic biological production, and how these respond to production changes in the Southern Ocean. In Chapter 1, we extended these studies by systematically quantifying the global distribution of the pathways and timescales of the combined physical/biogenic phosphorus transport in the ocean. *Holzer and Primeau* [2013] used an optimized restoring-type model of the silicon cycle to quantify the efficiency of the silicon pump, its pathways and timescales, and quantified the extent of silicon trapping in the Southern Ocean. We note that all these studies used biogeochemical models embedded in the same data-assimilated ocean circulation [*Primeau et al.*, 2013].

The Southern Ocean (SO) plays a particular role for the phosphorus and silicon cycles in the ocean: Biological production exports organic matter as sinking particles, a fraction of which remineralizes into upwelling circumpolar

water masses that return to the Southern Ocean surface. This mechanism was explored in detail for PO₄ by Primeau *et al.* [2013] who found that complete biological utilization in the Southern Ocean causes production to decrease by 44 % north of 40°S and to increase by more than 725 % in the Southern Ocean. Diatoms take up silicic acid in the euphotic zone and produce opal, which is dissolved deeper than phosphorus remineralizes. Thus in the current ocean, silicic acid is strongly trapped in the Southern Ocean. Holzer *et al.* [2014] quantified the Southern Ocean trapping efficiency of silicic acid and found that almost half of the Si(OH)₄ global inventory is in SO→SO transit between successive biological utilizations.

Perturbations of the iron input are also relevant for the silicic acid leakage hypothesis [Matsumoto *et al.*, 2002; Brzezinski *et al.*, 2002] which posits that during the LGM, Si(OH)₄ was untrapped from the iron-fertilized Southern Ocean and carried to lower latitudes by SAMW. While higher dFe concentrations enhance biological production in the Southern Ocean, they also lower diatom Si:N ratios [e.g., Takeda, 1998; Hutchins and Bruland, 1998; Franck *et al.*, 2000], which reduces opal export together with silicon trapping in the Southern Ocean [e.g., Matsumoto *et al.*, 2002; Brzezinski *et al.*, 2002; Beucher *et al.*, 2007]. Changes of Southern Ocean silicon trapping are thus conditional on the assumptions that go into the definition of the Si:P uptake ratio formulation of Chapter 2.

The ocean's response to perturbations in the aeolian source is complex, but the major mechanisms begin and end with pathways from and to the Southern Ocean, because it is the nexus for the biological pump pathways (Chapter 1) and has the potential to trap or release macronutrients.

3.2 Design of Iron Source Perturbations

3.2.1 Choice of Unperturbed States

The response of the nutrient cycles to perturbations in the aeolian source likely depends on the unperturbed strengths of the iron sources. For example, reducing the aeolian source of an iron-cycle state in which the unperturbed aeolian source is already small relative to the sedimentary and hydrothermal sources is likely to have modest consequences. Conversely, for an iron-cycle state in which the aeolian deposition is the dominant source [e.g., such as in Dutkiewicz *et al.*, 2005, who modelled only aeolian iron], perturbations of the aeolian source are likely to have a large impact.

There is no consensus in the literature on the strengths of the aeolian, sedimentary, and hydrothermal sources in the real ocean. The source strengths in current biogeochemical models that explicitly represent dFe span two or-

ders of magnitude [e.g., Tagliabue *et al.*, 2016]. In Chapter 2, we varied each source strength by roughly two orders of magnitude to produce a family of solutions, all of which are consistent with observations, demonstrating that the iron sources are not well constrained by the currently available dFe observations. (The ranges of iron sources of the family of solutions also helped to better understand how the dFe cycle works.) Thus investigating the control of the aeolian iron source on global biogeochemical cycles requires to take the sensitivity of perturbations to the initial model-estimate choice into consideration.

Estimate name	$\sigma_{A,0}$	$\sigma_{S,0}$	$\sigma_{H,0}$	$\sigma_{A,0} / \sum_k \sigma_{k,0}$
Typical	5.3	1.7	0.9	67 %
High aeolian	15.0	0.5	0.9	92 %
Low aeolian	1.8	6.2	0.9	20 %

Table 3.1: Unperturbed aeolian, sedimentary, and hydrothermal source strengths of the typical, high-aeolian-source, and low-aeolian-source estimates, in Gmol yr^{-1} chosen for the aeolian source perturbation experiments. (The fractional aeolian source is shown in the last column for convenience.)

To probe sensitivity to initial state, we select three members of the family of data-constrained estimates of Chapter 2 that have different fractional aeolian iron source strengths: A typical estimate, a high-aeolian-source estimate, and a low-aeolian-source estimate. The typical estimate of Chapter 2 is chosen as the typical state. The high-aeolian estimate is chosen to have an aeolian source about three times larger, a sedimentary source three times smaller, and the same hydrothermal source. Conversely, the low-aeolian estimate is chosen to have an aeolian source about three times smaller and a sedimentary source three times larger. The globally integrated aeolian, sedimentary, and hydrothermal iron sources of the typical, high-aeolian, and low-aeolian unperturbed states, along with the corresponding fractional aeolian source, are collected in Table 3.1.

3.2.2 Choice of Perturbations

The aeolian iron source perturbations that might occur in the future or that have occurred in the earth's past have complicated spatial and temporal patterns that depend on climate variables such as vegetation cover, wind patterns, and radiative and chemical processing of dust before it is deposited on the ocean either as dry dust or with precipitation. A detailed consideration of all these processes is beyond the scope of this study. However, the detailed modelling

of realistic perturbations in the aeolian iron source is not our goal here. Instead, we consider idealized perturbations of the aeolian iron source, chosen to highlight key features of the ocean’s global nutrient cycles and its limiting responses to large perturbations.

In the absence of information on the pattern of atmospheric dust perturbations, the simplest pattern to consider is globally uniform (GBL). This approach was also taken by *Dutkiewicz et al.* [2005]. Regional perturbations are also of interest, particularly those that increase or decrease the iron supply to iron limited regions. We therefore also consider spatially uniform perturbations to the Southern Ocean south of 38°S (the SO region), which is well known to be iron limited (see Figure 2.6, Chapter 2) and which controls global productivity through the “leakage” of preformed nutrients in mode and intermediate waters and the trapping of regenerated nutrients [*Sarmiento et al.*, 2004; *Marinov et al.*, 2006; *Primeau et al.*, 2013; *Holzer and Primeau*, 2013]. Other key iron-limited regions are located in the tropics which generally are upwelling regions with high nutrient supply. We therefore also perturb the aeolian iron source over the tropics between 18°S and 18°N (the TRP region). We chose 18° of latitude as an approximate boundary between tropical upwelling and downwelling subtropical gyres, as in the work by *DeVries et al.* [2017] who use a similar data-assimilated circulation. We thus consider perturbations of three regions: GBL, SO, and TRP.

We are interested in both reduced and increased aeolian input over the perturbation region. A reduction can be simply accomplished by scaling the aeolian source over the region by a spatially uniform factor α , where $\alpha = 0$ switches off the aeolian source of the region entirely. A multiplicative scaling for source increases is not desirable, however, because the unperturbed source pattern (Figure 2.14, Chapter 2) is heavily loaded into the tropics, with very low values at high latitudes and over many mid-latitude regions. For example, multiplying the aeolian source in the TRP region by 100 would be a huge increase in the tropical source, and thus very similar to multiplying the aeolian source by 100 globally because of the small sources outside of the tropics. We therefore increased the aeolian source not multiplicatively but by simply adding varying amounts of soluble iron spatially uniformly over the perturbation region of interest.

We next consider what a reasonable amplitude for our perturbations is. For the decreases, it is interesting to ask what happens in the limit as the aeolian source is decreased to zero over the perturbation region, so we let α range from unity all the way to zero. The question is what a reasonable amplitude for the iron addition is. For this it is useful to consider past fluctuations in the aeolian iron supply and what has been considered for geoengineering application. *Albani et al.* [2016] suggested that the largest increases in mineral dust

deposition were about ~ 4 times larger on the global scale and ~ 10 times larger in the southern hemisphere during the Last Glacial Maximum (LGM). However, taking into consideration atmospheric dust processing and sensitivity to aerosol abundance, *Albani et al.* [2016] estimated the increase in the aeolian source during the LGM to be $\sim 2.1\text{--}7.8 \text{ Gmol yr}^{-1}$ compared to the preindustrial climate. *Zeebe and Archer* [2005] showed that significantly reducing atmospheric $p\text{CO}_2$, by increasing oceanic carbon export by $1\text{--}10 \text{ Pg C yr}^{-1}$ via iron fertilization, which would require an additional equivalent aeolian source of $\sim 25\text{--}250 \text{ Gmol yr}^{-1}$, was not feasible.

Thus, to explore increased aeolian iron input scenarios, we incrementally strengthen the aeolian source by adding a spatially uniform aeolian source to the unperturbed state in the region of interest, until the globally integrated aeolian iron source is increased by 200 Gmol yr^{-1} . (We note that the Newton solver did not converge for large increases of the aeolian source of the low-aeolian estimate.) To reduce aeolian iron input, we multiply it by a factor α in the perturbation region with α decreasing incrementally from 1 to 0. For $\alpha = 0$, the aeolian source is completely switched off and only the sedimentary and hydrothermal sources supply iron. We increase and decrease the aeolian source in sufficiently small increments to ensure that the Newton solver converges in about five iterations for each value of the perturbed aeolian source.

As the aeolian source is perturbed, we assume that the concentration of the scavenging dust particles remains proportional to the aeolian source in the same ratio as for the unperturbed states. (We note that the dust deposition pattern differs slightly from the soluble iron source in the data of *Luo et al.* [2008] used in our model.) Scavenging by POP and opal particles is determined by the new equilibrium of the nutrient cycles.

We also note that our formulation of the iron cycle may not be valid for arbitrarily high dFe concentrations because of the following issues: (i) Free and chelated iron are in reality taken up at very different rates [e.g., *Sunda and Huntsman*, 1995, 1997; *Hutchins et al.*, 1999], yet we model uptake in terms of only the total dFe concentration. (ii) The formation of, and exchange with, a colloidal iron pool likely becomes important at high concentrations [e.g., *Fitzsimmons and Boyle*, 2014], but colloidal iron is ignored in our formulation. (iii) Our ligands are prescribed and cannot dynamically respond when free ligands become depleted.

3.3 Results

3.3.1 Response to Perturbations

3.3.1.1 Changes in Dissolved Iron

Iron inventories

In steady state, scavenging by POP, opal, and mineral dust exactly balances the sum of the aeolian, sedimentary, and hydrothermal iron sources. (We remind the reader that we do not explicitly represent precipitation of iron because scavenging increases rapidly with dFe concentrations — see Chapter 2, section 2.2.4.2.) Thus, changes in the globally integrated iron source imply an identical change in the globally integrated iron sink. However, unlike for PO_4 and Si(OH)_4 , the global inventory of dFe is not prescribed, so that the global mean dFe concentration will vary with the aeolian iron supply.

Figure 3.1 shows the changes in dFe concentration averaged over the global ocean, over the global euphotic zone, and over the Southern Ocean euphotic zone, as a function of the aeolian iron source of the GBL, SO, and TRP regions, respectively. The responses are quantified for the perturbations of the typical, low-aeolian, and high-aeolian unperturbed states.

Doubling the global mean dFe concentration of the unperturbed states, from $\sim 0.6 \text{ nM}$ to $\sim 1.2 \text{ nM}$, requires increases of the aeolian source by a factor of ~ 10 for the GBL, ~ 200 for the SO, and ~ 20 for the TRP perturbation regions. These increases in the aeolian source are thus unrealistic compared to the ranges of equivalent aeolian source increases considered in geoengineering iron fertilization projects and in past climates. The fact that such large increases in the aeolian iron source are required to double dFe concentrations is the consequence of the chemical equilibrium between ligands, total dFe, and free iron which results in a quadratic relationship between total and free iron (as in the model of [Frants et al., 2016]), and because the scavenging rate is proportional to the product of the concentrations of free iron and of the scavenging particles.

The unperturbed euphotic mean dFe concentration is less than the global mean, reflecting the iron nutricline set by uptake and organic scavenging. The dFe concentration in the euphotic layer affects the dFe Monod term of the uptake formulation and thus has direct influences on biological production. Similar to the global mean dFe concentration, increasing the global mean euphotic dFe concentration to above 1.2 nM requires a ~ 10 -fold increase of the aeolian source in the GBL, a ~ 500 -fold increase in the SO, or a ~ 20 -fold in the TRP region. This suggests that unrealistically large increases in aeolian deposition are necessary to sufficiently increase global surface dFe concentrations and relieve the ocean from iron deficiency globally.

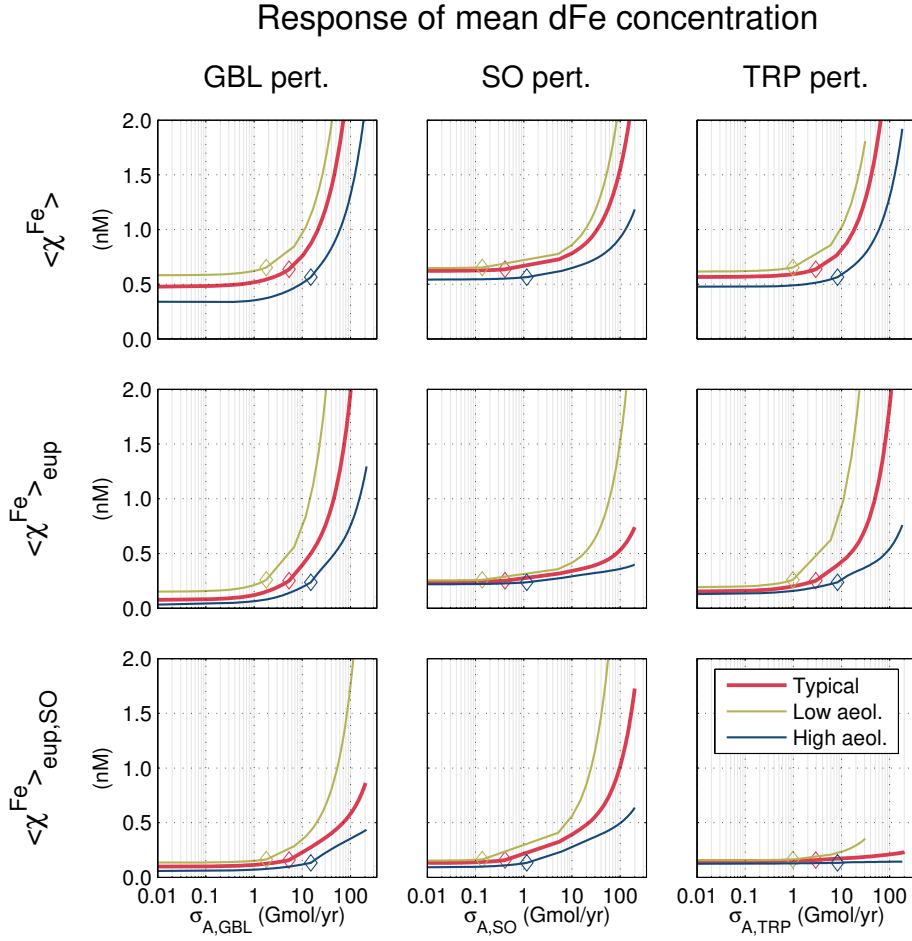


Figure 3.1: Changes in dFe concentrations averaged over the global ocean (top), the euphotic zone (middle), and the Southern Ocean euphotic zone (bottom), as a function of the perturbed aeolian iron source in the GBL (left), SO (center), and TRP (right) regions. The unperturbed states are indicated by diamonds.

Remarkably, adding a globally uniformly distributed 200 Gmol yr^{-1} to the aeolian source is not enough for the Southern Ocean euphotic mean dFe to reach 1 nM for the “typical” case. Even when the addition of aeolian iron is concentrated in the Southern Ocean only, $100 \text{ Gmol Fe yr}^{-1}$ are necessary to reach 1 nM in the SO euphotic zone. Adding as much as 200 Gmol yr^{-1} to the TRP region barely increases the Southern Ocean mean euphotic dFe concentration by $\sim 46\%$. This shows that completely relieving iron stress in the Southern Ocean is unrealistic.

Turning off the aeolian source entirely in the GBL, SO, and TRP regions

barely reduces global mean dFe, except for the case with a high-aeolian base state, which responds more strongly because its iron cycle is already primarily supported by the aeolian source in the unperturbed state. This underlines that the iron cycle's sensitivity to aeolian source perturbations depends on the unperturbed state. The larger sensitivity of the high aeolian case is particularly visible in the response to reductions in the global aeolian iron source, where a complete shutdown causes an almost complete depletion of the global euphotic mean dFe. In this case, the global mean dFe concentration is approximately halved, the remainder being sustained by the sedimentary and hydrothermal sources.

Surface Distributions

We now investigate the spatial patterns of the changes in dFe for the case of zero aeolian source, and for the case of a very large increase in the aeolian source. For the increase, we chose the addition of 50 Gmol yr^{-1} because an increase of that magnitude roughly corresponds to what has been considered for global iron fertilization proposals [Zeebe and Archer, 2005] and to the last glacial maximum anomaly [Albani *et al.*, 2016]. Large increases up to 200 Gmol yr^{-1} were also examined but are qualitatively similar. We examine the anomalies, $\delta\chi^{\text{Fe}} = \chi^{\text{Fe}} - \chi_0^{\text{Fe}}$, where χ^{Fe} and χ_0^{Fe} are the perturbed and unperturbed dFe concentrations.

Figure 3.2 shows the unperturbed vertically averaged euphotic concentration of dissolved iron, χ_0^{Fe} , together with the corresponding relative anomalies, $\delta\chi^{\text{Fe}}/\chi_0^{\text{Fe}}$, due to complete shutdown perturbations, and the absolute anomalies, $\delta\chi^{\text{Fe}}$, due to the 50 Gmol yr^{-1} aeolian addition. For the shutdown perturbations, we show the relative anomalies because small reductions in the surface dFe concentrations can have a significant impact on the uptake rate, especially where the unperturbed state is iron-deficient. Small reductions would not show on a linear scale for absolute anomalies.

Decreases in the aeolian iron source reduce euphotic concentrations of dissolved iron everywhere as expected. The global shutdown of the aeolian iron source almost completely removes dFe from the euphotic layer. In the North Atlantic subtropical gyre, where dFe concentrations and aeolian sources are highest in the unperturbed state, only $\sim 10\%$ remains for zero aeolian source. The largest relative reductions are located in the subtropical gyres, where biological utilization is macronutrient limited, which allows dFe to accumulate in the unperturbed state. Regions of vertical mixing/upwelling such as the eastern tropical Pacific, the subpolar North Pacific, and the Southern Ocean are less affected, with dFe concentrations that are already low in the unperturbed state. Remarkably, Southern Ocean dFe is maintained at $\sim 80\%$ of the unper-

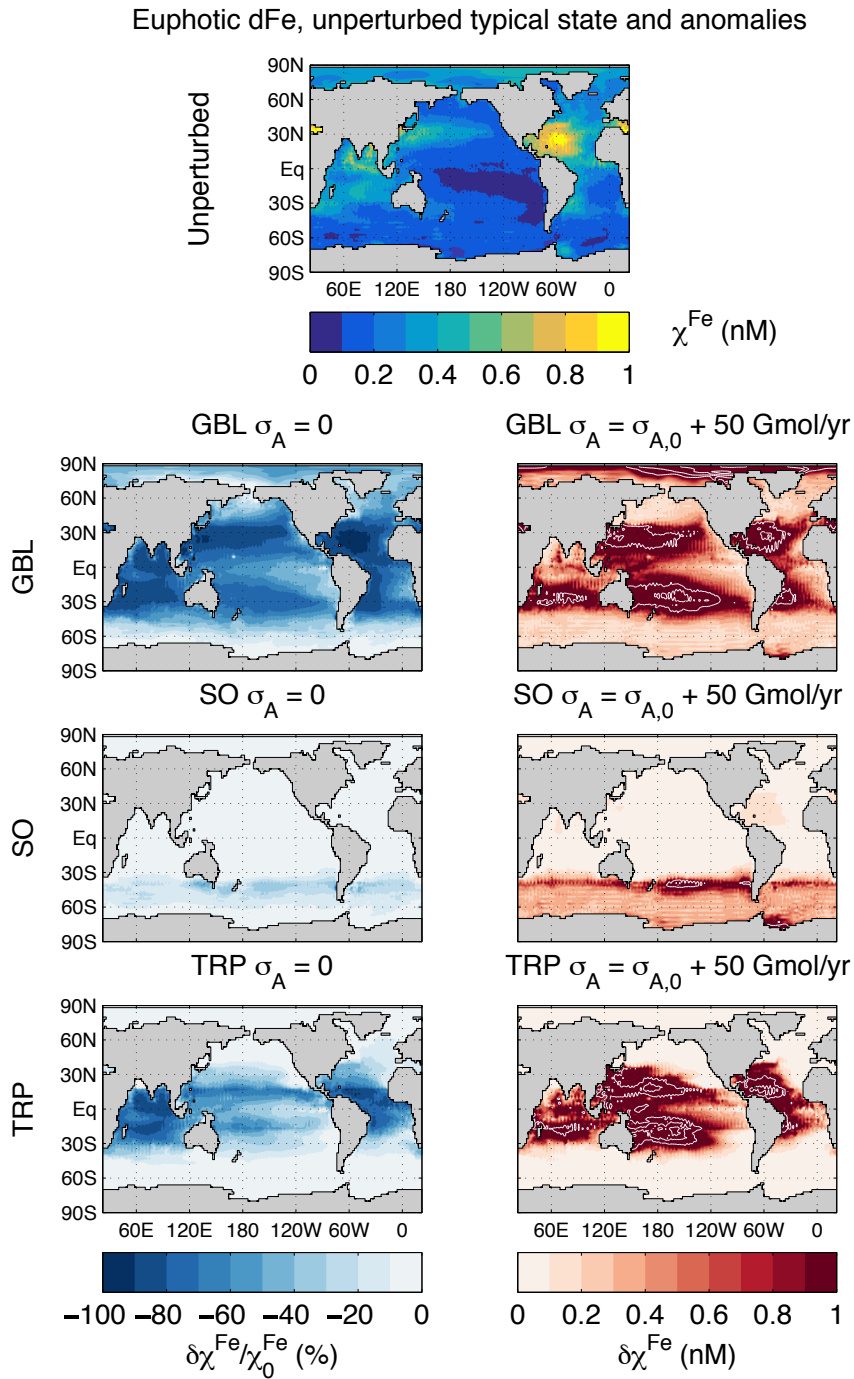


Figure 3.2: Top: Euphotic mean dFe for the unperturbed typical state. The two columns of plots show the corresponding anomalies for the complete shutdown (left) and for a 50 Gmol yr^{-1} increase (right) of the aeolian iron source in the GBL, SO, and TRP regions. White contours indicate dFe increases by 2, 4, and 6 nM.

turbed state, despite the fact that in the unperturbed state (current climate) a large fraction of Southern Ocean dFe is supplied by upwelling of regenerated aeolian iron [Holzer *et al.*, 2016]. This is due to reduced scavenging (due to reduced biological production, as will be seen in Figures 3.7 and 3.8 below), which enables more sedimentary and hydrothermal dFe to reach the Southern Ocean, thus compensating for the lack of aeolian iron.

Decreases of the aeolian source in the Southern Ocean have little effect. Even a complete SO shutdown of the aeolian source leaves the SO euphotic dFe concentrations virtually unchanged: Reductions by up to 20 % only occur within $\sim 50\text{--}40^\circ\text{S}$. This is because the bulk of Southern Ocean dFe is not supplied by local aeolian deposition [Holzer *et al.*, 2016] and because reduced scavenging allows upwelling sedimentary and hydrothermal dFe to compensate for losses in aeolian dFe.

Zeroing the tropical aeolian source reduces euphotic dFe concentrations mostly within 30°S and 30°N as expected. The largest relative reductions occur in the Atlantic and Indian Ocean, while the smallest relative reduction within the $30^\circ\text{S}\text{--}30^\circ\text{N}$ latitude band occurs in the productive eastern tropical Pacific consistent with the aeolian source pattern in the unperturbed state.

An increased aeolian source tends to increase euphotic dFe concentrations primarily where production, and hence scavenging, is low. The low scavenging in the subtropical gyres allows iron to accumulate and reach dramatically high levels for our steady-state model, up to 6 nM, for the 50 Gmol yr^{-1} aeolian source addition perturbations. (Recall that at such high dFe concentrations, some of the model assumptions break down.) Conversely, where there is significant biological production, such as in the eastern tropical upwelling regions or in the Southern Ocean, scavenging prevents large increases in dFe concentrations.

As a consequence, the pattern of the dFe anomaly for the global 50 Gmol yr^{-1} increase is strongly anticorrelated with the pattern of carbon export (see Figure 3.8 below). The SO aeolian addition strongly increases surface dFe within $\sim 35\text{--}45^\circ\text{S}$, by up to 4 nM, but only increases surface dFe in the remaining SO surface by about 0.2–0.4 nM. The response of surface dFe to the TRP aeolian addition is similar in pattern to the GBL aeolian addition, but is stronger in subtropical gyres, and weaker at high latitudes.

3.3.1.2 Changes in Euphotic Phosphate and Silicic Acid

We now investigate changes in the concentration of PO_4 and Si(OH)_4 in the euphotic zone where they support biological production. Because the global inventories of phosphate and silicic acid are fixed, perturbations can only redistribute macronutrients in the ocean. Perturbing the iron input impacts uptake

and hence export, which then feeds back on production through the redistributed macronutrient supply. We expect increased aeolian iron deposition to fertilize production, which then draws down surface concentrations and sharpens the nutricline.

Phosphate

Figure 3.3 shows the vertically averaged euphotic PO_4 concentrations for the unperturbed state, together with the anomalies for our perturbations. The plots on the left show the response to a complete shutdown of the aeolian source over the perturbation region. The right panels show the phosphate response to the 50 Gmol yr^{-1} additions over the perturbation regions.

The global shutdown of the aeolian source strongly increases euphotic PO_4 concentrations, in particular in the subtropical Pacific gyres where they increase by up to 1 mmol m^{-3} due to the reduced export from the increased dFe deficiency. However, an increase is not visible at high latitudes and particularly in the Southern Ocean, which is a consequence of the robustness of Southern Ocean dFe concentrations to the global aeolian shutdown. The response of PO_4 to the global shutdown of the aeolian source is strongly anticorrelated with the response in surface dFe concentrations: Reduced dFe concentrations limit phosphorus export, leading to higher surface PO_4 concentrations. For the GBL aeolian addition, the increases in surface dFe concentrations tend to decrease PO_4 surface concentrations where the perturbation and HNLC regions overlap because of relieved iron stress.

Turning off the aeolian source in the Southern Ocean, which was seen to have little effect on the dFe concentrations (Figure 3.2), barely increases euphotic PO_4 concentrations. For the SO increases, the response of PO_4 is propagated beyond the perturbation region into the South Pacific and South Atlantic basins by the gyre circulations.

Zeroing the aeolian source in the tropics increases euphotic PO_4 concentrations within the subtropical gyres and the Indian Ocean by up to 0.55 mmol m^{-3} . Hence for the aeolian shutdown perturbations, changes in euphotic PO_4 are strongly anticorrelated with changes in euphotic dFe. This is a direct consequence of the increased iron deficiency, which reduces phosphorus export. Similar to the case where the SO aeolian source is increased, surface PO_4 concentrations decrease and extend beyond the perturbation region for the TRP aeolian addition. We note that there are slight increases of PO_4 around the Antarctic coast, and in particular in the Wedell sea, where there is no biological production in our model (because of no photosynthetically available radiation – see Chapter 2).

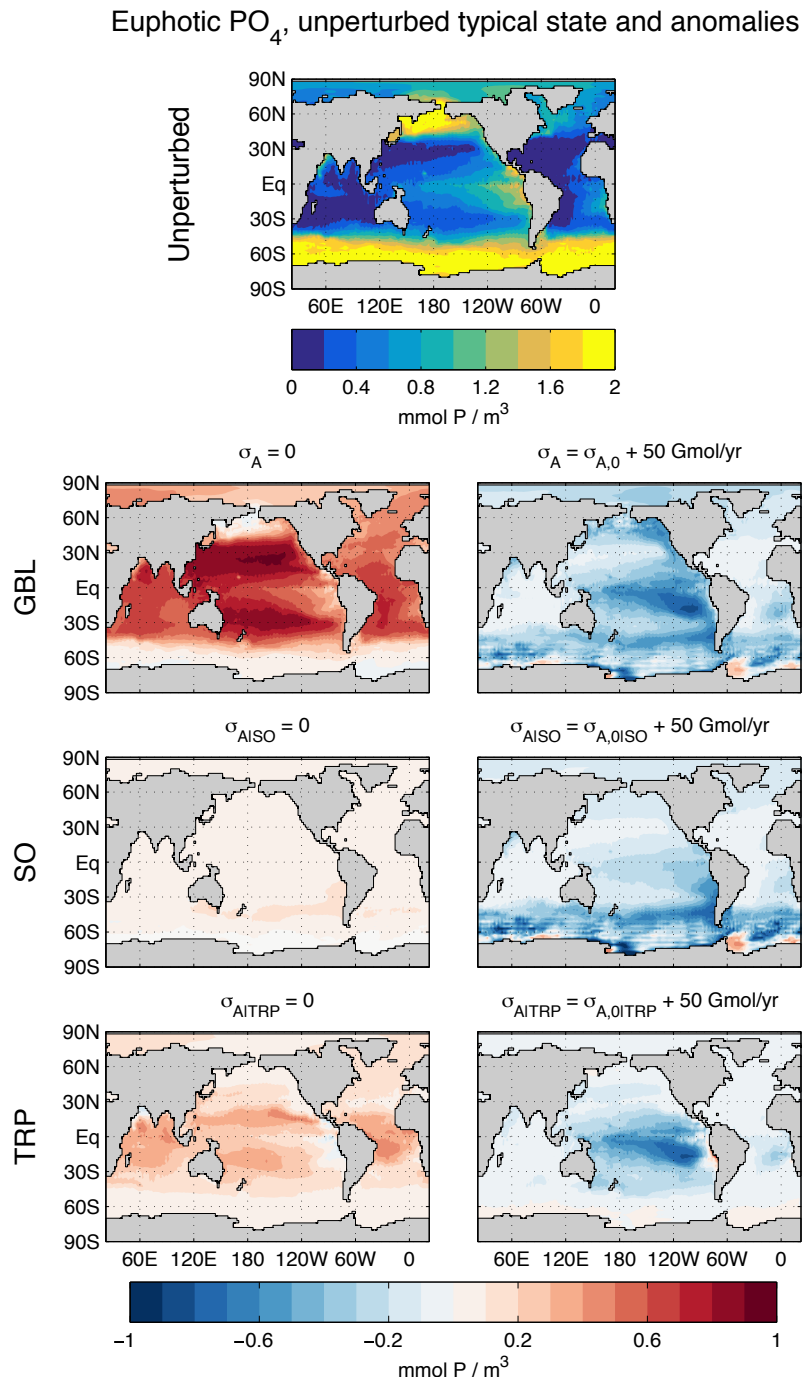


Figure 3.3: Top: Euphotic mean PO_4 for the typical unperturbed state. The two columns show the corresponding anomalies for the complete shutdown (left) and for a 50 Gmol yr^{-1} increase (right) of the aeolian iron source in the GBL, SO, and TRP regions.

Silicic Acid

Figure 3.4 shows the vertically averaged euphotic concentration of silicic acid in the unperturbed state, together with the anomalies in response to our perturbations. Surface changes in Si(OH)_4 differ from those of PO_4 in both amplitude, and, for some regions, sign.

The panels on the left show the response to shutting the aeolian source down over the perturbation region. When the global aeolian source is switched off, surface Si(OH)_4 concentrations increase mostly at high latitudes despite the small changes in dFe concentrations there. In the Southern Hemisphere, this increase reaches up to 6 mmol m^{-3} in the intermediate- and mode-water formation regions ($\sim 40\text{--}55^\circ\text{S}$), due to the decrease in dFe which reduces opal export. The increase is larger in the North Pacific where it reaches $\sim 10 \text{ mmol m}^{-3}$. There is a slight decrease in the North Atlantic and Indian Oceans, where surface Si(OH)_4 is already low in the unperturbed state. The SO aeolian shutdown increases euphotic Si(OH)_4 in the Southern Ocean by a mere $2\text{--}4 \text{ mmol m}^{-3}$. This relatively weak response is explained by the fact that the small decrease in biological production is compensated by an increase in the diatom Si:P uptake ratio because this ratio depends roughly inversely on dFe (see Equation 2.15, Chapter 2). For the same reason, and additionally because most of the diatoms are located in the Southern Ocean, the tropical shutdown barely causes any surface Si(OH)_4 changes at all.

The right panels of Figure 3.4 show the response to the 50 Gmol yr^{-1} increases. For opal export, fertilization by increased dFe is counteracted by a reduced Si:P ratio so that we expect a weaker response in opal export compared to carbon export. Only in the case of the GBL and SO aeolian iron additions is there a significant response in surface Si(OH)_4 concentrations which decrease by up to 20 mmol m^{-3} in the Southern Ocean where Si(OH)_4 is predominantly located in the unperturbed state. The euphotic Si(OH)_4 increase in the Southern Ocean is the consequence of a decreased opal export, as shown in the Section 3.3.1.3 below.

Changes in Nutrient Limitation Patterns

To gauge the significance of the changes in surface nutrient concentrations for biological uptake, the concentration changes must be compared to the half-saturation constants for uptake. This comparison is conveniently accomplished by the nutrient limitation pattern that we defined in Chapter 2: Where a nutrient falls below its half-saturation constant we deem uptake to be deficient in that nutrient. Figure 3.5 shows the thus defined nutrient limitation patterns for the Diatom functional class for the unperturbed state and for the aeolian source shutdown and for the 50 Gmol yr^{-1} addition perturbations. We only show the

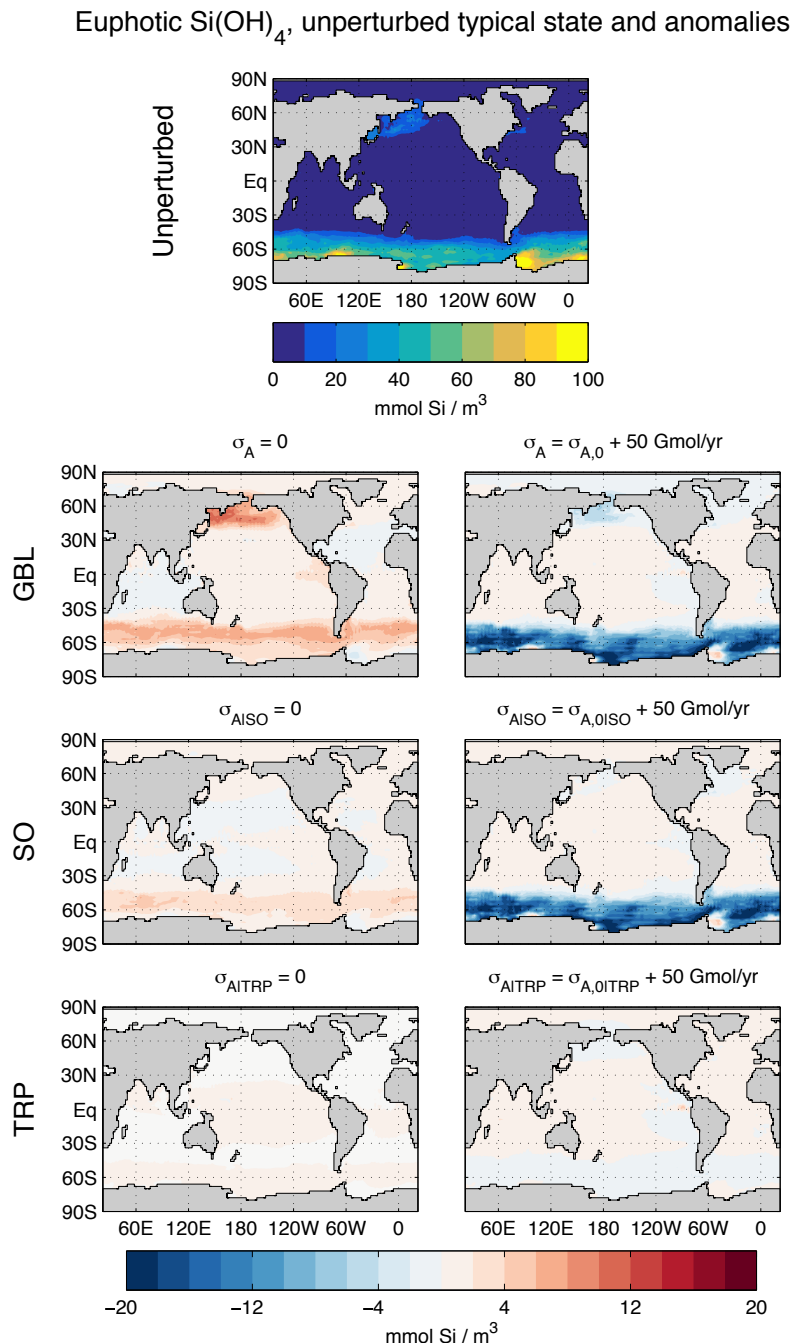


Figure 3.4: Top: Euphotic mean Si(OH)_4 for the typical unperturbed state. The two columns show the corresponding anomalies for the complete shutdown (left) and for a 50 Gmol yr^{-1} increase (right) of the aeolian iron source in the GBL, SO, and TRP regions.

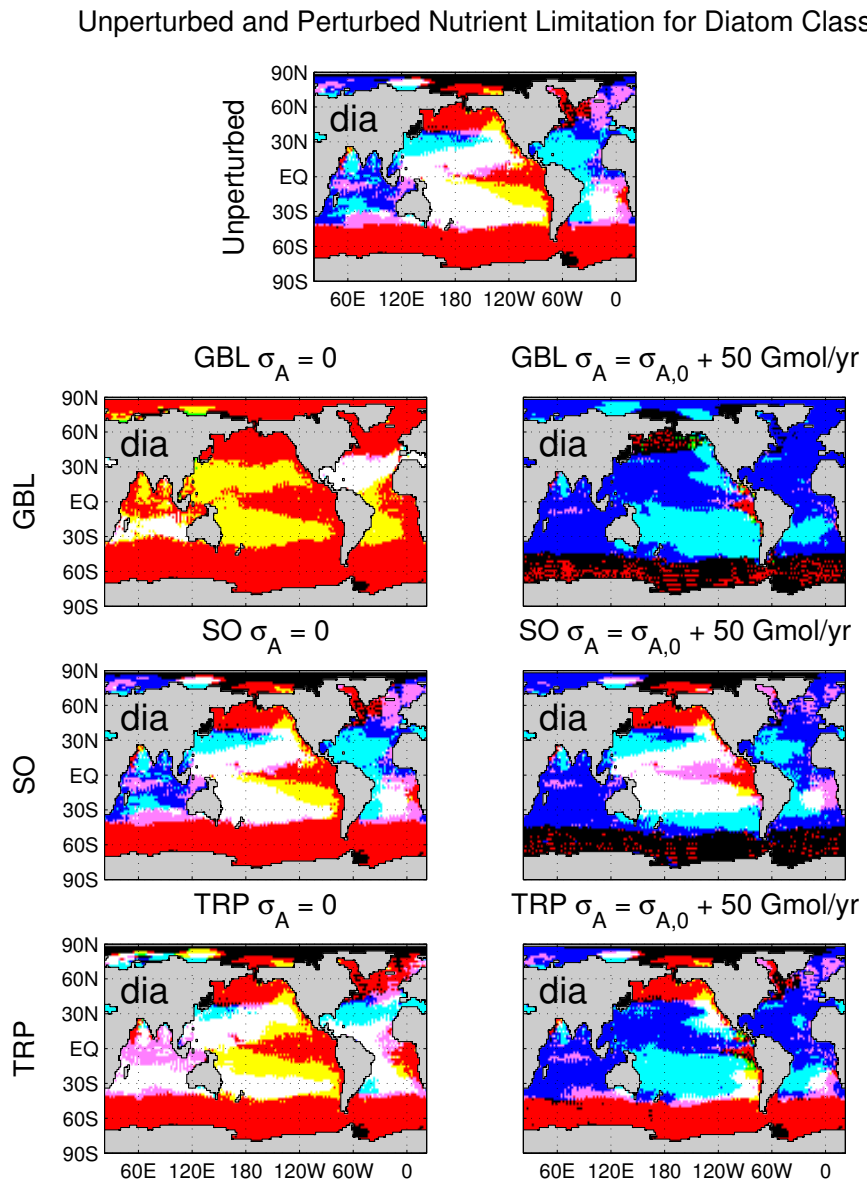


Figure 3.5: Diatom nutrient limitation patterns, calculated as in Figure 2.6 of Chapter 2, for the large perturbations of the aeolian source. Left column: Shutdown of the aeolian iron source in the perturbation region indicated (GBL, SO, TRP). Right column: Spatially uniform addition of 50 Gmol yr^{-1} to the aeolian iron source in the perturbation region.

limitation patterns for the Diatom class because its growth depends on all three nutrients. The nutrient limitation patterns of the Large and Small classes are plotted in Appendix Figures 3.17 and 3.18.

The global aeolian source shutdown decreases surface dFe while increasing PO₄ and Si(OH)₄. This expands the regions of iron deficiency (red) at the expense of areas of PO₄ and Si(OH)₄ deficiency (white, blue, cyan, and green). Thus, the iron-limited HNLC areas spread slightly. The Pacific subtropical gyres and the South Atlantic subtropical gyre, which are colimited by all three nutrients in the unperturbed state, become colimited by Fe and Si only, because of the additional surface PO₄. The North Atlantic subtropical gyre, which is iron replete in the unperturbed state, i.e., only PO₄ and Si(OH)₄ colimited, becomes additionally iron deficient. The Indian Ocean, which is limited mostly by PO₄ in the unperturbed state, becomes more iron limited and less PO₄ limited.

Conversely, globally increasing the aeolian source relieves most of the ocean from iron stress (e.g., white→cyan and red→black), except for a few patches at high latitudes and in the eastern tropical Pacific that remain iron limited. The increased surface Si(OH)₄ for 40°S–40°N latitudes additionally relieves Si(OH)₄ limitation (cyan→blue).

The SO aeolian addition relieves iron deficiency mostly in the Southern Ocean (red→black, white→cyan, and magenta→blue). The Southern Ocean remains replete in PO₄ and Si(OH)₄ (in the sense that concentrations are above half-saturation constants) as for the unperturbed state. The surface drawdown of PO₄ expands the regions of PO₄ limitation in the tropics. The SO aeolian shutdown slightly expands the northern edge of the Southern Ocean region of iron limitation, leaving the global limitation pattern otherwise unchanged.

The opposite of the SO response happens for the TRP perturbations, in the sense that these leave the Southern Ocean limitation unchanged, while most of the changes occur within 40°S–40°N. Similar to the GBL shutdown case, zeroing the TRP aeolian source expands the iron limited HNLC regions. However, changes in PO₄ and Si(OH)₄ are small compared to the global aeolian shutdown, leaving the Indian Ocean PO₄ deficient. In the Pacific and Atlantic subtropical gyres, the TRP shutdown relieves PO₄ deficiency, but to a lesser extent than for the GBL case. For the TRP increase, the response in the 40°S–40°N latitude band is strikingly similar to the GBL increase. However, the TRP increase leaves the Southern Ocean and the Subpolar Pacific strongly iron deficient as the corresponding surface dFe changes are small in these regions.

3.3.1.3 Changes in the Export Production

We now explore the response of the export production of carbon and opal to changes in the aeolian iron supply. Decreases in the aeolian source are expec-

ted to increase iron limitation, while increases in iron supply are expected to increase export. For opal export, the iron dependence of the Si:P uptake ratio (Equation 2.15, Chapter 2) also plays a role: Fertilization by increasing dFe is counteracted by a reduced Si:P ratio so that we expect a weaker response in opal export compared to carbon export.

Globally Integrated Export

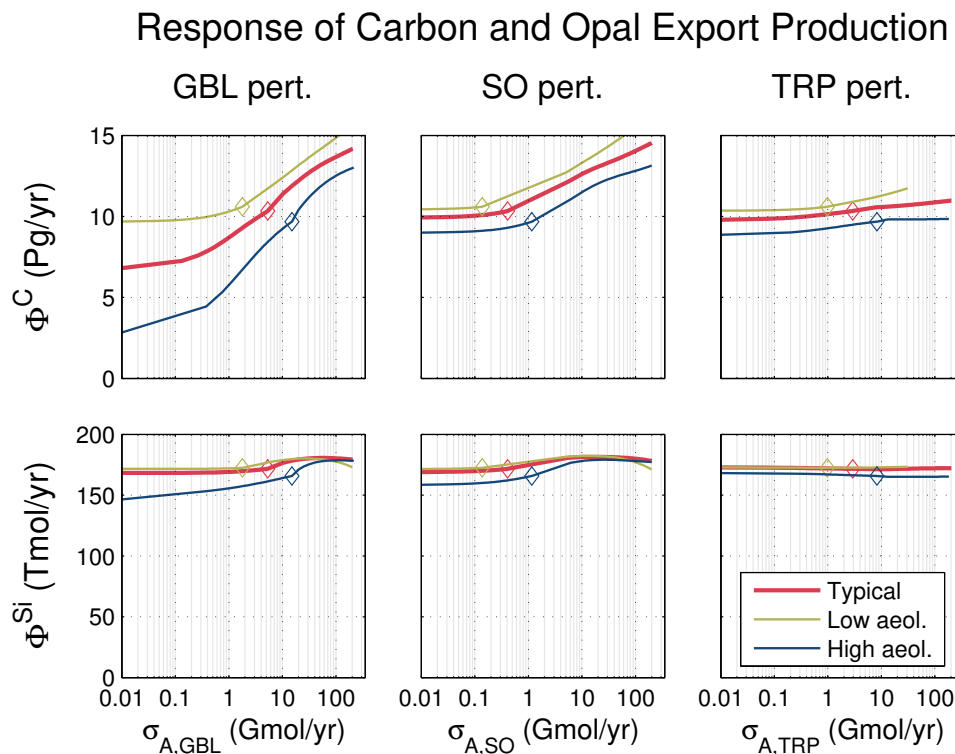


Figure 3.6: Carbon and opal export production as a function of the GBL, SO, and TRP perturbed aeolian iron source. The unperturbed states are indicated by diamonds.

Figure 3.6 shows the globally integrated carbon and opal export productions as a function of the perturbed aeolian source. As for Figure 3.1, each panel shows the curves of the typical, high-aeolian, and low-aeolian estimates. Changes in global carbon export due to *decreases* in aeolian iron supply are sensitive to the choice of the initial unperturbed state. This is because turning off the global aeolian source for a state with a small aeolian contribution has negligible consequences on the iron cycle, (e.g., for the low-aeolian estimate), while turning off the aeolian source for a state that heavily relies on the aeolian

source dramatically reduces export production (e.g., for the high-aeolian estimate). Changes due to decreases of aeolian iron supply in the Southern Ocean, which is already iron deficient, are small in comparison to global perturbations. Changes in the global carbon export due to *increases* in the aeolian iron supply are less sensitive to the choice of the initial unperturbed state. Because the Southern Ocean receives little directly deposited aeolian iron in the unperturbed state, carbon export rapidly increases with an increased SO aeolian iron supply.

Changes in opal export are relatively smaller than for carbon export. This is due to the compensating effect of changes in the Si:P ratio. Even for the high-aeolian unperturbed state, a complete shutdown of aeolian iron reduces opal export by less than 10 %, compared to a 60 % decrease in carbon export. This does not support the silicic acid leakage hypothesis, which posits that changes in the Si:P ratio dominate any change in opal export [e.g., Matsumoto *et al.*, 2002; Brzezinski *et al.*, 2002]. We acknowledge that this might be due to the particular parameter values in our Si:P ratio; a different choice of parameters might result in a different response. However small the response, we note that strong increases of the GBL or SO aeolian iron source lead to eventually saturating, and even reducing, the global opal export. This suggests that large increases in the aeolian iron supply saturate biological production, while the diatom Si:P ratio keeps declining with increasing dFe, eventually reducing opal export.

Zonally Integrated Export

We now explore spatial changes in carbon and opal export, by investigating how the zonally integrated exports respond to changes in the aeolian source. As detailed in Chapter 2, the zonally integrated export production of carbon and opal are well constrained within the family of estimates, despite the wide range of aeolian iron sources. For simplicity we therefore focus only on the typical estimate.

Figure 3.7 shows the zonal integral of the anomaly in export production of carbon, $\delta[\Phi^C] = [\Phi^C] - [\Phi_0^C]$, and opal, $\delta[\Phi^{Si}] = [\Phi^{Si}] - [\Phi_0^{Si}]$ as a function of the perturbed aeolian source strength. Also drawn are the unperturbed zonally integrated export productions to provide context for the changes.

Carbon Export For globally uniform perturbations, the strongest changes in carbon export (white contours) occur in the Southern Ocean within 40–70°S for large increases of the aeolian iron source. This can be understood by examining the euphotic response for the +50 Gmol yr⁻¹ GBL perturbations. Figures 3.1 and 3.2 show that the global addition of 50 Gmol yr⁻¹ leads to a

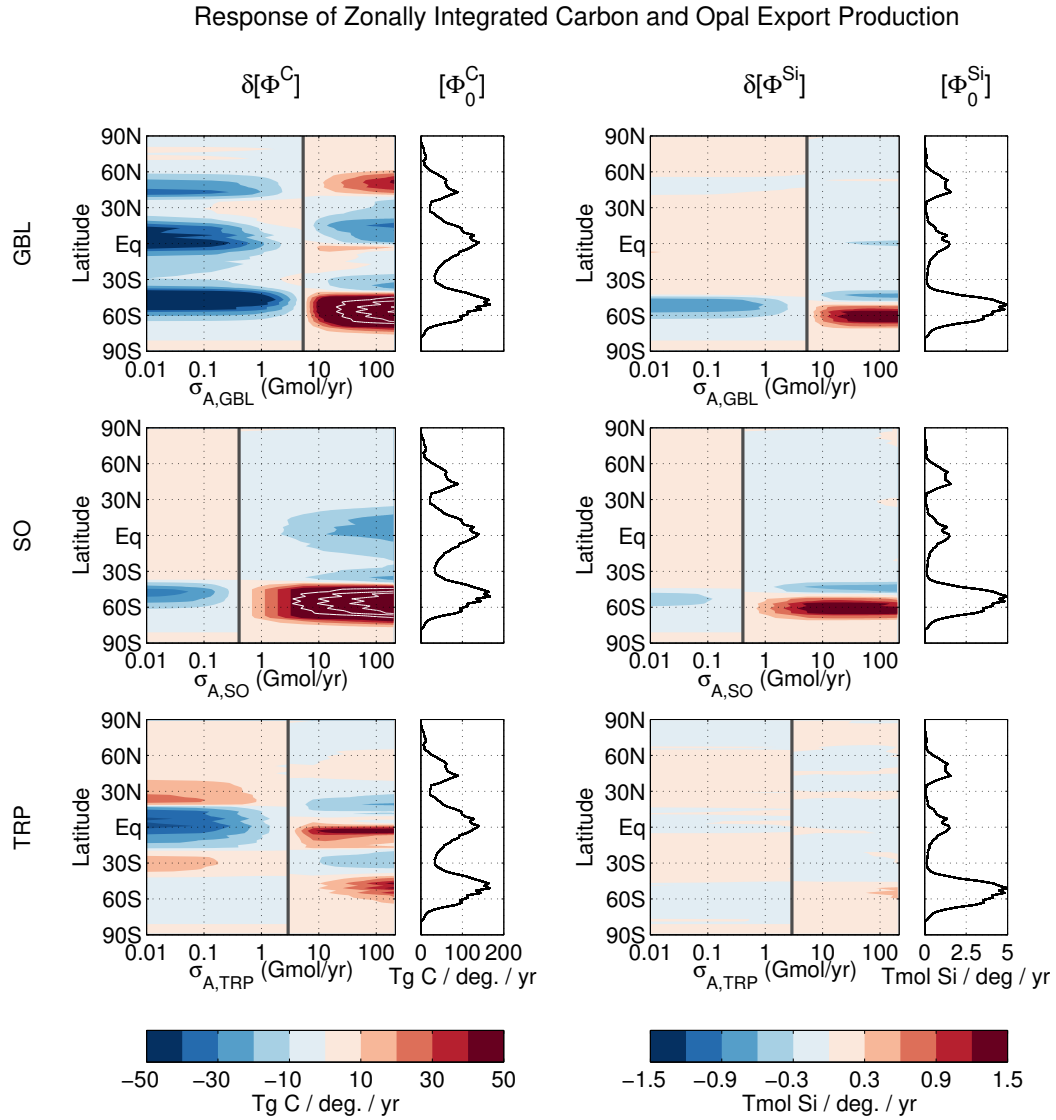


Figure 3.7: Changes, from our typical unperturbed state, in the zonally integrated carbon export (left) and opal export (right) for the GBL (top), SO (middle), and TRP (bottom) perturbations, as a function of the perturbed aeolian source strength. For the carbon export (left) additional white contours indicate increases of 100, 150, and 200 Tg C (deg. lat.) $^{-1}$ yr $^{-1}$. The unperturbed state is indicated by a heavy vertical line. For convenience, the unperturbed zonal integrals of the exports are repeated on the right of each panel.

~ 0.3 nM increase in euphotic dFe in the Southern Ocean, roughly a doubling of the unperturbed value. Dissolved iron concentration changes of this magnitude are important because they approach the ~ 0.3 nM half-saturation constants for the Large and Diatom phytoplankton classes. (Recall the bulk of carbon export is due to the Large and Diatom classes in our model, see Figure 2.8 of Chapter 2.) Changes in SO carbon export are not sensitive to the small decreases in SO surface PO₄ (Figure 3.3) because SO surface PO₄ concentrations are significantly larger than the half-saturation constants for the Large and Diatom classes. However, euphotic PO₄ concentrations within 30–40°S are small enough in the unperturbed state for small reductions in surface PO₄ to decrease carbon export, which coincides with the southward expansion of the PO₄ limitation region (Figure 3.5).

GBL aeolian decreases result in the largest carbon export decrease occurring within the thinner 40–55°S latitude band where the relative dFe anomalies are large (Figure 3.2). The primary driver for changes in carbon export in response to GBL perturbations of the aeolian source is the increase of Southern Ocean surface dFe. However, we note that carbon export changes do not go in the same direction as euphotic dFe changes everywhere. This is particularly visible in subtropical latitudes, where the expansion of the unproductive regions of the subtropical gyres due to macronutrient drawdown, consistent with [Dutkiewicz *et al.*, 2005], override the large increases in dFe concentrations where dFe is already replete. As a consequence, the carbon export decrease for the GBL aeolian shutdown case appears shifted north relative to the carbon export increase in the 50 Gmol yr⁻¹ GBL aeolian addition case. This is explained by the poleward shift, with increased GBL iron supply, of the boundary between the PO₄-limited subtropical gyres and the dFe-limited HNLC region of the Southern Ocean (see top panels of Figure 3.5).

The same mechanisms are at play for the SO perturbations of the aeolian source: The SO addition of aeolian dFe affects Southern Ocean euphotic PO₄, Si(OH)₄, and dFe concentrations similarly to the GBL aeolian source increases, resulting in the export increase in the Southern Ocean. However, decreases in the SO aeolian source do not reduce Southern Ocean dFe concentrations by as much as the GBL aeolian source reductions, particularly at 40–55°S latitudes, which results in a lower decrease of carbon export in the Southern Ocean. North of 40°S, decreases in euphotic PO₄ where PO₄ is limiting result in a decrease of carbon export, despite dFe increases.

TRP perturbations of the aeolian source do not trigger a strong Southern Ocean response in carbon export, because of the robustness of Southern Ocean euphotic PO₄ and dFe concentrations to these perturbations. For TRP aeolian increases, carbon export increases at the equator due to the relaxed iron deficiency, but decreases in the subtropical gyres due to the increased PO₄ limit-

ation together with the expansion of the associated PO₄-limited region. For TRP aeolian decreases, we find that equatorial carbon export decreases due to increased iron deficiency, while subtropical carbon export increases due to increases in PO₄ concentrations. The latitude range of the equatorial carbon export increase for the TRP aeolian reduction is larger than the latitude range of the equatorial carbon export decrease for the TRP aeolian increase. This is due to the expansion, with increasing iron supply, of the PO₄-limited regions associated with the subtropical gyres.

Opal Export For opal export, the same mechanisms apply, but in addition changes in the diatom Si:P uptake ratio play a role. The primary consequence of changes in the Si:P ratio is a weaker opal export response, compared to carbon export. Because Si(OH)₄ concentrations are relatively low outside of the Southern Ocean even in the perturbed states, the response is concentrated in the Southern Ocean, and only significant for the GBL and SO perturbations.

For the GBL and SO aeolian increases, the Southern Ocean response in opal export is asymmetrically dipolar, with a narrow band of decreases within $\sim 40\text{--}50^\circ\text{S}$ and a broader band of increases south of $\sim 50^\circ\text{S}$. The band of reductions is due to relatively large increases in euphotic-zone dFe in that region that reduce the Si:P uptake ratio, combined with a southward expansion of the PO₄-limited regions associated with the subtropical gyres, thus reducing uptake and export. South of 50°S , opal export increases and saturates with increasing aeolian source strength, but then declines again for very large source increases. The increases in opal export are due to a relief of iron stress, but are ultimately countered by a decreasing Si:P ratio. The overall effect of the dipolar anomaly is a strengthened and poleward-shifted Southern Ocean opal export in response to increased aeolian iron deposition.

GBL and SO aeolian decreases result in a decrease in opal export south of 45°S which, as for carbon export, appears shifted northward compared the carbon export increase in the GBL and SO iron supply addition cases. This is a consequence of the northward shift, with increasing aeolian iron supply, of the PO₄-limited regions associated with the Southern Hemisphere subtropical gyres. Opal export virtually remains unchanged for TRP perturbations of the aeolian source, because opal export is strongly concentrated in the Southern Ocean in which surface concentrations are barely affected by these perturbations.

Changes in Geographic Patterns of Carbon and Opal Export

The zonal integrals of the previous section, while providing a powerful summary of export changes, lose information about zonally asymmetric changes,

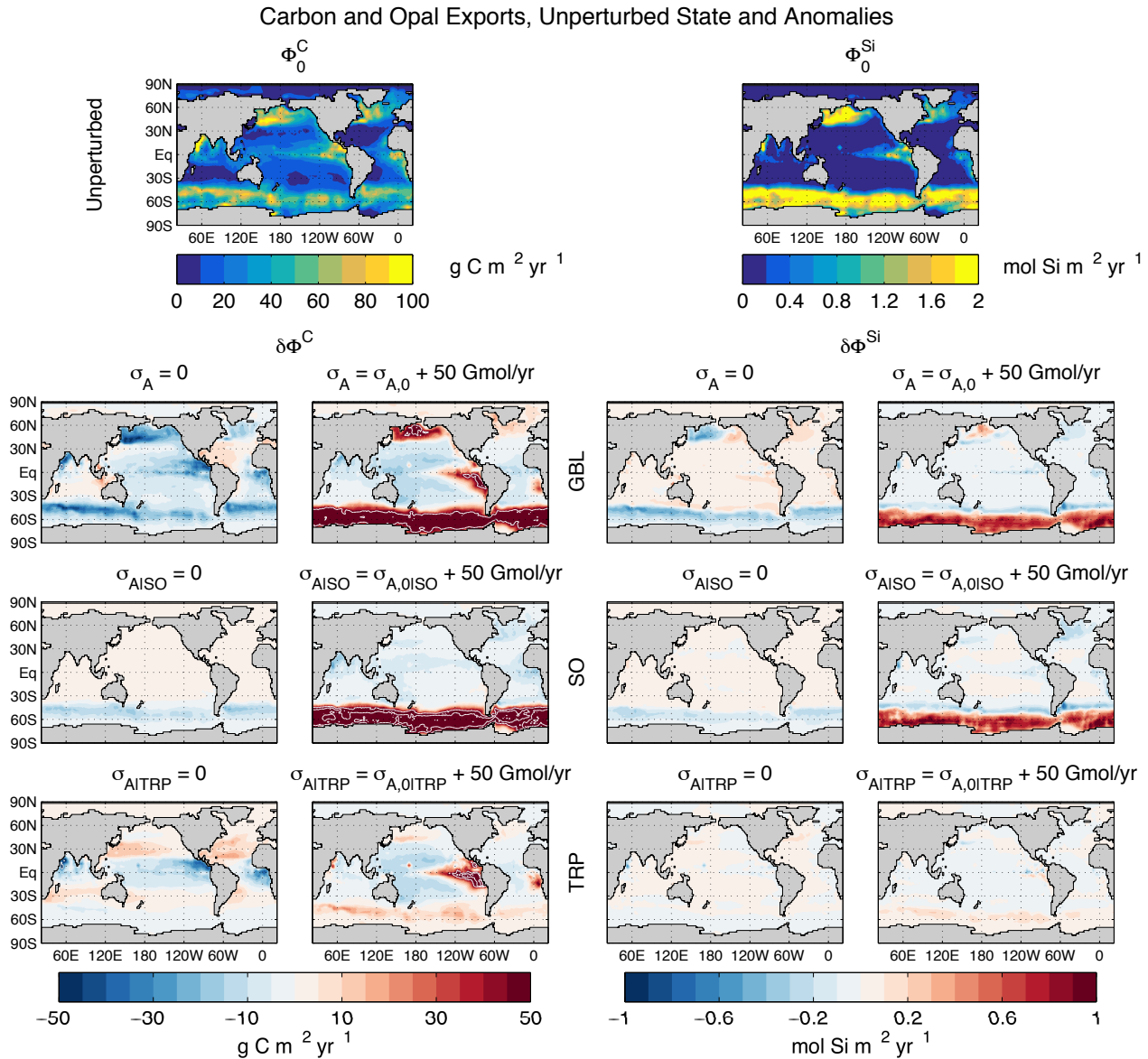


Figure 3.8: Local export production of carbon (left half) and opal (right half) for the unperturbed state (top) together with their anomalies for the aeolian source shutdown and the 50 Gmol yr^{-1} aeolian iron addition in the perturbation region indicated (GBL, SO, TRP). For carbon export anomalies, the white contours indicate 50, 75, and $100 \text{ mg C m}^{-2} \text{ yr}^{-1}$ increases.

which are particularly important at low latitudes. To help with the interpretation of the response of the biological pump, and the redistribution of preformed and regenerated nutrients that drive it, we plot in Figure 3.8 maps of the carbon and opal export changes. For ease of comparison, we also show the unperturbed exports, which are identical to those of Figure 2.7 (Chapter 2).

Carbon Export For the global shutdown of the aeolian source, carbon export decreases strongly due to increased iron stress in regions of high unperturbed production: the Southern Ocean, eastern tropical Pacific, and the northern-hemisphere subpolar gyres. The Southern Ocean response is roughly zonally symmetric, but shifted poleward in the Pacific sector, where the subtropical gyre extends further south. The global shutdown causes much weaker decreases in the oligotrophic subtropical gyres, where increased iron stress is compensated by increased PO_4 availability (Figure 3.3). An interesting exception is the subtropical North Atlantic, where increased PO_4 availability wins over increased iron stress and carbon export increases. This is consistent with the idealized perturbation experiments of *Holzer and Primeau* [2013], which were aimed at understanding the teleconnections between Southern Ocean export and North Atlantic production.

The shutdown of aeolian iron over the SO region decreases Southern Ocean carbon export due to yet further increased iron stress. Elsewhere, production slightly increases because phosphate is now less strongly trapped in the Southern Ocean with more leakage of preformed phosphate to the rest of the world.

The tropical aeolian source shutdown reduces carbon export over the perturbation region due to reduced iron fertilization, but increases export in the subtropical gyres. The reduced tropical utilization allows more preformed phosphate to transport laterally into the subtropical gyres thus relieving their PO_4 limitation (Figures 3.3 and 3.5).

The GBL 50 Gmol yr^{-1} aeolian addition increases carbon export in the tropical and high-latitude high-production regions of the unperturbed state where surface dFe concentrations increase and PO_4 concentrations remain high due to vertical mixing/upwelling and nutrient trapping. Conversely, carbon export decreases in the subtropical gyres, which become PO_4 deficient because of reduced preformed PO_4 transported laterally into the gyres.

The SO aeolian addition results in an even stronger increase in Southern Ocean carbon export (up to 100 % in some places) due to the larger increases in surface dFe compared to the GBL case. The SO aeolian addition reduces carbon export slightly north of 40°S where surface dFe concentrations remain mostly unchanged but PO_4 concentrations are decreased.

The TRP aeolian addition strongly increases carbon export in the eastern

tropical Pacific because of the strongly increased tropical iron fertilization, and because of the continuous supply of PO₄ from tropical upwelling. The TRP addition also increases carbon export in the tropical eastern Atlantic. Carbon export increases in the subpolar gyres of the Northern Hemisphere and in the Southern Ocean where biological production is fertilized by the slight increases in surface dFe.

Opal Export The relative changes in opal export are smaller than the corresponding changes in carbon export because of compensation by the dFe-dependent diatom Si:P uptake ratio (Equation 2.15, Chapter 2). equatorward of the subpolar oceans, Si(OH)₄ is strongly limiting so that small changes in surface Si(OH)₄ concentrations affect the opal export because the Si(OH)₄ concentrations there are close to the half-saturation constant for uptake.

The GBL aeolian shutdown results in a decrease in opal export south of ~45°S and in the subpolar North Pacific because of decreased iron fertilization in these already iron-stressed regions. For the rest of the ocean opal export increases slightly due to the small increase in Si(OH)₄, which is now less efficiently stripped out of the formation region of AAIW and SAMW which supply the ocean with preformed silicic acid. For the SO shutdown, the response in opal export is similar to the GBL case but of weaker amplitude because the reduction in Southern Ocean iron fertilization is weaker. The opal export response to the TRP shutdown is negligible.

The opal export responses to GBL and SO 50 Gmol yr⁻¹ aeolian additions are very similar. Opal export strongly increases south of ~50°S due to relieved iron stress. The decreases between ~40–50°S are due to the combined effects of a decrease in the Si:P uptake ratio and the southward expansion of the PO₄ limitation seen on both Figure 3.7 and 3.8. This results in the dipolar anomaly of Southern Ocean opal export. The TRP aeolian addition slightly increases Southern Ocean opal export due to long-range transport of iron to the Southern Ocean surface (see section 3.3.2.2 below).

3.3.1.4 Changes in the Biological Pump

Changes in carbon and opal export production change the inventories and distributions of regenerated and preformed PO₄ and Si(OH)₄. The inventory of regenerated phosphate defines the efficiency $E_{\text{bio}}^{\text{P}}$ of the biological (soft-tissue) carbon pump as explored in detail in Chapter 1. We can analogously define the efficiency $E_{\text{bio}}^{\text{Si}}$ of the ocean's silicon pump as the ratio of the regenerated silicic-acid inventory to the total silicic-acid inventory.

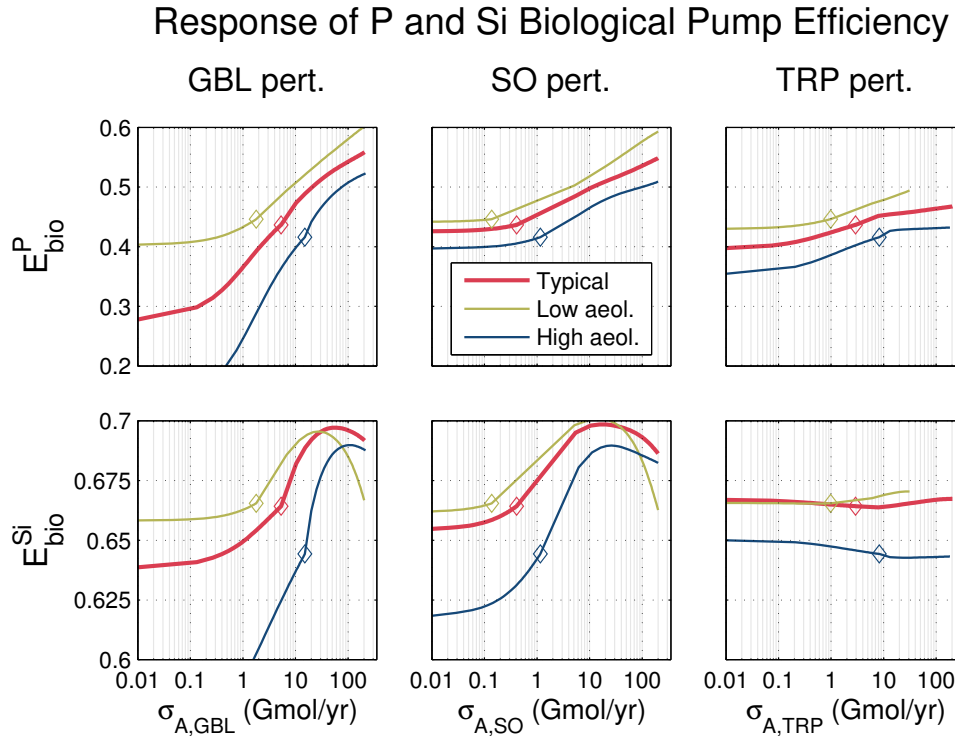


Figure 3.9: Global Biological pump efficiencies of phosphorus and silicon, as a function of the GBL, SO, and TRP perturbed aeolian iron source organised as in Figure 3.6.

Global Biological Pump Efficiencies

Changes in the biological pump efficiencies are tightly correlated with changes in export production (Figure 3.6) which control the regenerated nutrient inventories. Figure 3.9 shows $E_{\text{bio}}^{\text{P}}$ and $E_{\text{bio}}^{\text{Si}}$ as a function of the aeolian source of the perturbed region. As for Figures 3.1 and 3.6, we plot the curves of the typical, high-aeolian, and low-aeolian estimates to emphasize that the response to perturbations is sensitive to the initial state of the iron cycle. The sensitivity of $E_{\text{bio}}^{\text{P}}$ to the initial state of the iron cycle is greater for aeolian source decreases than for aeolian source increases, similar to what we saw for the response of the global export production (Figure 3.7). The $E_{\text{bio}}^{\text{P}}$ increases due to additional iron supply are predominantly due to more efficient phosphate utilization in the Southern Ocean (Figure 3.7), and are thus larger for GBL and SO aeolian increases than for the TRP aeolian increases.

The changes in $E_{\text{bio}}^{\text{Si}}$ are smaller than for $E_{\text{bio}}^{\text{P}}$, due to the compensating effect of changes in the Si:P uptake ratio. However, the compressed ordinate of Figure 3.9 shows interesting systematic variations of $E_{\text{bio}}^{\text{Si}}$. Consistent with changes in

opal export, increases of the GBL or SO aeolian iron source lead to a plateau of the silicon pump efficiency at a source of about $30 \text{ Gmol Fe yr}^{-1}$. For yet larger sources, $E_{\text{bio}}^{\text{Si}}$ decreases from its maximum. This suggests that large increases in the aeolian iron supply are eventually dominated by the diatom Si:P ratio.

To understand what drives the changes in the pump efficiencies, we consider the zonally averaged responses in the regenerated nutrient distributions. In order to compute the distributions of regenerated and preformed PO_4 and Si(OH)_4 , we use the same Green function techniques as in Chapter 1, applied to equivalent linear diagnostic models for the macronutrient cycles. (For details, see Appendix 3.B.1.)

Regenerated and Preformed Phosphate

Figure 3.10 shows the regenerated and preformed PO_4 concentrations, $\chi_{\text{reg}}^{\text{P}}$ and $\chi_{\text{pre}}^{\text{P}}$, zonally averaged over the global ocean, for the typical unperturbed state, together with the corresponding anomalies, $\delta\chi_{\text{reg}}^{\text{P}}$ and $\delta\chi_{\text{pre}}^{\text{P}}$, for the shutdown and the 50 Gmol yr^{-1} increase aeolian perturbations. The highest concentrations of regenerated PO_4 are found in old upwelling waters in the tropics and in old North Pacific waters around 1000 m depth, where regenerated PO_4 can accumulate over time. (The oldest waters of the ocean lie deeper in the North Pacific [e.g., Holzer and Primeau, 2006; DeVries and Primeau, 2011], but the Martin curve of the biogenic particle flux divergence top-loads the regenerated PO_4 profile.) Preformed PO_4 is dominantly “leaked” from the Southern Ocean via SAMW, AAIW, and AABW, and dispersed throughout the global ocean. This Southern Ocean leak is caused by iron limitation leading to incomplete nutrient utilization and because of eddy-diffusive leakage from Southern Ocean-trapped high PO_4 concentrations (see also Chapter 1). Here we show the perturbations of the typical state, because phosphorus export is well constrained for each member of our family of estimates (Chapter 2), so that the distributions of regenerated and preformed PO_4 are virtually the same for the unperturbed typical and high- and low-aeolian states (not shown).

Response to Aeolian Iron Shutdown Zeroing the aeolian source globally results in order 30 % decreases, which have the zonal mean pattern of the unperturbed regenerated PO_4 concentration. This is simply the result of globally reduced export production (c.f., Figure 3.7), which reduces the remineralization rate in the aphotic zone. The corresponding preformed response is an increase of regenerated PO_4 in surface and mode waters of similar magnitude, resulting from reduced uptake.

For the SO shutdown, the relatively small response in carbon export manifests as a small response in regenerated PO_4 : A tongue of slightly reduced

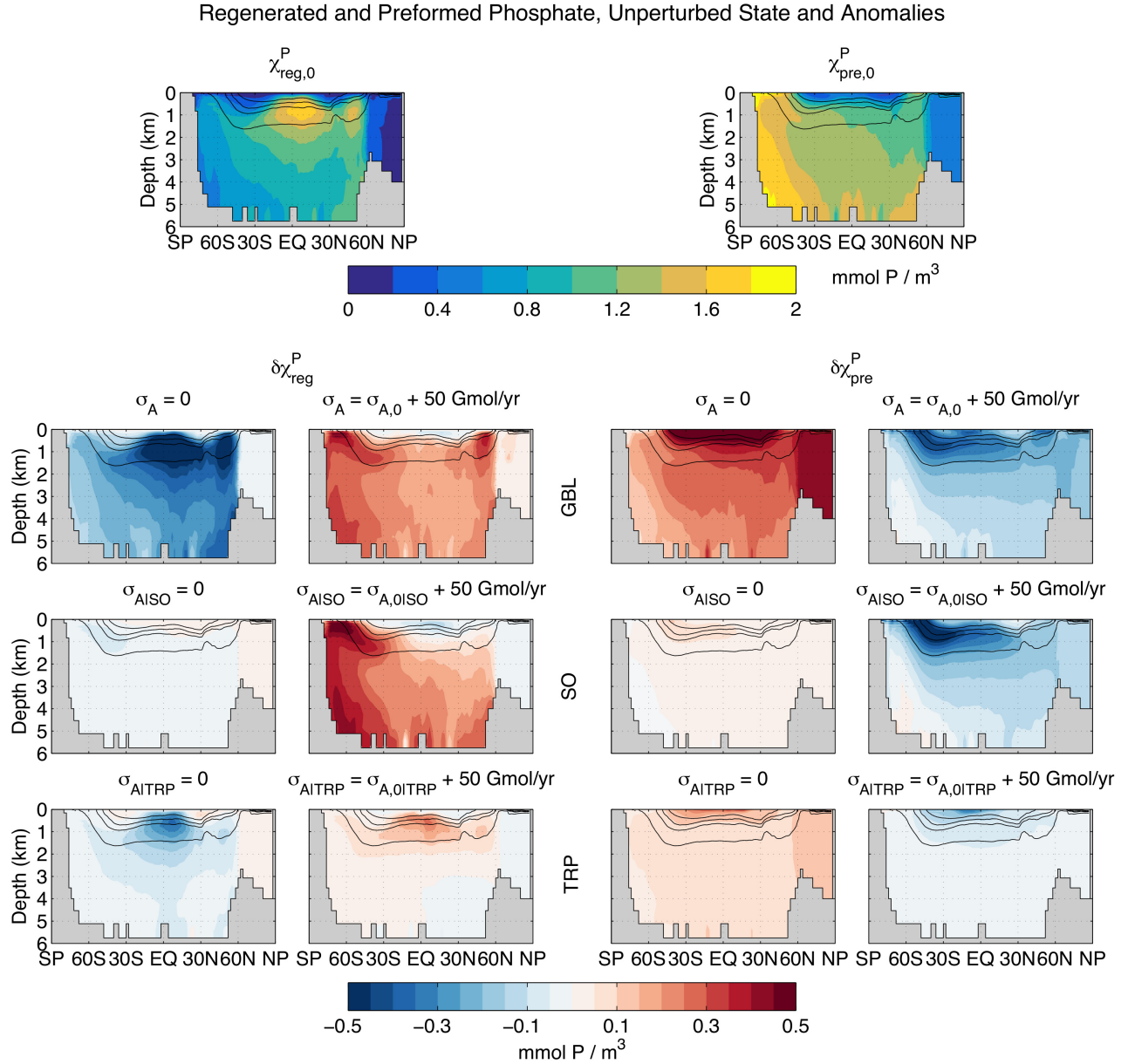


Figure 3.10: Global zonal averages of the regenerated and preformed phosphate for the unperturbed state (top) together with the anomalies for large perturbations of the typical state. Left columns: Shutdown of the aeolian iron source in the perturbation region indicated (GBL, SO, TRP). Right columns: Spatially uniform addition of 50 Gmol yr^{-1} to the aeolian iron source in the perturbation region. The black contours indicate the σ_0 isopycnals at $26.6, 27.0, 27.2$, and 27.6 kg m^{-3} .

($\sim 0.1 \text{ mmol m}^{-3}$) regenerated PO_4 can be seen to extend with AAIW. The reduced export implies that the Southern Ocean “leaks” a bit more and thus the corresponding preformed PO_4 response is a slight increase in SAMW, which supplies nutrients to low latitudes [e.g., Sarmiento *et al.*, 2004].

For the TRP shutdown, the zonal mean response is similar to that for the GBL shutdown, albeit with a lower magnitude and with an increase in subsurface regenerated PO_4 in the subtropics, due to the slightly increased carbon export in the subtropical gyres (Figure 3.7). Decreased carbon export in the tropics increases the preformed PO_4 content of tropical surface waters.

Response to Aeolian Iron Addition Instead, the response to GBL and SO aeolian iron additions occurs primarily in the intermediate and bottom waters of the Southern Ocean, where regenerated PO_4 increases by as much as 0.6 mmol m^{-3} . This suggests a strengthening of Southern Ocean PO_4 trapping for the GBL and SO perturbations, which is supported by the strongly increased Southern Ocean carbon export (Figure 3.7) and consistent with the accompanying slight decreases of regenerated PO_4 in mode waters. The GBL case also shows an increase in regenerated PO_4 in the North Pacific with a spatial structure similar to the Southern Ocean response, suggesting increased nutrient trapping occurs also in the North Pacific. The preformed phosphate response to the GBL and SO aeolian additions is a strong decrease in AAIW and SAMW, as expected from increased nutrient utilization that partially “plugs” the leak in the Southern Ocean and promotes stronger trapping.

The response of regenerated and preformed PO_4 to the TRP aeolian addition is almost a mirror image of the response to the TRP shutdown. The TRP addition increases regenerated PO_4 in old upwelling waters due to the increase in tropical carbon export. The increases extend to the polar oceans of both hemispheres in intermediate waters. The TRP addition decreases preformed PO_4 in surface waters due to more efficient biological utilization.

Regenerated and Preformed Silicic Acid

Figure 3.11 shows the regenerated and preformed silicic concentrations, $\chi_{\text{reg}}^{\text{Si}}$ and $\chi_{\text{pre}}^{\text{Si}}$, zonally averaged over the global ocean, for the typical unperturbed state, together with the corresponding anomalies, $\delta\chi_{\text{reg}}^{\text{Si}}$ and $\delta\chi_{\text{pre}}^{\text{Si}}$, due to the aeolian shutdown and 50 Gmol yr^{-1} increase perturbations. Because opal dissolution occurs deeper in the water column than phosphorus remineralization, regenerated Si(OH)_4 is mostly found deeper in the ocean. Most of the ocean’s preformed silicic acid is supplied by the Southern Ocean south of the Antarctic divergence [Holzer *et al.*, 2014], and is hence found primarily in deep ocean. Because opal export is well constrained for each member of our family of es-

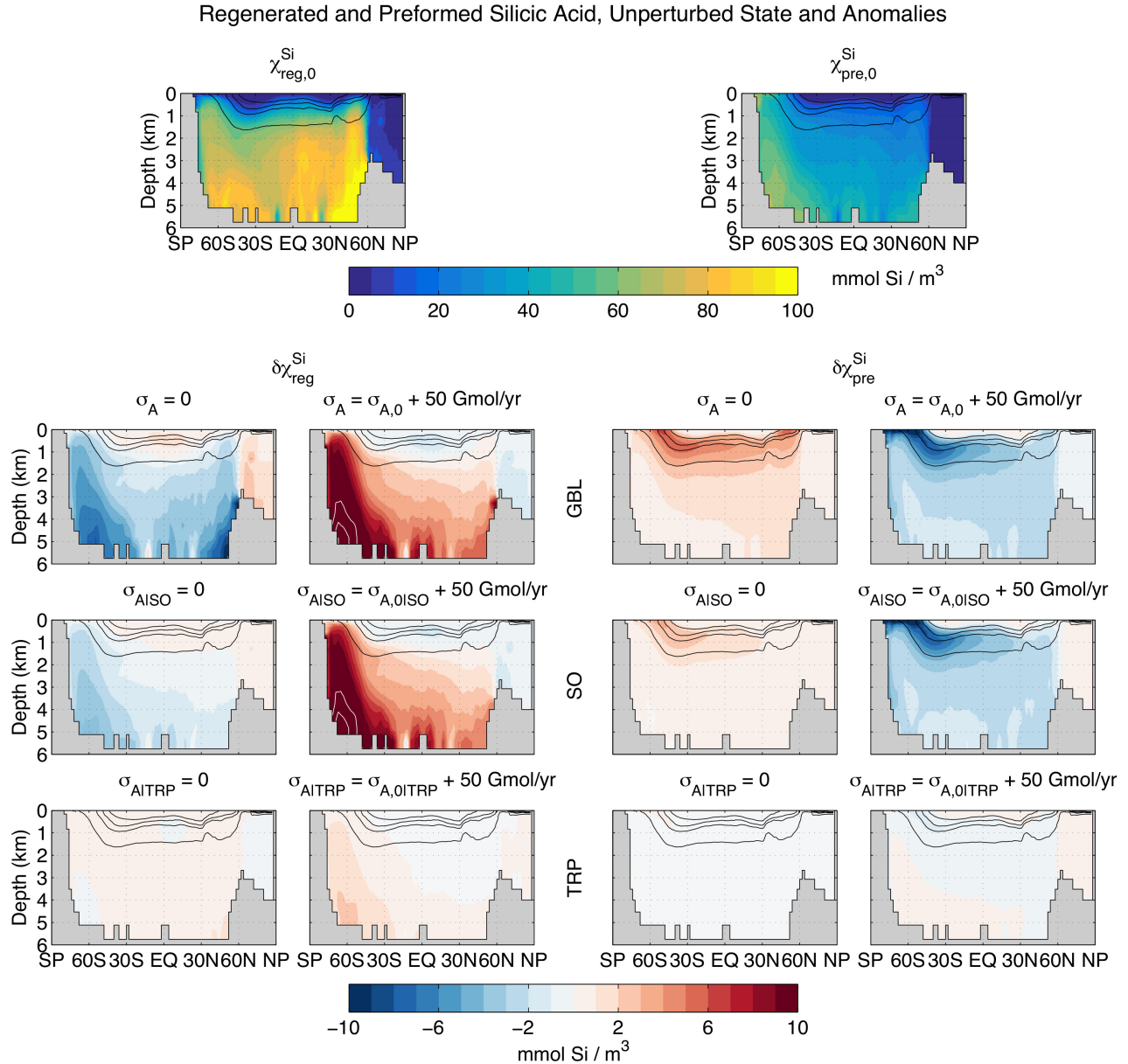


Figure 3.11: Global zonal averages of the regenerated and preformed silicic acid for the unperturbed state (top) together with the anomalies for large perturbations of the typical state. Left columns: Shutdown of the aeolian iron source in the perturbation region indicated (GBL, SO, TRP). Right columns: Spatially uniform addition of 50 Gmol yr^{-1} to the aeolian iron source in the perturbation region. The black contours indicate the isopycnals as in Figure 3.10.

timates (Chapter 2), the distributions of regenerated and preformed silicic acid are virtually the same for the unperturbed typical state and for the high- and low-aeolian estimates (not shown). As for PO_4 , we therefore focus on the perturbations of the typical state.

Response to Aeolian Iron Shutdown The GBL case results in a decrease in $\chi_{\text{reg}}^{\text{Si}}$ of up to 10 mmol m^{-3} in the deep North Pacific and of up to 7 mmol m^{-3} in the deep Southern Ocean, together with a slight increase in surface and mode waters. This is due to the reduced opal export in the Southern Ocean (Figure 3.7) The GBL shutdown increases preformed Si(OH)_4 by up to 5 mmol m^{-3} leaking out of the Southern Ocean with intermediate and mode waters, due to less efficient utilization in the Southern Ocean.

For the SO shutdown, the relatively smaller reduction in SO opal export results in a mere $\sim 2\text{--}3 \text{ mmol m}^{-3}$ reduction in regenerated Si(OH)_4 in the deep Southern Ocean, together with an even smaller increase in surface and mode waters. Similar to the GBL shutdown, the SO shutdown also causes increased leakage of preformed Si(OH)_4 with AAIW and SAMW.

The TRP shutdown has little effect on opal export. Correspondingly there is only a very weak response of order 1 mmol m^{-3} in the regenerated and preformed distributions.

Response to Aeolian Iron Addition GBL and SO additions have very similar responses, because opal export is concentrated in the Southern Ocean. Both perturbations result in a large increase in regenerated Si(OH)_4 of up to 20 mmol m^{-3} in the deep Southern Ocean, with increases of $\sim 5 \text{ mmol m}^{-3}$ extending into the deep North Pacific. This suggests increased Southern Ocean trapping as expected for increased SO opal export. The regenerated response in the Northern Hemisphere is stronger for the GBL aeolian addition as this also fertilizes the North Pacific, increasing its opal export. Up to 10 mmol m^{-3} decreases in preformed Si(OH)_4 with SAMW and AAIW result from the GBL and SO 50 Gmol yr^{-1} additions, which both increase Si(OH)_4 utilization in the Southern Ocean, “plugging” some of the Southern Ocean leakage.

For the TRP addition, which barely affects opal export (Figure 3.7), there is only a weak increase in regenerated Si(OH)_4 of up to 3 mmol m^{-3} in the deep Southern Ocean, and a weak globally distributed decrease of order 1 mmol m^{-3} in preformed Si(OH)_4 . This is because the TRP aeolian addition increases opal export south of 35°S . However, as for the TRP aeolian shutdown, this effect is weak compared to the GBL and SO perturbations.

3.3.2 Mechanisms of the Response

3.3.2.1 Southern Ocean Nutrient Trapping

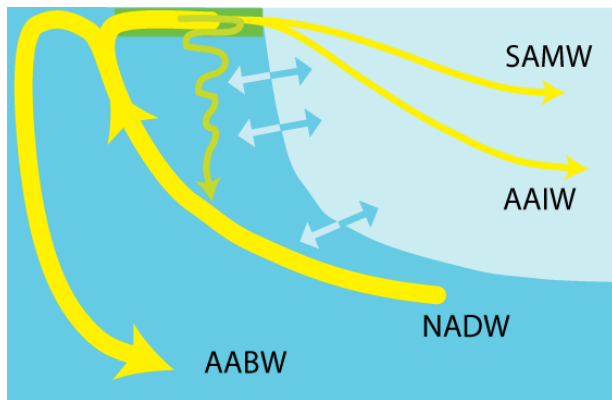


Figure 3.12: Schematic of Southern Ocean nutrient trapping. The large-scale advective transport (smooth yellow arrows) combined with the biogenic transport of regenerating nutrients at depth (serpentine yellow-green arrow) result in a convergence of nutrients in the Southern Ocean. Diapycnal mixing by eddy-diffusion (blue arrows) establishes a balance between trapping and escape that prevents complete Southern Ocean nutrient trapping.

Nutrients can be trapped in a region of the ocean when the biogenic particle transport short-circuits the transport of preformed nutrients out of the region by injecting regenerated nutrients into sub-surface convergent flow that returns the nutrients to the region's euphotic zone. Large-scale nutrient trapping is most pronounced in the Southern Ocean, where biological production strips nutrients out of the formation region of northward flowing mode and intermediate waters and injects organic matter into upwelling CDW, where the nutrients are remineralized and returned back to the Southern Ocean euphotic zone. This mechanism would draw ever more nutrients into the Southern Ocean if it were not balanced by eddy-diffusive transport out of the Southern Ocean when the concentration gradients at the edge of the trapping region become sufficiently high (see the schematic of Figure 3.12 similar to the schematic of Primeau *et al.* [2013]).

The response of the Southern Ocean phosphate trap to idealized nutrient drawdown experiments was investigated by Primeau *et al.* [2013] using the same data-constrained circulation used here. Holzer and Primeau [2013] quantified the phosphate pathways that connect the Southern Ocean to itself and to the North Atlantic and how these pathways change with increased Southern Ocean nutrient utilization. Silicic acid is trapped more strongly in the Southern

Ocean than phosphate, and *Holzer et al.* [2014] quantified the Southern Ocean silicon trap in terms of the density of paths between successive silicic-acid utilizations in the Southern Ocean.

Changes in Southern Ocean nutrient trapping due to changes in the aeolian iron supply is the predominant mechanism driving the redistribution of PO_4 and Si(OH)_4 in response to the perturbed biological utilization. Here, we employ the path density diagnostic (as used in Chapter 1) to elucidate how the trapped $\text{SO} \rightarrow \text{SO}$ nutrient paths respond to perturbations of the aeolian source for the typical state estimate of Chapter 2.

The phosphate and silicic acid $\text{SO} \rightarrow \text{SO}$ pathways between successive up-takes are quantified by their path densities, $\eta^{\text{P}}(\mathbf{r}|\text{SO} \rightarrow \text{SO})$ and $\eta^{\text{Si}}(\mathbf{r}|\text{SO} \rightarrow \text{SO})$ [e.g., *Holzer and Primeau*, 2013; *Holzer et al.*, 2014, and Chapter 1]. The path density, $\eta^i(\mathbf{r}|\text{SO} \rightarrow \text{SO})$, is defined as the concentration of nutrient i at location \mathbf{r} that was last taken up in the Southern Ocean, and that will next be taken up in the Southern Ocean. Using Green-function techniques, these path densities are easily computed in our model (details in Appendix 3.B.2).

Phosphate $\text{SO} \rightarrow \text{SO}$ Pathways

The left plots of Figure 3.13 show the $\text{SO} \rightarrow \text{SO}$ path densities of PO_4 , zonally averaged over the global ocean, for the typical unperturbed state, together with their anomalies due to both the aeolian shutdown (left column) and the 50 Gmol yr^{-1} increase (right column) perturbations. For the unperturbed typical state, most of the PO_4 trapped in $\text{SO} \rightarrow \text{SO}$ transit between successive up-takes lies close to the Southern Ocean surface or within AAIW and AABW. The trapped PO_4 pathways explore most of the deep ocean, extending into the deep North Pacific, where trapped PO_4 molecules can linger and accumulate for centuries before returning to the Southern Ocean surface (similar to the long-timescale $\text{SO} \rightarrow \text{SO}$ paths of Chapter 1) with the deep overturning circulation of the Pacific.

The GBL aeolian shutdown results in a slight decrease of phosphate $\text{SO} \rightarrow \text{SO}$ path density where it is large in the unperturbed state. This decrease is due to the small reduction in SO biological production. The decrease in $\text{SO} \rightarrow \text{SO}$ phosphate path density is concentrated near the SO surface (about -0.3 mmol m^{-3}) but extends into the deep North Pacific (about -0.1 mmol m^{-3}). For the SO shutdown, there is a similar but lower amplitude pattern of path density decrease due to the lower magnitude of the SO production decrease. In the TRP shutdown case, which barely affects SO production, the response is negligible.

The GBL and SO 50 Gmol yr^{-1} aeolian additions significantly increase SO trapping because of the large increase in SO production resulting from iron fertilization. For the GBL increase, the concentration of PO_4 in $\text{SO} \rightarrow \text{SO}$ transit

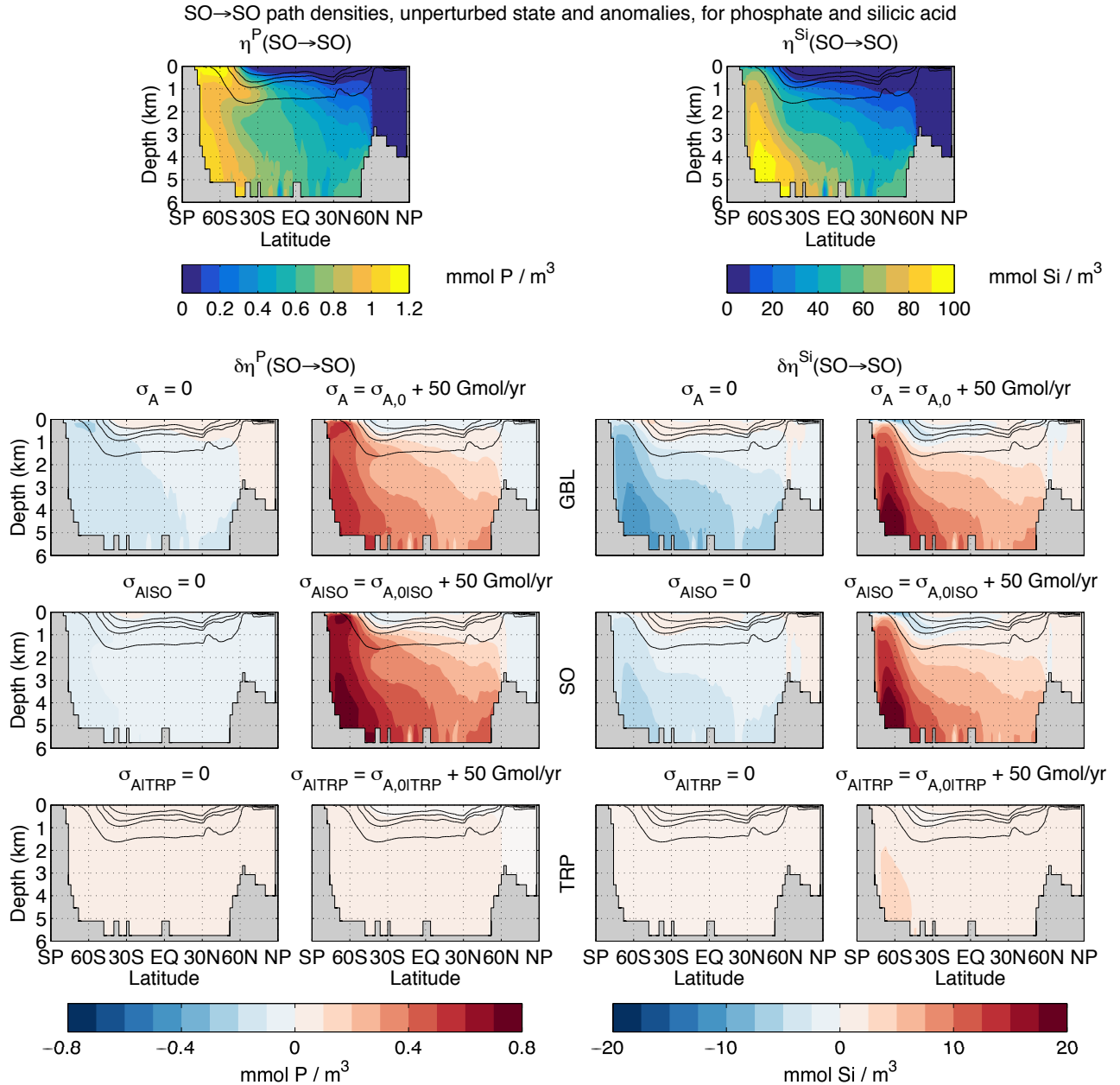


Figure 3.13: Global zonal averages of the SO \rightarrow SO uptake-to-uptake path densities of phosphate (left) and silicic acid (right) for the unperturbed state together with their anomalies for the aeolian shutdown and the 50 Gmol yr^{-1} aeolian increase in the perturbation region indicated (GBL, SO, TRP). The black contours indicate the isopycnals as in Figure 3.10.

increases by up to 0.5 mmol m^{-3} , i.e., with a similar magnitude to the regenerated PO_4 increase for the same perturbation. For the SO iron addition, the increase in trapped PO_4 is larger, reaching 0.8 mmol m^{-3} near the SO surface and in AABW, also similar in magnitude to the corresponding regenerated PO_4 increase. This also confirms that the regenerated PO_4 increase, for the GBL and SO aeolian addition cases, is due to increased SO phosphate trapping. Both the GBL and SO responses are qualitatively and quantitatively consistent with the results of *Holzer and Primeau* [2013] who explored the response of the SANTZ \rightarrow SANTZ phosphate for increased SANTZ production¹. For the TRP aeolian addition, the response is again negligible.

Silicic Acid SO \rightarrow SO Pathways

The right half of Figure 3.13 shows the SO \rightarrow SO path densities of silicic acid together with their anomalies. Opal dissolves in the deep overturning cell of the Pacific and in upwelling CDW, which return regenerated Si(OH)_4 to the Southern Ocean euphotic zone. In the unperturbed state, Southern Ocean trapping is stronger for silicic acid than for phosphate, due to the deeper redissolution of opal [*Holzer et al.*, 2014] resulting in a more efficient silicon biological pump in the Southern Ocean compared to the carbon pump (i.e., in a higher percentage of regenerated nutrient).

The GBL and SO aeolian shutdowns decrease the amount of Si(OH)_4 that is regenerated in upwelling CDW and thus decrease the SO \rightarrow SO silicic acid where it is large in the unperturbed state. However, the response to the SO shutdown is of lower magnitude than the response to the GBL shutdown. Both the GBL and SO aeolian shutdowns increase the concentrations of SO-trapped Si(OH)_4 in SAMW because the opal export actually slightly increased north of $\sim 45^\circ\text{S}$ in response to the decreased aeolian fertilization. The decreases in SO \rightarrow SO Si(OH)_4 path densities are concentrated in the deep Southern Ocean (about -10 mmol m^{-3} for the GBL shutdown) and extend into the deep North Pacific (about -5 mmol m^{-3} for the GBL shutdown), a response overall located deeper in the ocean than the corresponding response of trapped PO_4 . Because the TRP shutdown barely affects SO opal production, its trapping response is negligible.

The increases in the SO \rightarrow SO silicic-acid path density reach up to 20 mmol m^{-3} and are concentrated in the deep Southern Ocean (AABW and CDW) reflecting increased deep opal dissolution in response to iron fertilization. The changes in the path density for the GBL and SO cases are almost

¹In [*Holzer and Primeau*, 2013], the Subantarctic zone (SANTZ) is the Southern Ocean region between 40°S and the local latitude of maximum Ekman divergence, so that the SANTZ region can be considered as the formation region of AAIW and SAMW.

identical because iron fertilization outside of the Southern Ocean has minimal impact on opal export as was seen in Figures 3.7 and 3.8. The dipolar response of Southern Ocean opal export to iron fertilization (Figures 3.7 and 3.8), which actually decreases opal export between ~ 40 and 50°S , is reflected in the response of the silicon path density: The $\text{SO} \rightarrow \text{SO}$ silicon path density decreases in SAMW in response to the 50 Gmol yr^{-1} iron addition because reduced uptake in the formation region of SAMW means fewer $\text{SO} \rightarrow \text{SO}$ uptake-to-uptake paths explore this water mass.

Because aeolian perturbations mostly affect opal production in the Southern Ocean, the regenerated Si(OH)_4 response is dominated by silicic acid last utilized in the Southern Ocean. As a consequence, the responses of regenerated and SO-trapped silicic acid, to both the GBL and SO aeolian additions, are also almost identical. This underlines SO silicon trapping as the key mechanism for controlling the redistribution of silicic acid in response to perturbed biological production. (For the TRP aeolian addition, there is again almost no response.)

We note that the increases of opal export and Southern Ocean silicon trapping for increased iron supply are just attenuated by decreases in our diatom Si:P ratio, and thus do not result in silicic acid leakage out of the Southern Ocean. This goes against the findings of *Matsumoto et al.* [2002] and *Brzezinski et al.* [2002], which suggest that iron addition results in a decrease of Southern Ocean opal export, and hence leakage of preformed silicic acid into AAIW and SAMW. We acknowledge that changes of our diatom Si:P uptake ratio are entirely dependent on the parameters optimized in Chapter 2, but the sensitivity of the silicon pump to these parameters is beyond the scope of this study.

Response of SO Trapping Metrics

The changes of the path density discussed in the previous section can conveniently be summarized by two global metrics of nutrient trapping. The first metric, R_{trap} , is simply the global volume integral of the $\text{SO} \rightarrow \text{SO}$ uptake-to-uptake path density normalized by the global silicic-acid inventory. R_{trap} thus relates directly to the patterns discussed in the previous section and quantifies the fraction of the phosphate and silicic-acid inventory that is in transit between successive SO utilizations. The second metric, E_{trap} , is the fraction of the $\text{SO} \rightarrow \text{SO}$ flow rate to the $\text{SO} \rightarrow \text{GBL}$ flow rate of nutrients in transit between successive utilizations. While E_{trap} does not directly relate to the patterns of the previous section, it has the interpretation of being the probability that a nutrient molecule last taken up in the Southern Ocean will experience its next utilization again in the Southern Ocean, which can be used to estimate the expected number of successive utilizations in the Southern Ocean before the nutrient “escapes” the trap [*Holzer et al.*, 2014]. For details of the calculation of

both metrics, see Appendix 3.B.2.

Figure 3.14 plots both Southern Ocean trapping metrics for both phosphorus ($R_{\text{trap}}^{\text{P}}$, $E_{\text{trap}}^{\text{P}}$) and silicon ($R_{\text{trap}}^{\text{Si}}$, $E_{\text{trap}}^{\text{Si}}$) as a function of the aeolian source strength of the perturbation region. For the unperturbed states we find that $R_{\text{trap}}^{\text{P}} = (25 \pm 2)\%$, $E_{\text{trap}}^{\text{P}} = (76 \pm 2)\%$, $R_{\text{trap}}^{\text{Si}} = (41 \pm 2)\%$, and $E_{\text{trap}}^{\text{Si}} = (84 \pm 1)\%$ for the typical, high-aeolian, and low-aeolian estimates. Our silicon trapping metrics are lower than the estimates obtained by *Holzer et al. [2014]* of $R_{\text{trap}}^{\text{Si}} = (49 \pm 2)\%$ and $E_{\text{trap}}^{\text{Si}} = (95 \pm 2)\%$ because of our weaker opal export in the Southern Ocean (see Figure 2.7, Chapter 2). Conversely, for phosphate, our estimates are larger than the estimates from *Holzer et al. [2014]* of $R_{\text{trap}}^{\text{P}} = (15 \pm 1)\%$ and $E_{\text{trap}}^{\text{P}} = (56 \pm 2)\%$, which is explained by our stronger SO carbon export compared to the phosphorus cycling model of *Primeau et al. [2013]* (also Figure 2.7, Chapter 2).

For the GBL and SO perturbations, the responses of the PO_4 and Si(OH)_4 trapping metrics are strongly correlated with the response of the biological pump efficiencies (3.9). This is because changes in carbon and opal export are concentrated in the Southern Ocean for these perturbations. The GBL and SO shutdowns cannot completely untrap PO_4 and Si(OH)_4 because the reduced SO scavenging allows sedimentary and hydrothermal iron to sustain surface dFe and production in the Southern Ocean. Conversely, large GBL and SO aeolian iron increases do not completely trap PO_4 and Si(OH)_4 in the Southern Ocean because increased SO scavenging compensates aeolian iron supply and prevents SO surface dFe to sufficiently increase for SO production saturation, and because eddy-diffusion prohibits arbitrarily large lateral gradients. The compensating effects of the changes in Si:P uptake ratios additionally prevent large increases and decreases of the silicon trap for GBL and SO perturbations. The response of SO trapping metrics to TRP perturbations is negligible, similar to the response of SO carbon and opal export.

Also similar to the response of carbon and opal export, the response of R_{trap} and E_{trap} to changes in aeolian iron supply are sensitive to the choice of the initial unperturbed state. The largest sensitivity shows for decreases in aeolian iron supply of the high-aeolian estimate, and for the aeolian iron addition to the low-aeolian estimate.

3.3.2.2 Interior Distribution and Pathways of Dissolved Iron

Perturbations in the aeolian iron supply change biological production and thus drive the redistribution of the macronutrients that we saw in the previous section. However, the responses teleconnected to the aeolian perturbation region are in part driven by the long-range transport of aeolian dFe. *Holzer et al. [2016]* showed that some 70 % of the aeolian iron in the Southern Ocean euphotic zone

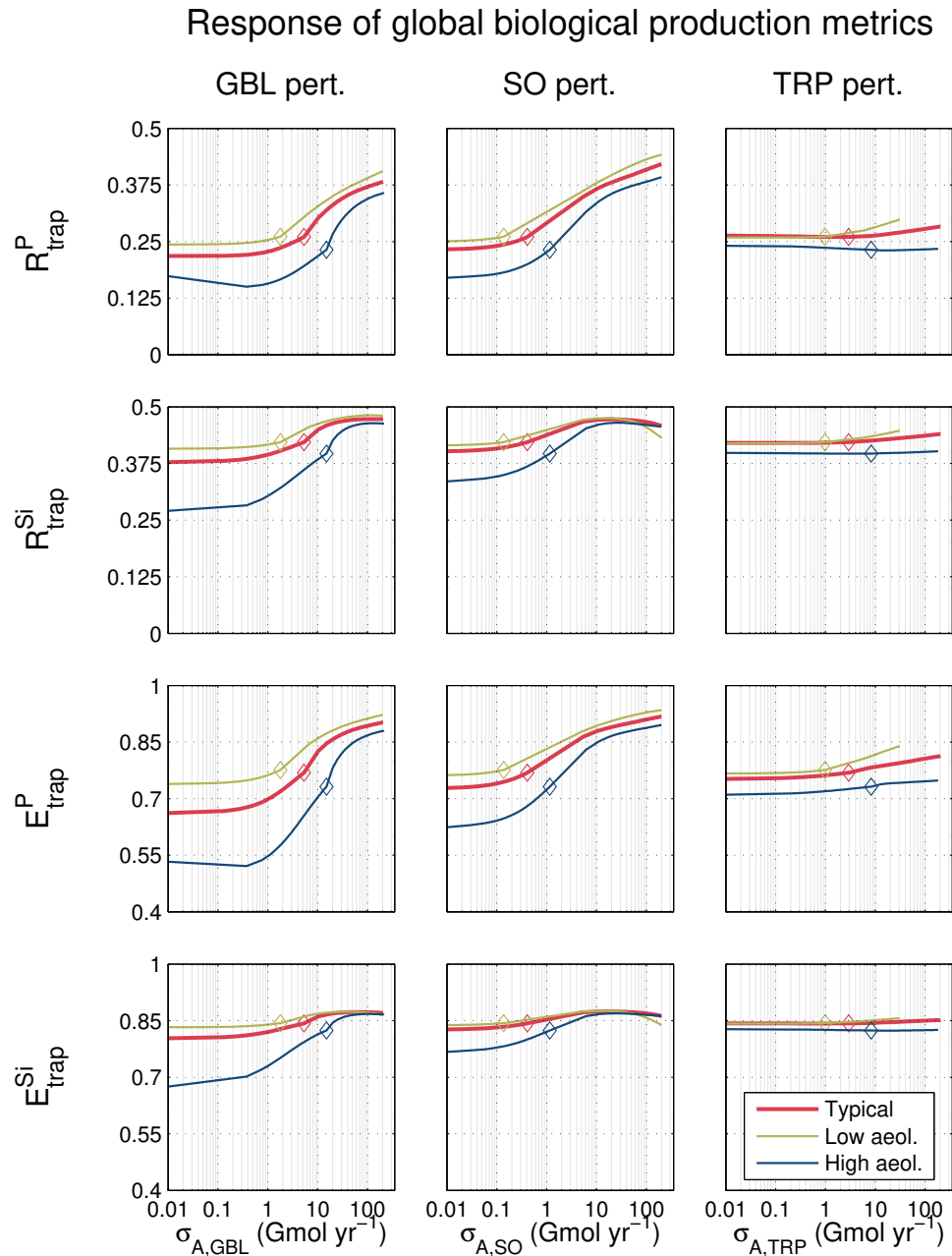


Figure 3.14: Trapping metric, R_{trap}^i , and trapping efficiency, E_{trap}^i , for phosphate and silicic acid, as a function of the perturbed aeolian source. The unperturbed states are indicated by diamonds.

is upwelled old iron that was deposited north of 40°S. Thus, increasing tropical aeolian iron deposition may be expected to affect Southern Ocean production, provided that the additional dFe can escape the enhanced scavenging driven by the tropical fertilization. Conversely, the Southern Ocean is known to supply the tropics with preformed nutrients in mode and intermediate waters [e.g., Sarmiento *et al.*, 2004], so that increasing the Southern Ocean iron supply can be expected to also increase transport of dFe from the Southern Ocean to the tropics. We begin by examining the changes in the interior dFe distribution and then quantify the interior pathways of dFe and how they change in response to perturbations in the aeolian source.

Interior Dissolved Iron

Because a fraction of dFe can avoid scavenging and eventually reemerge from the aphotic zone to fertilize biological production, we examine the response of the interior dFe concentrations to aeolian iron source perturbations. Figure 3.15 shows the dFe concentrations, χ^{Fe} , zonally averaged over the global ocean for the typical unperturbed state, together with the corresponding anomalies, $\delta\chi^{\text{Fe}}$, due to the aeolian perturbations. For the unperturbed state, the maximum dFe concentrations are found in the tropics at about 2000–3000 m depth. The basin zonal averages shown in Figure 2.9 of Chapter 2 show that this is the result of the high concentrations of the north Indian Ocean where aeolian input is large, of the Pacific old waters where scavenging is reduced by the elevated ligand protection, which allows iron to accumulate, and of the hydrothermal iron injected at mid-depths [e.g., Frants *et al.*, 2016].

Response to Aeolian Iron Shutdown For the GBL case, dFe is reduced predominantly in the upper ocean. In the subtropical gyres, almost all surface dFe is removed, as already seen in Figure 3.2. This dFe reduction is propagated below the thermocline by large-scale downwelling in the subtropical gyres but attenuates with depth, reaching ~40 % below 1000 m depth. In the deep ocean, losses in aeolian dFe are compensated by an increase in sedimentary and hydrothermal dFe, due to decreases in aeolian-fertilization-driven scavenging. The dFe reduction in the deep ocean extends into the Northern Hemisphere due to NADW, which is lower in dFe compared to the unperturbed state.

Because there is little aeolian deposition into the Southern Ocean in the unperturbed state, the SO shutdown has little effect on the interior dFe distribution. Only a small Southern Ocean surface dFe reduction (by about 20 %, Figure 3.2) extends to ~1000 m into intermediate and mode waters but limited mostly to the Southern Ocean. Additionally, the reduced SO export produc-

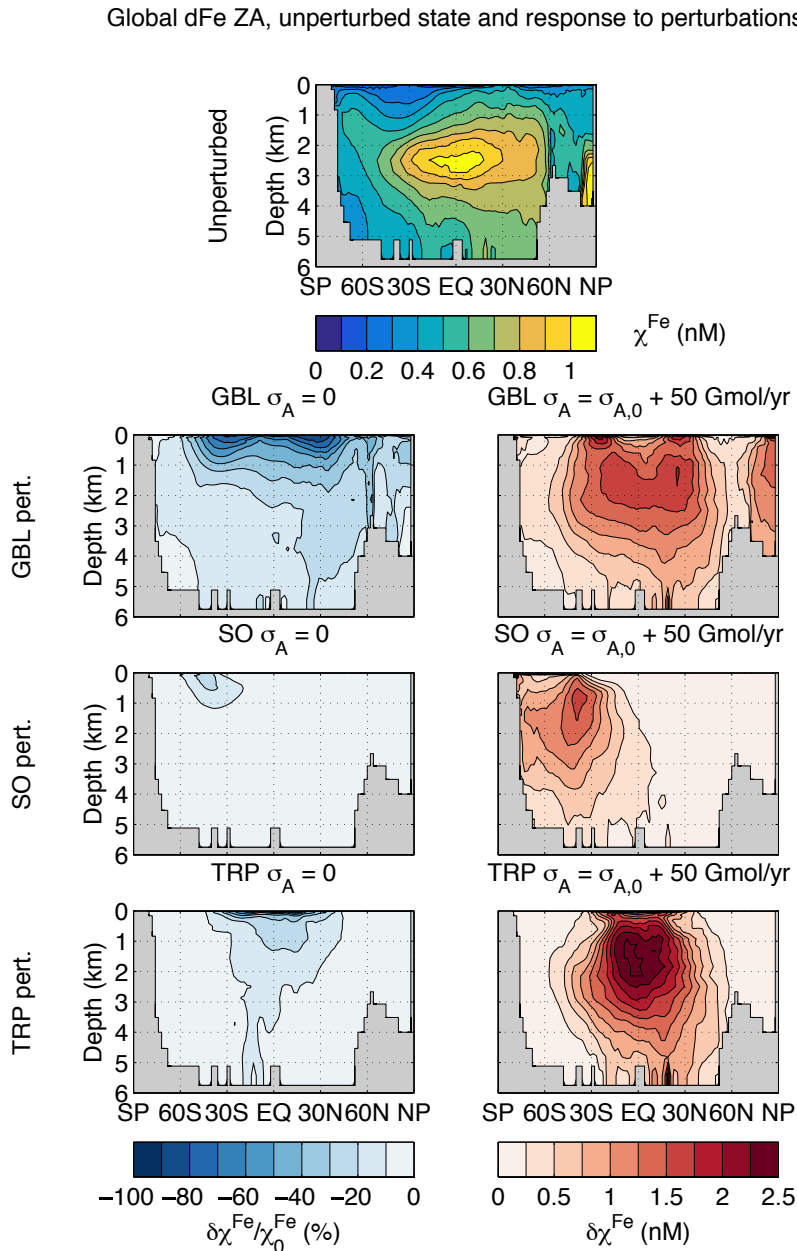


Figure 3.15: Global zonal averages of dFe for the unperturbed state (top) together with the anomalies for large perturbations of the typical state. Left column: Shutdown of the aeolian iron source in the perturbation region (GBL, SO, TRP). Right column: Spatially uniform additions of 50 Gmol yr^{-1} aeolian iron to the perturbation regions.

tion reduces scavenging, allowing more sedimentary and hydrothermal dFe to upwell with CDW, thus compensating for the loss of aeolian dFe.

The TRP shutdown has little effect on dFe away from the surface. The surface dFe reduction within 40°S–40°N (Figure 3.2) rapidly attenuates with depth. This is consistent with reduced regenerated and recycled iron when the tropical export decreases (Figure 3.7).

Response to Aeolian Iron Addition The GBL and TRP cases significantly increase surface dFe in the subtropical gyres (Figure 3.2) where production and hence scavenging remain low, even as iron is added to the system (Figures 3.7 and 3.8). As a result, downwelling in the subtropical gyres propagates the strong surface dFe increases several hundred meters below the subtropical gyres. The GBL and TRP additions increase deep dFe concentrations in the tropics and subtropics. These increases are due to the enhanced dFe remineralization from the increased tropical particle export and remineralization underneath the fertilized regions, and enhanced deep redissolution of dFe from remineralizing scavenging particles. (Recall 90 % of scavenged dFe can be recycled – for details, see Chapter 2.) The increased dFe concentrations at depth are the result of these interior sources of dFe (remineralization and recycling) in an environment where scavenging is low. The scavenging higher in the water column produces the minimum in dFe concentrations around 500 m depth.

The equatorial response is stronger for the TRP increase than for the GBL increase because the GBL fertilization reduces export production and scavenging in the subtropical gyres (Figure 3.7), reducing deep subtropical regeneration and recycling of dFe. However, the deep dFe increases for the GBL addition spread to higher latitudes because the high-latitude increases in carbon export, which supplies regenerated and recycled scavenged dFe to the deep ocean, are larger for the GBL addition than for the TRP addition.

For the SO addition, the dramatic increases in SO carbon export supplies more regenerated and recycled scavenged dFe to the deep Southern Ocean than is the case for the GBL addition. The maximum just northward of the SO perturbation region is due to accumulation in the low productivity and hence low scavenging southern edge of the South Pacific subtropical gyre.

TRP→SO and SO→TRP Iron Pathways

To investigate the long-range transport of iron from the perturbed source region, we quantify the pathways of aeolian dFe from the tropics to the Southern Ocean, and from the Southern Ocean to the tropics. To this end we define the $\Omega_i \rightarrow \Omega_f$ iron path density as the density of dFe that was deposited from the atmosphere into region Ω_i and that is destined for uptake in region Ω_f .

A key difference from the path densities discussed so far, aside from deposition taking the role of uptake at the beginning of the paths, is that we only terminate the path on uptake in the destination region, regardless if the iron molecules were utilized and regenerated en route to the destination region. In other words, for the macronutrients, we labeled nutrient molecules on uptake and then unlabeled them on first subsequent uptake, while here we unlabel iron only when taken up in the destination region. We refer to these paths of aeolian dFe as “deposition-to-uptake” paths. (We do not partition dFe into preformed and regenerated iron here, reserving that subject for a future publication that is beyond the scope of this thesis.)

Figure 3.16 shows TRP→SO (left) and SO→TRP (right) deposition-to-uptake iron path densities, zonally averaged over the global ocean, for the typical unperturbed state (top) and for the perturbed states due to the aeolian source perturbations. Note that the scale of these path densities is 2–3 orders of magnitude smaller than the mean dFe concentrations. This is because the path density is the density of only the subset of dFe molecules that were deposited in Ω_i and are destined for uptake in Ω_f . A significant fraction of dFe molecules will be scavenged before being taken up on Ω_f or will have originated from a different region.

TRP→SO Iron Pathways For the unperturbed state, the zonally averaged deposition-to-uptake TRP→SO path density displays three local maxima. One maximum lies just below the South Pacific subtropical gyre where TRP→SO dFe molecules can reach high concentrations without being scavenged. The other two maxima lie in the density class of AAIW between $\sim 30^\circ\text{S}$ and the equator, and in upwelling CDW in the Southern Ocean.

The maximum of the TRP→SO iron path density lies primarily in the Atlantic and the Indian Oceans, where aeolian deposition is high. (This was visible in horizontal slices of the path density, not shown.) Transport in the Pacific plays a minor role due to the small tropical Pacific aeolian deposition in the unperturbed state. In the Atlantic, the TRP→SO path density shows that NADW carries TRP-deposited dFe into upwelling CDW. In the Indian Ocean, where the aeolian source is large but biological production is relatively weak, TRP-deposited dFe disperses throughout the entire basin before upwelling and utilization in the Southern Ocean.

For the GBL and TRP shutdowns, the TRP→SO iron pathways disappear because the aeolian injection in the TRP region has been zeroed. For the SO shutdown, the reduced SO biological production and scavenging allows more dFe to upwell in CDW, thus increasing the TRP→SO iron path density.

For the GBL addition, the effects of the increased tropical iron on the

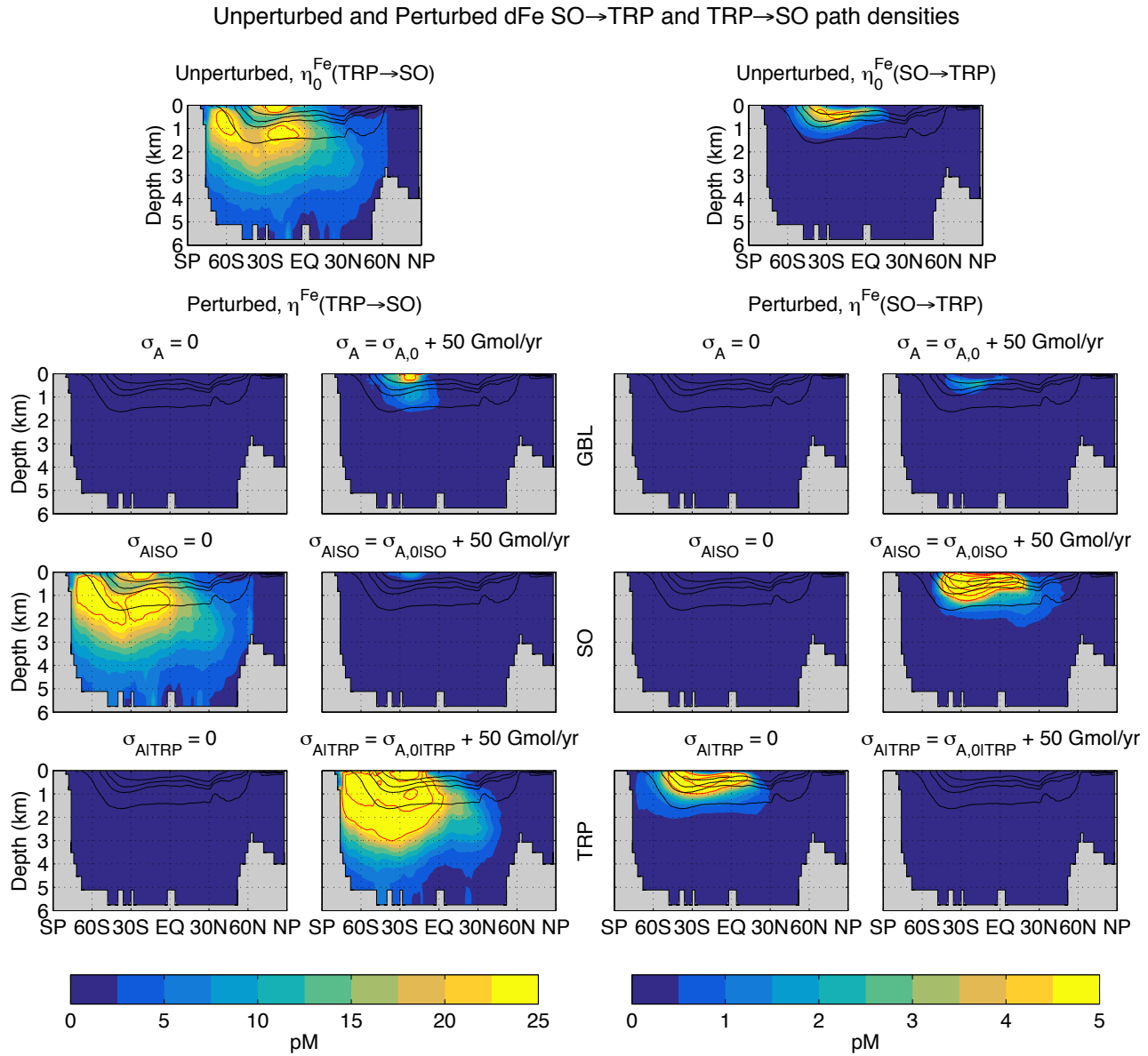


Figure 3.16: Left half: Global zonal averages of the TRP \rightarrow SO iron path densities, from aeolian deposition to uptake, for the unperturbed state (top) together with the responses to the aeolian shutdown and the 50 Gmol yr $^{-1}$ aeolian addition in the perturbation region indicated (GBL, SO, TRP). Red contours indicate 25, 50, and 100 pM. Right half: Same for the SO \rightarrow TRP iron path densities with red contours indicating 5, 10, 20, and 40 pM. The black contours indicate the isopycnals as in Figure 3.10.

$\text{TRP} \rightarrow \text{SO}$ iron paths are overwhelmed by increased SO scavenging, which removes dFe from upwelling CDW. As a consequence, the deep pathways of the Atlantic and Indian ocean to uptake in the Southern Ocean almost completely disappear, and the near surface path density in the subtropics is reduced. Similarly, the SO addition, which dramatically increases scavenging in the Southern Ocean, prevents even more TRP-deposited dFe from reaching the euphotic zone of the Southern Ocean, almost removing all $\text{TRP} \rightarrow \text{SO}$ deposition-to-uptake paths.

Adding 50 Gmol yr⁻¹ of aeolian iron to the TRP region strongly increases the $\text{TRP} \rightarrow \text{SO}$ deposition-to-uptake iron path density, as now many more paths start in the TRP region. The TRP addition also increases Southern Ocean export and decreases subtropical export, both by order 10 %, with corresponding changes in scavenging, but these effects are overwhelmed by the strong increase in deposition. In the deep subtropical ocean the $\text{TRP} \rightarrow \text{SO}$ path density increases about fourfold.

SO \rightarrow TRP Iron Pathways The unperturbed $\text{SO} \rightarrow \text{TRP}$ iron path density is concentrated in SAMW and AAIW which carry SO-deposited dFe into the eastern upwelling regions of the Atlantic and Pacific basins (visible in horizontal slices through the path density, not shown). Because SO aeolian deposition is weak in the unperturbed state, and because these short pathways are associated with shorter timescales than deep pathways, the $\text{SO} \rightarrow \text{TRP}$ path density is an order of magnitude smaller than the $\text{TRP} \rightarrow \text{SO}$ path density. (Recall short-timescale/fast pathways contribute less to long-range $\Omega_i \rightarrow \Omega_f$ path densities – see Figures 1.8 and 1.9, Chapter 1.)

For the GBL and SO shutdowns, which both turn off SO aeolian deposition, $\text{SO} \rightarrow \text{TRP}$ iron paths disappear. The TRP shutdown, which largely reduces scavenging in the productive tropical regions, increases dFe in $\text{SO} \rightarrow \text{TRP}$ transit about twofold.

For the GBL addition, the $\text{SO} \rightarrow \text{TRP}$ iron path density almost vanishes. The increased dFe deposition in the Southern Ocean is overwhelmed by the counteracting effects of the increased tropical scavenging in the uptake/destination TRP region. The SO aeolian addition, which injects dFe in the origin region and reduces scavenging outside of the Southern Ocean, results in the largest response in the $\text{SO} \rightarrow \text{TRP}$ iron path density, increasing it up to four times from the unperturbed value. The TRP aeolian addition switches off the $\text{SO} \rightarrow \text{TRP}$ iron paths due to the large increase in tropical scavenging which strips off dFe in productive tropical upwelling regions (similar to the $\text{TRP} \rightarrow \text{SO}$ response for the SO aeolian increase).

3.4 Discussion

Several of the model caveats discussed in Chapter 2 must be kept in mind when interpreting the model’s response to changes in the aeolian iron supply. Our biogeochemical model and the circulation in which it is embedded are steady. Thus, we cannot make any statements about possibly important covariances between iron supply perturbations that in reality would likely be highly seasonal and the seasonality of biological productivity. With our model we could, however, investigate the transient responses of the system to time-dependent perturbations. We have not done so here as this requires time stepping the model and is thus much more computationally demanding. Instead, we have only explored the steady equilibrium states that correspond to changed steady aeolian sources. An investigation of transients and the timescales of the response is beyond the scope of this work and will be considered in a separate study in the future.

Our model neglects a number of iron sources and source mechanisms that could play a role in the response of the real ocean to aeolian iron perturbations. Specifically, we neglect iron input from rivers [e.g., *Rijkenberg et al.*, 2014], icebergs [e.g., *Klunder et al.*, 2011, 2014; *Raiswell et al.*, 2008] and glaciers [e.g., *Gerringa et al.*, 2012], which might become locally important if the aeolian source were to shutdown completely. We also made approximations to the respiration (remineralization) of organic matter and therefore to the iron source from sediments. In reality, respiration rates depend on the concentration of dissolved oxygen, and the distribution of oxygen will almost certainly change with changes in global biological production. To investigate this potentially important feedback mechanism would have required us to carry an oxygen tracer, which would have significantly increased the computational cost of our model. We tacitly assume that the oxygen feedback is of second order.

Because changes in the external iron sources are exactly balanced by the iron sinks, the formulation of scavenging plays a key role in how the system responds. The scavenging processes are poorly constrained observationally. Our model captures scavenging by sinking POP, opal, and dust particles and relies on a prescribed distribution of a single ligand. However, Scavenging is also due to sinking calcium carbonate (CaCO_3), which we do not explicitly represent. The optimization strategy of Chapter 2 likely adjusts the strengths of scavenging by sinking POP, opal, and dust particles to compensate for the lack of scavenging by sinking CaCO_3 . Moreover, in the real ocean, there are multiple types of ligands which are transported by the circulation and which have their own sources and sinks. The sensitivity of ligand concentrations to environmental conditions has direct consequences for iron limitation [e.g., *Hunter and Boyd*, 2007; *Völker and Tagliabue*, 2015]. Hence it is possible ligand dynam-

ics play a role in the response of the real ocean to perturbations of the aeolian iron source. For simplicity, we also ignore colloidal iron, which affects bioavailable surface dFe concentrations [e.g., *Wells et al.*, 1991; *Fitzsimmons and Boyle*, 2014]. Representing the effects of colloidal iron formation, its aggregation into particulate iron, and its redissolution, is beyond the scope of this study.

We found that Southern Ocean silicon trapping increases with increases of the aeolian iron source in our model. This contradicts the silicic acid leakage hypothesis [e.g., *Brzezinski et al.*, 2002; *Matsumoto et al.*, 2002; *Beucher et al.*, 2007], which posits that $\text{Si}(\text{OH})_4$ leaked out from the Southern Ocean due to increased aeolian iron supply during the last glacial maximum. The Si:P formulation (Equation 2.15, Chapter 2) is key for the response of the opal export to perturbations of the aeolian source. Specifically, the Diatom class minimum Si:P ratio, R_0^{Si} , and the iron hyperbolic constant, $k_{\text{Si:P}}^{\text{Fe}}$, set the sensitivity of the Si:P uptake ratio to changes in dFe concentrations, and thus the sensitivity of the opal export. The parameter optimization strategy of Chapter 2 objectively adjusted the Si:P parameters to reduce the mismatch of PO_4 , $\text{Si}(\text{OH})_4$, and dFe with observations. (The optimized parameter values are collected in Table 2.2, Chapter 2.) Accurately modeling changes in the diatom Si:P uptake ratio directly from observations would require a broader collection of observations of diatom elemental stoichiometry than currently available. Exploring the sensitivity of the response of opal export and silicon trapping to these parameters is beyond the scope of this study.

We found that the response of primary production is stronger for global decreases than for global increases of the aeolian source. This is consistent with the response of the coupled phosphorus, silicon, and iron cycle model of *Dutkiewicz et al.* [2005] to global aeolian perturbations. A key difference between our model and the model of *Dutkiewicz et al.* [2005] is that their model did not include sedimentary and hydrothermal sources. However, even though we found that sedimentary and hydrothermal dFe can compensate for losses in aeolian dFe, our results are similar, suggesting that aeolian deposition dominates the response of global biological productivity. Similar to *Dutkiewicz et al.* [2005], we also found that more efficient utilization of PO_4 prevents its lateral transport into subtropical gyres, where carbon export decreases. This is because the two mechanisms that control the regional macronutrient budgets, namely export production and circulation, are similar in both models.

The response in biological production in the subpolar and subtropical North Atlantic for changes in biological utilization in the Southern Ocean are similar to the findings of *Holzer and Primeau* [2013]. Specifically we found changes in North Atlantic production of the same sign, with a stronger response for decreases than for increases of uptake in the Southern Ocean. We note that the circulation used here is the same as for the model of *Holzer and Primeau*

[2013], but that they used a much simpler phosphorus-cycling model and directly perturbed nutrient utilization whereas we indirectly perturbed iron limitation. For our largest Southern Ocean perturbations (complete shutdown and 200 Gmol yr⁻¹ increase of the aeolian source), although we could not reach the complete removal of biological uptake nor complete utilization in the Southern Ocean [unlike *Holzer and Primeau*, 2013], we similarly found that eddy diffusion ultimately prevents complete trapping/untrapping of PO₄. This is because the interplay between biogenic transport and circulation are similar in both models.

3.5 Conclusions

We explored the response of the phosphorus, silicon, and iron cycles to perturbations of the aeolian iron supply. The aeolian iron source was varied from 0 to 200 Gmol Fe yr⁻¹ over three perturbation regions (GBL, SO, TRP). Southern Ocean perturbations were considered because the Southern Ocean is known to play a major role in controlling global nutrient distributions [e.g. *Sarmiento et al.*, 2004]. The tropics are a key region because this is where the aeolian source is concentrated in the unperturbed state. Our main findings are as follows:

- The response of the system is sensitive to the particular state of the iron cycle that is fitted to the current state of the ocean. Unperturbed states with a high aeolian source generally respond strongly to decreases in aeolian iron input, while states with a low aeolian source generally respond strongly to increases in the aeolian iron input. The sensitivity of the perturbations to the fractional iron sources in the unperturbed state are important because the iron source strengths, which span two orders of magnitude in the literature, are not well known [e.g., *Tagliabue et al.*, 2016].
- The response of carbon export is stronger for decreases than for increases of the aeolian iron source, consistent with the iron-modelling of *Dutkiewicz et al.* [2005] and the idealized uptake perturbations of *Holzer and Primeau* [2013]. Decreased aeolian iron input increases iron deficiency in HNLC regions, reducing their export production. The reduced utilization allows more preformed nutrients to be transported laterally into the subtropical gyres [e.g., *Holzer and Primeau*, 2013; *Letscher et al.*, 2016] where biological productivity increases as a result, similar to the findings of *Dutkiewicz et al.* [2005]. Conversely, increased aeolian input relieves iron stress globally and fertilizes HNLC regions where carbon export is increased by as much as 100 mg C m⁻² yr⁻¹, trapping macronutrients and preventing their lateral transport into the subtropical gyres where export production drops.

- The response of opal export is concentrated at high latitudes, particularly in the Southern Ocean. The opal export changes less than carbon export when the aeolian input is perturbed, because of the counteracting effects of the iron dependence of the diatom Si:P uptake ratio [e.g., *Takeda*, 1998; *Hutchins and Bruland*, 1998; *Franck et al.*, 2000; *Brzezinski et al.*, 2003]. While increased dFe concentrations increase carbon export, they decrease the Si:P uptake ratio, muting the response of opal export. Shutting down the aeolian iron supply increases iron deficiency and reduces opal export. The reduced utilization in the Southern Ocean untraps some silicic acid, which is then supplied as preformed Si(OH)_4 to low latitudes. Conversely, increased aeolian iron input fertilizes the Southern Ocean thereby strongly increasing opal export and the silicon trap.
- Shutting down the aeolian iron source reduces surface dFe concentrations globally. Surface dFe concentrations decrease most where the unperturbed aeolian iron supply is large and in the subtropical gyres, which receive dFe supplied laterally. However, surface dFe concentrations are maintained close their unperturbed values in high-productivity regions where export production and thus scavenging are reduced, allowing upwelling sedimentary and hydrothermal dFe to compensate for losses in aeolian dFe. Conversely, increased aeolian iron input results in strongly increased surface dFe concentrations in the subtropical gyres where export production and thus scavenging are low, allowing dFe to accumulate. Even for large increases of the aeolian source, efficient iron export and scavenging in highly productive regions prevent large increases in surface dFe concentrations in these regions. However, in HNLC regions, small increases in dFe are important because the iron Monod term in the uptake formulation is most sensitive to changes at low dFe concentrations.
- Perturbations of the aeolian iron supply also have a strong influence on dFe concentrations in the aphotic zone. Shutting down the aeolian source reduces dFe concentrations predominantly near the surface, while at depth sedimentary and hydrothermal dFe compensate for losses in aeolian dFe. Conversely, increasing the aeolian source strongly increases iron export and scavenging in HNLC regions which supply regenerated and recycled dFe to the ocean interior. The deep local maxima due to regenerated and recycled dFe are found away from upwelling regions and where scavenging is low which allows dFe to accumulate. Increasing the aeolian source also increases dFe concentrations just below the subtropical gyres where scavenging is low.
- Changes in PO_4 concentrations are set by the balance between the circulation and the perturbed biogenic transport. Shutting down the aeolian source decreases the efficiency of the biological pump by reducing carbon export in highly productive regions. Increases in surface PO_4 , which weakens the nutri-

cline, are particularly pronounced in the subtropical gyres, which are supplied by laterally-transported preformed PO_4 . Decreases in surface PO_4 are smaller in highly productive regions where PO_4 is supplied by upwelling. Conversely, increased aeolian iron input fertilizes HNLC regions which increases their carbon export and ships PO_4 out of the euphotic zone, strengthening the nutricline. Increased aeolian iron input thus results in an global increase of regenerated PO_4 and of the global biological pump efficiency.

- The aeolian source shutdown, which decreases the global silicon pump efficiency, increases surface Si(OH)_4 concentrations in the Southern Ocean. As a consequence, additional preformed Si(OH)_4 leaks from the Southern Ocean with SAMW and AAIW and upwells in the eastern tropical Atlantic and Pacific where surface Si(OH)_4 concentrations increase. Conversely, increasing the aeolian source relieves iron stress and increases opal export at high latitudes. This increases the global inventory of regenerated Si(OH)_4 , strengthens the Southern Ocean silicon trap, and reduces the supply of preformed Si(OH)_4 to low latitudes.
- The geographic patterns of nutrient limitation change predominantly in the vicinity of the aeolian iron perturbation region. The aeolian source shutdown expands iron-limited regions and contracts PO_4 -limited regions. In particular, the shrinkage of the PO_4 -limited regions of the subtropical gyres forces an equatorward shift of the Southern Ocean's carbon and opal export. Conversely, for large increases of the aeolian iron source, the global ocean euphotic zone becomes iron replete, while PO_4 limitation is increased. The PO_4 -limited regions expand into higher latitudes, reducing carbon and opal export at the northern edge of the Southern Ocean, and shifting Southern Ocean carbon and opal export poleward.
- Southern Ocean nutrient trapping is a key mechanism in the response to aeolian iron input perturbations. Shutting down the aeolian iron source in regions that overlap with the Southern Ocean untraps some nutrients which then leak as preformed nutrients out of the Southern Ocean with SAMW and AAIW. Neither PO_4 nor Si(OH)_4 are completely untrapped because the Southern Ocean carbon and opal export are sustained by increases in upwelling sedimentary and hydrothermal dFe which are possible due to reduced scavenging. Increases of the aeolian iron source increase Southern Ocean nutrient trapping. This draws more nutrients into the Southern Ocean, which therefore lowers the nutricline at lower latitudes. However, even for extremely large increases of the aeolian source, neither PO_4 nor Si(OH)_4 are completely trapped because export production is capped by the maximum phytoplankton growth rates. Even in the case of complete utilization, eddy diffusion prohibits infinitely large lat-

eral gradients, preventing ever more nutrients from being trapped [e.g., *Primeau et al.*, 2013; *Holzer and Primeau*, 2013].

- Long-range transport in the interior from aeolian deposition to eventual uptake is another key mechanism that mediates the teleconnections of the system. This transport was quantified with the deposition-to-uptake iron path densities ($\text{TRP} \rightarrow \text{SO}$ and $\text{SO} \rightarrow \text{TRP}$). Shutting down or increasing aeolian iron deposition in a given region respectively removes or increases the iron pathways that originate with deposition into that region. Shutting down the aeolian source in the destination region reduces scavenging of upwelling dFe destined for uptake in that region and increases the corresponding path density. Conversely, increasing the aeolian source in the destination region strengthens scavenging which terminates the paths of upwelling dFe before uptake in that region. We find that for increased aeolian input in both the origin and destination regions, the reduction of iron pathways due to increased scavenging at destination dominates the increase of iron pathways due to the additional iron supply in the origin region, so that overall the number of iron pathways is significantly reduced. This is an interesting counterintuitive result that would not easily have been revealed without our new diagnostics.

We hope that future laboratory and field measurements will provide more precise data for constraining the iron dependence of the Si:P uptake ratio. In this study, the parameters of the Si:P ratio were not well constrained, and we can therefore not conclude definitively that our findings prove the silicic-acid-leakage hypothesis [e.g., *Matsumoto et al.*, 2002; *Brzezinski et al.*, 2002; *Beucher et al.*, 2007] to be false. Similarly, advances in quantifying the complex processes of iron scavenging and the role of ligands would allow better constraints on the sinks of dFe and hence narrow the possible source strengths and overall state of the iron cycle. Moreover, more precisely known scavenging processes will narrow the possible responses of the system to iron source perturbations, as we have shown here that this response is sensitive to the unperturbed state of the iron cycle.

Appendices

3.A Changes in Nutrient Limitation

Figure 3.17 shows the resulting nutrient limitation patterns for the Large phytoplankton class, as calculated in Chapter 2, for the shutdown and 50 Gmol yr⁻¹ addition, organised as in Figure 3.5. The patterns are simpler than for the Diatom class (Figure 3.5) because silicic acid is not taken up by the Large class. The GBL shutdown decreases surface dFe and increases surface PO₄. This reinforces iron-only deficiency which almost covers the entire ocean surface (red) at the expense of PO₄ deficiency regions (blue and magenta). The SO aeolian shutdown slightly strengthens iron deficiency while relieving PO₄ deficiency, leaving the global limitation pattern globally unchanged, similar to the response in the case of the Diatom class. Similarly to the GBL shutdown, the TRP shutdown spreads the iron limited HNLC regions (red) at the expense of PO₄ limitation regions (blue and magenta), particularly in the tropics, as expected.

Similar to the Diatom class, the GBL addition relieves iron deficiency almost everywhere and increases PO₄ deficiency due to the increased export. The SO addition relieves SO iron deficiency and shifts the SO boundary of PO₄ limitation poleward. The decrease in surface PO₄ also spreads topical PO₄ limitation regions. The TRP addition relieves the Pacific, 40°S–40°N iron deficiency and does not affect SO and subarctic limitation patterns.

Similarly to Figure 3.17, Figure 3.18 shows the perturbed dFe and PO₄ colimitation patterns for the Small phytoplankton class. Because the Small phytoplankton class is better adapted to low nutrient conditions, it suffers less from nutrient limitations (see Chapter 2). The GBL shutdown decreases surface dFe and increases surface PO₄, resulting in global iron-limitation. The SO aeolian shut down slightly decreases SO surface dFe, spreading the SO iron limitation patches. The TRP shutdown spreads the tropical iron limitation regions and removes PO₄ limitation globally.

Conversely, the Small phytoplankton class in the GBL addition case is globally relieved from iron deficiency and increases PO₄ limitation which spreads everywhere except in HNLC regions. The SO addition completely removes iron

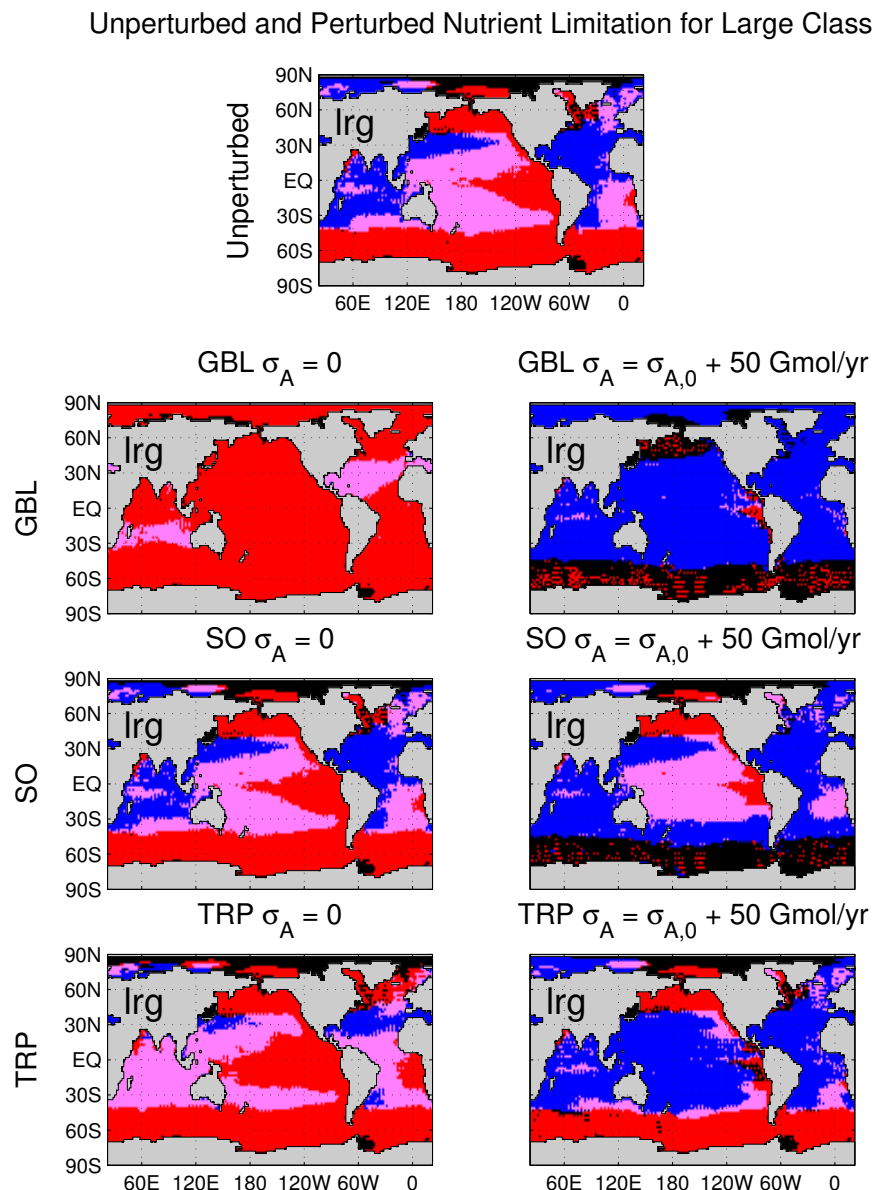


Figure 3.17: Same as figure 3.5 for the Large phytoplankton class.

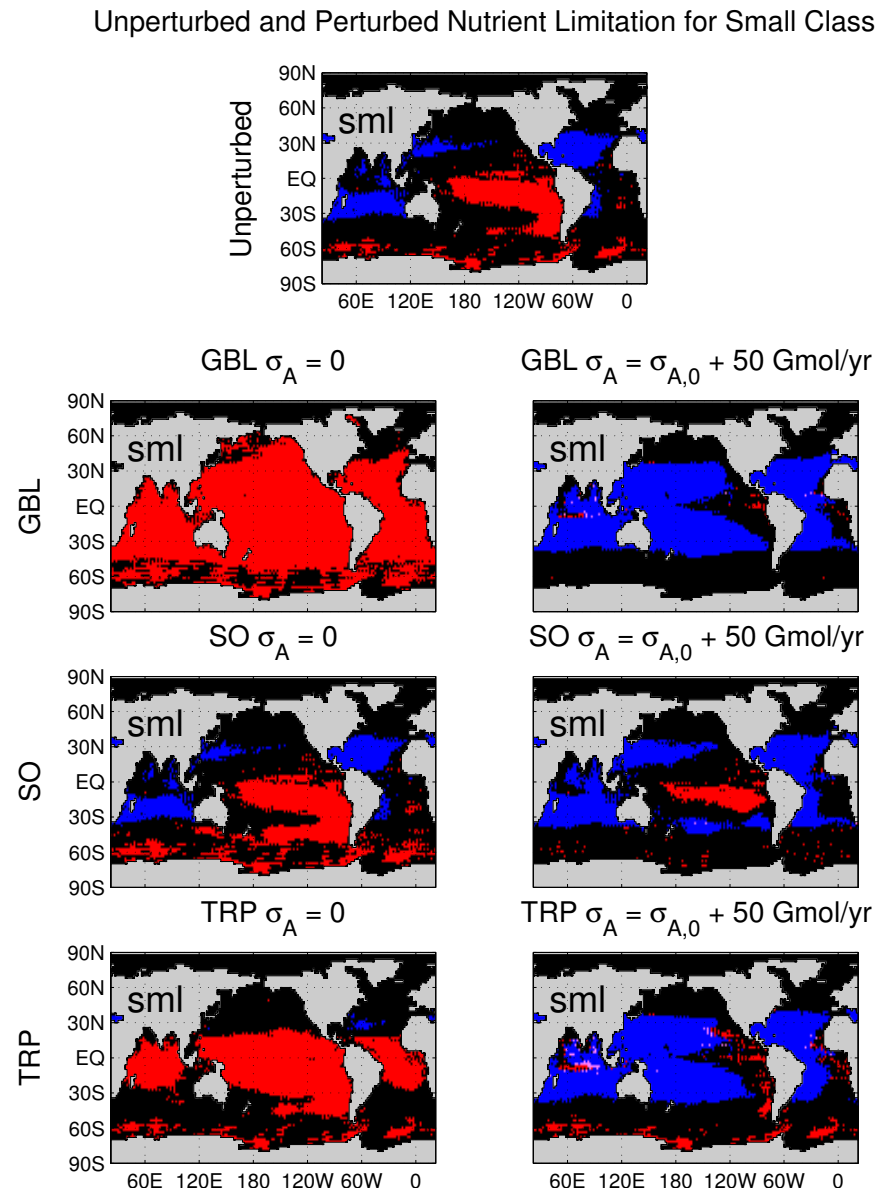


Figure 3.18: Same as figures 3.5 and 3.17 for the Small phytoplankton class.

deficiency in the Southern Ocean together with a significant reduction in tropical Pacific, while PO₄ limitation spreads into subtropical gyres. The TRP addition removes the Pacific iron deficiency almost completely, and, similar to the GBL addition case, the subtropical gyres become largely PO₄ limited.

3.B Computations

3.B.1 Regenerated Nutrients

The regenerated concentration of nutrient i that was last taken up a time t ago during dt is denoted by $g_{\text{reg}}^i(\mathbf{r}, t)dt$. It is given by

$$(\partial_t + \mathcal{T})g_{\text{reg}}^i = \gamma_0 g_{\text{reg}}^i \quad \text{with } g_{\text{reg}}^i(0) = \sum_c U_c^i , \quad (3.1)$$

where $\gamma_0 = 1 \text{ s}^{-1}$ in the euphotic zone only, quickly taking out nutrients entering the euphotic zone. The steady-state concentration of regenerated nutrient i is then given by integrating Equation (3.1) over all times, i.e., $\chi_{\text{reg}}^i = \int_0^\infty g_{\text{reg}}^i(t)dt$, and is efficiently computed by direct inversion (see Appendix 1.A, Chapter 1). The preformed nutrient concentration is computed directly as the difference between total and regenerated nutrient concentrations, i.e., $\chi_{\text{pre}}^i = \chi^i - \chi_{\text{reg}}^i$.

3.B.2 SO→SO path densities for phosphate and silicic acid

The path density, $\eta^i(\mathbf{r}|\text{SO} \rightarrow \text{SO})$, is the concentration of nutrient i at \mathbf{r} that was last taken up in the Southern Ocean and that will next be taken up in the Southern Ocean, regardless of residence time. It is given by

$$\eta^i(\mathbf{r}|\text{SO} \rightarrow \text{SO}) = \chi^i(\mathbf{r}) f_i^\downarrow(\mathbf{r}|\text{SO}) f_i^\uparrow(\mathbf{r}|\text{SO}) , \quad (3.2)$$

where $f_i^\downarrow(\mathbf{r}|\text{SO})$ is the fraction of the nutrient i at \mathbf{r} last taken up biologically in region SO, and $f_i^\uparrow(\mathbf{r}|\text{SO})$ is the fraction of nutrient i at \mathbf{r} that will next be taken up in region SO. We note the remark from Holzer *et al.* [2014] that the fractions $f_i^\downarrow(\mathbf{r}|\text{SO})$ and $f_i^\uparrow(\mathbf{r}|\text{SO})$ partition the nutrient concentration at \mathbf{r} regardless of the nutrient being regenerated or not. (That is, they include nutrients that passed or will pass through the euphotic zone, thereby becoming preformed en route.) The fractions $f_i^\downarrow(\mathbf{r}|\text{SO})$ and $f_i^\uparrow(\mathbf{r}|\text{SO})$ are efficiently computed for steady flow using matrix inversions in the time-forward and time-reversed-adjoint flows, respectively, as detailed by Holzer and Primeau [2013] for phosphate. (We apply the same method for silicic acid.)

The SO trapping metric, R_{trap}^i , is defined as the fraction of the mass of nutrient i that is in SO→SO transit between successive biological uptakes. For each nutrient i , it is given by

$$R_{\text{trap}}^i = \frac{\mu^i(\text{SO} \rightarrow \text{SO})}{\mu^i} \quad , \quad (3.3)$$

where μ^i is the mass of the global inventory of nutrient i , and $\mu^i(\text{SO} \rightarrow \text{SO})$ is the mass of nutrient i in SO→SO transit between successive biological uptakes. These masses are computed by direct inversion as in Appendix 1.B of Chapter 1.

The trapping efficiency, E_{trap}^i , is defined as the ratio of the SO→SO to the SO→Ω nutrient flow rates, where Ω is the entire ocean surface. It is given by

$$E_{\text{trap}}^i = \frac{\Phi^i(\text{SO} \rightarrow \text{SO})}{\Phi^i(\text{SO} \rightarrow \Omega)} \quad , \quad (3.4)$$

where flow rates are calculated by direct inversions (also in Appendix 1.B, Chapter 1).

3.B.3 Deposition-to-Uptake Path densities of Dissolved Iron

To explore the long-range transport of aeolian dFe and its response to perturbations of the aeolian iron source, we define the deposition-to-uptake iron path densities for transports connecting the tropics and the Southern Ocean. The deposition-to-uptake iron path density $\eta^{\text{Fe}}(\mathbf{r}|\Omega_i \rightarrow \Omega_f)$ is the concentration of aeolian dFe at \mathbf{r} that was deposited from the atmosphere in region Ω_i and that will eventually be taken up in region Ω_f , regardless of residence time and regardless of whether the iron was utilized and recycled en route. This path density is given by

$$\eta^{\text{Fe}}(\mathbf{r}|\Omega_i \rightarrow \Omega_f) = \chi^{\text{Fe}}(\mathbf{r}) f_{\text{Fe}}^{\uparrow}(\mathbf{r}|\Omega_f) f_{\text{Fe}}^{\downarrow}(\mathbf{r}|\Omega_i, \Omega_f) \quad , \quad (3.5)$$

where $f_{\text{Fe}}^{\uparrow}(\mathbf{r}|\Omega_f)$ is the fraction of dFe at \mathbf{r} that will eventually be taken in Ω_f and where $f_{\text{Fe}}^{\downarrow}(\mathbf{r}|\Omega_i, \Omega_f)$ is the fraction of dFe at \mathbf{r} that was deposited on Ω_i and that was never taken up in Ω_f . Similar to the steady-state macronutrient fractions, $f_i^{\uparrow}(\mathbf{r}|\text{SO})$ and $f_i^{\downarrow}(\mathbf{r}|\text{SO})$, the steady-state iron fractions, $f_{\text{Fe}}^{\uparrow}(\mathbf{r}|\Omega_f)$ and $f_{\text{Fe}}^{\downarrow}(\mathbf{r}|\Omega_i, \Omega_f)$, are efficiently computed in our model by direct inversions.

Closing Remarks

Truly, we do live on a “water planet”. For us, water is that critical issue that we need. It’s the most precious substance on the planet, and it links us to pretty much every environmental issue, including climate change, that we’re facing.

Jacques-Yves Cousteau, in Interview [Walter, 2009]

This thesis has explored the three-dimensional pathways of the biological pump, has developed a new inverse model of the ocean's coupled phosphorus, silicon, and iron cycles, and has applied this inverse model to explore the role of the iron cycle in shaping biological production and how the system responds to perturbations in aeolian iron input. The work reported here seems to raise at least as many questions as it answers, and I hope to address some of them in future research.

In the near future, we will further apply Green-function techniques to elucidate the detailed workings of the iron cycle, such as a quantification of the importance of iron recycled from scavenging particles, and the pathways of the different source types, i.e., of aeolian, sedimentary, and hydrothermal iron.

Some future research will be directed at addressing the model caveats. For example, we used PO_4 as the main macronutrient and omitted the nitrogen cycle to avoid the complexities of denitrification and nitrogen fixation. However, these complexities also make the nitrogen cycle interesting, and nitrate is often the key nutrient in many observation-based investigations. Moreover there is an abundance of high-quality nitrate and nitrogen isotope data [e.g., *Altabet and McCarthy, 1985; Altabet, 1988; Sigman et al., 2009; Garcia et al., 2014*]. A natural extension of our model would be to couple it to the nitrogen cycle and to subject it to our path and timescale diagnostics. Similarly, adding oxygen would remove uncertainty about our parameterization of remineralization and produce a more realistic sedimentary iron source that would then include feedbacks that are currently missing.

The models explored here have relied on a steady ocean circulation and we have therefore not addressed any aspect of the seasonal cycle of the biological pump [e.g., *Shadwick et al., 2015*] nor the effects of temporal covariance between circulation, biological productivity, and iron sources [e.g., *Gao et al., 2001; Chen and Siefert, 2004*]. In the future, data-assimilated seasonal circulation estimates will become available with which efficient implicit solvers can also be used. A natural extension of the work of this thesis is to explore the interaction of a seasonal circulation with seasonal biological production.

The interactions of the biological pump with the climate system were beyond the scope of this thesis. However, the inner workings of the biological pump together with the coupled nutrient cycles are key to understand the interaction of ocean biogeochemistry and climate change, one of the most pressing science issues of our time. Exploring these interactions quantitatively would require the addition of an explicit carbon cycle to the models used here. An important aspect of the carbon cycle is ocean acidification [e.g., *Orr et al., 2005; Hoegh-Guldberg et al., 2007; Fabry et al., 2008; Doney et al., 2009*], which provides further avenues for important research. The ocean's circulation will change with the climate so that research in this area would ultimately also require

model predictions of future (or past) ocean circulations organized in “transport-matrix” form to permit efficient solvers of the biogeochemistry.

Finally, the ongoing GEOTRACES measurement program provides many exciting opportunities for new perspectives on ocean biogeochemical cycles. Trace metals such as zinc and cobalt are biologically important, but their cycling has yet to be fully understood and modeled [e.g., *Saito et al.*, 2004; *Shelley et al.*, 2012; *Dulaquais et al.*, 2014; *Wyatt et al.*, 2014].

Bibliography

- Albani, S., et al., Paleodust variability since the last glacial maximum and implications for iron inputs to the ocean, *Geophys. Res. Lett.*, 43(8), 3944–3954, doi:10.1002/2016GL067911, 2016GL067911, 2016.
- Altabet, M., Variations in nitrogen isotopic composition between sinking and suspended particles: implications for nitrogen cycling and particle transformation in the open ocean, *Deep Sea Research Part A. Oceanographic Research Papers*, 35(4), 535 – 554, doi:10.1016/0198-0149(88)90130-6, 1988.
- Altabet, M. A., and J. J. McCarthy, Temporal and spatial variations in the natural abundance of ^{15}N in PON from a warm-core ring, *Deep Sea Research Part A. Oceanographic Research Papers*, 32(7), 755 – 772, doi:10.1016/0198-0149(85)90113-X, 1985.
- Alton, P. B., and P. E. Bodin, Model estimates of the land and ocean contributions to biospheric carbon and water fluxes using MODIS satellite data, *J. Climate*, 24(14), 3558–3574, doi:10.1175/2011JCLI3957.1, 2011.
- Archer, D. E., G. Eshel, A. Winguth, W. Broecker, R. Pierrehumbert, M. Tobis, and R. Jacob, Atmospheric pCO_2 sensitivity to the biological pump in the ocean, *Global Biogeochem. Cycles*, 14(4), 1219–1230, doi:10.1029/1999GB001216, 2000.
- Arrigo, K. R., Marine microorganisms and global nutrient cycles, *Nature*, 437(7057), 349–355, doi:10.1038/nature04159, Review, 2005.
- Aumont, O., and L. Bopp, Globalizing results from ocean in situ iron fertilization studies, *GBC*, 20(2), doi:10.1029/2005GB002591, GB2017, 2006.
- Aumont, O., E. Maier-Reimer, S. Blain, and P. Monfray, An ecosystem model of the global ocean including Fe, Si, P colimitations, *Global Biogeochem. Cycles*, 17, doi:10.1029/2001GB001745, 2003.
- Aumont, O., C. Ethé, A. Tagliabue, L. Bopp, and M. Gehlen, PISCES-v2: an ocean biogeochemical model for carbon and ecosystem studies, *Geoscientific Model Development*, 8(8), 2465–2513, doi:10.5194/gmd-8-2465-2015, 2015.

- Bennett, S. A., E. P. Achterberg, D. P. Connolly, P. J. Statham, G. R. Fones, and C. R. German, The distribution and stabilisation of dissolved Fe in deep-sea hydrothermal plumes, *Earth and Planetary Science Letters*, 270(3–4), 157–167, doi:10.1016/j.epsl.2008.01.048, 2008.
- Beucher, C. P., M. A. Brzezinski, and X. Crosta, Silicic acid dynamics in the glacial subantarctic: Implications for the silicic acid leakage hypothesis, *Global Biogeochem. Cycles*, 21, GB3105, doi:3110.1029/2006GB002746, 2007.
- Box, G. E. P., and N. R. Draper, *Empirical Model-building and Response Surface*, John Wiley & Sons, Inc., New York, NY, USA, <http://tocs.ulb.tu-darmstadt.de/205603718.pdf>, 1986.
- Boyd, P. W., and M. J. Ellwood, The biogeochemical cycle of iron in the ocean, *Nature Geosci.*, 3(10), 675–682, doi:10.1038/ngeo964, 2010.
- Boyd, P. W., et al., Mesoscale iron enrichment experiments 1993–2005: Synthesis and future directions, *Science*, 315(5812), 612–617, doi:10.1126/science.1131669, 2007.
- Broecker, W. S., Ocean chemistry during glacial time, *Geochimica et Cosmochimica Acta*, 46(10), 1689–1705, doi:10.1016/0016-7037(82)90110-7, 1982.
- Broecker, W. S., T.-H. Peng, and Z. Beng, *Tracers in the Sea*, Lamont-Doherty Geological Observatory, Columbia University, doi:10.1017/S0033822200005221, 1982.
- Brzezinski, M. A., The Si:C:N ratio of marine diatoms: Interspecific variability and the effect of some environmental variables, *Journal of Phycology*, 21(3), 347–357, doi:10.1111/j.0022-3646.1985.00347.x, 1985.
- Brzezinski, M. A., C. J. Pride, V. M. Franck, D. M. Sigman, J. L. Sarmiento, K. Matsumoto, N. Gruber, G. H. Rau, and K. H. Coale, A switch from $\text{Si}(\text{OH})_4$ to NO_3^- depletion in the glacial Southern Ocean, *Geophys. Res. Lett.*, 29(12), 1564, doi:10.1029/2001GL014349, 2002.
- Brzezinski, M. A., M.-L. Dickson, D. M. Nelson, and R. Sambrotto, Ratios of Si, C and N uptake by microplankton in the Southern Ocean, *Deep Sea Research Part II: Topical Studies in Oceanography*, 50(3-4), 619–633, doi:10.1016/s0967-0645(02)00587-8, 2003.
- Brzezinski, M. A., J. W. Krause, M. J. Church, D. M. Karl, B. Li, J. L. Jones, and B. Updyke, The annual silica cycle of the North Pacific subtropical gyre, *Deep Sea Research Part I: Oceanographic Research Papers*, 58(10), 1988–1001, doi:10.1016/j.dsr.2011.08.001, 2011a.
- Brzezinski, M. A., et al., Co-limitation of diatoms by iron and silicic acid in the equatorial Pacific, *Deep Sea Research Part II: Topical Studies in Oceanography*, 58(3-4), 493–511, doi:10.1016/j.dsr2.2010.08.005, 2011b.

- Buesseler, K. O., The decoupling of production and particulate export in the surface ocean, *Global Biogeochem. Cycles*, 12(2), 297–310, doi:10.1029/97GB03366, 1998.
- Chen, Y., and R. L. Siefert, Seasonal and spatial distributions and dry deposition fluxes of atmospheric total and labile iron over the tropical and subtropical North Atlantic Ocean, *Journal of Geophysical Research: Atmospheres*, 109(D9), doi:10.1029/2003JD003958, d09305, 2004.
- Croot, P. L., P. Streu, and A. R. Baker, Short residence time for iron in surface seawater impacted by atmospheric dry deposition from Saharan dust events, *Geophys. Res. Lett.*, 31, L23S08, doi:10.1029/2004GL020153, 2004.
- de Baar, H., von Liebig's law of the minimum and plankton ecology (1899–1991), *Progress in Oceanography*, 33(4), 347–386, doi:10.1016/0079-6611(94)90022-1, 1994.
- de Baar, H. J. W., J. T. M. de Jong, D. C. E. Bakker, B. M. Loscher, C. Veth, U. Bathmann, and V. Smetacek, Importance of iron for plankton blooms and carbon dioxide drawdown in the Southern Ocean, *Nature*, 373, 412–415, doi:10.1038/373412a0, 1995.
- de Baar, H. J. W., et al., Synthesis of iron fertilization experiments: From the iron age in the age of enlightenment, *Journal of Geophysical Research: Oceans*, 110(C9), doi:10.1029/2004JC002601, C09S16, 2005.
- Deutsch, C., and T. Weber, Nutrient ratios as a tracer and driver of ocean biogeochemistry, *Annual Review of Marine Science*, 4(1), 113–141, doi:10.1146/annurev-marine-120709-142821, 2012.
- DeVries, T., The oceanic anthropogenic CO₂ sink: Storage, air-sea fluxes, and transports over the industrial era, *Global Biogeochem. Cycles*, 28(7), 631–647, doi:10.1002/2013GB004739, 2014.
- DeVries, T., and F. Primeau, Dynamically and observationally constrained estimates of water-mass distributions and ages in the global ocean, *J. Phys. Oceanogr.*, 41, 2381–2401, doi:10.1175/JPO-D-10-05011.1, 2011.
- DeVries, T., F. Primeau, and C. Deutsch, The sequestration efficiency of the biological pump, *Geophys. Res. Lett.*, 39, L13601, doi:10.1029/2012GL051963, 2012.
- DeVries, T., M. Holzer, and F. Primeau, Recent increase in oceanic carbon uptake driven by weaker upper-ocean overturning, *Nature*, 542(7640), 215–218, doi:10.1038/nature21068, 2017.
- Doney, S. C., K. Lindsay, I. Fung, and J. John, Natural variability in a stable, 1000-yr global coupled climate-carbon cycle simulation, *J. Climate*, 19(13), 3033–3054, doi:10.1175/JCLI3783.1, 2006.

- Doney, S. C., V. J. Fabry, R. A. Feely, and J. A. Kleypas, Ocean acidification: the other CO₂ problem, *Annual review of marine science*, 1, 169–192, doi:10.1146/annurev.marine.010908.163834, 2009.
- Droop, M. R., The nutrient status of algal cells in continuous culture, *Journal of the Marine Biological Association of the United Kingdom*, 54(4), 825–855, doi:10.1017/S002531540005760X, 2009.
- Dulaquais, G., M. Boye, R. Middag, S. Owens, V. Puigcorbe, K. Buesseler, P. Masqué, H. J. W. de Baar, and X. Carton, Contrasting biogeochemical cycles of cobalt in the surface western Atlantic Ocean, *Global Biogeochem. Cycles*, 28(12), 1387–1412, doi:10.1002/2014GB004903, 2014.
- Dunne, J. P., R. A. Armstrong, A. Gnanadesikan, and J. L. Sarmiento, Empirical and mechanistic models for the particle export ratio, *Global Biogeochem. Cycles*, 19(4), doi:10.1029/2004gb002390, 2005.
- Dunne, J. P., J. L. Sarmiento, and A. Gnanadesikan, A synthesis of global particle export from the surface ocean and cycling through the ocean interior and on the seafloor, *Global Biogeochem. Cycles*, 21, GB4006, doi:10.1029/2006GB002907, 2007.
- Dunne, J. P., et al., GFDL's ESM2 global coupled climate-carbon earth system models. part II: Carbon system formulation and baseline simulation characteristics, *J. Climate*, 26(7), 2247–2267, doi:10.1175/JCLI-D-12-00150.1, 2013.
- Dutay, J.-C., et al., Evaluation of OCMIP-2 ocean models' deep circulation with mantle helium-3, *Journal of Marine Systems*, 48(1–4), 15–36, doi:10.1016/j.jmarsys.2003.05.010, 2004.
- Dutkiewicz, S., M. J. Follows, and P. Parekh, Interactions of the iron and phosphorus cycles: A three-dimensional model study, *Global Biogeochem. Cycles*, 19(1), doi:10.1029/2004GB002342, GB1021, 2005.
- Dutkiewicz, S., M. J. Follows, P. Heimbach, and J. Marshall, Controls on ocean productivity and air-sea carbon flux: An adjoint model sensitivity study, *Geophys. Res. Lett.*, 33, doi:10.1029/2005GL024987, 2006.
- Dutkiewicz, S., B. A. Ward, F. Monteiro, and M. J. Follows, Interconnection of nitrogen fixers and iron in the Pacific Ocean: Theory and numerical simulations, *Global Biogeochem. Cycles*, 26(1), doi:10.1029/2011GB004039, GB1012, 2012.
- Dutkiewicz, S., J. R. Scott, and M. J. Follows, Winners and losers: Ecological and biogeochemical changes in a warming ocean, *Global Biogeochem. Cycles*, 27(2), 463–477, doi:10.1002/gbc.20042, 2013.

- Dutkiewicz, S., B. A. Ward, J. R. Scott, and M. J. Follows, Understanding predicted shifts in diazotroph biogeography using resource competition theory, *Biogeosciences*, 11(19), 5445–5461, doi:10.5194/bg-11-5445-2014, 2014.
- Dutkiewicz, S., A. E. Hickman, O. Jahn, W. W. Gregg, C. B. Mouw, and M. J. Follows, Capturing optically important constituents and properties in a marine biogeochemical and ecosystem model, *Biogeosciences*, 12(14), 4447–4481, doi:10.5194/bg-12-4447-2015, 2015.
- Elrod, V. A., W. M. Berelson, K. H. Coale, and K. S. Johnson, The flux of iron from continental shelf sediments: A missing source for global budgets, *Geophys. Res. Lett.*, 31(12), doi:10.1029/2004GL020216, L12307, 2004.
- Eppley, R. W., Temperature and phytoplankton growth in the sea, *Fish. Bull.*, 70(4), 1063–1085, <http://fishbull.noaa.gov/70-4/eppley.pdf>, 1972.
- Fabry, V. J., B. A. Seibel, R. A. Feely, and J. C. Orr, Impacts of ocean acidification on marine fauna and ecosystem processes, *ICES Journal of Marine Science: Journal du Conseil*, 65(3), 414–432, doi:10.1093/icesjms/fsn048, 2008.
- Falkowski, P. G., R. T. Barber, and V. Smetacek, Biogeochemical controls and feedbacks on ocean primary production, *Science*, 281(5374), 200–206, doi:10.1126/science.281.5374.200, 1998.
- Field, C. B., M. J. Behrenfeld, J. T. Randerson, and P. Falkowski, Primary production of the biosphere: Integrating terrestrial and oceanic components, *Science*, 281(5374), 237–240, doi:10.1126/science.281.5374.237, 1998.
- Fitzsimmons, J. N., and E. A. Boyle, Both soluble and colloidal iron phases control dissolved iron variability in the tropical North Atlantic Ocean, *Geochimica et Cosmochimica Acta*, 125, 539–550, doi:10.1016/j.gca.2013.10.032, 2014.
- Flynn, K. J., Modelling multi-nutrient interactions in phytoplankton - balancing simplicity and realism, *Progress in Oceanography*, 56(2), 249–279, doi:10.1016/s0079-6611(03)00006-5, 2003.
- Follows, M. J., S. Dutkiewicz, S. Grant, and S. W. Chisholm, Emergent biogeography of microbial communities in a model ocean, *Science*, 315(5820), 1843–1846, doi:10.1126/science.1138544, 2007.
- Franck, V. M., M. A. Brzezinski, K. H. Coale, and D. M. Nelson, Iron and silicic acid concentrations regulate Si uptake north and south of the Polar Frontal Zone in the Pacific Sector of the Southern Ocean, *Deep Sea Research Part II: Topical Studies in Oceanography*, 47(15–16), 3315–3338, doi:10.1016/S0967-0645(00)00070-9, US Southern Ocean JGOFS Program (AESOPS), 2000.

- Frants, M., M. Holzer, T. DeVries, and R. Matear, Constraints on the global marine iron cycle from a simple inverse model, *Journal of Geophysical Research: Biogeosciences*, 121(1), 28–51, doi:10.1002/2015jg003111, 2016.
- Galbraith, E. D., A. Gnanadesikan, J. P. Dunne, and M. R. Hiscock, Regional impacts of iron-light colimitation in a global biogeochemical model, *Biogeosciences*, 7(3), 1043–1064, doi:10.5194/bg-7-1043-2010, 2010.
- Galbraith, E. D., et al., Complex functionality with minimal computation: Promise and pitfalls of reduced-tracer ocean biogeochemistry models, *Journal of Advances in Modeling Earth Systems*, 7(4), 2012–2028, doi:10.1002/2015MS000463, 2015.
- Ganachaud, A., and C. Wunsch, Improved estimates of global ocean circulation, heat transport and mixing from hydrographic data, *Nature*, 408(6811), 453–457, doi:10.1038/35044048, 2000.
- Ganachaud, A., and C. Wunsch, Oceanic nutrient and oxygen transports and bounds on export production during the World Ocean Circulation Experiment, *Global Biogeochem. Cycles*, 16, 1057, doi:10.1029/2000GB001333, 2002.
- Gao, Y., Y. J. Kaufman, D. Tanré, D. Kolber, and P. G. Falkowski, Seasonal distributions of aeolian iron fluxes to the global ocean, *Geophys. Res. Lett.*, 28(1), 29–32, doi:10.1029/2000GL011926, 2001.
- Garcia, H. E., R. A. Locarnini, T. P. Boyer, and J. I. Antonov, World Ocean Atlas 2005, *NOAA Atlas NESDIS 64*, U.S. Government Printing Office, Washington, D.C., Volume 4: Nutrients (phosphate, nitrate, silicate), 396pp, S. Levitus, Ed., 2006.
- Garcia, H. E., R. A. Locarnini, T. P. Boyer, and J. I. Antonov, World Ocean Atlas 2009, *NOAA Atlas NESDIS 71*, U.S. Government Printing Office, Washington, D.C., Volume 4: Nutrients (phosphate, nitrate, silicate), 398pp, S. Levitus Ed., 2010.
- Garcia, H. E., R. A. Locarnini, T. P. Boyer, J. I. Antonov, O. K. Baranova, M. M. Zweng, J. R. Reagan, and D. R. Johnson, World Ocean Atlas 2013, *NOAA Atlas NESDIS 76*, U.S. Government Printing Office, Washington, D.C., Volume 4: Dissolved Inorganic Nutrients (phosphate, nitrate, silicate), S. Levitus, Ed., A. Mishonov Technical Ed., 2014.
- Garnier, J., A. Beusen, V. Thieu, G. Billen, and L. Bouwman, N:P:Si nutrient export ratios and ecological consequences in coastal seas evaluated by the ICEP approach, *Global Biogeochem. Cycles*, 24(4), doi:10.1029/2009GB003583, GB0A05, 2010.
- Geider, R., and J. L. Roche, Redfield revisited: variability of C:N:P in marine microalgae and its biochemical basis, *European Journal of Phycology*, 37(1), 1–17, doi:10.1017/S0967026201003456, 2002.

- Gerringa, L. J., A.-C. Alderkamp, P. Laan, C.-E. Thuróczy, H. J. D. Baar, M. M. Mills, G. L. van Dijken, H. van Haren, and K. R. Arrigo, Iron from melting glaciers fuels the phytoplankton blooms in Amundsen Sea (Southern Ocean): Iron biogeochemistry, *Deep Sea Research Part II: Topical Studies in Oceanography*, 71–76, 16–31, doi:10.1016/j.dsr2.2012.03.007, 2012.
- Gilpin, L., K. Davidson, and E. Roberts, The influence of changes in nitrogen:silicon ratios on diatom growth dynamics, *Journal of Sea Research*, 51(1), 21–35, doi:10.1016/j.seares.2003.05.005, 2004.
- Gnanadesikan, A., A global model of silicon cycling: Sensitivity to eddy parameterization and dissolution, *Global Biogeochem. Cycles*, 13(1), 199–220, doi:10.1029/1998GB900013, 1999.
- Gnanadesikan, A., J. P. Dunne, R. M. Key, K. Matsumoto, J. L. Sarmiento, R. D. Slater, and P. S. Swathi, Oceanic ventilation and biogeochemical cycling: Understanding the physical mechanisms that produce realistic distributions of tracers and productivity, *Global Biogeochem. Cycles*, 18(4), doi:10.1029/2003GB002097, GB4010, 2004.
- Gran, H. H., et al., On the conditions for the production of plankton in the sea, *Rapp. Proc. Verb. Cons. Int. Explor. Mer.*, 75, 37–46, 1931.
- Hall, T. M., and M. Holzer, Advective-diffusive mass flux and implications for stratosphere-troposphere exchange, *Geophys. Res. Lett.*, 30(5), 1222, doi:10.1029/2002GL016419, 2003.
- Hall, T. M., T. W. N. Haine, M. Holzer, D. A. LeBel, F. Terenzi, and D. W. Waugh, Ventilation rates estimated from tracers in the presence of mixing, *J. Phys. Oceanogr.*, 37, 2599–2611, doi:10.1175/2006JPO3471.1, 2007.
- Hart, T. J., On the phytoplankton of the south-west atlantic and the bellingshausen sea, 1929–31, *Discovery Reports*, VIII, 1–268, 1934.
- Hauck, J., P. Köhler, D. Wolf-Gladrow, and C. Völker, Iron fertilisation and century-scale effects of open ocean dissolution of olivine in a simulated CO₂ removal experiment, *Environmental Research Letters*, 11(2), 024,007, doi:10.1088/1748-9326/11/2/024007, 2016.
- Hawkes, J., D. Connelly, M. Gledhill, and E. Achterberg, The stabilisation and transportation of dissolved iron from high temperature hydrothermal vent systems, *Earth and Planetary Science Letters*, 375, 280–290, doi:10.1016/j.epsl.2013.05.047, 2013.
- Heinze, C., A. Hupe, E. Maier-Reimer, N. Dittert, and O. Ragueneau, Sensitivity of the marine biospheric Si cycle for biogeochemical parameter variations, *Global Biogeochem. Cycles*, 17, 1086, doi:10.1029/2002GB001943, 2003.

- Hoegh-Guldberg, O., et al., Coral reefs under rapid climate change and ocean acidification, *Science*, 318(5857), 1737–1742, doi:10.1126/science.1152509, 2007.
- Hofmann, M., and H.-J. Schellnhuber, Oceanic acidification affects marine carbon pump and triggers extended marine oxygen holes, *Proceedings of the National Academy of Sciences*, 106(9), 3017–3022, doi:10.1073/pnas.0813384106, 2009.
- Holzer, M., The path density of interhemispheric surface-to-surface transport. Part I: Development of the diagnostic and illustration with an analytic model, *J. Atmos. Sci.*, 66, 2159–2171, doi:10.1175/2009JAS2894.1, 2009.
- Holzer, M., and T. M. Hall, Transit-time and tracer-age distributions in geophysical flows, *J. Atmos. Sci.*, 57(21), 3539–3558, doi:10.1175/1520-0469(2000)057<3539:TTATAD>2.0.CO;2, 2000.
- Holzer, M., and F. W. Primeau, The diffusive ocean conveyor, *Geophys. Res. Lett.*, 33, L14618, doi:10.1029/2006GL026232, 2006.
- Holzer, M., and F. W. Primeau, The path-density distribution of oceanic surface-to-surface transport, *J. Geophys. Res.*, 113, C01018, doi:10.1029/2006JC003976, 2008.
- Holzer, M., and F. W. Primeau, Global teleconnections in the oceanic phosphorus cycle: patterns, paths, and timescales, *J. Geophys. Res.*, 118, 1775–1796, doi:10.1002/jgrc.20072, 2013.
- Holzer, M., C. Orbe, and F. W. Primeau, Stratospheric mean residence time and mean age at the tropopause: Connections and implications for observational constraints, *J. Geophys. Res.*, 117, D12314, doi:10.1029/2012JD017547, 2012.
- Holzer, M., F. W. Primeau, T. DeVries, and R. Matear, The southern ocean silicon trap: Data-constrained estimates of regenerated silicic acid, trapping efficiencies, and global transport paths, *Journal of Geophysical Research: Oceans*, 119(1), 313–331, doi:10.1002/2013JC009356, 2014.
- Holzer, M., M. Frants, and B. Pasquier, The age of iron and iron source attribution in the ocean, *Global Biogeochem. Cycles*, doi:10.1002/2016GB005418, 2016GB005418, 2016.
- Holzer, M., T. DeVries, D. Bianchi, R. Newton, P. Schlosser, and G. Winckler, Objective estimates of mantle ^3He in the ocean and implications for constraining the deep ocean circulation, *Earth and Planetary Science Letters*, 458, 305–314, doi:10.1016/j.epsl.2016.10.054, 2017.
- Howarth, R. W., Nutrient limitation of net primary production in marine ecosystems, *Annual Review of Ecology and Systematics*, 19(1), 89–110, doi:10.1146/annurev.es.19.110188.000513, 1988.

- Hunter, K. A., and P. W. Boyd, Iron-binding ligands and their role in the ocean biogeochemistry of iron, *Environmental Chemistry*, 4(4), 221–232, doi:10.1071/EN07012, 2007.
- Hutchins, D. A., and P. W. Boyd, Marine phytoplankton and the changing ocean iron cycle, *Nature Clim. Change*, 6(12), 1072–1079, doi:10.1038/nclimate3147, 2016.
- Hutchins, D. A., and K. W. Bruland, Iron-limited diatom growth and Si:N uptake ratios in a coastal upwelling regime, *Nature*, 393(6685), 561–564, doi:10.1038/31203, 1998.
- Hutchins, D. A., A. E. Witter, A. Butler, and G. W. Luther, Competition among marine phytoplankton for different chelated iron species, *Nature*, 400(6747), 858–861, doi:10.1038/23680, 1999.
- Ito, T., and M. J. Follows, Preformed phosphate, soft-tissue pump and atmospheric CO₂, *Journal of Marine Research*, 63, 813–839, doi:10.1357/0022240054663231, 2005.
- Jin, X., N. Gruber, J. P. Dunne, J. L. Sarmiento, and R. A. Armstrong, Diagnosing the contribution of phytoplankton functional groups to the production and export of particulate organic carbon, CaCO₃, and opal from global nutrient and alkalinity distributions, *Global Biogeochem. Cycles*, 20, GB2015, doi:10.1029/2005GB002532, 2006.
- Johnson, H. P., S. L. Hautala, T. A. Bjorklund, and M. R. Zarnetske, Quantifying the North Pacific silica plume, *Geochem. Geophys. Geosyst.*, 7(5), Q05011, doi:10.1029/2005GC001065, 2006.
- Johnson, M. S., et al., Modeling dust and soluble iron deposition to the South Atlantic Ocean, *J. Geophys. Res.*, 115, D15202, doi:10.1029/2009JD013311, 2010.
- Kelley, C. T., *Solving Nonlinear Equations with Newton's Method*, chap. 1. Introduction, pp. 1–25, SIAM, doi:10.1137/1.9780898718898.ch1, 2003a.
- Kelley, C. T., *Solving Nonlinear Equations with Newton's Method*, chap. 2. Finding the Newton Step with Gaussian Elimination, pp. 27–55, SIAM, doi:10.1137/1.9780898718898.ch2, 2003b.
- Klunder, M., P. Laan, R. Middag, H. D. Baar, and J. van Ooijen, Dissolved iron in the Southern Ocean (Atlantic sector), *Deep Sea Research Part II: Topical Studies in Oceanography*, 58(25–26), 2678–2694, doi:10.1016/j.dsr2.2010.10.042, 2011.
- Klunder, M. B., P. Laan, H. J. W. De Baar, R. Middag, I. Neven, and J. Van Ooijen, Dissolved Fe across the Weddell Sea and Drake Passage: impact of DFe on nutrient uptake, *Biogeosciences*, 11(3), 651–669, doi:10.5194/bg-11-651-2014, 2014.
- Kostadinov, T. S., D. A. Siegel, and S. Maritorena, Retrieval of the particle size distribution from satellite ocean color observations, *Journal of Geophysical Research: Oceans*, 114(C9), doi:10.1029/2009JC005303, 2009.

- Kostadinov, T. S., S. Milutinović, I. Marinov, and A. Cabré, Carbon-based phytoplankton size classes retrieved via ocean color estimates of the particle size distribution, *Ocean Science*, 12(2), 561–575, doi:10.5194/os-12-561-2016, 2016.
- Kostadinov, T. S., S. Milutinović, I. Marinov, and A. Cabré, Size-partitioned phytoplankton carbon concentrations retrieved from ocean color data, links to data in netCDF format, doi:10.1594/PANGAEA.859005, 2016.
- Kriest, I., and A. Oschlies, On the treatment of particulate organic matter sinking in large-scale models of marine biogeochemical cycles, *Biogeosciences*, 5(1), 55–72, doi:10.5194/bg-5-55-2008, 2008.
- Kwon, E. Y., and F. Primeau, Sensitivity and optimization study of a biogeochemistry ocean model using an implicit solver and in-situ phosphate data, *Global Biogeochem. Cycles*, 20, GB4009, doi:10.1029/2005GB002631, 2006.
- Kwon, E. Y., and F. Primeau, Optimization and sensitivity of a global biogeochemistry ocean model using combined in situ DIC, alkalinity, and phosphate data, *Journal of Geophysical Research: Oceans*, 113(C8), doi:10.1029/2007JC004520, C08011, 2008.
- Letscher, R. T., F. Primeau, and J. K. Moore, Nutrient budgets in the subtropical ocean gyres dominated by lateral transport, *Nature Geosci*, 9(11), 815–819, doi:10.1038/ngeo2812, 2016.
- Levitus, S., Climatological atlas of the world ocean, *Eos, Transactions American Geophysical Union*, 64(49), 962–963, doi:10.1029/EO064i049p00962-02, 1983.
- Levitus, S., M. E. Conkright, J. L. Reid, R. G. Najjar, and A. Mantyla, Distribution of nitrate, phosphate and silicate in the world oceans, *Progress in Oceanography*, 31, 245–273, doi:10.1016/0079-6611(93)90003-V, 1993.
- Lill, G. G., and A. E. Maxwell, The earth's mantle, *Science*, 129(3360), 1407–1410, doi:10.1126/science.129.3360.1407, 1959.
- Loladze, I., and J. J. Elser, The origins of the Redfield nitrogen-to-phosphorus ratio are in a homoeostatic protein-to-rRNA ratio, *Ecology Letters*, 14(3), 244–250, doi:10.1111/j.1461-0248.2010.01577.x, 2011.
- Lumpkin, R., and K. Speer, Global Ocean Meridional Overturning, *J. Phys. Oceanogr.*, 37, 2550–2562, doi:10.1175/JPO3130.1, 2007.
- Lundry, M. R., et al., Iron and grazing constraints on primary production in the central equatorial Pacific: An EqPac synthesis, *Limnology and Oceanography*, 42(3), 405–418, doi:10.4319/lo.1997.42.3.0405, 1997.
- Luo, C., N. Mahowald, T. Bond, P. Y. Chuang, P. Artaxo, R. Siefert, Y. Chen, and J. Schauer, Combustion iron distribution and deposition, *Global Biogeochem. Cycles*, 22(1), doi:10.1029/2007GB002964, GB1012, 2008.

- Marchetti, A., M. S. Parker, L. P. Moccia, E. O. Lin, A. L. Arrieta, F. Ribalet, M. E. P. Murphy, M. T. Maldonado, and E. V. Armbrust, Ferritin is used for iron storage in bloom-forming marine pennate diatoms, *Nature*, 457(7228), 467–470, doi:10.1038/nature07539, 2009a.
- Marchetti, A., D. E. Varela, V. P. Lance, V. P. Lance, M. Palmucci, M. Giordano, and E. V. Armbrust, Iron and silicic acid effects on phytoplankton productivity, diversity, and chemical composition in the central equatorial Pacific Ocean, *Limnol. Oceanogr.*, 55(1), 11–29, doi:10.4319/lo.2010.55.1.0011, 2009b.
- Marinov, I., A. Gnanadesikan, J. R. Toggweiler, and J. L. Sarmiento, The Southern Ocean biogeochemical divide, *Nature*, 441, 964–967, doi:10.1038/nature04883, 2006.
- Marinov, I., M. Follows, A. Gnanadesikan, J. L. Sarmiento, and R. D. Slater, How does ocean biology affect atmospheric $p\text{CO}_2$? Theory and models, *J. Geophys. Res.*, 113(C7), doi:10.1029/2007JC004598, C07032, 2008a.
- Marinov, I., A. Gnanadesikan, J. L. Sarmiento, J. R. Toggweiler, M. Follows, and B. K. Mignone, Impact of oceanic circulation on biological carbon storage in the ocean and atmospheric $p\text{CO}_2$, *Global Biogeochem. Cycles*, 22, GB3007, doi:10.1029/2007GB002958, 2008b.
- Martin, J. H., Glacial-interglacial CO_2 change: The Iron Hypothesis, *Paleoceanography*, 5(1), 1–13, doi:10.1029/PA005i001p00001, 1990.
- Martin, J. H., and S. E. Fitzwater, Iron deficiency limits phytoplankton growth in the north-east Pacific subarctic, *Nature*, 331(6154), 341–343, doi:10.1038/331341a0, 1988.
- Massoth, G. J., E. T. Baker, R. A. Feely, D. A. Butterfield, R. E. Embley, J. E. Lupton, R. E. Thomson, and G. A. Cannon, Observations of manganese and iron at the CoAxial Seafloor Eruption Site, Juan de Fuca Ridge, *Geophys. Res. Lett.*, 22(2), 151–154, doi:10.1029/94GL02662, 1995.
- Matsumoto, K., J. L. Sarmiento, and M. A. Brzezinski, Silicic acid leakage from the Southern Ocean: A possible explanation for glacial atmospheric $p\text{CO}_2$, *Global Biogeochem. Cycles*, 16(3), 1031, doi:10.1029/2001GB001442, 2002.
- Matsumoto, K., K. S. Tokos, A. R. Price, and S. J. Cox, First description of the Minnesota Earth System Model for Ocean biogeochemistry (MESMO 1.0), *Geoscientific Model Development*, 1(1), 1–15, doi:10.5194/gmd-1-1-2008, 2008.
- Matsumoto, K., K. Tokos, A. Huston, and H. Joy-Warren, MESMO 2: a mechanistic marine silica cycle and coupling to a simple terrestrial scheme, *Geoscientific Model Development*, 6(2), 477–494, doi:10.5194/gmd-6-477-2013, 2013.
- Mawji, E., et al., The GEOTRACES intermediate data product 2014, *Marine Chemistry*, 177, Part 1, 1–8, doi:10.1016/j.marchem.2015.04.005, 2015.

- Measures, C. I., W. M. Landing, M. T. Brown, and C. S. Buck, A commercially available rosette system for trace metal-clean sampling, *Limnology and Oceanography: Methods*, 6(9), 384–394, doi:10.4319/lom.2008.6.384, 2008.
- Misumi, K., K. Lindsay, J. K. Moore, S. C. Doney, D. Tsumune, and Y. Yoshida, Humic substances may control dissolved iron distributions in the global ocean: Implications from numerical simulations, *Global Biogeochem. Cycles*, 27(2), 450–462, doi:10.1002/gbc.20039, 2013.
- Monod, J., *Microbiologie: Recherches sur la croissance des cultures bactériennes. I, Actualités scientifiques et industrielles*, Hermann & cie, <https://books.google.com.au/books?id=uF58nQEACAAJ>, 1942.
- Moore, C. M., et al., Processes and patterns of oceanic nutrient limitation, *Nature Geoscience*, 6, 701–710, doi:10.1038/NGEO1765, 2013a.
- Moore, J., S. C. Doney, D. M. Glover, and I. Y. Fung, Iron cycling and nutrient-limitation patterns in surface waters of the World Ocean, *Deep Sea Research Part II: Topical Studies in Oceanography*, 49(1-3), 463–507, doi:10.1016/S0967-0645(01)00109-6, the US JGOFS Synthesis and Modeling Project: Phase 1, 2001.
- Moore, J. K., and O. Braucher, Sedimentary and mineral dust sources of dissolved iron to the world ocean, *Biogeosciences*, 5(3), 631–656, doi:10.5194/bg-5-631-2008, 2008.
- Moore, J. K., S. C. Doney, and K. Lindsay, Upper ocean ecosystem dynamics and iron cycling in a global three-dimensional model, *Global Biogeochem. Cycles*, 18, GB4028, doi:10.1029/2004GB002220, 2004.
- Moore, J. K., K. Lindsay, S. C. Doney, M. C. Long, and K. Misumi, Marine ecosystem dynamics and biogeochemical cycling in the Community Earth System Model [CESM1(BGC)]: Comparison of the 1990s with the 2090s under the RCP4.5 and RCP8.5 scenarios, *J. Climate*, 26(23), 9291–9312, doi:10.1175/JCLI-D-12-00566.1, 2013b.
- Morel, A., and R. C. Smith, Relation between total quanta and total energy for aquatic photosynthesis, *Limnology and Oceanography*, 19(4), 591–600, doi:10.4319/lo.1974.19.4.0591, 1974.
- Morse, P. M., H. Feshbach, et al., *Methods of theoretical physics*, 997 pp., McGraw-Hill New York, 1953.
- Najjar, R. G., J. L. Sarmiento, and J. R. Toggweiler, Downward transport and fate of organic matter in the ocean: Simulations with a general circulation model, *Global Biogeochem. Cycles*, 6(1), 45–76, doi:10.1029/91GB02718, 1992.

- Najjar, R. G., et al., Impact of circulation on export production, dissolved organic matter, and dissolved oxygen in the ocean: Results from Phase II of the Ocean Carbon-cycle Model Intercomparison Project (OCMIP-2), *Global Biogeochem. Cycles*, 21(3), doi:10.1029/2006GB002857, GB3007, 2007.
- NASA Goddard Space Flight Center, O. B. P. G., Ocean Ecology Laboratory, Modis-aqua ocean color data, doi:10.5067/AQUA/MODIS_OC.2014.0, 2014.
- National Geophysical Data Center, ETOPO2v2 2-minute Global Relief Model, doi:10.7289/V5J1012Q, 2006.
- Needham, J., and W. Pagel (Eds.), *Background to Modern Science: Ten Lectures at Cambridge Arranged by the History of Science Committee*, 99–100 pp., Cambridge University Press, 1938.
- Nelson, D. M., P. Tréguer, M. A. Brzezinski, A. Leynaert, and B. Quéguiner, Production and dissolution of biogenic silica in the ocean: Revised global estimates, comparison with regional data and relationship to biogenic sedimentation, *Global Biogeochem. Cycles*, 9(3), 359–372, doi:10.1029/95GB01070, 1995.
- Nickelsen, L., and A. Oschlies, Enhanced sensitivity of oceanic CO₂ uptake to dust deposition by iron-light colimitation, *Geophys. Res. Lett.*, 42(2), 492–499, doi:10.1002/2014GL062969, 2014GL062969, 2015.
- Orr, J. C., et al., Anthropogenic ocean acidification over the twenty-first century and its impact on calcifying organisms, *Nature*, 437(7059), 681–686, doi:10.1038/nature04095, 2005.
- Palter, J. B., J. L. Sarmiento, A. Gnanadesikan, J. Simeon, and R. D. Slater, Fueling export production: nutrient return pathways from the deep ocean and their dependence on the Meridional Overturning Circulation, *Biogeosciences*, 7, 3549–3568, doi:10.5194/bg-7-3549-2010, 2010.
- Parekh, P., M. J. Follows, and E. Boyle, Modeling the global ocean iron cycle, *Global Biogeochem. Cycles*, 18(1), doi:10.1029/2003GB002061, GB1002, 2004.
- Parekh, P., M. J. Follows, and E. A. Boyle, Decoupling of iron and phosphate in the global ocean, *Global Biogeochem. Cycles*, 19(2), doi:10.1029/2004GB002280, GB2020, 2005.
- Pasquier, B., and M. Holzer, The plumbing of the global biological pump: Efficiency control through leaks, pathways, and time scales, *Journal of Geophysical Research: Oceans*, 121(8), 6367–6388, doi:10.1002/2016JC011821, 2016.
- Pelegrí, J. L., G. T. Csanady, and A. Martins, The North Atlantic nutrient stream, *Journal of Oceanography*, 52(3), 275–299, doi:10.1007/BF02235924, 1996.

- Pelegrí, J. L., and G. T. Csanady, Nutrient transport and mixing in the Gulf Stream, *Journal of Geophysical Research: Oceans*, 96(C2), 2577–2583, doi:10.1029/90JC02535, 1991.
- Press, W. H., B. P. Flannery, S. A. Teukolsky, W. T. Vetterling, et al., *Numerical recipes*, vol. 3, cambridge University Press, cambridge, 1989.
- Primeau, F. W., and M. Holzer, The ocean's memory of the atmosphere: Residence-time and ventilation-rate distributions of water masses, *J. Phys. Oceanogr.*, 36, 1439–1456, doi:10.1175/JPO2919.1, 2006.
- Primeau, F. W., M. Holzer, and T. DeVries, Southern Ocean nutrient trapping and the efficiency of the biological pump, *J. Geophys. Res.*, 118, 2547–2564, doi:10.1002/jgrc.20181, 2013.
- Raiswell, R., L. G. Benning, M. Tranter, and S. Tulaczyk, Bioavailable iron in the Southern Ocean: the significance of the iceberg conveyor belt, *Geochemical Transactions*, 9(1), 7, doi:10.1186/1467-4866-9-7, 2008.
- Raven, J. A., and P. G. Falkowski, Oceanic sinks for atmospheric CO₂, *Plant, Cell & Environment*, 22(6), 741–755, doi:10.1046/j.1365-3040.1999.00419.x, 1999.
- Redfield, A. C., On the proportions of organic derivatives in sea water and their relation to the composition of plankton, *Daniel, R.J. (ed James Johnstone Memorial Volume)*, pp. 177–192, 1934.
- Rhee, G.-Y., Effects of n:p atomic ratios and nitrate limitation on algal growth, cell composition, and nitrate uptake 1, *Limnology and Oceanography*, 23(1), 10–25, doi:10.4319/lo.1978.23.1.00010, 1978.
- Rijkenberg, M. J. A., R. Middag, P. Laan, L. J. A. Gerringa, H. M. van Aken, V. Schöemann, J. T. M. de Jong, and H. J. W. de Baar, The distribution of dissolved iron in the West Atlantic Ocean, *PLoS ONE*, 9(6), e101323, doi:10.1371/journal.pone.0101323, 2014.
- Saito, M. A., J. W. Moffett, and G. R. DiTullio, Cobalt and nickel in the Peru upwelling region: A major flux of labile cobalt utilized as a micronutrient, *Global Biogeochem. Cycles*, 18(4), doi:10.1029/2003GB002216, gB4030, 2004.
- Saito, M. A., T. J. Goepfert, and J. T. Ritt, Some thoughts on the concept of colimitation: Three definitions and the importance of bioavailability, *Limnology and Oceanography*, 53(1), 276–290, doi:10.4319/lo.2008.53.1.0276, 2008.
- Sarmiento, J. L., and N. Gruber, *Ocean Biogeochemical Dynamics*, 503 pp., Princeton Univ. Press, Princeton and Oxford, 2006.

- Sarmiento, J. L., N. Gruber, M. A. Brzezinski, and J. P. Dunne, High-latitude controls of thermocline nutrients and low latitude biological productivity, *Nature*, 427(6969), 56–60, doi:10.1038/nature02127, 2004.
- Sarmiento, J. L., J. Simeon, A. Gnanadesikan, N. Gruber, R. M. Key, and R. Schlitzer, Deep ocean biogeochemistry of silicic acid and nitrate, *Global Biogeochem. Cycles*, 21, GB1S9, doi:10.1029/2006GB002720, 2007.
- Schmitz, W. J., On the interbasin-scale thermohaline circulation, *Reviews of Geophysics*, 33(2), 151–173, doi:10.1029/95RG00879, 1995.
- Shadwick, E. H., T. W. Trull, B. Tilbrook, A. J. Sutton, E. Schulz, and C. L. Sabine, Seasonality of biological and physical controls on surface ocean CO₂ from hourly observations at the Southern Ocean Time Series site south of Australia, *Global Biogeochem. Cycles*, 29(2), 223–238, doi:10.1002/2014GB004906, 2014GB004906, 2015.
- Shelley, R. U., et al., Controls on dissolved cobalt in surface waters of the Sargasso Sea: Comparisons with iron and aluminum, *Global Biogeochem. Cycles*, 26(2), doi:10.1029/2011GB004155, gB2020, 2012.
- Sigman, D., K. Karsh, and K. Casciotti, Nitrogen isotopes in the ocean, in *Encyclopedia of Ocean Sciences (Second Edition)*, edited by J. H. Steele, second edition ed., pp. 40–54, Academic Press, Oxford, doi:10.1016/B978-012374473-9.00632-9, 2009.
- Sigman, D. M., M. P. Hain, and G. H. Haug, The polar ocean and glacial cycles in atmospheric CO₂ concentration, *Nature*, 466(7302), 47–55, doi:10.1038/nature09149, 2010.
- Smith, S. V., Phosphorus versus nitrogen limitation in the marine environment, *Limnology and Oceanography*, 29(6), 1149–1160, doi:10.4319/lo.1984.29.6.1149, 1984.
- Sonnerup, R. E., S. Mecking, and J. L. Bullister, Transit time distributions and oxygen utilization rates in the Northeast Pacific Ocean from chlorofluorocarbons and sulfur hexafluoride, *Deep Sea Research Part I: Oceanographic Research Papers*, 72, 61–71, doi:10.1016/j.dsr.2012.10.013, 2013.
- Sonnerup, R. E., S. Mecking, J. L. Bullister, and M. J. Warner, Transit time distributions and oxygen utilization rates from chlorofluorocarbons and sulfur hexafluoride in the Southeast Pacific Ocean, *Journal of Geophysical Research: Oceans*, 120(5), 3761–3776, doi:10.1002/2015JC010781, 2015.
- Sterner, R. W., T. Andersen, J. J. Elser, D. O. Hessen, J. M. Hood, E. McCauley, and J. Urabe, Scale-dependent carbon:nitrogen:phosphorus seston stoichiometry in marine and freshwaters, *Limnology and Oceanography*, 53(3), 1169–1180, doi:10.4319/lo.2008.53.3.1169, 2008.

- Stock, C. A., J. P. Dunne, and J. G. John, Global-scale carbon and energy flows through the marine planktonic food web: An analysis with a coupled physical-biological model, *Progress in Oceanography*, 120, 1–28, doi:10.1016/j.pocean.2013.07.001, 2014.
- Strzepek, R. F., K. A. Hunter, R. D. Frew, P. J. Harrison, and P. W. Boyd, Iron-light interactions differ in Southern Ocean phytoplankton, *Limnol. Oceanogr.*, 57(4), 1182–1200, doi:10.4319/lo.2012.57.4.1182, 2012.
- Sun, S., and R. Bleck, Thermohaline circulation studies with an isopycnic coordinate ocean model, *J. Phys. Oceanogr.*, 31(9), 2761–2782, doi:10.1175/1520-0485(2001)031<2761:TCSWAI>2.0.CO;2, 2001.
- Sunda, W. G., and S. A. Huntsman, Iron uptake and growth limitation in oceanic and coastal phytoplankton, *Marine Chemistry*, 50(1), 189 – 206, doi:10.1016/0304-4203(95)00035-P, the Chemistry of Iron in Seawater and its Interaction with Phytoplankton, 1995.
- Sunda, W. G., and S. A. Huntsman, Interrelated influence of iron, light and cell size on marine phytoplankton growth, *Nature*, 390(6658), 389–392, doi:10.1038/37093, 1997.
- Tagliabue, A., T. Mtshali, O. Aumont, A. R. Bowie, M. B. Klunder, A. N. Roychoudhury, and S. Swart, A global compilation of dissolved iron measurements: focus on distributions and processes in the Southern Ocean, *Biogeosciences*, 9(6), 2333–2349, doi:10.5194/bg-9-2333-2012, 2012.
- Tagliabue, A., O. Aumont, and L. Bopp, The impact of different external sources of iron on the global carbon cycle, *Geophys. Res. Lett.*, 41(3), 920–926, doi:10.1002/2013GL059059, 2013GL059059, 2014.
- Tagliabue, A., et al., How well do global ocean biogeochemistry models simulate dissolved iron distributions?, *Global Biogeochem. Cycles*, 30(2), 149–174, doi:10.1002/2015gb005289, 2016.
- Takeda, S., Influence of iron availability on nutrient consumption ratio of diatoms in oceanic waters, *Nature*, 393(6687), 774–777, doi:10.1038/31674, 1998.
- Talley, L. D., Antarctic Intermediate Water in the South Atlantic, in *The South Atlantic: Present and Past Circulation*, edited by G. W. et al., pp. 219–238, Springer, Berlin, doi:10.1007/978-3-642-80353-6_11, 1996.
- Teng, Y.-C., F. W. Primeau, J. K. Moore, M. W. Lomas, and A. C. Martiny, Global-scale variations of the ratios of carbon to phosphorus in exported marine organic matter, *Nature Geosci.*, 7(12), 895–898, doi:10.1038/ngeo2303, 2014.
- Toggweiler, J. R., and B. Samuels, New radiocarbon constraints on the upwelling of abyssal water to the ocean's surface, in *The Global Carbon Cycle, NATO ASI Ser. I, Global Environ. Change*, edited by M. Heinmann, pp. 333–366, Springer, Berlin, doi:10.1007/978-3-642-84608-3_14, 1993.

- Trenberth, K. E., W. G. Large, and J. G. Olson, A global ocean wind stress climatology based on ECMWF analyses, *Tech. Rep. TN-3381STR*, National Center for Atmospheric Research, doi:10.5065/D6ST7MR9, 1989.
- Twining, B. S., et al., Differential remineralization of major and trace elements in sinking diatoms, *Limnol. Oceanogr.*, 59, 689–704, doi:10.4319/lo.2014.59.3.0689, 2014.
- Tyrrell, T., The relative influences of nitrogen and phosphorus on oceanic primary production, *Nature*, 400(6744), 525–531, doi:10.1038/22941, 1999.
- Tyrrell, T., and C. S. Law, Low nitrate:phosphate ratios in the global ocean, *Nature*, 387(6635), 793–796, 1997.
- Uitz, J., H. Claustre, B. Gentili, and D. Stramski, Phytoplankton class-specific primary production in the world's oceans: Seasonal and interannual variability from satellite observations, *Global Biogeochem. Cycles*, 24, GB3016, doi:10.1029/2009GB003680, 2010.
- Vichi, M., N. Pinardi, and S. Masina, A generalized model of pelagic biogeochemistry for the global ocean ecosystem. Part I: Theory, *Journal of Marine Systems*, 64(1-4), 89–109, doi:10.1016/j.jmarsys.2006.03.006, 2007.
- Volk, T., and M. I. Hoffert, Ocean carbon pumps: Analysis of relative strengths and efficiencies in ocean-driven atmospheric CO₂ changes, in *The Carbon Cycle and Atmospheric CO₂: Natural Variations Archean to Present*, *Geophysical Monograph* 32, edited by E. T. Sundquist and W. S. Broecker, American Geophysical Union, 1985.
- Völker, C., and A. Tagliabue, Modeling organic iron-binding ligands in a three-dimensional biogeochemical ocean model, *Marine Chemistry*, 173, 67–77, doi:10.1016/j.marchem.2014.11.008, 2015.
- Walter, K., Water tops conservation issues, Cousteau Jr. says, *Newsmax*, Interview, 2009.
- Weber, T., and C. Deutsch, Local versus basin-scale limitation of marine nitrogen fixation, *Proceedings of the National Academy of Sciences*, 111(24), 8741–8746, doi:10.1073/pnas.1317193111, 2014.
- Weber, T., J. A. Cram, S. W. Leung, T. DeVries, and C. Deutsch, Deep ocean nutrients imply large latitudinal variation in particle transfer efficiency, *Proc. Natl. Acad. Sci.*, 113, 8606–8611, doi:10.1073/pnas.1604414113, 2016.
- Weber, T. S., and C. Deutsch, Ocean nutrient ratios governed by plankton biogeography, *Nature*, 467(7315), 550–554, doi:10.1038/nature09403, 2010.
- Weier, J., On the shoulders of giants, [accessed online on the 10th of March 2017] earthobservatory.nasa.gov/Features/Martin, 2001.

- Wells, M. L., L. M. Mayer, O. F. X. Donard, M. M. de Souza Sierra, and S. G. Ackelson, The photolysis of colloidal iron in the oceans, *Nature*, 353(6341), 248–250, doi:10.1038/353248a0, 1991.
- Williams, R. G., V. Roussenov, and M. J. Follows, Nutrient streams and their induction into the mixed layer, *Global Biogeochem. Cycles*, 20, GB1016, doi:10.1029/2005GB002586, 2006.
- Williams, R. G., E. McDonagh, V. M. Roussenov, S. Torres-Valdés, B. King, R. Sanders, and D. A. Hansell, Nutrient streams in the North Atlantic: Advective pathways of inorganic and dissolved organic nutrients, *Global Biogeochem. Cycles*, 25, GB4008, doi:10.1029/2010GB003853, 2011.
- Wyatt, N. J., A. Milne, E. M. S. Woodward, A. P. Rees, T. J. Browning, H. A. Bouman, P. J. Worsfold, and M. C. Lohan, Biogeochemical cycling of dissolved zinc along the GEOTRACES South Atlantic transect GA10 at 40°S, *Global Biogeochem. Cycles*, 28(1), 44–56, doi:10.1002/2013GB004637, 2013GB004637, 2014.
- Yool, A., E. E. Popova, and T. R. Anderson, Medusa-1.0: a new intermediate complexity plankton ecosystem model for the global domain, *Geoscientific Model Development*, 4(2), 381–417, doi:10.5194/gmd-4-381-2011, 2011.
- Yool, A., E. E. Popova, and T. R. Anderson, Medusa-2.0: an intermediate complexity biogeochemical model of the marine carbon cycle for climate change and ocean acidification studies, *Geoscientific Model Development*, 6(5), 1767–1811, doi:10.5194/gmd-6-1767-2013, 2013.
- Zeebe, R. E., and D. Archer, Feasibility of ocean fertilization and its impact on future atmospheric CO₂ levels, *Geophys. Res. Lett.*, 32(9), doi:10.1029/2005GL022449, l09703, 2005.